

# 1 Global Carbon Budget 2022

2  
3 Pierre Friedlingstein<sup>1,2</sup>, Michael O'Sullivan<sup>1</sup>, Matthew W. Jones<sup>3</sup>, Robbie M. Andrew<sup>4</sup>, Luke  
4 Gregor<sup>5</sup>, Judith Hauck<sup>6</sup>, Corinne Le Quééré<sup>3</sup>, Ingrid T. Luijckx<sup>7</sup>, Are Olsen<sup>8,9</sup>, Glen P. Peters<sup>4</sup>,  
5 Wouter Peters<sup>7,10</sup>, Julia Pongratz<sup>11,12</sup>, Clemens Schwingshackl<sup>11</sup>, Stephen Sitch<sup>1</sup>, Josep G.  
6 Canadell<sup>13</sup>, Philippe Ciais<sup>14</sup>, Robert B. Jackson<sup>15</sup>, Simone Alin<sup>16</sup>, Ramdane Alkama<sup>17</sup>, Almut  
7 Armeth<sup>18</sup>, Vivek K. Arora<sup>19</sup>, Nicholas R. Bates<sup>20,21</sup>, Meike Becker<sup>8,9</sup>, Nicolas Bellouin<sup>22</sup>, Henry  
8 C. Bittig<sup>23</sup>, Laurent Bopp<sup>2</sup>, Frédéric Chevallier<sup>14</sup>, Louise P. Chini<sup>24</sup>, Margot Cronin<sup>25</sup>, Wiley  
9 Evans<sup>26</sup>, Stefanie Falk<sup>11</sup>, Richard A. Feely<sup>16</sup>, Thomas Gasser<sup>27</sup>, Marion Gehlen<sup>14</sup>, Thanos  
10 Gkritzalis<sup>28</sup>, Lucas Gloege<sup>29,30</sup>, Giacomo Grassi<sup>17</sup>, Nicolas Gruber<sup>5</sup>, Özgür Gürses<sup>6</sup>, Ian  
11 Harris<sup>31</sup>, Matthew Hefner<sup>32,33</sup>, Richard A. Houghton<sup>34</sup>, George C. Hurtt<sup>24</sup>, Yosuke Iida<sup>35</sup>,  
12 Tatiana Ilyina<sup>12</sup>, Atul K. Jain<sup>36</sup>, Annika Jersild<sup>12</sup>, Koji Kadono<sup>35</sup>, Etsushi Kato<sup>37</sup>, Daniel  
13 Kennedy<sup>38</sup>, Kees Klein Goldewijk<sup>39</sup>, Jürgen Knauer<sup>40,41</sup>, Jan Ivar Korsbakken<sup>4</sup>, Peter  
14 Landschützer<sup>12,28</sup>, Nathalie Lefèvre<sup>42</sup>, Keith Lindsay<sup>43</sup>, Junjie Liu<sup>44</sup>, Zhu Liu<sup>45</sup>, Gregg  
15 Marland<sup>32,33</sup>, Nicolas Mayot<sup>3</sup>, Matthew J. McGrath<sup>14</sup>, Nicolas Metzler<sup>42</sup>, Natalie M. Monacci<sup>46</sup>,  
16 David R. Munro<sup>47,48</sup>, Shin-Ichiro Nakaoka<sup>49</sup>, Yosuke Niwa<sup>49,50</sup>, Kevin O'Brien<sup>51,16</sup>, Tsuneo  
17 Ono<sup>52</sup>, Paul I. Palmer<sup>53,54</sup>, Naiqing Pan<sup>55,56</sup>, Denis Pierrot<sup>57</sup>, Katie Pocock<sup>26</sup>, Benjamin  
18 Poulter<sup>58</sup>, Laure Resplandy<sup>59</sup>, Eddy Robertson<sup>60</sup>, Christian Rödenbeck<sup>61</sup>, Carmen Rodriguez<sup>62</sup>,  
19 Thais M. Rosan<sup>1</sup>, Jörg Schwinger<sup>63,9</sup>, Roland Séférian<sup>64</sup>, Jamie D. Shutler<sup>1</sup>, Ingunn Skjelvan<sup>63,9</sup>,  
20 Tobias Steinhoff<sup>65</sup>, Qing Sun<sup>66</sup>, Adrienne J. Sutton<sup>16</sup>, Colm Sweeney<sup>48</sup>, Shintaro Takao<sup>49</sup>, Toste  
21 Tanhua<sup>65</sup>, Pieter P. Tans<sup>67,68</sup>, Xiangjun Tian<sup>69</sup>, Hanqin Tian<sup>56</sup>, Bronte Tilbrook<sup>70,71</sup>, Hiroyuki  
22 Tsujino<sup>50</sup>, Francesco Tubiello<sup>72</sup>, Guido R. van der Werf<sup>73</sup>, Anthony P. Walker<sup>74</sup>, Rik  
23 Wanninkhof<sup>57</sup>, Chris Whitehead<sup>75</sup>, Anna Willstrand Wranne<sup>76</sup>, Rebecca Wright<sup>3</sup>, Wenping  
24 Yuan<sup>77</sup>, Chao Yue<sup>78</sup>, Xu Yue<sup>79</sup>, Sönke Zaehle<sup>61</sup>, Jiye Zeng<sup>49</sup>, Bo Zheng<sup>80</sup>

25  
26 <sup>1</sup> Faculty of Environment, Science and Economy, University of Exeter, Exeter EX4 4QF, UK  
27 <sup>2</sup> Laboratoire de Météorologie Dynamique / Institut Pierre-Simon Laplace, CNRS, Ecole Normale  
28 Supérieure / Université PSL, Sorbonne Université, Ecole Polytechnique, Paris, France  
29 <sup>3</sup> Tyndall Centre for Climate Change Research, School of Environmental Sciences, University of  
30 East Anglia, Norwich Research Park, Norwich NR4 7TJ, UK  
31 <sup>4</sup> CICERO Center for International Climate Research, Oslo 0349, Norway  
32 <sup>5</sup> Environmental Physics Group, ETH Zürich, Institute of Biogeochemistry and Pollutant Dynamics  
33 and Center for Climate Systems Modeling (C2SM), Zurich, Switzerland  
34 <sup>6</sup> Alfred-Wegener-Institut Helmholtz-Zentrum für Polar- und Meeresforschung, Postfach 120161,  
35 27515 Bremerhaven, Germany  
36 <sup>7</sup> Wageningen University, Environmental Sciences Group, P.O. Box 47, 6700AA, Wageningen, The  
37 Netherlands  
38 <sup>8</sup> Geophysical Institute, University of Bergen, Bergen, Norway  
39 <sup>9</sup> Bjerknes Centre for Climate Research, Bergen, Norway  
40 <sup>10</sup> University of Groningen, Centre for Isotope Research, Groningen, The Netherlands  
41 <sup>11</sup> Ludwig-Maximilians-Universität Munich, Luisenstr. 37, 80333 München, Germany  
42 <sup>12</sup> Max Planck Institute for Meteorology, Hamburg, Germany  
43 <sup>13</sup> CSIRO Oceans and Atmosphere, Canberra, ACT 2101, Australia  
44 <sup>14</sup> Laboratoire des Sciences du Climat et de l'Environnement, LSCE/IPSL, CEA-CNRS-UVSQ,  
45 Université Paris-Saclay, F-91191 Gif-sur-Yvette, France  
46 <sup>15</sup> Department of Earth System Science, Woods Institute for the Environment, and Precourt  
47 Institute for Energy, Stanford University, Stanford, CA 94305-2210, United States of America  
48 <sup>16</sup> National Oceanic & Atmospheric Administration, Pacific Marine Environmental Laboratory  
49 (NOAA/PMEL), 7600 Sand Point Way NE, Seattle, WA 98115, USA  
50 <sup>17</sup> Joint Research Centre, European Commission, Ispra, Italy  
51 <sup>18</sup> Karlsruhe Institute of Technology, Institute of Meteorology and Climate Research/Atmospheric  
52 Environmental Research, 82467 Garmisch-Partenkirchen, Germany  
53

**Style Definition:** Heading 1: Outline numbered + Level: 1 +  
Numbering Style: 1, 2, 3, ... + Start at: 1 + Alignment: Left +  
Aligned at: 0.63 cm + Indent at: 1.27 cm

**Style Definition:** Heading 2: Outline numbered + Level: 2 +  
Numbering Style: a, b, c, ... + Start at: 1 + Alignment: Left +  
Aligned at: 1.9 cm + Indent at: 2.54 cm

**Style Definition:** Heading 3: Outline numbered + Level: 3 +  
Numbering Style: i, ii, iii, ... + Start at: 1 + Alignment: Right  
+ Aligned at: 3.49 cm + Indent at: 3.81 cm

**Style Definition:** Heading 4: Outline numbered + Level: 4 +  
Numbering Style: 1, 2, 3, ... + Start at: 1 + Alignment: Left +  
Aligned at: 4.44 cm + Indent at: 5.08 cm

**Style Definition:** Heading 5: Outline numbered + Level: 5 +  
Numbering Style: a, b, c, ... + Start at: 1 + Alignment: Left +  
Aligned at: 5.71 cm + Indent at: 6.35 cm

**Style Definition:** Heading 6: Outline numbered + Level: 6 +  
Numbering Style: i, ii, iii, ... + Start at: 1 + Alignment: Right  
+ Aligned at: 7.3 cm + Indent at: 7.62 cm

**Style Definition:** Heading 7: Outline numbered + Level: 7 +  
Numbering Style: 1, 2, 3, ... + Start at: 1 + Alignment: Left +  
Aligned at: 8.25 cm + Indent at: 8.89 cm

**Style Definition:** Heading 8: Outline numbered + Level: 8 +  
Numbering Style: a, b, c, ... + Start at: 1 + Alignment: Left +  
Aligned at: 9.52 cm + Indent at: 10.16 cm

**Style Definition:** Heading 9: Outline numbered + Level: 9 +  
Numbering Style: i, ii, iii, ... + Start at: 1 + Alignment: Right  
+ Aligned at: 11.11 cm + Indent at: 11.43 cm

**Formatted:** Numbering: Continuous

**Formatted:** Add space between paragraphs of the same style

**Formatted:** Space Before: 0 pt, Add space between  
paragraphs of the same style

**Deleted:** Tian<sup>68</sup>

**Deleted:** Tilbrook<sup>69,70</sup>

**Formatted:** Font: Superscript

**Deleted:** Tubiello<sup>71</sup>

**Deleted:** Werf<sup>72</sup>

**Deleted:** Walker<sup>73</sup>

**Deleted:** Whitehead<sup>74</sup>

**Deleted:** Wranne<sup>75</sup>

**Deleted:** Yuan<sup>76</sup>

**Deleted:** Yue<sup>77</sup>, Xu

**Deleted:** Zheng<sup>79</sup>

**Formatted:** Font: English (UK)

**Formatted:** Font: English (UK)

**Formatted:** Font: (Default) Calibri, 12 pt, Not Superscript/  
Subscript

64 <sup>19</sup> Canadian Centre for Climate Modelling and Analysis, Climate Research Division, Environment  
65 and Climate Change Canada, Victoria, BC, Canada  
66 <sup>20</sup> Bermuda Institute of Ocean Sciences (BIOS), 17 Biological Lane, St. Georges, GE01, Bermuda  
67 <sup>21</sup> Department of Ocean and Earth Science, University of Southampton, European Way,  
68 Southampton, SO14 3ZH, UK  
69 <sup>22</sup> Department of Meteorology, University of Reading, Reading, UK  
70 <sup>23</sup> Leibniz Institute for Baltic Sea Research Warnemuende (IOW), Seestrasse 15; 18119 Rostock,  
71 Germany  
72 <sup>24</sup> Department of Geographical Sciences, University of Maryland, College Park, Maryland 20742,  
73 USA  
74 <sup>25</sup> Marine Institute, Galway, Ireland  
75 <sup>26</sup> Hakai Institute, Heriot Bay, BC, Canada  
76 <sup>27</sup> International Institute for Applied Systems Analysis (IIASA), Schlossplatz 1  
77 A-2361 Laxenburg, Austria  
78 <sup>28</sup> Flanders Marine Institute (VLIZ), InnovOceanSite, Wandelaarkaai 7, 8400 Ostend, Belgium  
79 <sup>29</sup> Lamont-Doherty Earth Observatory and Department of Earth and Environmental Sciences,  
80 Columbia University, New York, NY, USA  
81 <sup>30</sup> Open Earth Foundation, Marina del Rey, CA, USA  
82 <sup>31</sup> NCAS-Climate, Climatic Research Unit, School of Environmental Sciences, University of East  
83 Anglia, Norwich Research Park, Norwich, NR4 7TJ, UK  
84 <sup>32</sup> Research Institute for Environment, Energy, and Economics, Appalachian State University,  
85 Boone, North Carolina, USA  
86 <sup>33</sup> Department of Geological and Environmental Sciences, Appalachian State University, Boone,  
87 North Carolina, USA  
88 <sup>34</sup> Woodwell Climate Research Center, Falmouth, MA 02540, USA  
89 <sup>35</sup> Atmosphere and Ocean Department, Japan Meteorological Agency, Minato-Ku, Tokyo 105-  
90 8431, Japan  
91 <sup>36</sup> Department of Atmospheric Sciences, University of Illinois, Urbana, IL 61821, USA  
92 <sup>37</sup> Institute of Applied Energy (IAE), Minato-ku, Tokyo 105-0003, Japan  
93 <sup>38</sup> National Center for Atmospheric Research, Climate and Global Dynamics, Terrestrial Sciences  
94 Section, Boulder, CO 80305, USA  
95 <sup>39</sup> Utrecht University, Faculty of Geosciences, Department IMEW, Copernicus Institute of  
96 Sustainable Development, Heidelberglaan 2, P.O. Box 80115, 3508 TC, Utrecht, the Netherlands  
97 <sup>40</sup> Hawkesbury Institute for the Environment, Western Sydney University, Penrith, New South  
98 Wales, Australia  
99 <sup>41</sup> Climate Science Centre, CSIRO Oceans and Atmosphere, Canberra, ACT, Australia  
100 <sup>42</sup> LOCEAN/IPSL laboratory, Sorbonne Université, CNRS/IRD/MNHN, Paris, France  
101 <sup>43</sup> National Center for Atmospheric Research, Climate and Global Dynamics, Oceanography  
102 Section, Boulder, CO 80305, USA  
103 <sup>44</sup> Jet Propulsion Laboratory, California Institute of Technology, Pasadena, CA, USA  
104 <sup>45</sup> Department of Earth System Science, Tsinghua University, Beijing, China  
105 <sup>46</sup> University of Alaska Fairbanks, College of Fisheries and Ocean Sciences, PO Box 757220,  
106 Fairbanks, AK, USA  
107 <sup>47</sup> Cooperative Institute for Research in Environmental Sciences, University of Colorado, Boulder,  
108 CO, 80305, USA  
109 <sup>48</sup> National Oceanic & Atmospheric Administration/Global Monitoring Laboratory (NOAA/GML),  
110 Boulder, CO, 80305, USA  
111 <sup>49</sup> Earth System Division, National Institute for Environmental Studies (NIES), 16-2 Onogawa,  
112 Tsukuba Ibaraki, 305-8506, Japan  
113 <sup>50</sup> Meteorological Research Institute, 1-1 Nagamine, Tsukuba, Ibaraki, 305-0052 Japan  
114 <sup>51</sup> Cooperative Institute for Climate, Ocean and Ecosystem Studies (CICOES), University of  
115 Washington, Seattle, WA, USA  
116 <sup>52</sup> Japan Fisheries Research and Education Agency, 2-12-4 Fukuura, Kanazawa-Ku, Yokohama 236-  
117 8648, Japan  
118 <sup>53</sup> National Centre for Earth Observation, University of Edinburgh, UK  
119 <sup>54</sup> School of GeoSciences, University of Edinburgh, UK  
120 <sup>55</sup> College of Forestry, Wildlife and Environment, Auburn University, Auburn, AL 36849, USA  
121 <sup>56</sup> Schiller Institute for Integrated Science and Society, Department of Earth and Environmental  
122 Sciences, Boston College, Chestnut Hill, MA 02467, USA  
123

Formatted: Space Before: 0 pt, Add space between paragraphs of the same style

Deleted: Forestry

Formatted: Font: (Default) Calibri, 12 pt, Not Superscript/ Subscript

125 <sup>57</sup> National Oceanic & Atmospheric Administration/Atlantic Oceanographic & Meteorological  
 126 Laboratory (NOAA/AOML), Miami, FL 33149, USA  
 127 <sup>58</sup> NASA Goddard Space Flight Center, Biospheric Sciences Laboratory, Greenbelt, Maryland  
 128 20771, USA  
 129 <sup>59</sup> Princeton University, Department of Geosciences and Princeton Environmental Institute,  
 130 Princeton, NJ, USA  
 131 <sup>60</sup> Met Office Hadley Centre, FitzRoy Road, Exeter EX1 3PB, UK  
 132 <sup>61</sup> Max Planck Institute for Biogeochemistry, P.O. Box 600164, Hans-Knöll-Str. 10, 07745 Jena,  
 133 Germany  
 134 <sup>62</sup> University of Miami, RSMAS, 4600 Rickenbacker Causeway, Miami, FL 33149, USA  
 135 <sup>63</sup> NORCE Norwegian Research Centre, Jahnebakken 5, 5007 Bergen, Norway  
 136 <sup>64</sup> CNRM, Université de Toulouse, Météo-France, CNRS, Toulouse, France  
 137 <sup>65</sup> GEOMAR Helmholtz Centre for Ocean Research Kiel, Düsternbrooker Weg 20, 24105 Kiel,  
 138 Germany  
 139 <sup>66</sup> Climate and Environmental Physics, Physics Institute and Oeschger Centre for Climate Change  
 140 Research, University of Bern, Bern, Switzerland  
 141 <sup>67</sup> National Oceanic & Atmospheric Administration, [Global Monitoring Laboratory](#)  
 142 (NOAA [GML](#)), Boulder, CO 80305, USA  
 143 <sup>68</sup> Institute of [Arctic and Alpine Research](#), [University of Colorado, Boulder, CO 80309, USA](#)  
 144 <sup>69</sup> Institute of Tibetan Plateau Research, Chinese Academy of Sciences, Beijing 100101, China  
 145 <sup>70</sup> CSIRO Oceans and Atmosphere, PO Box 1538, Hobart, Tasmania 7001, Australia  
 146 <sup>71</sup> Australian Antarctic Partnership Program, University of Tasmania, Hobart, Australia  
 147 <sup>72</sup> Statistics Division, Food and Agriculture Organization of the United Nations, Via Terme di  
 148 Caracalla, Rome 00153, Italy  
 149 <sup>73</sup> Department of Earth sciences, Faculty of Science, Vrije Universiteit, Amsterdam, the  
 150 Netherlands  
 151 <sup>74</sup> Environmental Sciences Division and Climate Change Science Institute, Oak Ridge National  
 152 Laboratory, Oak Ridge, TN, 37831, USA  
 153 <sup>75</sup> Sitka Tribe of Alaska, 456 Katlian Street, Sitka, Alaska 99835, USA  
 154 <sup>76</sup> Swedish Meteorological and Hydrological Institute, Sven Källfeltsgata 15, 426 68 Västra  
 155 Frölunda, Sweden  
 156 <sup>77</sup> School of Atmospheric Sciences, Sun Yat-sen University, Zhuhai, Guangdong 510245, China.  
 157 <sup>78</sup> Institute of Soil and Water Conservation, Northwest A&F University, Yangling, Shaanxi 712100,  
 158 P.R. China  
 159 <sup>79</sup> School of Environmental Science and Engineering, Nanjing University of Information Science  
 160 and Technology (NUIST), China  
 161 <sup>80</sup> Institute of Environment and Ecology, Tsinghua Shenzhen International Graduate School,  
 162 Tsinghua University, Shenzhen 518055, China  
 163

164 *Correspondence to:* Pierre Friedlingstein (p.friedlingstein@exeter.ac.uk)

165 **Abstract**

166 Accurate assessment of anthropogenic carbon dioxide (CO<sub>2</sub>) emissions and their redistribution among the  
 167 atmosphere, ocean, and terrestrial biosphere in a changing climate is critical to better understand the global  
 168 carbon cycle, support the development of climate policies, and project future climate change. Here we describe  
 169 and synthesise data sets and methodology to quantify the five major components of the global carbon budget  
 170 and their uncertainties. Fossil CO<sub>2</sub> emissions (E<sub>FOS</sub>) are based on energy statistics and cement production data,  
 171 while emissions from land-use change (E<sub>LUC</sub>), mainly deforestation, are based on land-use and land-use change  
 172 data and bookkeeping models. Atmospheric CO<sub>2</sub> concentration is measured directly, and its growth rate (G<sub>ATM</sub>)  
 173 is computed from the annual changes in concentration. The ocean CO<sub>2</sub> sink (S<sub>OCEAN</sub>) is estimated with global  
 174 ocean biogeochemistry models and observation-based data-products. The terrestrial CO<sub>2</sub> sink (S<sub>LAND</sub>) is  
 175 estimated with dynamic global vegetation models. The resulting carbon budget imbalance (B<sub>IM</sub>), the difference  
 176 between the estimated total emissions and the estimated changes in the atmosphere, ocean, and terrestrial

Formatted: Space Before: 0 pt, Add space between paragraphs of the same style

Deleted: Earth System Research

Deleted: ESRL

Formatted: Font: Superscript

Formatted: Space Before: 0 pt, Add space between paragraphs of the same style

Deleted: <sup>69</sup>

Deleted: <sup>70</sup>

Deleted: <sup>71</sup>

Deleted: <sup>72</sup>

Deleted: <sup>73</sup>

Deleted: <sup>74</sup>

Deleted: <sup>75</sup>

Deleted: <sup>76</sup>

Deleted: <sup>77</sup>

Deleted: <sup>78</sup>

Deleted: <sup>79</sup>

Deleted: ¶

Formatted: Subscript

Formatted: Normal, Indent: Left: 0.16 cm, First line: 0 cm

Formatted: Subscript

192 biosphere, is a measure of imperfect data and understanding of the contemporary carbon cycle. All  
 193 uncertainties are reported as  $\pm 1\sigma$ .

194 For the year 2021,  $E_{FOS}$  increased by 5.1% relative to 2020, with fossil emissions at  $10.1 \pm 0.5 \text{ GtC yr}^{-1}$  ( $9.9 \pm$   
 195  $0.5 \text{ GtC yr}^{-1}$  when the cement carbonation sink is included),  $E_{LUC}$  was  $1.1 \pm 0.7 \text{ GtC yr}^{-1}$ , for a total  
 196 anthropogenic  $\text{CO}_2$  emission (including the cement carbonation sink) of  $10.9 \pm 0.8 \text{ GtC yr}^{-1}$  ( $10.0 \pm 2.9$   
 197  $\text{GtCO}_2$ ). Also, for 2021,  $G_{ATM}$  was  $5.2 \pm 0.2 \text{ GtC yr}^{-1}$  ( $2.5 \pm 0.1 \text{ ppm yr}^{-1}$ ),  $S_{OCEAN}$  was  $2.9 \pm 0.4 \text{ GtC yr}^{-1}$  and  
 198  $S_{LAND}$  was  $3.5 \pm 0.9 \text{ GtC yr}^{-1}$ , with a  $B_{IM}$  of  $-0.6 \text{ GtC yr}^{-1}$  (i.e. total estimated sources too low or sinks too high).  
 199 The global atmospheric  $\text{CO}_2$  concentration averaged over 2021 reached  $414.71 \pm 0.1 \text{ ppm}$ . Preliminary data for  
 200 2022, suggest an increase in  $E_{FOS}$  relative to 2021 of +1.1% (0% to 1.7%) globally, and atmospheric  $\text{CO}_2$   
 201 concentration reaching 417.3 ppm, more than 50% above pre-industrial level (around 278 ppm). Overall, the  
 202 mean and trend in the components of the global carbon budget are consistently estimated over the period 1959-  
 203 2021, but discrepancies of up to  $1 \text{ GtC yr}^{-1}$  persist for the representation of annual to semi-decadal variability in  
 204  $\text{CO}_2$  fluxes. Comparison of estimates from multiple approaches and observations shows: (1) a persistent large  
 205 uncertainty in the estimate of land-use changes emissions, (2) a low agreement between the different methods  
 206 on the magnitude of the land  $\text{CO}_2$  flux in the northern extra-tropics, and (3) a discrepancy between the different  
 207 methods on the strength of the ocean sink over the last decade. This living data update documents changes in  
 208 the methods and data sets used in this new global carbon budget and the progress in understanding of the  
 209 global carbon cycle compared with previous publications of this data set. The data presented in this work are  
 210 available at <https://doi.org/10.18160/GCP-2022> (Friedlingstein et al., 2022b).

211

Deleted:

Formatted: Subscript

Formatted: Superscript

Formatted: Normal, Indent: Left: 0.11 cm, Hanging: 0.05 cm

Formatted: Superscript

Formatted: Subscript

Formatted: Superscript

Deleted: 11.1

Deleted: 8

Formatted: Subscript

Formatted: Superscript

Formatted: Subscript

Formatted: Subscript

Formatted: Superscript

Formatted: Superscript

Formatted: Subscript

Formatted: Superscript

Formatted: Subscript

Formatted: Superscript

Formatted: Subscript

Formatted: Subscript

Formatted: Subscript

Formatted: Subscript

Deleted: .

Deleted: (Friedlingstein et al., 2022a; Friedlingstein et al., 2020; Friedlingstein et al., 2019; Le Quéré et al., 2018b, 2018a, 2016, 2015b, 2015a, 2014, 2013).

Deleted:

Deleted: <https://doi.org/10.18160/GCP-2022>

Formatted: Font: Times New Roman, 10 pt

Deleted: ¶

Formatted: Font: (Default) Calibri, 12 pt

222 **Executive Summary**

223 **Global fossil CO<sub>2</sub> emissions (including cement carbonation) further increased in 2022, being now slightly**  
224 **above their pre-COVID-19 pandemic 2019 level.** The 2021 emission increase was 0.46 GtC yr<sup>-1</sup> (1.7 GtCO<sub>2</sub>  
225 yr<sup>-1</sup>), bringing 2021 emissions to 9.9 ± 0.5 GtC yr<sup>-1</sup> (36.1 ± 1.8 GtCO<sub>2</sub> yr<sup>-1</sup>), slightly below the emissions level of  
226 2019 (9.9 ± 0.5 GtC yr<sup>-1</sup>, 36.2 ± 1.8 GtCO<sub>2</sub> yr<sup>-1</sup>). Preliminary estimates based on data available suggest fossil  
227 CO<sub>2</sub> emissions continued to increase in 2022, by 1.1% relative to 2021 (0% to 1.7%), bringing emissions at 10.0  
228 GtC yr<sup>-1</sup> (36.5 GtCO<sub>2</sub> yr<sup>-1</sup>), slightly above the 2019 level.

229 Emissions from coal, oil, and gas in 2022 are expected to be above their 2021 levels (by 0.8%, 2.2% and 1.1%  
230 respectively). Regionally, emissions in 2022 are expected to have been decreasing by 1.5% in China (3.0 GtC,  
231 11.1 GtCO<sub>2</sub>), and 1% in the European Union (0.8 GtC, 2.8 GtCO<sub>2</sub>), but increasing by 1.6% in the United States  
232 (1.4 GtC, 5.1 GtCO<sub>2</sub>), 5.6% in India (0.8 GtC, 2.9 GtCO<sub>2</sub>) and 2.5% for the rest of the world (4.2 GtC, 15.5  
233 GtCO<sub>2</sub>).

234 **Fossil CO<sub>2</sub> emissions decreased in 24 countries during the decade 2012-2021.** Altogether, these 24 countries  
235 contribute to about 2.4 GtC yr<sup>-1</sup> (8.8 GtCO<sub>2</sub>) fossil fuel CO<sub>2</sub> emissions over the last decade, about one quarter of  
236 world CO<sub>2</sub> fossil emissions.

237 **Global CO<sub>2</sub> emissions from land-use, land-use change, and forestry (LUC) averaged at 1.2 ± 0.7 GtC yr<sup>-1</sup>**  
238 **(4.5 ± 2.6 GtCO<sub>2</sub> yr<sup>-1</sup>) for the 2012-2021 period with a preliminary projection for 2022 of 1.0 ± 0.7 GtC yr<sup>-1</sup>**  
239 **(3.6 ± 2.6 GtCO<sub>2</sub> yr<sup>-1</sup>).** A small decrease over the past two decades is not robust given the large model  
240 **uncertainty.** Emissions from deforestation, the main driver of global gross sources, remain high at 1.8 ± 0.4  
241 GtC yr<sup>-1</sup> over the 2012-2021 period, highlighting the strong potential of halting deforestation for emissions  
242 reductions. Sequestration of 0.9 ± 0.3 GtC yr<sup>-1</sup> through re-/afforestation and forestry offsets one half of the  
243 deforestation emissions. Emissions from other land-use transitions and from peat drainage and peat fire add  
244 further, small contributions. The highest emitters during 2012-2021 in descending order were Brazil, Indonesia,  
245 and the Democratic Republic of the Congo, with these 3 countries contributing more than half of the global total  
246 land-use emissions.

247 **The remaining carbon budget for a 50% likelihood to limit global warming to 1.5°C, 1.7°C and 2°C has**  
248 **respectively reduced to 105 GtC (380 GtCO<sub>2</sub>), 200 GtC (730 GtCO<sub>2</sub>) and 335 GtC (1230 GtCO<sub>2</sub>) from the**  
249 **beginning of 2023, equivalent to 9, 18 and 30 years, assuming 2022 emissions levels.** Total anthropogenic  
250 emissions were 10.9 GtC yr<sup>-1</sup> (40.0 GtCO<sub>2</sub> yr<sup>-1</sup>) in 2021, with a preliminary estimate of 10.9 GtC yr<sup>-1</sup> (40.1  
251 GtCO<sub>2</sub> yr<sup>-1</sup>) for 2022. The remaining carbon budget to keep global temperatures below these climate targets has  
252 shrunk by 32 GtC (121 GtCO<sub>2</sub>) since the IPCC AR6 Working Group 1 assessment, based on data up to 2019.  
253 Reaching zero CO<sub>2</sub> emissions by 2050 entails a total anthropogenic CO<sub>2</sub> emissions linear decrease by about 0.4  
254 GtC (1.4 GtCO<sub>2</sub>) each year, comparable to the decrease during 2020, highlighting the scale of the action needed.

255 **The concentration of CO<sub>2</sub> in the atmosphere is set to reach 417.3 ppm in 2022, 51% above pre-industrial**  
256 **levels.** The atmospheric CO<sub>2</sub> growth was 5.2 ± 0.02 GtC yr<sup>-1</sup> during the decade 2012-2021 (48% of total CO<sub>2</sub>  
257 emissions) with a preliminary 2022 growth rate estimate of around 5.5 GtC yr<sup>-1</sup> (2.6 ppm).

Formatted: Indent: Left: 0 cm, First line: 0 cm

Deleted: excluding

Deleted: COVID19

Deleted: 10.1

Deleted: 9

Deleted: .

Deleted: 2

Deleted: 37.3

Deleted: (10.1 ± 0.5 GtC yr<sup>-1</sup>, 37.0 ± 1.8 GtCO<sub>2</sub> yr<sup>-1</sup>).

Deleted: 2010-2019

Deleted: only

Deleted: Deforestation emissions

Formatted: Font: 9 pt

Deleted: a substantial mitigation

Deleted: 1959

Deleted: 11.1

Deleted: 8

Deleted: 11.1

Deleted: 9

Deleted: 33

Deleted: release of the

Deleted: in

Deleted: cutting

Deleted: on average

280 The ocean CO<sub>2</sub> sink resumed a more rapid growth in the past ~~two decades~~, after low or no growth during  
281 the 1991-2002 period. However, the growth of the ocean CO<sub>2</sub> sink in the past decade has an uncertainty of a  
282 factor of three, with estimates based on data products and estimates based on models showing an ocean sink  
283 trend of +0.7 GtC yr<sup>-1</sup> decade<sup>-1</sup> and +0.2 GtC yr<sup>-1</sup> decade<sup>-1</sup> since 2010, respectively. The discrepancy in the trend  
284 originates from all latitudes but is largest in the Southern Ocean. The ocean CO<sub>2</sub> sink was 2.9 ± 0.4 GtC yr<sup>-1</sup>  
285 during the decade ~~2012-2021~~ (26% of total CO<sub>2</sub> emissions), with a similar preliminary estimate of 2.9 GtC yr<sup>-1</sup>  
286 for 2022.

Deleted: decade

Deleted: 2011-2020

287 The land CO<sub>2</sub> sink continued to increase during the 2012-2021 period primarily in response to increased  
288 atmospheric CO<sub>2</sub>, albeit with large interannual variability. The land CO<sub>2</sub> sink was 3.1 ± 0.6 GtC yr<sup>-1</sup>  
289 during the 2012-2021 decade (29% of total CO<sub>2</sub> emissions), 0.4 GtC yr<sup>-1</sup> larger than during the previous decade  
290 (2000-2009), with a preliminary 2022 estimate of around 3.4 GtC yr<sup>-1</sup>. Year to year variability in the land sink is  
291 about 1 GtC yr<sup>-1</sup> and dominates the year-to-year changes in the global atmospheric CO<sub>2</sub> concentration, implying  
292 that small annual changes in anthropogenic emissions (such as the fossil fuel emission decrease in 2020) are  
293 hard to detect in the atmospheric CO<sub>2</sub> observations.  
294

Formatted: Font: (Default) Calibri, 12 pt

Formatted: Not Superscript/ Subscript

Deleted: , making

Deleted: global

Deleted: concentration

Formatted: Font: (Default) Calibri, 12 pt

300

## 301 1 Introduction

302 The concentration of carbon dioxide (CO<sub>2</sub>) in the atmosphere has increased from approximately 278 parts per  
 303 million (ppm) in 1750 (Gulev et al., 2021), the beginning of the Industrial Era, to 414.7 ± 0.1 ppm in 2021  
 304 (Dlugokencky and Tans, 2022); Figure 1). The atmospheric CO<sub>2</sub> increase above pre-industrial levels was,  
 305 initially, primarily caused by the release of carbon to the atmosphere from deforestation and other land-use  
 306 change activities (Canadell et al., 2021). While emissions from fossil fuels started before the Industrial Era, they  
 307 became the dominant source of anthropogenic emissions to the atmosphere from around 1950 and their relative  
 308 share has continued to increase until present. Anthropogenic emissions occur on top of an active natural carbon  
 309 cycle that circulates carbon between the reservoirs of the atmosphere, ocean, and terrestrial biosphere on time  
 310 scales from sub-daily to millennia, while exchanges with geologic reservoirs occur at longer timescales (Archer  
 311 et al., 2009).

312 The global carbon budget (GCB) presented here refers to the mean, variations, and trends in the perturbation of  
 313 CO<sub>2</sub> in the environment, referenced to the beginning of the Industrial Era (defined here as 1750). This paper  
 314 describes the components of the global carbon cycle over the historical period with a stronger focus on the  
 315 recent period (since 1958, onset of atmospheric CO<sub>2</sub> measurements), the last decade (2012-2021), the last year  
 316 (2021) and the current year (2022). Finally, it provides cumulative emissions from fossil fuels and land-use  
 317 change since the year 1750 (the pre-industrial period), and since the year 1850 (the reference year for historical  
 318 simulations in IPCC AR6) (Eyring et al., 2016).

319 We quantify the input of CO<sub>2</sub> to the atmosphere by emissions from human activities, the growth rate of  
 320 atmospheric CO<sub>2</sub> concentration, and the resulting changes in the storage of carbon in the land and ocean  
 321 reservoirs in response to increasing atmospheric CO<sub>2</sub> levels, climate change and variability, and other  
 322 anthropogenic and natural changes (Figure 2). An understanding of this perturbation budget over time and the  
 323 underlying variability and trends of the natural carbon cycle is necessary to understand the response of natural  
 324 sinks to changes in climate, CO<sub>2</sub> and land-use change drivers, and to quantify emissions compatible with a given  
 325 climate stabilisation target.

326 The components of the CO<sub>2</sub> budget that are reported annually in this paper include separate and independent  
 327 estimates for the CO<sub>2</sub> emissions from (1) fossil fuel combustion and oxidation from all energy and industrial  
 328 processes; also including cement production and carbonation ( $E_{FOS}$ ; GtC yr<sup>-1</sup>) and (2) the emissions resulting  
 329 from deliberate human activities on land, including those leading to land-use change ( $E_{LUC}$ ; GtC yr<sup>-1</sup>); and their  
 330 partitioning among (3) the growth rate of atmospheric CO<sub>2</sub> concentration ( $G_{ATM}$ ; GtC yr<sup>-1</sup>), and the uptake of  
 331 CO<sub>2</sub> (the 'CO<sub>2</sub> sinks') in (4) the ocean ( $S_{OCEAN}$ ; GtC yr<sup>-1</sup>) and (5) on land ( $S_{LAND}$ ; GtC yr<sup>-1</sup>). The CO<sub>2</sub> sinks as  
 332 defined here conceptually include the response of the land (including inland waters and estuaries) and ocean  
 333 (including coastal and marginal seas) to elevated CO<sub>2</sub> and changes in climate and other environmental  
 334 conditions, although in practice not all processes are fully accounted for (see Section 2.7). Global emissions and  
 335 their partitioning among the atmosphere, ocean and land are in balance in the real world. Due to the combination  
 336 of imperfect spatial and/or temporal data coverage, errors in each estimate, and smaller terms not included in our  
 337 budget estimate (discussed in Section 2.7), the independent estimates (1) to (5) above do not necessarily add up

Formatted: Outline numbered + Level: 1 + Numbering  
 Style: 1, 2, 3, ... + Start at: 1 + Alignment: Left + Aligned at:  
 0 cm + Indent at: 0.76 cm

Deleted: 277

Deleted: Joos and Spahni, 2008

Deleted: ,

Deleted: ;

Deleted: ;

343 to zero. We therefore (a) additionally assess a set of global atmospheric inversion system results that by design  
344 close the global carbon balance (see Section 2.6), and (b) estimate a budget imbalance ( $B_{IM}$ ), which is a measure  
345 of the mismatch between the estimated emissions and the estimated changes in the atmosphere, land and ocean,  
346 as follows:

$$347 \quad B_{IM} = E_{FOS} + E_{LUC} - (G_{ATM} + S_{OCEAN} + S_{LAND}) \quad (1)$$

348  $G_{ATM}$  is usually reported in  $\text{ppm yr}^{-1}$ , which we convert to units of carbon mass per year,  $\text{GtC yr}^{-1}$ , using  $1 \text{ ppm}$   
349  $= 2.124 \text{ GtC}$  (Ballantyne et al., 2012; Table 1). All quantities are presented in units of gigatonnes of carbon  
350 ( $\text{GtC}$ ,  $10^{15} \text{ gC}$ ), which is the same as petagrams of carbon ( $\text{PgC}$ ; Table 1). Units of gigatonnes of  $\text{CO}_2$  (or billion  
351 tonnes of  $\text{CO}_2$ ) used in policy are equal to 3.664 multiplied by the value in units of  $\text{GtC}$ .

352 We also quantify  $E_{FOS}$  and  $E_{LUC}$  by country, including both territorial and consumption-based accounting for  
353  $E_{FOS}$  (see Section 2), and discuss missing terms from sources other than the combustion of fossil fuels (see  
354 Section 2.7, [Appendix D1 and D2](#)).

Deleted: ).

355 The global  $\text{CO}_2$  budget has been assessed by the Intergovernmental Panel on Climate Change (IPCC) in all  
356 assessment reports (Prentice et al., 2001; Schimel et al., 1995; Watson et al., 1990; Denman et al., 2007; Ciais et  
357 al., 2013; Canadell et al., 2021), and by others (e.g. Ballantyne et al., 2012). The Global Carbon Project (GCP,  
358 [www.globalcarbonproject.org](http://www.globalcarbonproject.org), last access: 25 September 2022) has coordinated this cooperative community  
359 effort for the annual publication of global carbon budgets for the year 2005 (Raupach et al., 2007; including  
360 fossil emissions only), year 2006 (Canadell et al., 2007), year 2007 (GCP, 2008), year 2008 (Le Quéré et al.,  
361 2009), year 2009 (Friedlingstein et al., 2010), year 2010 (Peters et al., 2012b), year 2012 (Le Quéré et al., 2013;  
362 Peters et al., 2013), year 2013 (Le Quéré et al., 2014), year 2014 (Le Quéré et al., 2015a; Friedlingstein et al.,  
363 2014), year 2015 (Jackson et al., 2016; Le Quéré et al., 2015b), year 2016 (Le Quéré et al., 2016), year 2017 (Le  
364 Quéré et al., 2018a; Peters et al., 2017), year 2018 (Le Quéré et al., 2018b; Jackson et al., 2018), year 2019  
365 (Friedlingstein et al., 2019; Jackson et al., 2019; Peters et al., 2020), year 2020 (Friedlingstein et al., 2020; Le  
366 Quéré et al., 2021) and more recently the year 2021 (Friedlingstein et al., 2022a; Jackson et al., 2022). Each of  
367 these papers updated previous estimates with the latest available information for the entire time series.

368 We adopt a range of  $\pm 1$  standard deviation ( $\sigma$ ) to report the uncertainties in our estimates, representing a  
369 likelihood of 68% that the true value will be within the provided range if the errors have a Gaussian distribution,  
370 and no bias is assumed. This choice reflects the difficulty of characterising the uncertainty in the  $\text{CO}_2$  fluxes  
371 between the atmosphere and the ocean and land reservoirs individually, particularly on an annual basis, as well  
372 as the difficulty of updating the  $\text{CO}_2$  emissions from land-use change. A likelihood of 68% provides an  
373 indication of our current capability to quantify each term and its uncertainty given the available information.

374 The uncertainties reported here combine statistical analysis of the underlying data, assessments of uncertainties  
375 in the generation of the data sets, and expert judgement of the likelihood of results lying outside this range. The  
376 limitations of current information are discussed in the paper and have been examined in detail elsewhere  
377 (Ballantyne et al., 2015; Zscheischler et al., 2017). We also use a qualitative assessment of confidence level to  
378 characterise the annual estimates from each term based on the type, amount, quality, and consistency of the  
379 evidence as defined by the IPCC (Stocker et al., 2013).

381 This paper provides a detailed description of the data sets and methodology used to compute the global carbon  
382 budget estimates for the industrial period, from 1750 to 2022, and in more detail for the period since 1959. This  
383 paper is updated every year using the format of ‘living data’ to keep a record of budget versions and the changes  
384 in new data, revision of data, and changes in methodology that lead to changes in estimates of the carbon  
385 budget. Additional materials associated with the release of each new version will be posted at the Global Carbon  
386 Project (GCP) website (<http://www.globalcarbonproject.org/carbonbudget>, last access: 25 September 2022),  
387 with fossil fuel emissions also available through the Global Carbon Atlas (<http://www.globalcarbonatlas.org>,  
388 last access: 25 September 2022). All underlying data used to produce the budget can also be found at  
389 <https://globalcarbonbudget.org/> (last access: 25 September 2022). With this approach, we aim to provide the  
390 highest transparency and traceability in the reporting of CO<sub>2</sub>, the key driver of climate change.

391

## 392 2 Methods

393 Multiple organisations and research groups around the world generated the original measurements and data used  
394 to complete the global carbon budget. The effort presented here is thus mainly one of synthesis, where results  
395 from individual groups are collated, analysed, and evaluated for consistency. We facilitate access to original  
396 data with the understanding that primary data sets will be referenced in future work (see Table 2 for how to cite  
397 the data sets). Descriptions of the measurements, models, and methodologies follow below, and detailed  
398 descriptions of each component are provided elsewhere.

399 This is the 17th version of the global carbon budget and the 11th revised version in the format of a living data  
400 update in Earth System Science Data. It builds on the latest published global carbon budget of Friedlingstein et  
401 al. (2022a). The main changes are: the inclusion of (1) data to year 2021 and a projection for the global carbon  
402 budget for year 2022; (2) the inclusion of country level estimates of E<sub>LUC</sub>; (3) a process-based decomposition of  
403 E<sub>LUC</sub> into its main components (deforestation, [re/afforestation and wood harvest](#), emissions from organic soils,  
404 and net flux from other transitions).

405 The main methodological differences between recent annual carbon budgets (2018-2022) are summarised in  
406 Table 3 and previous changes since 2006 are provided in Table A7.

### 407 2.1 Fossil CO<sub>2</sub> emissions (E<sub>FOS</sub>)

#### 408 2.1.1 Historical period 1850-2021

409 The estimates of global and national fossil CO<sub>2</sub> emissions (E<sub>FOS</sub>) include the oxidation of fossil fuels through  
410 both combustion (e.g., transport, heating) and chemical oxidation (e.g. carbon anode decomposition in  
411 aluminium refining) activities, and the decomposition of carbonates in industrial processes (e.g. the production  
412 of cement). We also include CO<sub>2</sub> uptake from the cement carbonation process. Several emissions sources are not  
413 estimated or not fully covered: coverage of emissions from lime production are not global, and decomposition of  
414 carbonates in glass and ceramic production are included only for the “Annex 1” countries of the United Nations  
415 Framework Convention on Climate Change (UNFCCC) for lack of activity data. These omissions are  
416 considered to be minor. Short-cycle carbon emissions - for example from combustion of biomass - are not  
417 included here but are accounted for in the CO<sub>2</sub> emissions from land use (see section 2.2).

Formatted: Outline numbered + Level: 1 + Numbering  
Style: 1, 2, 3, ... + Start at: 1 + Alignment: Left + Aligned at:  
0 cm + Indent at: 0.76 cm

Deleted: carbon uptake on forests

Deleted:

Formatted: Outline numbered + Level: 2 + Numbering  
Style: 1, 2, 3, ... + Start at: 1 + Alignment: Left + Aligned at:  
0 cm + Indent at: 1.02 cm

Formatted: Outline numbered + Level: 3 + Numbering  
Style: 1, 2, 3, ... + Start at: 1 + Alignment: Left + Aligned at:  
0 cm + Indent at: 1.27 cm

420 Our estimates of fossil CO<sub>2</sub> emissions are derived using the standard approach of activity data and emission  
421 factors, relying on data collection by many other parties. Our goal is to produce the best estimate of this flux,  
422 and we therefore use a prioritisation framework to combine data from different sources that have used different  
423 methods, while being careful to avoid double counting and undercounting of emissions sources. The CDIAC-FF  
424 emissions dataset, derived largely from UN energy data, forms the foundation, and we extend emissions to year  
425 Y-1 using energy growth rates reported by BP [energy company](#). We then proceed to replace estimates using data  
426 from what we consider to be superior sources, for example Annex 1 countries' official submissions to the  
427 UNFCCC. All data points are potentially subject to revision, not just the latest year. For full details see Andrew  
428 and Peters (2021).

429 Other estimates of global fossil CO<sub>2</sub> emissions exist, and these are compared by Andrew (2020a). The most  
430 common reason for differences in estimates of global fossil CO<sub>2</sub> emissions is a difference in which emissions  
431 sources are included in the datasets. Datasets such as those published by the energy company BP, the US Energy  
432 Information Administration, and the International Energy Agency's 'CO<sub>2</sub> emissions from fuel combustion' are  
433 all generally limited to emissions from combustion of fossil fuels. In contrast, datasets such as PRIMAP-hist,  
434 CEDS, EDGAR, and GCP's dataset aim to include all sources of fossil CO<sub>2</sub> emissions. See Andrew (2020a) for  
435 detailed comparisons and discussion.

436 Cement absorbs CO<sub>2</sub> from the atmosphere over its lifetime, a process known as 'cement carbonation'. We  
437 estimate this CO<sub>2</sub> sink, [from 1931, onwards](#) as the average of two studies in the literature (Cao et al., 2020; Guo  
438 et al., 2021). Both studies use the same model, developed by Xi et al. (2016), with different parameterisations  
439 and input data, [with the estimate of Guo and colleagues being a revision of Xi et al \(2016\). The trends of the two](#)  
440 [studies are very similar](#). Since carbonation is a function of both current and previous cement production, we  
441 extend these estimates to [2022](#) by using the growth rate derived from the smoothed cement emissions (10-year  
442 smoothing) fitted to the carbonation data. [In the present budget, we always include the cement carbonation](#)  
443 [carbon sink in the fossil CO<sub>2</sub> emission component \(E<sub>FOS</sub>\)](#).

444 We use the Kaya Identity for a simple decomposition of CO<sub>2</sub> emissions into the key drivers (Raupach et al.,  
445 2007). While there are variations (Peters et al., 2017), we focus here on a decomposition of CO<sub>2</sub> emissions into  
446 population, GDP per person, energy use per GDP, and CO<sub>2</sub> emissions per energy. Multiplying these individual  
447 components together returns the CO<sub>2</sub> emissions. Using the decomposition, it is possible to attribute the change  
448 in CO<sub>2</sub> emissions to the change in each of the drivers. This method gives a first order understanding of what  
449 causes CO<sub>2</sub> emissions to change each year.

### 450 2.1.2 2022 projection

451 We provide a projection of global CO<sub>2</sub> emissions in 2022 by combining separate projections for China, USA,  
452 EU, India, and for all other countries combined. The methods are different for each of these. For China we  
453 combine monthly fossil fuel production data from the National Bureau of Statistics, import/export data from the  
454 Customs Administration, and monthly coal consumption estimates from SX Coal (2022), giving us partial data  
455 for the growth rates to date of natural gas, petroleum, and cement, and of the consumption itself for raw coal.  
456 We then use a regression model to project full-year emissions based on historical observations. For the USA our  
457 projection is taken directly from the Energy Information Administration's (EIA) Short-Term Energy Outlook  
458 (EIA, 2022), combined with the year-to-date growth rate of cement clinker production. For the EU we use

Deleted: .

Moved down [1]: The Global Cement and Concrete Association reports a much lower carbonation rate, but this is based on the highly conservative assumption of 0% mortar (GCCA, 2021). , wi

Deleted: .

Deleted: by one year

Deleted: 2021

Formatted: Outline numbered + Level: 3 + Numbering Style: 1, 2, 3, ... + Start at: 1 + Alignment: Left + Aligned at: 0 cm + Indent at: 1.27 cm

467 monthly energy data from Eurostat to derive estimates of monthly CO<sub>2</sub> emissions through July, with coal  
 468 emissions extended through August using a statistical relationship with reported electricity generation from coal  
 469 and other factors. Given the very high uncertainty in European energy markets in 2022, we forego our usual  
 470 history-based projection techniques and use instead the year-to-date growth rate as the full-year growth rate for  
 471 both coal and natural gas. EU emissions from oil are derived using the EIA's projection of oil consumption for  
 472 Europe. EU cement emissions are based on available year-to-date data from three of the largest producers,  
 473 Germany, Poland, and Spain. India's projected emissions are derived from estimates through July (August for  
 474 oil) using the methods of Andrew (2020b) and extrapolated assuming normal seasonal patterns. Emissions for  
 475 the rest of the world are derived using projected growth in economic production from the IMF (2022) combined  
 476 with extrapolated changes in emissions intensity of economic production. More details on the Efos methodology  
 477 and its 2022 projection can be found in Appendix C.1.

## 478 2.2 CO<sub>2</sub> emissions from land-use, land-use change and forestry (ELUC)

### 479 2.2.1 Historical period 1850-2021

480 The net CO<sub>2</sub> flux from land-use, land-use change and forestry (ELUC, called land-use change emissions in the  
 481 rest of the text) includes CO<sub>2</sub> fluxes from deforestation, afforestation, logging and forest degradation (including  
 482 harvest activity), shifting cultivation (cycle of cutting forest for agriculture, then abandoning), and regrowth of  
 483 forests (following wood harvest or agriculture abandonment). Emissions from peat burning and drainage are  
 484 added from external datasets, peat drainage being averaged from three spatially explicit independent datasets  
 485 (see Appendix C.2.1).

486 Three bookkeeping approaches (updated estimates each of BLUE (Hansis et al., 2015), OSCAR (Gasser et al.,  
 487 2020), and H&N2017 (Houghton and Nassikas, 2017)) were used to quantify gross sources and sinks and the  
 488 resulting net ELUC. Uncertainty estimates were derived from the Dynamic Global vegetation Models (DGVMs)  
 489 ensemble for the time period prior to 1960, using for the recent decades an uncertainty range of  $\pm 0.7$  GtC yr<sup>-1</sup>,  
 490 which is a semi-quantitative measure for annual and decadal emissions and reflects our best value judgement  
 491 that there is at least 68% chance ( $\pm 1\sigma$ ) that the true land-use change emission lies within the given range, for the  
 492 range of processes considered here. This uncertainty range had been increased from 0.5 GtC yr<sup>-1</sup> after new  
 493 bookkeeping models were included that indicated a larger spread than assumed before (Le Quéré et al., 2018).  
 494 Projections for 2021 are based on fire activity from tropical deforestation and degradation as well as emissions  
 495 from peat fires and drainage.

496 Our ELUC estimates follow the definition of global carbon cycle models of CO<sub>2</sub> fluxes related to land-use and  
 497 land management and differ from IPCC definitions adopted in National GHG Inventories (NGHGI) for  
 498 reporting under the UNFCCC, which additionally generally include, through adoption of the IPCC so-called  
 499 managed land proxy approach, the terrestrial fluxes occurring on land defined by countries as managed. This  
 500 partly includes fluxes due to environmental change (e.g. atmospheric CO<sub>2</sub> increase), which are part of S<sub>LAND</sub> in  
 501 our definition. This causes the global emission estimates to be smaller for NGHGI than for the global carbon  
 502 budget definition (Grassi et al., 2018). The same is the case for the Food Agriculture Organization (FAO)  
 503 estimates of carbon fluxes on forest land, which include both anthropogenic and natural sources on managed  
 504 land (Tubiello et al., 2021). We map the two definitions to each other, to provide a comparison of the  
 505 anthropogenic carbon budget to the official country reporting to the climate convention.

**Formatted:** Outline numbered + Level: 2 + Numbering Style: 1, 2, 3, ... + Start at: 1 + Alignment: Left + Aligned at: 0 cm + Indent at: 1.02 cm

**Deleted:** Period

**Formatted:** Pattern: Clear (Custom Colour (RGB(253,252,252)))

**Formatted:** Outline numbered + Level: 3 + Numbering Style: 1, 2, 3, ... + Start at: 1 + Alignment: Left + Aligned at: 0 cm + Indent at: 1.27 cm

**Deleted:** of agriculture.

**Deleted:** . Compared to our earlier assessments, this year we include spatially explicit information also for

**Deleted:** and combine

**Deleted:** for peat drainage.

**Deleted:** , compared to S<sub>LAND</sub>,

**Deleted:** Using the approach outlined in Grassi et al. (2021), here we...

**Deleted:** as additional information

516 **2.2.2 2022 Projection**

517 We project the 2022 land-use emissions for BLUE, the updated H&N2017 and OSCAR, starting from their  
518 estimates for 2021 assuming unaltered peat drainage, which has low interannual variability, but adjusting, the  
519 highly variable emissions from peat fires, tropical deforestation and degradation as estimated using active fire  
520 data (MCD14ML; Giglio et al., 2016). More details on the ELUC methodology can be found in Appendix C.2

521 **2.3 Growth rate in atmospheric CO<sub>2</sub> concentration (G<sub>ATM</sub>)**

522 **2.3.1 Historical period 1850-2021**

523 The rate of growth of the atmospheric CO<sub>2</sub> concentration is provided for years 1959-2021 by the US National  
524 Oceanic and Atmospheric Administration Global Monitoring Laboratory (NOAA/GML; Dlugokencky and  
525 Tans, 2022), which is updated from Ballantyne et al. (2012) and includes recent revisions to the calibration scale  
526 of atmospheric CO<sub>2</sub> measurements (Hall et al., 2021). For the 1959-1979 period, the global growth rate is based  
527 on measurements of atmospheric CO<sub>2</sub> concentration averaged from the Mauna Loa and South Pole stations, as  
528 observed by the CO<sub>2</sub> Program at Scripps Institution of Oceanography (Keeling et al., 1976). For the 1980-2020  
529 time period, the global growth rate is based on the average of multiple stations selected from the marine  
530 boundary layer sites with well-mixed background air (Ballantyne et al., 2012), after fitting a smooth curve  
531 through the data for each station as a function of time, and averaging by latitude band (Masarie and Tans, 1995).  
532 The annual growth rate is estimated by Dlugokencky and Tans (2022) from atmospheric CO<sub>2</sub> concentration by  
533 taking the average of the most recent December-January months corrected for the average seasonal cycle and  
534 subtracting this same average one year earlier. The growth rate in units of ppm yr<sup>-1</sup> is converted to units of GtC  
535 yr<sup>-1</sup> by multiplying by a factor of 2.124 GtC per ppm, assuming instantaneous mixing of CO<sub>2</sub> throughout the  
536 atmosphere (Ballantyne et al., 2012; Table 1).

537 Since 2020, NOAA/GML provides estimates of atmospheric CO<sub>2</sub> concentrations with respect to a new  
538 calibration scale, referred to as WMO-CO<sub>2</sub>-X2019, in line with the recommendation of the World  
539 Meteorological Organization (WMO) Global Atmosphere Watch (GAW) community (Hall et al., 2021). The  
540 "X" in the scale name indicates that it is a mole fraction scale, how many micro-moles of CO<sub>2</sub> in one mole of  
541 (dry) air. The word "concentration" only loosely reflects this. The WMO-CO<sub>2</sub>-X2019 scale improves upon the  
542 earlier WMO-CO<sub>2</sub>-X2007 scale by including a broader set of standards, which contain CO<sub>2</sub> in a wider range of  
543 concentrations that span the range 250-800 ppm (versus 250–520 ppm for WMO-CO<sub>2</sub>-X2007). In addition,  
544 NOAA/GML made two minor corrections to the analytical procedure used to quantify CO<sub>2</sub> concentrations,  
545 fixing an error in the second virial coefficient of CO<sub>2</sub> and accounting for loss of a small amount of CO<sub>2</sub> to  
546 materials in the manometer during the measurement process. The difference in concentrations measured using  
547 WMO-CO<sub>2</sub>-X2019 versus WMO-CO<sub>2</sub>-X2007 is ~+0.18 ppm at 400 ppm and the observational record of  
548 atmospheric CO<sub>2</sub> concentrations have been revised accordingly. The revisions have been applied retrospectively  
549 in all cases where the calibrations were performed by NOAA/GML, thus affecting measurements made by  
550 members of the WMO-GAW programme and other regionally coordinated programmes (e.g., Integrated Carbon  
551 Observing System, ICOS). Changes to the CO<sub>2</sub> concentrations measured across these networks propagate to the  
552 global mean CO<sub>2</sub> concentrations. The re-calibrated data were first used to estimate G<sub>ATM</sub> in the 2021 edition of  
553 the global carbon budget (Friedlingstein et al., 2022a). Friedlingstein et al. (2022a) verified that the change of

Formatted: Outline numbered + Level: 3 + Numbering Style: 1, 2, 3, ... + Start at: 1 + Alignment: Left + Aligned at: 0 cm + Indent at: 1.27 cm

Deleted: and

Formatted: Outline numbered + Level: 2 + Numbering Style: 1, 2, 3, ... + Start at: 1 + Alignment: Left + Aligned at: 0 cm + Indent at: 1.02 cm

Formatted: Pattern: Clear (Custom Colour (RGB(253,252,252)))

Formatted: Outline numbered + Level: 3 + Numbering Style: 1, 2, 3, ... + Start at: 1 + Alignment: Left + Aligned at: 0 cm + Indent at: 1.27 cm

Deleted: Earth System Research

Deleted: ESRL

Deleted: ESRL

Deleted: 2021).

Deleted: ESRL

Deleted: ESRL

561 scales from WMO-CO2-X2007 to WMO-CO2-X2019 made a negligible difference to the value of  $G_{ATM}$  (-0.06  
562 GtC yr<sup>-1</sup> during 2010-2019 and -0.01 GtC yr<sup>-1</sup> during 1959-2019, well within the uncertainty range reported  
563 below).

564 The uncertainty around the atmospheric growth rate is due to four main factors. First, the long-term  
565 reproducibility of reference gas standards (around 0.03 ppm for 1 $\sigma$  from the 1980s; Dlugokencky and Tans,  
566 2022). Second, small unexplained systematic analytical errors that may have a duration of several months to two  
567 years come and go. They have been simulated by randomising both the duration and the magnitude (determined  
568 from the existing evidence) in a Monte Carlo procedure. Third, the network composition of the marine boundary  
569 layer with some sites coming or going, gaps in the time series at each site, etc (Dlugokencky and Tans, 2022).

570 The latter uncertainty was estimated by NOAA/GML, with a Monte Carlo method by constructing 100  
571 "alternative" networks (Masarie and Tans, 1995; NOAA/GML, 2019). The second and third uncertainties,  
572 summed in quadrature, add up to 0.085 ppm on average (Dlugokencky and Tans, 2022). Fourth, the uncertainty  
573 associated with using the average CO<sub>2</sub> concentration from a surface network to approximate the true  
574 atmospheric average CO<sub>2</sub> concentration (mass-weighted, in 3 dimensions) as needed to assess the total  
575 atmospheric CO<sub>2</sub> burden. In reality, CO<sub>2</sub> variations measured at the stations will not exactly track changes in  
576 total atmospheric burden, with offsets in magnitude and phasing due to vertical and horizontal mixing. This  
577 effect must be very small on decadal and longer time scales, when the atmosphere can be considered well  
578 mixed. [The CO<sub>2</sub> increase in the stratosphere lags the increase \(meaning lower concentrations\) that we observe  
579 in the marine boundary layer, while the continental boundary layer \(where most of the emissions take place\)  
580 leads the marine boundary layer with higher concentrations. These effects nearly cancel each other. In addition  
581 the growth rate is nearly the same everywhere \(Ballantyne et al., 2012\).](#) We therefore maintain an uncertainty  
582 around the annual growth rate based on the multiple stations data set ranges between 0.11 and 0.72 GtC yr<sup>-1</sup>,  
583 with a mean of 0.61 GtC yr<sup>-1</sup> for 1959-1979 and 0.17 GtC yr<sup>-1</sup> for 1980-2020, when a larger set of stations were  
584 available as provided by Dlugokencky and Tans (2022). We estimate the uncertainty of the decadal averaged  
585 growth rate after 1980 at 0.02 GtC yr<sup>-1</sup> based on the calibration and the annual growth rate uncertainty but  
586 stretched over a 10-year interval. For years prior to 1980, we estimate the decadal averaged uncertainty to be  
587 0.07 GtC yr<sup>-1</sup> based on a factor proportional to the annual uncertainty prior and after 1980 (0.02 \* [0.61/0.17]  
588 GtC yr<sup>-1</sup>).

589 We assign a high confidence to the annual estimates of  $G_{ATM}$  because they are based on direct measurements  
590 from multiple and consistent instruments and stations distributed around the world (Ballantyne et al., 2012; Hall  
591 et al., 2021).

592 To estimate the total carbon accumulated in the atmosphere since 1750 or 1850, we use an atmospheric CO<sub>2</sub>  
593 concentration of [278.3 ± 3 ppm](#) or [285.1 ± 3 ppm](#), respectively (Gulev et al., 2021). For the construction of the  
594 cumulative budget shown in Figure 3, we use the fitted estimates of CO<sub>2</sub> concentration from Joos and Spahni  
595 (2008) to estimate the annual atmospheric growth rate using the conversion factors shown in Table 1. The  
596 uncertainty of ±3 ppm (converted to ±1 $\sigma$ ) is taken directly from the IPCC's AR5 assessment (Ciais et al., 2013).  
597 Typical uncertainties in the growth rate in atmospheric CO<sub>2</sub> concentration from ice core data are equivalent to  
598 ±0.1-0.15 GtC yr<sup>-1</sup> as evaluated from the Law Dome data (Etheridge et al., 1996) for individual 20-year intervals  
599 over the period from 1850 to 1960 (Bruno and Joos, 1997).

Deleted: ESRL

Deleted: ESRL

Deleted: Preliminary estimates suggest this effect would increase the annual uncertainty, but a full analysis is not yet available.

Deleted: ) but recognise further exploration of this uncertainty is required. At this time, we

Deleted: 277

Deleted: 286

Deleted: , based on a cubic spline fit to ice core data (Joos and Spahni, 2008)

611 **2.3.2 2022 projection**

612 We provide an assessment of  $G_{ATM}$  for 2022 based on the monthly calculated global atmospheric  $CO_2$   
613 concentration (GLO) through August (Dlugokencky and Tans, 2022), and bias-adjusted Holt–Winters  
614 exponential smoothing with additive seasonality (Chatfield, 1978) to project to January 2023. Additional  
615 analysis suggests that the first half of the year (the boreal winter-spring-summer transition) shows more  
616 interannual variability than the second half of the year (the boreal summer-autumn-winter transition), so that the  
617 exact projection method applied to the second half of the year has a relatively smaller impact on the projection  
618 of the full year. Uncertainty is estimated from past variability using the standard deviation of the last 5 years'  
619 monthly growth rates.

620 **2.4 Ocean  $CO_2$  sink**

621 **2.4.1 Historical period 1850-2021**

622 The reported estimate of the global ocean anthropogenic  $CO_2$  sink  $SO_{CEAN}$  is derived as the average of two  
623 estimates. The first estimate is derived as the mean over an ensemble of ten global ocean biogeochemistry  
624 models (GOBMs, Table 4 and Table A2). The second estimate is obtained as the mean over an ensemble of  
625 seven observation-based data-products (Table 4 and Table A3). An eighth product (Watson et al., 2020) is  
626 shown, but is not included in the ensemble average as it differs from the other products by adjusting the flux to a  
627 cool, salty ocean surface skin (see Appendix C.3.1 for a discussion of the Watson product). The GOBMs  
628 simulate both the natural and anthropogenic  $CO_2$  cycles in the ocean. They constrain the anthropogenic air-sea  
629  $CO_2$  flux (the dominant component of  $SO_{CEAN}$ ) by the transport of carbon into the ocean interior, which is also  
630 the controlling factor of present-day ocean carbon uptake in the real world. They cover the full globe and all  
631 seasons and were recently evaluated against surface ocean carbon observations, suggesting they are suitable to  
632 estimate the annual ocean carbon sink (Hauck et al., 2020). The data-products are tightly linked to observations  
633 of  $fCO_2$  (fugacity of  $CO_2$ , which equals  $pCO_2$  corrected for the non-ideal behaviour of the gas; Pfeil et al.,  
634 2013), which carry imprints of temporal and spatial variability, but are also sensitive to uncertainties in gas-  
635 exchange parameterizations and data-sparsity. Their asset is the assessment of interannual and spatial variability  
636 (Hauck et al., 2020). We further use two diagnostic ocean models to estimate  $SO_{CEAN}$  over the industrial era  
637 (1781-1958).

638 The global  $fCO_2$ -based flux estimates were adjusted to remove the pre-industrial ocean source of  $CO_2$  to the  
639 atmosphere of  $0.65 \text{ GtC yr}^{-1}$  from river input to the ocean (Regnier et al., 2022), to satisfy our definition of  
640  $SO_{CEAN}$  (Hauck et al., 2020). The river flux adjustment was distributed over the latitudinal bands using the  
641 regional distribution of Aumont et al. (2001; North:  $0.17 \text{ GtC yr}^{-1}$ , Tropics:  $0.16 \text{ GtC yr}^{-1}$ , South:  $0.32 \text{ GtC yr}^{-1}$ ),  
642 acknowledging that the boundaries of Aumont et al (2001; namely  $20^\circ S$  and  $20^\circ N$ ) are not consistent with the  
643 boundaries otherwise used in the GCB ( $30^\circ S$  and  $30^\circ N$ ). A recent study based on one ocean biogeochemical  
644 model (Lacroix et al., 2020) suggests that more of the riverine outgassing is located in the tropics than in the  
645 Southern Ocean; and hence this regional distribution is associated with a major uncertainty. Anthropogenic  
646 perturbations of river carbon and nutrient transport to the ocean are not considered (see section 2.7 [and](#)  
647 [Appendix D.3](#)).

Formatted: Outline numbered + Level: 3 + Numbering  
Style: 1, 2, 3, ... + Start at: 1 + Alignment: Left + Aligned at:  
0 cm + Indent at: 1.27 cm

Formatted: Outline numbered + Level: 2 + Numbering  
Style: 1, 2, 3, ... + Start at: 1 + Alignment: Left + Aligned at:  
0 cm + Indent at: 1.02 cm

Deleted: Period

Formatted: Pattern: Clear (Custom Colour  
(RGB(253,252,252)))

Formatted: Outline numbered + Level: 3 + Numbering  
Style: 1, 2, 3, ... + Start at: 1 + Alignment: Left + Aligned at:  
0 cm + Indent at: 1.27 cm

649 We derive  $S_{OCEAN}$  from GOBMs by using a simulation (sim A) with historical forcing of climate and  
 650 atmospheric  $CO_2$ , accounting for model biases and drift from a control simulation (sim B) with constant  
 651 atmospheric  $CO_2$  and normal year climate forcing. A third simulation (sim C) with historical atmospheric  $CO_2$   
 652 increase and normal year climate forcing is used to attribute the ocean sink to  $CO_2$  (sim C minus sim B) and  
 653 climate (sim A minus sim C) effects. A fourth simulation (sim D; historical climate forcing and constant  
 654 atmospheric  $CO_2$ ) is used to compare the change in anthropogenic carbon inventory in the interior ocean (sim A  
 655 minus sim D) to the observational estimate of Gruber et al. (2019) with the same flux components (steady state  
 656 and non-steady state anthropogenic carbon flux). Data-products are adjusted to represent the full ice-free ocean  
 657 area by a simple scaling approach when coverage is below 99%. GOBMs and data-products fall within the  
 658 observational constraints over the 1990s ( $2.2 \pm 0.7 \text{ GtC yr}^{-1}$ , Ciais et al., 2013) after applying adjustments.  
 659  $S_{OCEAN}$  is calculated as the average of the GOBM ensemble mean and data-product ensemble mean from 1990  
 660 onwards. Prior to 1990, it is calculated as the GOBM ensemble mean plus half of the offset between GOBMs  
 661 and data-products ensemble means over 1990-2001.  
 662 We assign an uncertainty of  $\pm 0.4 \text{ GtC yr}^{-1}$  to the ocean sink based on a combination of random (ensemble  
 663 standard deviation) and systematic uncertainties (GOBMs bias in anthropogenic carbon accumulation,  
 664 previously reported uncertainties in  $fCO_2$ -based data-products; see [Appendix C.3.3](#)). We assess a medium  
 665 confidence level to the annual ocean  $CO_2$  sink and its uncertainty because it is based on multiple lines of  
 666 evidence, it is consistent with ocean interior carbon estimates (Gruber et al., 2019, see section 3.5.5) and the  
 667 interannual variability in the GOBMs and data-based estimates is largely consistent and can be explained by  
 668 climate variability. We refrain from assigning a high confidence because of the systematic deviation between  
 669 the GOBM and data-product trends since around 2002. More details on the  $S_{OCEAN}$  methodology can be found in  
 670 Appendix C.3.

#### 671 2.4.2 2022 Projection

672 The ocean  $CO_2$  sink forecast for the year 2022 is based on the annual historical and estimated 2022 atmospheric  
 673  $CO_2$  concentration (Dlugokencky and Tans 2021), the historical and estimated 2022 annual global fossil fuel  
 674 emissions from this year's carbon budget, and the spring (March, April, May) Oceanic Niño Index (ONI)  
 675 (NCEP, 2022). Using a non-linear regression approach, i.e., a feed-forward neural network, atmospheric  $CO_2$ ,  
 676 ONI, and the fossil fuel emissions are used as training data to best match the annual ocean  $CO_2$  sink (i.e.  
 677 combined  $S_{OCEAN}$  estimate from GOBMs and data products) from 1959 through 2021 from this year's carbon  
 678 budget. Using this relationship, the 2022  $S_{OCEAN}$  can then be estimated from the projected 2021 input data using  
 679 the non-linear relationship established during the network training. To avoid overfitting, the neural network was  
 680 trained with a variable number of hidden neurons (varying between 2-5) and 20% of the randomly selected  
 681 training data were withheld for independent internal testing. Based on the best output performance (tested using  
 682 the 20% withheld input data), the best performing number of neurons was selected. In a second step, we trained  
 683 the network 10 times using the best number of neurons identified in step 1 and different sets of randomly  
 684 selected training data. The mean of the 10 trainings is considered our best forecast, whereas the standard  
 685 deviation of the 10 ensembles provides a first order estimate of the forecast uncertainty. This uncertainty is then  
 686 combined with the  $S_{OCEAN}$  uncertainty ( $0.4 \text{ GtC yr}^{-1}$ ) to estimate the overall uncertainty of the 2022 projection.

Deleted: section

Formatted: Outline numbered + Level: 3 + Numbering Style: 1, 2, 3, ... + Start at: 1 + Alignment: Left + Aligned at: 0 cm + Indent at: 1.27 cm

Deleted: index

Deleted: the

Deleted: index

691 2.5 [Land CO<sub>2</sub> sink](#)

692 2.5.1 Historical Period

693 The terrestrial land sink ( $S_{LAND}$ ) is thought to be due to the combined effects of fertilisation by rising  
694 atmospheric CO<sub>2</sub> and N inputs on plant growth, as well as the effects of climate change such as the lengthening  
695 of the growing season in northern temperate and boreal areas.  $S_{LAND}$  does not include land sinks directly  
696 resulting from land-use and land-use change (e.g., regrowth of vegetation) as these are part of the land-use flux  
697 ( $E_{LUC}$ ), although system boundaries make it difficult to attribute exactly CO<sub>2</sub> fluxes on land between  $S_{LAND}$  and  
698  $E_{LUC}$  (Erb et al., 2013).

699  $S_{LAND}$  is estimated from the multi-model mean of 16 DGVMs (Table A1). As described in Appendix C.4,  
700 DGVMs simulations include all climate variability and CO<sub>2</sub> effects over land. [In addition to the carbon cycle](#)  
701 [represented in all DGVMs, 11 models also account for the nitrogen cycle and hence can include](#) the effect of N  
702 inputs [on  \$S\_{LAND}\$](#) . The DGVMs estimate of  $S_{LAND}$  does not include the export of carbon to aquatic systems or its  
703 historical perturbation, which is discussed in Appendix D3. See Appendix C.4 for DGVMs evaluation and  
704 uncertainty assessment for  $S_{LAND}$ , using the International Land Model Benchmarking system (ILAMB; Collier et  
705 al., 2018). More details on the  $S_{LAND}$  methodology can be found in Appendix C.4.

706 2.5.2 2022 Projection

707 Like for the ocean forecast, the land CO<sub>2</sub> sink ( $S_{LAND}$ ) forecast is based on the annual historical and estimated  
708 2022 atmospheric CO<sub>2</sub> concentration (Dlugokencky and Tans 2021), historical and estimated 2022 annual  
709 global fossil fuel emissions from this year's carbon budget, and the summer (June, July, August) ONI (NCEP,  
710 2022). All training data are again used to best match  $S_{LAND}$  from 1959 through 2021 from this year's carbon  
711 budget using a feed-forward neural network. To avoid overfitting, the neural network was trained with a  
712 variable number of hidden neurons (varying between 2-15), larger than for  $S_{OCEAN}$  prediction due to the stronger  
713 land carbon interannual variability. As done for  $S_{OCEAN}$ , a pre-training selects the optimal number of hidden  
714 neurons based on 20% withheld input data, and in a second step, an ensemble of 10 forecasts is produced to  
715 provide the mean forecast plus uncertainty. This uncertainty is then combined with the  $S_{LAND}$  uncertainty for  
716 2021 (0.9 GtC yr<sup>-1</sup>) to estimate the overall uncertainty of the 2022 projection.

717 2.6 The atmospheric perspective

718 The world-wide network of in-situ atmospheric measurements and satellite derived atmospheric CO<sub>2</sub> column  
719 ( $xCO_2$ ) observations put a strong constraint on changes in the atmospheric abundance of CO<sub>2</sub>. This is true  
720 globally (hence our large confidence in  $G_{ATM}$ ), but also regionally in regions with sufficient observational  
721 density found mostly in the extra-tropics. This allows atmospheric inversion methods to constrain the magnitude  
722 and location of the combined total surface CO<sub>2</sub> fluxes from all sources, including fossil and land-use change  
723 emissions and land and ocean CO<sub>2</sub> fluxes. The inversions assume  $E_{FOS}$  to be well known, and they solve for the  
724 spatial and temporal distribution of land and ocean fluxes from the residual gradients of CO<sub>2</sub> between stations  
725 that are not explained by fossil fuel emissions. By design, such systems thus close the carbon balance ( $B_{IM} = 0$ )  
726 and thus provide an additional perspective on the independent estimates of the ocean and land fluxes.

Deleted: Terrestrial

Formatted: Heading 3, Outline numbered + Level: 2 +  
Numbering Style: 1, 2, 3, ... + Start at: 1 + Alignment: Left +  
Aligned at: 0 cm + Indent at: 1.02 cm

Formatted: Outline numbered + Level: 3 + Numbering  
Style: 1, 2, 3, ... + Start at: 1 + Alignment: Left + Aligned at:  
0 cm + Indent at: 1.27 cm

Deleted: , with 11

Deleted: including

Formatted: Outline numbered + Level: 3 + Numbering  
Style: 1, 2, 3, ... + Start at: 1 + Alignment: Left + Aligned at:  
0 cm + Indent at: 1.27 cm

Deleted: index

Formatted: Outline numbered + Level: 2 + Numbering  
Style: 1, 2, 3, ... + Start at: 1 + Alignment: Left + Aligned at:  
0 cm + Indent at: 1.02 cm

731 This year's release includes nine inversion systems that are described in Table A4. Each system is rooted in  
732 Bayesian inversion principles but uses different methodologies. These differences concern the selection of  
733 atmospheric CO<sub>2</sub> data or xCO<sub>2</sub>, and the choice of a-priori fluxes to refine. They also differ in spatial and  
734 temporal resolution, assumed correlation structures, and mathematical approach of the models (see references in  
735 Table A4 for details). Importantly, the systems use a variety of transport models, which was demonstrated to be  
736 a driving factor behind differences in atmospheric inversion-based flux estimates, and specifically their  
737 distribution across latitudinal bands (Gaubert et al., 2019; Schuh et al., 2019). Four inversion systems (CAMS-  
738 FT21r2, CMS-flux, GONGGA, THU) used satellite xCO<sub>2</sub> retrievals from GOSAT and/or OCO-2, scaled to the  
739 WMO 2019 calibration scale. One inversion this year (CMS-Flux) used these xCO<sub>2</sub> datasets in addition to the  
740 in-situ observational CO<sub>2</sub> mole fraction records.

741 The original products delivered by the inverse modellers were modified to facilitate the comparison to the other  
742 elements of the budget, specifically on two accounts: (1) global total fossil fuel emissions including cement  
743 carbonation CO<sub>2</sub> uptake, and (2) riverine CO<sub>2</sub> transport. Details are given below. We note that with these  
744 adjustments the inverse results no longer represent the net atmosphere-surface exchange over land/ocean areas  
745 as sensed by atmospheric observations. Instead, for land, they become the net uptake of CO<sub>2</sub> by vegetation and  
746 soils that is not exported by fluvial systems, similar to the DGVMs estimates. For oceans, they become the net  
747 uptake of anthropogenic CO<sub>2</sub>, similar to the GOBMs estimates.

748 The inversion systems prescribe global fossil fuel emissions based on the GCP's Gridded Fossil Emissions  
749 Dataset versions 2022.1 or 2022.2 (GCP-GridFED; Jones et al., 2022), which are updates to GCP-  
750 GridFEDv2021 presented by Jones et al. (2021). GCP-GridFEDv2022 scales gridded estimates of CO<sub>2</sub>  
751 emissions from EDGARv4.3.2 (Janssens-Maenhout et al., 2019) within national territories to match national  
752 emissions estimates provided by the GCB for the years 1959-2021, which were compiled following the  
753 methodology described in Section 2.1. Small differences between the systems due to for instance regridding to  
754 the transport model resolution, or use of different GridFED versions with different cement carbonation sinks  
755 (which were only present starting with GridFEDv2022.1), are adjusted in the latitudinal partitioning we present,  
756 to ensure agreement with the estimate of E<sub>FOS</sub> in this budget. We also note that the ocean fluxes used as prior by  
757 6 out of 9 inversions are part of the suite of the ocean process model or fCO<sub>2</sub> data products listed in Section 2.4.  
758 Although these fluxes are further adjusted by the atmospheric inversions, it makes the inversion estimates of the  
759 ocean fluxes not completely independent of S<sub>OCEAN</sub> assessed here.

760 To facilitate comparisons to the independent S<sub>OCEAN</sub> and S<sub>LAND</sub>, we used the same corrections for transport and  
761 outgassing of carbon transported from land to ocean, as done for the observation-based estimates of S<sub>OCEAN</sub> (see  
762 Appendix C.3).

763 The atmospheric inversions are evaluated using vertical profiles of atmospheric CO<sub>2</sub> concentrations (Figure B4).  
764 More than 30 aircraft programs over the globe, either regular programs or repeated surveys over at least 9  
765 months (except for SH programs), have been used to assess system performance (with space-time observational  
766 coverage sparse in the SH and tropics, and denser in NH mid-latitudes; Table A6). The nine systems are  
767 compared to the independent aircraft CO<sub>2</sub> measurements between 2 and 7 km above sea level between 2001 and  
768 2021. Results are shown in Figure B4 and discussed in [Appendix C.5.2](#).

Deleted: Section 3.7.

770 With a relatively small ensemble (N=9) of systems that moreover share some a-priori fluxes used with one  
771 another, or with the process-based models, it is difficult to justify using their mean and standard deviation as a  
772 metric for uncertainty across the ensemble. We therefore report their full range (min-max) without their mean.  
773 More details on the atmospheric inversions methodology can be found in Appendix C.5.

## 774 2.7 Processes not included in the global carbon budget

775 The contribution of anthropogenic CO and CH<sub>4</sub> to the global carbon budget is not fully accounted for in Eq. (1)  
776 and is described in Appendix D1. The contributions to CO<sub>2</sub> emissions of decomposition of carbonates not  
777 accounted for is described in Appendix D2. The contribution of anthropogenic changes in river fluxes is  
778 conceptually included in Eq. (1) in SO<sub>CEAN</sub> and in S<sub>LAND</sub>, but it is not represented in the process models used to  
779 quantify these fluxes. This effect is discussed in Appendix D3. Similarly, the loss of additional sink capacity  
780 from reduced forest cover is missing in the combination of approaches used here to estimate both land fluxes  
781 (E<sub>LUC</sub> and S<sub>LAND</sub>) and its potential effect is discussed and quantified in Appendix D4.  
782

## 783 3 Results

784 For each component of the global carbon budget, we present results for three different time periods: the full  
785 historical period, from 1850 to 2021, the six decades in which we have atmospheric concentration records from  
786 Mauna Loa (1960-2021), a specific focus on last year (2021), and the projection for the current year (2022).  
787 Subsequently, we assess the combined constraints from the budget components (often referred to as a bottom-up  
788 budget) against the top-down constraints from inverse modelling of atmospheric observations. We do this for  
789 the global balance of the last decade, as well as for a regional breakdown of land and ocean sinks by broad  
790 latitude bands.

### 791 3.1 Fossil CO<sub>2</sub> Emissions

#### 792 3.1.1 Historical period 1850-2021

793 Cumulative fossil CO<sub>2</sub> emissions for 1850-2021 were 465 ± 25 GtC, including the cement carbonation sink  
794 (Figure 3, Table 8, all cumulative numbers are rounded to the nearest 5GtC).

795 In this period, 46% of fossil CO<sub>2</sub> emissions came from coal, 35% from oil, 15% from natural gas, 3% from  
796 decomposition of carbonates, and 1% from flaring.

797 In 1850, the UK stood for 62% of global fossil CO<sub>2</sub> emissions. In 1891 the combined cumulative emissions of  
798 the current members of the European Union reached and subsequently surpassed the level of the UK. Since  
799 1917 US cumulative emissions have been the largest. Over the entire period 1850-2021, US cumulative  
800 emissions amounted to 115GtC (24% of world total), the EU's to 80 GtC (17%), and China's to 70 GtC (14%).

801 ~~In addition to the estimates of fossil CO<sub>2</sub> emissions that we provide here (see Methods), there~~ are three  
802 additional global datasets with long time series that include all sources of fossil CO<sub>2</sub> emissions: CDIAC-FF  
803 (Gilfillan and Marland, 2021), CEDS version v\_2021\_04\_21 (Hoesly et al., 2018, O'Rourke et al., 2021) and  
804 PRIMAP-hist version 2.3.1 (Gütschow et al., 2016, 2021), although these datasets are not entirely independent  
805 from each other (Andrew, 2020a). CDIAC-FF has the lowest cumulative emissions over 1750-2018 at 437 GtC,  
806 GCP has 443 GtC, CEDS 445 GtC, PRIMAP-hist TP 453 GtC, and PRIMAP-hist CR 455 GtC. CDIAC-FF

Formatted: Outline numbered + Level: 2 + Numbering Style: 1, 2, 3, ... + Start at: 1 + Alignment: Left + Aligned at: 0 cm + Indent at: 1.02 cm

Formatted: Indent: Left: 0 cm, First line: 0 cm, Outline numbered + Level: 1 + Numbering Style: 1, 2, 3, ... + Start at: 1 + Alignment: Left + Aligned at: 0 cm + Indent at: 0.76 cm

Formatted: Outline numbered + Level: 2 + Numbering Style: 1, 2, 3, ... + Start at: 1 + Alignment: Left + Aligned at: 0 cm + Indent at: 1.02 cm

Formatted: Outline numbered + Level: 3 + Numbering Style: 1, 2, 3, ... + Start at: 1 + Alignment: Left + Aligned at: 0 cm + Indent at: 1.27 cm

Deleted: There

Deleted: );

Deleted: .

810 excludes emissions from lime production, while neither CDIAC-FF nor GCP explicitly include emissions from  
811 international bunker fuels prior to 1950. CEDS has higher emissions from international shipping in recent years,  
812 while PRIMAP-hist has higher fugitive emissions than the other datasets. However, in general these four  
813 datasets are in relative agreement as to total historical global emissions of fossil CO<sub>2</sub>.

### 814 3.1.2 Recent period 1960-2021

815 Global fossil CO<sub>2</sub> emissions, E<sub>FOS</sub> (including the cement carbonation sink), have increased every decade from an  
816 average of 3.0 ± 0.2 GtC yr<sup>-1</sup> for the decade of the 1960s to an average of 9.6 ± 0.5 GtC yr<sup>-1</sup> during 2012-2021  
817 (Table 6, Figure 2 and Figure 5). The growth rate in these emissions decreased between the 1960s and the  
818 1990s, from 4.3% yr<sup>-1</sup> in the 1960s (1960-1969), 3.2% yr<sup>-1</sup> in the 1970s (1970-1979), 1.6% yr<sup>-1</sup> in the 1980s  
819 (1980-1989), to 0.9% yr<sup>-1</sup> in the 1990s (1990-1999). After this period, the growth rate began increasing again in  
820 the 2000s at an average growth rate of 3.0% yr<sup>-1</sup>, decreasing to 0.5% yr<sup>-1</sup> for the last decade (2012-2021).  
821 China's emissions increased by +1.5% yr<sup>-1</sup> on average over the last 10 years dominating the global trend, and  
822 India's emissions increased by +3.8% yr<sup>-1</sup>, while emissions decreased in EU27 by -1.8% yr<sup>-1</sup>, and in the USA  
823 by -1.1% yr<sup>-1</sup>. Figure 6 illustrates the spatial distribution of fossil fuel emissions for the 2012-2021 period.

824 E<sub>FOS</sub> includes the uptake of CO<sub>2</sub> by cement via carbonation which has increased with increasing stocks of  
825 cement products, from an average of 20 MtC yr<sup>-1</sup> (0.02 GtC yr<sup>-1</sup>) in the 1960s to an average of 200 MtC yr<sup>-1</sup> (0.2  
826 GtC yr<sup>-1</sup>) during 2012-2021 (Figure 5).

### 827 3.1.3 Final year 2021

828 Global fossil CO<sub>2</sub> emissions were 5.1% higher in 2021 than in 2020, because of the global rebound from the  
829 worst of the COVID-19 pandemic, with an increase of 0.5 GtC to reach 9.9 ± 0.5 GtC (including the cement  
830 carbonation sink) in 2021 (Figure 5), distributed among coal (41%), oil (32%), natural gas (22%), cement (5%)  
831 and others (1%). Compared to the previous year, 2021 emissions from coal, oil and gas increased by 5.7%, 5.8%  
832 and 4.8% respectively, while emissions from cement increased by 2.1%. All growth rates presented are adjusted  
833 for the leap year, unless stated otherwise.

834 In 2021, the largest absolute contributions to global fossil CO<sub>2</sub> emissions were from China (31%), the USA  
835 (14%), the EU27 (8%), and India (7%). These four regions account for 59% of global CO<sub>2</sub> emissions, while the  
836 rest of the world contributed 41%, including international aviation and marine bunker fuels (2.8% of the total).  
837 Growth rates for these countries from 2020 to 2021 were 3.5% (China), 6.2% (USA), 6.8% (EU27), and 11.1%  
838 (India), with +4.5% for the rest of the world. The per-capita fossil CO<sub>2</sub> emissions in 2021 were 1.3 tC person<sup>-1</sup>  
839 yr<sup>-1</sup> for the globe, and were 4.0 (USA), 2.2 (China), 1.7 (EU27) and 0.5 (India) tC person<sup>-1</sup> yr<sup>-1</sup> for the four  
840 highest emitting countries (Figure 5).

841 The post-COVID-19 rebound in emissions of 5.1% in 2021 is close to the projected increase of 4.8% published  
842 in Friedlingstein et al. (2021) (Table 7). Of the regions, the projection for the 'rest of world' region was least  
843 accurate (off by -1.3%), largely because of poorly projected emissions from international transport (bunker  
844 fuels), which were subject to very large changes during this period.

Formatted: Outline numbered + Level: 3 + Numbering  
Style: 1, 2, 3, ... + Start at: 1 + Alignment: Left + Aligned at:  
0 cm + Indent at: 1.27 cm

Formatted: Outline numbered + Level: 3 + Numbering  
Style: 1, 2, 3, ... + Start at: 1 + Alignment: Left + Aligned at:  
0 cm + Indent at: 1.27 cm

Deleted: 10.1 ± 0.5 GtC (

Deleted: when

Deleted: ,

848 **3.1.4 Year 2022 Projection**

849 Globally, we estimate that global fossil CO<sub>2</sub> emissions (including cement carbonation) will grow by 1.1% in  
850 2022 (0.0% to 1.7%) to 10.0 GtC (36.5 GtCO<sub>2</sub>), exceeding their 2019 emission levels of 9.9 GtC (36.2 GtCO<sub>2</sub>).  
851 Global increase in 2022 emissions per fuel types are projected to be +0.8% (range 0.0% to 1.7%) for coal,  
852 +2.2% (range -0.7% to 2.9%) for oil, +1.1% (range 0.0% to 2.2%) for natural gas, and -2.8% (range -5.5% to -  
853 0.2%) for cement.

854 For China, projected fossil emissions in 2022 are expected to decline by 1.5% (range -3.0% to +0.1%) compared  
855 with 2021 emissions, bringing 2022 emissions for China around 3.0 GtC yr<sup>-1</sup> (11.1 GtCO<sub>2</sub> yr<sup>-1</sup>). Changes in fuel  
856 specific projections for China are -0.5% for coal, -2.3% for oil, -1.1% natural gas, and -9.2% for cement.

857 For the USA, the Energy Information Administration (EIA) emissions projection for 2022 combined with  
858 cement clinker data from USGS gives an increase of 1.6% (range -0.9% to +4.1%) compared to 2021, bringing  
859 USA 2022 emissions to around 1.4 GtC yr<sup>-1</sup> (5.1 GtCO<sub>2</sub> yr<sup>-1</sup>). This is based on separate projections for coal -  
860 2.8%, oil +1.9%, natural gas +4.1%, and cement +0.7%.

861 For the European Union, our projection for 2022 is for a decline of 1.0% (range -2.9% to +1.0%) over 2021,  
862 with 2022 emissions around 0.8 GtC yr<sup>-1</sup> (2.8 GtCO<sub>2</sub> yr<sup>-1</sup>). This is based on separate projections for coal of  
863 +7.5%, oil +0.6%, natural gas -11.0%, and cement unchanged.

864 For India, our projection for 2022 is an increase of 5.6% (range of 3.5% to 7.7%) over 2021, with 2022  
865 emissions around 0.8 GtC yr<sup>-1</sup> (2.9 GtCO<sub>2</sub> yr<sup>-1</sup>). This is based on separate projections for coal of +5.0%, oil  
866 +8.0%, natural gas -3.0%, and cement +10.0%.

867 For the rest of the world, the expected growth rate for 2022 is 2.5% (range 0.1% to 2.3%). The fuel-specific  
868 projected 2022 growth rates for the rest of the world are: +1.4% (range -0.6% to +3.4%) for coal, +3.2% (1.6%  
869 to +4.9%) for oil, +2.6% (1.1% to 4.1%) for natural gas, +2.8% (+0.6% to +5.1%) for cement.

870 **3.2 Emissions from Land Use Changes**

871 **3.2.1 Historical period 1850-2021**

872 Cumulative CO<sub>2</sub> emissions from land-use changes (ELUC) for 1850-2021 were 205 ± 60 GtC (Table 8; Figure 3;  
873 Figure 14). The cumulative emissions from ELUC show a large spread among individual estimates of 140 GtC  
874 (updated H&N2017), 280 GtC (BLUE), and 190 GtC (OSCAR) for the three bookkeeping models and a similar  
875 wide estimate of 185 ± 60 GtC for the DGVMS (all cumulative numbers are rounded to the nearest 5GtC). These  
876 estimates are broadly consistent with indirect constraints from vegetation biomass observations, giving a  
877 cumulative source of 155 ± 50 GtC over the 1901-2012 period (Li et al., 2017). However, given the large  
878 spread, a best estimate is difficult to ascertain.

879 **3.2.2 Recent period 1960-2021**

880 In contrast to growing fossil emissions, CO<sub>2</sub> emissions from land-use, land-use change, and forestry have  
881 remained relatively constant, over the 1960-1999 period, but showing a slight decrease of about 0.1 GtC per  
882 decade since the 1990s, reaching 1.2 ± 0.7 GtC yr<sup>-1</sup> for the 2012-2021 period (Table 6), but with large spread  
883 across estimates (Table 5, Figure 7). Different from the bookkeeping average, the DGVMS model average grows

Formatted: Outline numbered + Level: 3 + Numbering  
Style: 1, 2, 3, ... + Start at: 1 + Alignment: Left + Aligned at:  
0 cm + Indent at: 1.27 cm

Deleted: 2

Deleted: 37.3

Deleted: 10.0

Deleted: 7

Formatted: Outline numbered + Level: 2 + Numbering  
Style: 1, 2, 3, ... + Start at: 1 + Alignment: Left + Aligned at:  
0 cm + Indent at: 1.02 cm

Formatted: Outline numbered + Level: 3 + Numbering  
Style: 1, 2, 3, ... + Start at: 1 + Alignment: Left + Aligned at:  
0 cm + Indent at: 1.27 cm

Deleted:

Deleted: are particularly uncertain, with

Formatted: Outline numbered + Level: 3 + Numbering  
Style: 1, 2, 3, ... + Start at: 1 + Alignment: Left + Aligned at:  
0 cm + Indent at: 1.27 cm

890 slightly larger over the 1970-2021 period and shows no sign of decreasing emissions in the recent decades  
891 (Table 5, Figure 7). This is, however, expected as DGVM-based estimates include the loss of additional sink  
892 capacity, which grows with time, while the bookkeeping estimates do not (Appendix D4).

893  $E_{LUC}$  is a net term of various gross fluxes, which comprise emissions and removals. Gross emissions on average  
894 over the 1850-2021 period are two (BLUE, OSCAR) to three (updated H&N2017) times larger than the net  $E_{LUC}$   
895 emissions. Gross emissions show a moderate increase from an average of  $3.2 \pm 0.9 \text{ GtC yr}^{-1}$  for the decade of  
896 the 1960s to an average of  $3.8 \pm 0.7 \text{ GtC yr}^{-1}$  during 2012-2021 (Figure 7). Increases in gross removals, from  
897  $1.8 \pm 0.4 \text{ GtC yr}^{-1}$  for the 1960s to  $2.6 \pm 0.4 \text{ GtC yr}^{-1}$  for 2012-2021, were slightly larger than the increase in  
898 gross emissions. Since the processes behind gross removals, foremost forest regrowth and soil recovery, are all  
899 slow, while gross emissions include a large instantaneous component, short-term changes in land-use dynamics,  
900 such as a temporary decrease in deforestation, influences gross emissions dynamics more than gross removals  
901 dynamics. It is these relative changes to each other that explain the small decrease in net  $E_{LUC}$  emissions over  
902 the last two decades and the last few years. Gross fluxes often differ more across the three bookkeeping  
903 estimates than net fluxes, which is expected due to different process representation; in particular, treatment of  
904 shifting cultivation, which increases both gross emissions and removals, differs across models.

905 There is a smaller decrease in net  $\text{CO}_2$  emissions from land-use change in the last few years (Figure 7) than in  
906 our last year's estimate (Friedlingstein et al., 2021), which places our updated estimates between last year's  
907 estimate and the estimate from the GCB2020 (Friedlingstein et al., 2020). This change is principally attributable  
908 to changes in  $E_{LUC}$  estimates from BLUE and OSCAR, which relate to improvements in the underlying land-use  
909 forcing (see Appendix C.2.2 for details). These changes address issues identified with last year's land-use  
910 forcing (see Friedlingstein et al., 2022) and remove/attenuate several emission peaks in Brazil and the  
911 Democratic Republic of the Congo and lead to higher net emissions in Brazil in the last decades compared to  
912 last year's global carbon budget (the emissions averaged over the three bookkeeping models for Brazil for the  
913 2011-2020 period were  $168 \text{ MtC yr}^{-1}$  in GCB2021 as compared to  $289 \text{ MtC yr}^{-1}$  in GCB2022). A remaining,  
914 caveat is that global land-use change data for model input does not capture forest degradation, which often  
915 occurs on small scale or without forest cover changes easily detectable from remote sensing and poses a  
916 growing threat to forest area and carbon stocks that may surpass deforestation effects (e.g., Matricardi et al.,  
917 2020, Qin et al., 2021). While independent pan-tropical or global estimates of vegetation cover dynamics or  
918 carbon stock changes based on satellite remote sensing have become available in recent years, a direct  
919 comparison to our estimates is not possible, most importantly because satellite-based estimates usually do not  
920 distinguish between anthropogenic drivers and natural forest cover losses (e.g. from drought or natural  
921 wildfires) (Pongratz et al., 2021).

922 We additionally separate the net  $E_{LUC}$  into four component fluxes to gain further insight into the drivers of  
923 emissions: deforestation, re/afforestation, and wood harvest (i.e. all fluxes on forest lands), emissions from  
924 organic soils (i.e. peat drainage and peat fires), and fluxes associated with all other transitions (Figure 7; Sec.  
925 C.2.1). On average over the 2012-2021 period and over the three bookkeeping estimates, fluxes from  
926 deforestation amount to  $1.8 \pm 0.4 \text{ GtC yr}^{-1}$  and from re/afforestation and wood harvest to  $-0.9 \pm 0.3 \text{ GtC yr}^{-1}$   
927 (Table 5). Emissions from organic soils ( $0.2 \pm 0.1 \text{ GtC yr}^{-1}$ ) and the net flux from other transitions ( $0.2 \pm 0.1$   
928  $\text{GtC yr}^{-1}$ ) are substantially less important globally. Deforestation is thus the main driver of global gross sources.

Deleted: , and remained largely constant over the last 60 years, with...

Deleted: showing the relevance of land management such as harvesting or rotational agriculture.

Deleted: changes

Deleted: DR

Deleted: . While we deem these changes in land-use forcing and emissions an improvement, the estimated emissions based on the new land-use forcing still do not fully reflect the rise in Brazilian deforestation in the recent few years (Silva Junior, 2021), and associated increasing emissions from deforestation would have been missed here. Differences still exist, which highlight the need for accurate knowledge of land-use transitions and their spatial and temporal variability. A further...

Deleted: 2021).

Deleted: gross sources

Deleted: sinks and how the bookkeeping models compare to each...

Deleted: emissions

Deleted: carbon uptake in forests

Deleted: caused by peat drainage or peat fires (with

Deleted: with

Deleted: 1

Deleted: , but emissions from organic soils contribute over proportionally to interannual variability (related in particular to peat fires in dry years in Southeast Asia).

956 The relatively small deforestation flux ( $1.8 \pm 0.4 \text{ GtC yr}^{-1}$ ) in comparison to the gross [emission](#) estimate above  
957 ( $3.8 \pm 0.7 \text{ GtC yr}^{-1}$ ) is explained by the fact that emissions associated with wood harvesting [do not count as](#)  
958 [deforestation as they do not change the land cover](#). This split into component fluxes clarifies the potentials for  
959 emission reduction and carbon dioxide removal; the emissions from deforestation could be halted (largely)  
960 without compromising carbon uptake [by forests and would contribute to emissions reduction](#). By contrast,  
961 reducing wood harvesting [would have limited potential to reduce emissions as it would be associated with less](#)  
962 forest regrowth; sinks and sources cannot be decoupled here. [Carbon dioxide removal in forests could instead be](#)  
963 [increased by re/afforestation](#).

964 Overall, highest land-use emissions occur in the tropical regions of all three continents. The top three emitters  
965 (both cumulatively 1959-2021 and on average over 2012-2021) are Brazil (in particular the Amazon Arc of  
966 Deforestation), Indonesia and the Democratic Republic of the Congo, with these 3 countries contributing 0.7  
967  $\text{GtC yr}^{-1}$  or 58% of the global total land-use emissions (average over 2012-2021) (Figure 6b). This is related to  
968 massive expansion of cropland, particularly in the last few decades in Latin America, Southeast Asia, and sub-  
969 Saharan Africa Emissions (Hong et al., 2021), to a substantial part for export [of agricultural products](#) (Pendrill et  
970 al., 2019). Emission intensity is high in many tropical countries, particularly of Southeast Asia, due to high rates  
971 of land conversion in regions of carbon-dense and often still pristine, undegraded natural forests (Hong et al.,  
972 2021). Emissions are further increased by peat fires in equatorial Asia (GFED4s, van der Werf et al., 2017).  
973 Uptake due to land-use change occurs, particularly in Europe, partly related to expanding forest area as a  
974 consequence of the forest transition in the 19<sup>th</sup> and 20<sup>th</sup> century and subsequent regrowth of forest (Figure 6b)  
975 (Mather 2001; McGrath et al., 2015).

976 While the mentioned patterns are supported by independent literature and robust, we acknowledge that model  
977 spread is substantially larger on regional than global level, as has been shown for bookkeeping models (Bastos  
978 et al., 2021) as well as DGVMs (Obermeier et al., 2021). [Assessments for individual regions will be performed](#)  
979 as part of REgional Carbon Cycle Assessment and Processes (RECCAP2; Ciais et al., 2020) or already exist for  
980 selected regions (e.g., for Europe by Petrescu et al., 2020, for Brazil by Rosan et al., 2021, for 8 selected  
981 countries/regions in comparison to inventory data by Schwingshackl et al., *subm.*).

982 National GHG inventory data (NGHGI) under the LULUCF sector or data submitted by countries to FAOSTAT  
983 differ from the global models' definition of  $E_{LUC}$  we adopt here in that in the NGHGI reporting, the natural  
984 fluxes ( $S_{LAND}$ ) are counted towards  $E_{LUC}$  when they occur on managed land (Grassi et al., 2018). In order to  
985 compare our results to the NGHGI approach, we perform a re-mapping of our  $E_{LUC}$  estimates, [by adding  \$S\_{LAND}\$  in](#)  
986 managed forest from the DGVMs simulations (following Grassi et al., 2021) to the bookkeeping  $E_{LUC}$  estimate  
987 (see Appendix C.2.3). For the 2012-2021 period, we estimate that  $1.8 \text{ GtC yr}^{-1}$  of  $S_{LAND}$  occurred [in managed](#)  
988 forests and is then reallocated to  $E_{LUC}$  here, as done in the NGHGI method. Doing so, our mean estimate of  $E_{LUC}$   
989 is reduced from a source of  $1.2 \text{ GtC}$  to a sink of  $0.6 \text{ GtC}$ , very similar to the NGHGI estimate of a  $0.5 \text{ GtC}$  sink  
990 (Table 9). The re-mapping approach has been shown to be generally applicable also on country-level ([Grassi et](#)  
991 [al., 2022b](#); Schwingshackl et al., *subm.*). Country-level analysis suggests, e.g., that the bookkeeping mean  
992 estimates higher deforestation emissions than the national report in Indonesia, but estimates less  $\text{CO}_2$  removal  
993 by afforestation than the national report in China. The fraction of the natural  $\text{CO}_2$  sinks that the NGHGI  
994 estimates include differs substantially across countries, related to varying proportions of managed vs all forest

Deleted: source

Deleted: , while

Deleted: constitute a source of emissions to the atmosphere, are contained in the component flux on forest, together with the associated carbon uptake in regrowth, because wood harvesting does ...

Deleted: For the same reason the flux on forest, being a net flux of sources from slash and product decay following wood harvest and sinks due to regrowth after wood harvest or after abandonment, is smaller than the gross sink estimates above.

Deleted: thus

Deleted: better

Deleted: than the gross fluxes do

Deleted: in other component fluxes

Deleted: ; reforestation following agricultural abandonment does not directly depend on deforestation and can independently provide carbon dioxide removal.

Deleted: to

Deleted: to the atmosphere is

Moved down [2]: A reason for this lies in the fact that country reports do not (fully) capture the carbon flux consequences of shifting cultivation.

Deleted: Last, we compare our component flux estimates to NGHGI (Grassi et al., 2022b): With  $1.1 \text{ GtC yr}^{-1}$  averaged over 2012-2021, deforestation emissions are reported to be smaller by countries than the bookkeeping estimate.

Deleted: With  $0.3 \text{ GtC yr}^{-1}$  and  $0.2 \text{ GtC yr}^{-1}$ , emissions from organic soils and the net flux from other transitions, respectively, are similar (slightly larger) than the estimates based on the bookkeeping approach and the external peat drainage and burning datasets. With  $1.75 \text{ GtC yr}^{-1}$ , carbon uptake...

Deleted: is substantially larger, owing to the inclusion of natural  $\text{CO}_2$  fluxes on managed land in the NGHGI (see below)...

Deleted: A detailed analysis of country-level or regional uncertainties is beyond the scope of this study.

Deleted: estimate

Deleted: including the

Deleted: over

Deleted: on

1036 areas (Schwingshackl et al., *subm.*). [Comparing E<sub>LUC</sub> and NGHGI on the basis of the four component fluxes](#)  
1037 [\(Grassi et al., 2022b\)](#) we find that NGHGI deforestation emissions are reported to be smaller than the  
1038 [bookkeeping estimate \(1.1 GtC yr<sup>-1</sup> averaged over 2012-2021\)](#). ~~A reason for this lies in the fact that country~~  
1039 ~~reports do not (fully) capture the carbon flux consequences of shifting cultivation.~~ [Conversely, carbon uptake in](#)  
1040 [forests \(re/afforestation and forestry\) is substantially larger than the bookkeeping estimate \(1.75 GtC yr<sup>-1</sup>](#)  
1041 [averaged over 2012-2021\), owing to the inclusion of natural CO<sub>2</sub> fluxes on managed land in the NGHGI.](#)  
1042 [Emissions from organic soils and the net flux from other transitions are similar to the estimates based on the](#)  
1043 [bookkeeping approach and the external peat drainage and burning datasets. Though estimates between NGHGI,](#)  
1044 FAOSTAT, individual process-based models and the mapped budget estimates still differ in value and need  
1045 further analysis, the approach taken here provides a possibility to relate the global models' and NGHGI  
1046 approach to each other routinely and thus link the anthropogenic carbon budget estimates of land CO<sub>2</sub> fluxes  
1047 directly to the Global Stocktake, as part of UNFCCC Paris Agreement.

### 1048 3.2.3 Final year 2021

1049 The global CO<sub>2</sub> emissions from land-use change are estimated as 1.1 ± 0.7 GtC in 2021, similar to the 2020  
1050 estimate. However, confidence in the annual change remains low.

1051 Land-use change and related emissions may have been affected by the COVID-19 pandemic (e.g. Poulter et al.,  
1052 2021). During the period of the pandemic, environmental protection policies and their implementation may have  
1053 been weakened in Brazil (Vale et al., 2021). In other countries, too, monitoring capacities and legal enforcement  
1054 of measures to reduce tropical deforestation have been reduced due to budget restrictions of environmental  
1055 agencies or impairments to ground-based monitoring that prevents land grabs and tenure conflicts (Brancaion et  
1056 al., 2020, Amador-Jiménez et al., 2020). Effects of the pandemic on trends in fire activity or forest cover  
1057 changes are hard to separate from those of general political developments and environmental changes and the  
1058 long-term consequences of disruptions in agricultural and forestry economic activities (e.g., Gruère and Brooks,  
1059 2020; Golar et al., 2020; Beckman and Countryman, 2021) remain to be seen. Overall, there is limited evidence  
1060 so far that COVID-19 was a key driver of changes in LULUCF emissions at global scale. Impacts vary across  
1061 countries and deforestation-curbing and enhancing factors may partly compensate each other (Wunder et al.,  
1062 2021).

### 1063 3.2.4 Year 2022 Projection

1064 In Indonesia, peat fire emissions are very low, potentially related to a relatively wet dry season (GFED4.1s, van  
1065 der Werf et al., 2017). In South America, the trajectory of tropical deforestation and degradation fires resembles  
1066 the long-term average; global emissions from tropical deforestation and degradation fires were estimated to be  
1067 116 TgC by August 23 (GFED4.1s, van der Werf et al., 2017). Our preliminary estimate of E<sub>LUC</sub> for 2022 is  
1068 substantially lower than the 2012-2021 average, which saw years of anomalously dry conditions in Indonesia  
1069 and high deforestation fires in South America (Friedlingstein et al., 2022). Based on the fire emissions until  
1070 August 23, we expect E<sub>LUC</sub> emissions of around 1.0 GtC in 2022. Note that although our extrapolation is based  
1071 on tropical deforestation and degradation fires, degradation attributable to selective logging, edge-effects or  
1072 fragmentation will not be captured. Further, deforestation and fires in deforestation zones may become more  
1073 disconnected, partly due changes in legislation in some regions. For example, Van Wees et al. (2021) found that

Moved (insertion) [2]

Deleted: ¶  
Though estimates between GHGI

Formatted: Outline numbered + Level: 3 + Numbering  
Style: 1, 2, 3, ... + Start at: 1 + Alignment: Left + Aligned at:  
0 cm + Indent at: 1.27 cm

Formatted: Outline numbered + Level: 3 + Numbering  
Style: 1, 2, 3, ... + Start at: 1 + Alignment: Left + Aligned at:  
0 cm + Indent at: 1.27 cm

1076 the contribution from fires to forest loss decreased in the Amazon and in Indonesia over the period of 2003-  
1077 2018. More recent years, however, saw an uptick in the Amazon again (Tyukavina et al., 2022 with update) and  
1078 more work is needed to understand fire-deforestation relations.

Deleted:

1079 The fires in Mediterranean Europe in summer 2022 and in the U.S. in spring 2022, though above average for  
1080 those regions, only contribute a small amount to global emissions. However, they were unrelated to land-use  
1081 change and are thus not attributed to  $E_{LUC}$ , but would be [be part of](#) the natural land sink.

Deleted: captured by

1082 Land use dynamics may be influenced by the disruption to the global food market associated with the war in  
1083 Ukraine, but scientific evidence so far is very limited. High food prices, which preceded but were exacerbated  
1084 by the war (Torero 2022), are generally linked to higher deforestation (Angelsen and Kaimowitz 1999), while  
1085 high prices on agricultural inputs such as fertilizers and fuel, which are also under pressure from embargoes,  
1086 may impair yields.

### 1087 3.3 Total anthropogenic emissions

Formatted: Outline numbered + Level: 2 + Numbering Style: 1, 2, 3, ... + Start at: 1 + Alignment: Left + Aligned at: 0 cm + Indent at: 1.02 cm

1088 Cumulative anthropogenic CO<sub>2</sub> emissions for 1850-2021 totalled 670 ± 65 GtC (2455 ± 240 GtCO<sub>2</sub>), of which  
1089 70% (470 GtC) occurred since 1960 and 33% (220 GtC) since 2000 (Table 6 and 8). Total anthropogenic  
1090 emissions more than doubled over the last 60 years, from 4.5 ± 0.7 GtC yr<sup>-1</sup> for the decade of the 1960s to an  
1091 average of 10.8 ± 0.8 GtC yr<sup>-1</sup> during 2012-2021, and reaching 10.9 ± 0.9 GtC (40.0 ± 3.3 GtCO<sub>2</sub>) in 2021. For  
1092 2022, we project global total anthropogenic CO<sub>2</sub> emissions from fossil and land use changes to be also around  
1093 10.9 GtC (40.1 GtCO<sub>2</sub>). All values here include the cement carbonation sink (currently about 0.2 GtC yr<sup>-1</sup>).

Deleted: 9

Deleted: 11.1

Deleted: 8

Deleted: 11.1

Deleted: 9

Deleted: 79

1094 During the historical period 1850-2021, 30% of historical emissions were from land use change and 70% from  
1095 fossil emissions. However, fossil emissions have grown significantly since 1960 while land use changes have  
1096 not, and consequently the contributions of land use change to total anthropogenic emissions were smaller during  
1097 recent periods (18% during the period 1960-2021 and 11% during 2012-2021).

### 1098 3.4 Atmospheric CO<sub>2</sub>

Formatted: Indent: Left: 0 cm, First line: 0 cm, Outline numbered + Level: 2 + Numbering Style: 1, 2, 3, ... + Start at: 1 + Alignment: Left + Aligned at: 0 cm + Indent at: 1.02 cm

#### 1099 3.4.1 Historical period 1850-2021

Formatted: Outline numbered + Level: 3 + Numbering Style: 1, 2, 3, ... + Start at: 1 + Alignment: Left + Aligned at: 0 cm + Indent at: 1.27 cm

1100 Atmospheric CO<sub>2</sub> concentration was approximately 278 parts per million (ppm) in 1750, reaching 300 ppm in  
1101 the 1910s, 350 ppm in the late 1980s, and reaching 414.71 ± 0.1 ppm in 2021 (Dlugokencky and Tans, 2022);  
1102 Figure 1). The mass of carbon in the atmosphere increased by 48% from 590 GtC in 1750 to 879 GtC in 2021.  
1103 Current CO<sub>2</sub> concentrations in the atmosphere are unprecedented in the last 2 million years and the current rate  
1104 of atmospheric CO<sub>2</sub> increase is at least 10 times faster than at any other time during the last 800,000 years  
1105 (Canadell et al., 2021).

Deleted: 277

Deleted: (Joos and Spahni, 2008),

#### 1106 3.4.2 Recent period 1960-2021

Formatted: Outline numbered + Level: 3 + Numbering Style: 1, 2, 3, ... + Start at: 1 + Alignment: Left + Aligned at: 0 cm + Indent at: 1.27 cm

1107 The growth rate in atmospheric CO<sub>2</sub> level increased from 1.7 ± 0.07 GtC yr<sup>-1</sup> in the 1960s to 5.2 ± 0.02 GtC yr<sup>-1</sup>  
1108 during 2012-2022 with important decadal variations (Table 6, Figure 3 and Figure 4). During the last decade  
1109 (2012-2021), the growth rate in atmospheric CO<sub>2</sub> concentration continued to increase, albeit with large  
1110 interannual variability (Figure 4).

1121 The airborne fraction (AF), defined as the ratio of atmospheric CO<sub>2</sub> growth rate to total anthropogenic  
1122 emissions:

$$1123 \quad AF = G_{ATM} / (E_{FOS} + E_{LUC}) \quad (2)$$

1124 provides a diagnostic of the relative strength of the land and ocean carbon sinks in removing part of the  
1125 anthropogenic CO<sub>2</sub> perturbation. The evolution of AF over the last 60 years shows no significant trend,  
1126 remaining at around 44%, albeit showing a large interannual and decadal variability driven by the year-to-year  
1127 variability in G<sub>ATM</sub> (Figure 9). The observed stability of the airborne fraction over the 1960-2020 period  
1128 indicates that the ocean and land CO<sub>2</sub> sinks have been removing on average about 55% of the anthropogenic  
1129 emissions (see sections 3.5 and 3.6).

### 1130 3.4.3 Final year 2021

1131 The growth rate in atmospheric CO<sub>2</sub> concentration was 5.2 ± 0.2 GtC (2.46 ± 0.08 ppm) in 2021 (Figure 4;  
1132 Dlugokencky and Tans, 2022), slightly above the 2020 growth rate (5.0 GtC) but similar to the 2011-2020  
1133 average (5.2 GtC).

### 1134 3.4.4 Year 2022 Projection

1135 The 2022 growth in atmospheric CO<sub>2</sub> concentration (G<sub>ATM</sub>) is projected to be about 5.5 GtC (2.58 ppm) based  
1136 on GLO observations until August 2022, bringing the atmospheric CO<sub>2</sub> concentration to an expected level of  
1137 417.3 ppm averaged over the year, 51% over the pre-industrial level.

## 1138 3.5 Ocean Sink

### 1139 3.5.1 Historical period 1850-2021

1140 Cumulated since 1850, the ocean sink adds up to 175 ± 35 GtC, with more than two thirds of this amount (120  
1141 GtC) being taken up by the global ocean since 1960. Over the historical period, the ocean sink increased in pace  
1142 with the anthropogenic emissions exponential increase (Figure 3b). Since 1850, the ocean has removed 26% of  
1143 total anthropogenic emissions.

### 1144 3.5.2 Recent period 1960-2021

1145 The ocean CO<sub>2</sub> sink increased from 1.1 ± 0.4 GtC yr<sup>-1</sup> in the 1960s to 2.9 ± 0.4 GtC yr<sup>-1</sup> during 2012-2021  
1146 (Table 6), with interannual variations of the order of a few tenths of GtC yr<sup>-1</sup> (Figure 10). The ocean-borne  
1147 fraction (S<sub>OCEAN</sub>/(E<sub>FOS</sub>+E<sub>LUC</sub>)) has been remarkably constant around 25% on average (Figure 9). Variations  
1148 around this mean illustrate decadal variability of the ocean carbon sink. So far, there is no indication of a  
1149 decrease in the ocean-borne fraction from 1960 to 2021. The increase of the ocean sink is primarily driven by  
1150 the increased atmospheric CO<sub>2</sub> concentration, with the strongest CO<sub>2</sub> induced signal in the North Atlantic and  
1151 the Southern Ocean (Figure 11a). The effect of climate change is much weaker, reducing the ocean sink globally  
1152 by 0.11 ± 0.09 GtC yr<sup>-1</sup> (4.2% during 2012-2021 (nine models simulate a weakening of the ocean sink by  
1153 climate change, range -3.2 to -8.9%, and only one model simulates a strengthening by 4.8%), and does not show  
1154 clear spatial patterns across the GOBMs ensemble (Figure 11b). This is the combined effect of change and

Formatted: Outline numbered + Level: 3 + Numbering  
Style: 1, 2, 3, ... + Start at: 1 + Alignment: Left + Aligned at:  
0 cm + Indent at: 1.27 cm

Formatted: Outline numbered + Level: 3 + Numbering  
Style: 1, 2, 3, ... + Start at: 1 + Alignment: Left + Aligned at:  
0 cm + Indent at: 1.27 cm

Formatted: Indent: Left: 0 cm, First line: 0 cm, Outline  
numbered + Level: 2 + Numbering Style: 1, 2, 3, ... + Start  
at: 1 + Alignment: Left + Aligned at: 0 cm + Indent at: 1.02  
cm

Formatted: Outline numbered + Level: 3 + Numbering  
Style: 1, 2, 3, ... + Start at: 1 + Alignment: Left + Aligned at:  
0 cm + Indent at: 1.27 cm

Formatted: Outline numbered + Level: 3 + Numbering  
Style: 1, 2, 3, ... + Start at: 1 + Alignment: Left + Aligned at:  
0 cm + Indent at: 1.27 cm

Deleted: or

Deleted: % (

Deleted: ,

Deleted: %

1159 variability in all atmospheric forcing fields, previously attributed to wind and temperature changes in one model  
1160 (LeQuéré et al., 2010).

1161 The global net air-sea CO<sub>2</sub> flux is a residual of large natural and anthropogenic CO<sub>2</sub> fluxes into and out of the  
1162 ocean with distinct regional and seasonal variations (Figure 6 and B1). Natural fluxes dominate on regional  
1163 scales, but largely cancel out when integrated globally (Gruber et al., 2009). Mid-latitudes in all basins and the  
1164 high-latitude North Atlantic dominate the ocean CO<sub>2</sub> uptake where low temperatures and high wind speeds  
1165 facilitate CO<sub>2</sub> uptake at the surface (Takahashi et al., 2009). In these regions, formation of mode, intermediate  
1166 and deep-water masses transport anthropogenic carbon into the ocean interior, thus allowing for continued CO<sub>2</sub>  
1167 uptake at the surface. Outgassing of natural CO<sub>2</sub> occurs mostly in the tropics, especially in the equatorial  
1168 upwelling region, and to a lesser extent in the North Pacific and polar Southern Ocean, mirroring a well-  
1169 established understanding of regional patterns of air-sea CO<sub>2</sub> exchange (e.g., Takahashi et al., 2009, Gruber et  
1170 al., 2009). These patterns are also noticeable in the Surface Ocean CO<sub>2</sub> Atlas (SOCAT) dataset, where an ocean  
1171 fCO<sub>2</sub> value above the atmospheric level indicates outgassing (Figure B1). This map further illustrates the data-  
1172 sparsity in the Indian Ocean and the southern hemisphere in general.

1173 Interannual variability of the ocean carbon sink is driven by climate variability with a first-order effect from a  
1174 stronger ocean sink during large El Niño events (e.g., 1997-1998) (Figure 10; Rödenbeck et al., 2014, Hauck et  
1175 al., 2020). The GOBMs show the same patterns of decadal variability as the mean of the fCO<sub>2</sub>-based data  
1176 products, with a stagnation of the ocean sink in the 1990s and a strengthening since the early 2000s (Figure 10,  
1177 Le Quéré et al., 2007; Landschützer et al., 2015, 2016; DeVries et al., 2017; Hauck et al., 2020; McKinley et al.,  
1178 2020). Different explanations have been proposed for this decadal variability, ranging from the ocean's response  
1179 to changes in atmospheric wind and pressure systems (e.g., Le Quéré et al., 2007, Keppler and Landschützer,  
1180 2019), including variations in upper ocean overturning circulation (DeVries et al., 2017) to the eruption of  
1181 Mount Pinatubo and its effects on sea surface temperature and slowed atmospheric CO<sub>2</sub> growth rate in the 1990s  
1182 (McKinley et al., 2020). The main origin of the decadal variability is a matter of debate with a number of studies  
1183 initially pointing to the Southern Ocean (see review in Canadell et al., 2021), but also contributions from the  
1184 North Atlantic and North Pacific (Landschützer et al., 2016, DeVries et al., 2019), or a global signal (McKinley  
1185 et al., 2020) were proposed.

1186 Although all individual GOBMs and data-products fall within the observational constraint, the ensemble means  
1187 of GOBMs, and data-products adjusted for the riverine flux diverge over time with a mean offset increasing  
1188 from 0.28 GtC yr<sup>-1</sup> in the 1990s to 0.61 GtC yr<sup>-1</sup> in the decade 2012-2021 and reaching 0.79 GtC yr<sup>-1</sup> in 2021.  
1189 The SOCEAN positive trend over time diverges by a factor two since 2002 (GOBMs: 0.28 ± 0.07 GtC yr<sup>-1</sup> per  
1190 decade, data-products: 0.61 ± 0.17 GtC yr<sup>-1</sup> per decade, SOCEAN: 0.45 GtC yr<sup>-1</sup> per decade) and by a factor of  
1191 three since 2010 (GOBMs: 0.21 ± 0.14 GtC yr<sup>-1</sup> per decade, data-products: 0.66 ± 0.38 GtC yr<sup>-1</sup> per decade  
1192 SOCEAN: 0.44 GtC yr<sup>-1</sup> per decade). The GOBMs estimate is slightly higher (<0.1 GtC yr<sup>-1</sup>) than in the previous  
1193 global carbon budget (Friedlingstein et al., 2022), because ~~two new models are~~ included (CESM2, MRI) and  
1194 four models revised their ~~estimates~~ upwards (CESM-ETHZ, CNRM, FESOM2-REcoM, PlankTOM). The data-  
1195 product estimate is higher by about 0.1 GtC yr<sup>-1</sup> compared to Friedlingstein et al. (2022) as a result of an upward  
1196 correction in three products (Jena-MLS, MPI-SOMFFN, OS-ETHZ-Gracer), the submission of LDEO-HPD

Deleted: one

Deleted: model is

Deleted: estimate

1200 which is above average, the non-availability of the CSIR product, and the small upward correction of the river  
1201 flux adjustment.

1202 The discrepancy between the two types of estimates stems mostly from a larger Southern Ocean sink in the data-  
1203 products prior to 2001, and from a larger *SOCEAN* trend in the northern and southern extra-tropics since then  
1204 (Figure 13). Note that the location of the mean offset (but not its trend) depends strongly on the choice of  
1205 regional river flux adjustment and would occur in the tropics rather than in the Southern Ocean when using the  
1206 dataset of Lacroix et al. (2020) instead of Aumont et al. (2001). Other possible explanations for the discrepancy  
1207 in the Southern Ocean could be missing winter observations and data sparsity in general (Bushinsky et al., 2019,  
1208 Gloege et al., 2021), or model biases (as indicated by the large model spread in the South, Figure 13, and the  
1209 larger model-data mismatch, Figure B2).

1210 In GCB releases until 2021, the ocean sink 1959-1989 was only estimated by GOBMs due to the absence of  
1211  $f\text{CO}_2$  observations. Now, the first data-based estimates extending back to 1957/58 are becoming available (Jena-  
1212 MLS, Rödenbeck et al., 2022, LDEO-HPD, Bennington et al., 2022; Gloege et al. 2022). These are based on a  
1213 multi-linear regression of  $p\text{CO}_2$  with environmental predictors (Rödenbeck et al., 2022, included here) or on  
1214 model-data  $p\text{CO}_2$  misfits and their relation to environmental predictors (Bennington et al., 2022). The Jena-MLS  
1215 estimate falls well within the range of GOBM estimates and has a correlation of 0.98 with *SOCEAN* (1959-2021 as  
1216 well as 1959-1989). It agrees well on the mean *SOCEAN* estimate since 1977 with a slightly higher amplitude of  
1217 variability (Figure 10). Until 1976, Jena-MLS is  $0.2\text{-}0.3 \text{ GtCyr}^{-1}$  below the central *SOCEAN* estimate. The  
1218 agreement especially on phasing of variability is impressive, and the discrepancies in the mean flux 1959-1976  
1219 could be explained by an overestimated trend of Jena-MLS (Rödenbeck et al., 2022). Bennington et al. (2022)  
1220 report a larger flux into the pre-1990 ocean than in Jena-MLS.

1221 The reported *SOCEAN* estimate from GOBMs and data-products is  $2.1 \pm 0.4 \text{ GtC yr}^{-1}$  over the period 1994 to  
1222 2007, which is in agreement with the ocean interior estimate of  $2.2 \pm 0.4 \text{ GtC yr}^{-1}$  which accounts for the  
1223 climate effect on the natural  $\text{CO}_2$  flux of  $-0.4 \pm 0.24 \text{ GtC yr}^{-1}$  (Gruber et al., 2019) to match the  
1224 definition of *SOCEAN* used here (Hauck et al., 2020). This comparison depends critically on the estimate of the  
1225 climate effect on the natural  $\text{CO}_2$  flux, which is smaller from the GOBMs ( $-0.1 \text{ GtC yr}^{-1}$ ) than in Gruber et al.  
1226 (2019). Uncertainties of these two estimates would also overlap when using the GOBM estimate of the climate  
1227 effect on the natural  $\text{CO}_2$  flux.

1228 During 2010-2016, the ocean  $\text{CO}_2$  sink appears to have intensified in line with the expected increase from  
1229 atmospheric  $\text{CO}_2$  (McKinley et al., 2020). This effect is stronger in the  $f\text{CO}_2$ -based data products (Figure 10,  
1230 ocean sink 2016 minus 2010, GOBMs:  $+0.42 \pm 0.09 \text{ GtC yr}^{-1}$ , data-products:  $+0.52 \pm 0.22 \text{ GtC yr}^{-1}$ ). The  
1231 reduction of  $-0.09 \text{ GtC yr}^{-1}$  (range:  $-0.39$  to  $+0.01 \text{ GtC yr}^{-1}$ ) in the ocean  $\text{CO}_2$  sink in 2017 is consistent with the  
1232 return to normal conditions after the El Niño in 2015/16, which caused an enhanced sink in previous years.  
1233 After 2017, the GOBMs ensemble mean suggests the ocean sink levelling off at about  $2.6 \text{ GtC yr}^{-1}$ , whereas the  
1234 data-products' estimate increases by  $0.24 \pm 0.17 \text{ GtC yr}^{-1}$  over the same period.

### 1235 3.5.3 Final year 2021

1236 The estimated ocean  $\text{CO}_2$  sink was  $2.9 \pm 0.4 \text{ GtC}$  in 2021. This is a decrease of  $0.12 \text{ GtC}$  compared to 2020, in  
1237 line with the expected sink weakening from persistent La Niña conditions. GOBM and data-product estimates

Formatted: Font: (Default) Gungsuh

Formatted: Font: (Default) Gungsuh

Formatted: Font: (Default) Gungsuh

Formatted: Font: (Default) Gungsuh

Formatted: Outline numbered + Level: 3 + Numbering  
Style: 1, 2, 3, ... + Start at: 1 + Alignment: Left + Aligned at:  
0 cm + Indent at: 1.27 cm

1238 consistently result in a stagnation of  $S_{OCEAN}$  (GOBMs:  $-0.09 \pm 0.15$  GtC, data-products:  $-0.15 \pm 0.24$  GtC). Seven  
1239 models and six data products show a decrease in  $S_{OCEAN}$  (GOBMs down to  $-0.31$  GtC, data-products down to  $-$   
1240  $0.58$  GtC), while three models and two data products show an increase in  $S_{OCEAN}$  (GOBMs up to  $0.15$  GtC, data-  
1241 products up to  $0.12$  GtC; Figure 10). The data-products have a larger uncertainty at the tails of the reconstructed  
1242 time series (e.g., Watson et al., 2020). Specifically, the data-products' estimate of the last year is regularly  
1243 adjusted in the following release owing to the tail effect and an incrementally increasing data availability with 1-  
1244 5 years lag (Figure 10 inset).

#### 1245 3.5.4 Year 2022 Projection

1246 Using a feed-forward neural network method (see section 2.4) we project an ocean sink of 2.9 GtC for 2022.  
1247 This is similar to the year 2021 as the La Niña conditions persist in 2022.

#### 1248 3.5.5 Model Evaluation

1249 The additional simulation D allows to separate the anthropogenic carbon component (steady state and non-  
1250 steady state, sim D - sim A) and to compare the model flux and DIC inventory change directly to the interior  
1251 ocean estimate of Gruber et al. (2019) without further assumptions. The GOBMs ensemble average of  
1252 anthropogenic carbon inventory changes 1994-2007 amounts to  $2.2$  GtC yr<sup>-1</sup> and is thus lower than the  $2.6 \pm 0.3$   
1253 GtC yr<sup>-1</sup> estimated by Gruber et al (2019). Only four models with the highest sink estimate fall within the range  
1254 reported by Gruber et al. (2019). This suggests that the majority of the GOBMs underestimate anthropogenic  
1255 carbon uptake by 10-20%. Analysis of Earth System Models indicate that an underestimation by about 10% may  
1256 be due to biases in ocean carbon transport and mixing from the surface mixed layer to the ocean interior (Goris  
1257 et al., 2018, Terhaar et al., 2021, Bourgeois et al., 2022, Terhaar et al., 2022.), biases in the chemical buffer  
1258 capacity (Revelle factor) of the ocean (Vaittinada Ayar et al., 2022; Terhaar et al., 2022) and partly due to a late  
1259 starting date of the simulations (mirrored in atmospheric CO<sub>2</sub> chosen for the preindustrial control simulation,  
1260 Table A2, Bronselaer et al., 2017, Terhaar et al., 2022). Interestingly, and in contrast to the uncertainties in the  
1261 surface CO<sub>2</sub> flux, we find the largest mismatch in interior ocean carbon accumulation in the tropics (93% of the  
1262 mismatch), with minor contribution from the north (1%) and the south (6%). This highlights the role of interior  
1263 ocean carbon redistribution for those inventories (Khatiwala et al., 2009).

1264 The evaluation of the ocean estimates (Figure B2) shows an RMSE from annually detrended data of 0.4 to 2.6  
1265  $\mu\text{atm}$  for the seven fCO<sub>2</sub>-based data products over the globe, relative to the fCO<sub>2</sub> observations from the SOCAT  
1266 v2022 dataset for the period 1990-2021. The GOBMs RMSEs are larger and range from 3.0 to 4.8  $\mu\text{atm}$ . The  
1267 RMSEs are generally larger at high latitudes compared to the tropics, for both the data products and the  
1268 GOBMs. The data products have RMSEs of 0.4 to 3.2  $\mu\text{atm}$  in the tropics, 0.8 to 2.8  $\mu\text{atm}$  in the north, and 0.8  
1269 to 3.6  $\mu\text{atm}$  in the south. Note that the data products are based on the SOCAT v2022 database, hence the  
1270 SOCAT is not an independent dataset for the evaluation of the data products. The GOBMs RMSEs are more  
1271 spread across regions, ranging from 2.5 to 3.9  $\mu\text{atm}$  in the tropics, 3.1 to 6.5  $\mu\text{atm}$  in the North, and 5.4 to 7.9  
1272  $\mu\text{atm}$  in the South. The higher RMSEs occur in regions with stronger climate variability, such as the northern  
1273 and southern high latitudes (poleward of the subtropical gyres). The upper range of the model RMSEs have  
1274 decreased somewhat relative to Friedlingstein et al. (2022).

Formatted: Outline numbered + Level: 3 + Numbering  
Style: 1, 2, 3, ... + Start at: 1 + Alignment: Left + Aligned at:  
0 cm + Indent at: 1.27 cm

Formatted: Outline numbered + Level: 3 + Numbering  
Style: 1, 2, 3, ... + Start at: 1 + Alignment: Left + Aligned at:  
0 cm + Indent at: 1.27 cm

Deleted: most

Deleted: the ocean.

Deleted: this

Deleted:

Deleted:

Deleted:

1281 **3.6 Land Sink**

1282 **3.6.1 Historical period 1850-2021**

1283 Cumulated since 1850, the terrestrial CO<sub>2</sub> sink amounts to 210 ± 45 GtC, 31% of total anthropogenic emissions.  
1284 Over the historical period, the sink increased in pace with the anthropogenic emissions exponential increase  
1285 (Figure 3b).

1286 **3.6.2 Recent period 1960-2021**

1287 The terrestrial CO<sub>2</sub> sink increased from 1.2 ± 0.4 GtC yr<sup>-1</sup> in the 1960s to 3.1 ± 0.6 GtC yr<sup>-1</sup> during 2012-2021,  
1288 with important interannual variations of up to 2 GtC yr<sup>-1</sup> generally showing a decreased land sink during El  
1289 Niño events (Figure 8), responsible for the corresponding enhanced growth rate in atmospheric CO<sub>2</sub>  
1290 concentration. The larger land CO<sub>2</sub> sink during 2012-2021 compared to the 1960s is reproduced by all the  
1291 DGVMs in response to the increase in both atmospheric CO<sub>2</sub> and nitrogen deposition, and the changes in  
1292 climate, and is consistent with constraints from the other budget terms (Table 5).

1293 Over the period 1960 to present the increase in the global terrestrial CO<sub>2</sub> sink is largely attributed to the CO<sub>2</sub>  
1294 fertilisation effect (Prentice et al., 2001, Piao et al., 2009), directly stimulating plant photosynthesis and  
1295 increased plant water use in water limited systems, with a small negative contribution of climate change (Figure  
1296 11). There is a range of evidence to support a positive terrestrial carbon sink in response to increasing  
1297 atmospheric CO<sub>2</sub>, albeit with uncertain magnitude (Walker et al., 2021). As expected from theory, the greatest  
1298 CO<sub>2</sub> effect is simulated in the tropical forest regions, associated with warm temperatures and long growing  
1299 seasons (Hickler et al., 2008) (Figure 11a). However, evidence from tropical intact forest plots indicate an  
1300 overall decline in the land sink across Amazonia (1985-2011), attributed to enhanced mortality offsetting  
1301 productivity gains (Brienen et al., 2005, Hubau et al., 2020). During 2012-2021 the land sink is positive in all  
1302 regions (Figure 6) with the exception of eastern Brazil, Southwest USA, Southeast Europe and Central Asia,  
1303 North and South Africa, and eastern Australia, where the negative effects of climate variability and change (i.e.  
1304 reduced rainfall) counterbalance CO<sub>2</sub> effects. This is clearly visible on Figure 11 where the effects of CO<sub>2</sub>  
1305 (Figure 11a) and climate (Figure 11b) as simulated by the DGVMs are isolated. The negative effect of climate is  
1306 the strongest in most of South America, Central America, Southwest US, Central Europe, western Sahel,  
1307 southern Africa, Southeast Asia and southern China, and eastern Australia (Figure 11b). Globally, climate  
1308 change reduces the land sink by 0.63 ± 0.52 GtC yr<sup>-1</sup> or 17% (2012-2021).

1309 Since 2020 the globe has experienced La Niña conditions which would be expected to lead to an increased land  
1310 carbon sink. A clear peak in the global land sink is not evident in S<sub>LAND</sub>, and we find that a La Niña- driven  
1311 increase in tropical land sink is offset by a reduced high latitude extra-tropical land sink, which may be linked to  
1312 the land response to recent climate extremes. In the past years several regions experienced record-setting fire  
1313 events. While global burned area has declined over the past decades mostly due to declining fire activity in  
1314 savannas (Andela et al., 2017), forest fire emissions are rising and have the potential to counter the negative fire  
1315 trend in savannas (Zheng et al., 2021). Noteworthy events include the 2019-2020 Black Summer event in  
1316 Australia (emissions of roughly 0.2 GtC; van der Velde et al., 2021) and Siberia in 2021 where emissions  
1317 approached 0.4 GtC or three times the 1997-2020 average according to GFED4s. While other regions, including

Formatted: Outline numbered + Level: 2 + Numbering  
Style: 1, 2, 3, ... + Start at: 1 + Alignment: Left + Aligned at:  
0 cm + Indent at: 1.02 cm

Formatted: Outline numbered + Level: 3 + Numbering  
Style: 1, 2, 3, ... + Start at: 1 + Alignment: Left + Aligned at:  
0 cm + Indent at: 1.27 cm

Formatted: Outline numbered + Level: 3 + Numbering  
Style: 1, 2, 3, ... + Start at: 1 + Alignment: Left + Aligned at:  
0 cm + Indent at: 1.27 cm

1318 Western US and Mediterranean Europe, also experienced intense fire seasons in 2021 their emissions are  
1319 substantially lower.

1320 Despite these regional negative effects of climate change on  $S_{LAND}$ , the efficiency of land to remove  
1321 anthropogenic  $CO_2$  emissions has remained broadly constant over the last six decades, with a land-borne  
1322 fraction ( $S_{LAND}/(E_{FOS}+E_{LUC})$ ) of ~30% (Figure 9).

### 1323 3.6.3 Final year 2021

1324 The terrestrial  $CO_2$  sink from the DGVMs ensemble was  $3.5 \pm 0.9$  GtC in 2021, slightly above the decadal  
1325 average of  $3.1 \pm 0.6$  GtC  $yr^{-1}$  (Figure 4, Table 6). We note that the DGVMs estimate for 2021 is larger, but  
1326 within the uncertainty, than the  $2.8 \pm 0.9$  GtC  $yr^{-1}$  estimate from the residual sink from the global budget  
1327 ( $E_{FOS}+E_{LUC}-G_{ATM}-S_{OCEAN}$ ) (Table 5).

### 1328 3.6.4 Year 2022 Projection

1329 Using a feed-forward neural network method we project a land sink of 3.4 GtC for 2022, very similar to the  
1330 2021 estimate. As for the ocean sink, we attribute this to the persistence of La Niña conditions in 2022.

### 1331 3.6.5 Model Evaluation

1332 The evaluation of the DGVMs (Figure B3) shows generally high skill scores across models for runoff, and to a  
1333 lesser extent for vegetation biomass, GPP, and ecosystem respiration (Figure B3, left panel). Skill score was  
1334 lowest for leaf area index and net ecosystem exchange, with a widest disparity among models for soil carbon.  
1335 These conclusions are supported by a more comprehensive analysis of DGVM performance in comparison with  
1336 benchmark data (Seiler et al., 2022). Furthermore, results show how DGVM differences are often of similar  
1337 magnitude compared with the range across observational datasets.

## 1338 3.7 Partitioning the carbon sinks

### 1339 3.7.1 Global sinks and spread of estimates

1340 In the period 2012-2021, the bottom-up view of total global carbon sinks provided by the GCB,  $S_{OCEAN}$  for the  
1341 ocean and  $S_{LAND}-E_{LUC}$  for the land (to be comparable to inversions), agrees closely with the top-down global  
1342 carbon sinks delivered by the atmospheric inversions. Figure 12 shows both total sink estimates of the last  
1343 decade split by ocean and land (including  $E_{LUC}$ ), which match the difference between  $G_{ATM}$  and  $E_{FOS}$  to within  
1344 0.01-0.12 GtC  $yr^{-1}$  for inverse systems, and to 0.34 GtC  $yr^{-1}$  for the GCB mean. The latter represents the BIM  
1345 discussed in Section 3.8, which by design is minimal for the inverse systems.

1346 The distributions based on the individual models and data products reveal substantial spread but converge near  
1347 the decadal means quoted in Tables 5 and 6. Sink estimates for  $S_{OCEAN}$  and from inverse systems are mostly  
1348 non-Gaussian, while the ensemble of DGVMs appears more normally distributed justifying the use of a multi-  
1349 model mean and standard deviation for their errors in the budget. Noteworthy is that the tails of the distributions  
1350 provided by the land and ocean bottom-up estimates would not agree with the global constraint provided by the  
1351 fossil fuel emissions and the observed atmospheric  $CO_2$  growth rate ( $E_{FOS}-G_{ATM}$ ). This illustrates the power of  
1352 the atmospheric joint constraint from  $G_{ATM}$  and the global  $CO_2$  observation network it derives from.

Formatted: Outline numbered + Level: 3 + Numbering  
Style: 1, 2, 3, ... + Start at: 1 + Alignment: Left + Aligned at:  
0 cm + Indent at: 1.27 cm

Formatted: Outline numbered + Level: 3 + Numbering  
Style: 1, 2, 3, ... + Start at: 1 + Alignment: Left + Aligned at:  
0 cm + Indent at: 1.27 cm

Formatted: Outline numbered + Level: 3 + Numbering  
Style: 1, 2, 3, ... + Start at: 1 + Alignment: Left + Aligned at:  
0 cm + Indent at: 1.27 cm

Deleted:

Deleted: ¶

Formatted: Outline numbered + Level: 2 + Numbering  
Style: 1, 2, 3, ... + Start at: 1 + Alignment: Left + Aligned at:  
0 cm + Indent at: 1.02 cm

Formatted: Indent: Left: 0 cm, First line: 0 cm, Outline  
numbered + Level: 3 + Numbering Style: 1, 2, 3, ... + Start  
at: 1 + Alignment: Left + Aligned at: 0 cm + Indent at: 1.27  
cm

1355 **3.7.2 Total atmosphere-to-land fluxes**

1356 The total atmosphere-to-land fluxes ( $S_{LAND} - E_{LUC}$ ), calculated here as the difference between  $S_{LAND}$  from the  
1357 DGVMs and  $E_{LUC}$  from the bookkeeping models, amounts to a  $1.9 \pm 0.9$  GtC yr<sup>-1</sup> sink during 2012-2021 (Table  
1358 5). Estimates of total atmosphere-to-land fluxes ( $S_{LAND} - E_{LUC}$ ) from the DGVMs alone ( $1.5 \pm 0.5$  GtC yr<sup>-1</sup>) are  
1359 consistent with this estimate and also with the global carbon budget constraint ( $E_{FOS} - G_{ATM} - S_{OCEAN}$ ,  $1.5 \pm 0.6$   
1360 GtC yr<sup>-1</sup> Table 5). For the last decade (2012-2021), the inversions estimate the net atmosphere-to-land uptake to  
1361 lie within a range of 1.1 to 1.7 GtC yr<sup>-1</sup>, consistent with the GCB and DGVMs estimates of  $S_{LAND} - E_{LUC}$  (Figure  
1362 13 top row).

1363 **3.7.3 Total atmosphere-to-ocean fluxes**

1364 For the 2012-2021 period, the GOBMs ( $2.6 \pm 0.5$  GtC yr<sup>-1</sup>) produce a lower estimate for the ocean sink than the  
1365 fCO<sub>2</sub>-based data products ( $3.2 \pm 0.6$  GtC yr<sup>-1</sup>), which shows up in Figure 12 as a separate peak in the  
1366 distribution from the GOBMs (triangle symbols pointing right) and from the fCO<sub>2</sub>-based products (triangle  
1367 symbols pointing left). Atmospheric inversions ( $2.7$  to  $3.3$  GtC yr<sup>-1</sup>) also suggest higher ocean uptake in the  
1368 recent decade (Figure 13 top row). In interpreting these differences, we caution that the riverine transport of  
1369 carbon taken up on land and outgassing from the ocean is a substantial ( $0.65$  GtC yr<sup>-1</sup>) and uncertain term that  
1370 separates the various methods. A recent estimate of decadal ocean uptake from observed O<sub>2</sub>/N<sub>2</sub> ratios (Tohjima  
1371 et al., 2019) also points towards a larger ocean sink, albeit with large uncertainty (2012-2016:  $3.1 \pm 1.5$  GtC yr  
1372 <sup>-1</sup>).

1373 **3.7.4 Regional breakdown and interannual variability**

1374 Figure 13 also shows the latitudinal partitioning of the total atmosphere-to-surface fluxes excluding fossil CO<sub>2</sub>  
1375 emissions ( $S_{OCEAN} + S_{LAND} - E_{LUC}$ ) according to the multi-model average estimates from GOBMs and ocean  
1376 fCO<sub>2</sub>-based products ( $S_{OCEAN}$ ) and DGVMs ( $S_{LAND} - E_{LUC}$ ), and from atmospheric inversions ( $S_{OCEAN}$  and  $S_{LAND}$   
1377  $- E_{LUC}$ ).

1378 **3.7.4.1 North**

1379 Despite being one of the most densely observed and studied regions of our globe, annual mean carbon sink  
1380 estimates in the northern extra-tropics (north of 30°N) continue to differ. The atmospheric inversions suggest an  
1381 atmosphere-to-surface sink ( $S_{OCEAN} + S_{LAND} - E_{LUC}$ ) for 2012-2021 of 2.0 to 3.2 GtC yr<sup>-1</sup>, which is higher than  
1382 the process models' estimate of  $2.2 \pm 0.4$  GtC yr<sup>-1</sup> (Figure 13). The GOBMs ( $1.2 \pm 0.2$  GtC yr<sup>-1</sup>), fCO<sub>2</sub>-based  
1383 data products ( $1.4 \pm 0.1$  GtC yr<sup>-1</sup>), and inversion systems ( $0.9$  to  $1.4$  GtC yr<sup>-1</sup>) produce consistent estimates of  
1384 the ocean sink. Thus, the difference mainly arises from the total land flux ( $S_{LAND} - E_{LUC}$ ) estimate, which is  $1.0$   
1385  $\pm 0.4$  GtC yr<sup>-1</sup> in the DGVMs compared to  $0.6$  to  $2.0$  GtC yr<sup>-1</sup> in the atmospheric inversions (Figure 13, second  
1386 row).

1387 Discrepancies in the northern land fluxes conforms with persistent issues surrounding the quantification of the  
1388 drivers of the global net land CO<sub>2</sub> flux (Arneth et al., 2017; Huntzinger et al., 2017; O'Sullivan et al., 2022) and  
1389 the distribution of atmosphere-to-land fluxes between the tropics and high northern latitudes (Baccini et al.,  
1390 2017; Schimel et al., 2015; Stephens et al., 2007; Ciais et al. 2019; Gaubert et al., 2019).

Formatted: Outline numbered + Level: 3 + Numbering  
Style: 1, 2, 3, ... + Start at: 1 + Alignment: Left + Aligned at:  
0 cm + Indent at: 1.27 cm

Formatted: Outline numbered + Level: 3 + Numbering  
Style: 1, 2, 3, ... + Start at: 1 + Alignment: Left + Aligned at:  
0 cm + Indent at: 1.27 cm

Formatted: Outline numbered + Level: 3 + Numbering  
Style: 1, 2, 3, ... + Start at: 1 + Alignment: Left + Aligned at:  
0 cm + Indent at: 1.27 cm

Formatted: Outline numbered + Level: 4 + Numbering  
Style: 1, 2, 3, ... + Start at: 1 + Alignment: Left + Aligned at:  
0 cm + Indent at: 1.52 cm

1391 In the northern extratropics, the process models, inversions, and fCO<sub>2</sub>-based data products consistently suggest  
1392 that most of the variability stems from the land (Figure 13). Inversions generally estimate similar interannual  
1393 variations (IAV) over land to DGVMs (0.30 – 0.37 vs 0.17 – 0.69 GtC yr<sup>-1</sup>, averaged over 1990-2021), and  
1394 they have higher IAV in ocean fluxes (0.05 – 0.09 GtC yr<sup>-1</sup>) relative to GOBMs (0.02 – 0.06 GtC yr<sup>-1</sup>, Figure  
1395 B2), and fCO<sub>2</sub>-based data products (0.03 – 0.09 GtC yr<sup>-1</sup>).

Formatted: Font: (Default) Gungsuh

Formatted: Font: (Default) Gungsuh

Formatted: Font: (Default) Gungsuh

Formatted: Font: (Default) Gungsuh

#### 1396 3.7.4.2 Tropics

1397 In the tropics (30°S-30°N), both the atmospheric inversions and process models estimate a total carbon balance  
1398 (SO<sub>CEAN</sub>+SL<sub>AND</sub>-EL<sub>UC</sub>) that is close to neutral over the past decade. The GOBMs (0.06 ± 0.34 GtC yr<sup>-1</sup>), fCO<sub>2</sub>-  
1399 based data products (0.00 ± 0.06 GtC yr<sup>-1</sup>), and inversion systems (-0.2 to 0.5 GtC yr<sup>-1</sup>) all indicate an  
1400 approximately neutral tropical ocean flux (see Figure B1 for spatial patterns). DGVMs indicate a net land sink  
1401 (SL<sub>AND</sub>-EL<sub>UC</sub>) of 0.5 ± 0.3 GtC yr<sup>-1</sup>, whereas the inversion systems indicate a net land flux between -0.9 and 0.7  
1402 GtC yr<sup>-1</sup>, though with high uncertainty (Figure 13, third row).

Formatted: Outline numbered + Level: 4 + Numbering  
Style: 1, 2, 3, ... + Start at: 1 + Alignment: Left + Aligned at:  
0 cm + Indent at: 1.52 cm

1403 The tropical lands are the origin of most of the atmospheric CO<sub>2</sub> interannual variability (Ahlström  
1404 et al., 2015), consistently among the process models and inversions (Figure 13).  
1405 The interannual variability in the tropics is similar among the ocean data  
1406 products (0.07 – 0.16 GtC yr<sup>-1</sup>) and the GOBMs (0.07 – 0.16 GtC yr<sup>-1</sup>, Figure B2), which is  
1407 the highest ocean sink variability of all regions. The DGVMs and inversions indicate that atmosphere-to-land  
1408 CO<sub>2</sub> fluxes are more variable than atmosphere-to-ocean CO<sub>2</sub> fluxes in the tropics, with interannual variability of  
1409 0.5 to 1.1 and 0.8 to 1.0 GtC yr<sup>-1</sup> for DGVMs and inversions, respectively.

Formatted: Font: (Default) Gungsuh

Formatted: Font: (Default) Gungsuh

Formatted: Font: (Default) Gungsuh

#### 1410 3.7.4.3 South

1411 In the southern extra-tropics (south of 30°S), the atmospheric inversions suggest a total atmosphere-to-surface  
1412 sink (SO<sub>CEAN</sub>+SL<sub>AND</sub>-EL<sub>UC</sub>) for 2012-2021 of 1.6 to 1.9 GtC yr<sup>-1</sup>, slightly higher than the process models'  
1413 estimate of 1.4 ± 0.3 GtC yr<sup>-1</sup> (Figure 13). An approximately neutral total land flux (SL<sub>AND</sub>-EL<sub>UC</sub>) for the  
1414 southern extra-tropics is estimated by both the DGVMs (0.02 ± 0.06 GtC yr<sup>-1</sup>) and the inversion systems (sink of  
1415 -0.2 to 0.2 GtC yr<sup>-1</sup>). This means nearly all carbon uptake is due to oceanic sinks south of 30°S. The Southern  
1416 Ocean flux in the fCO<sub>2</sub>-based data products (1.8 ± 0.1 GtC yr<sup>-1</sup>) and inversion estimates (1.6 to 1.9 GtCyr-1) is  
1417 higher than in the GOBMs (1.4 ± 0.3 GtC yr<sup>-1</sup>) (Figure 13, bottom row). This discrepancy in the mean flux is  
1418 likely explained by the uncertainty in the regional distribution of the river flux adjustment (Aumont et al., 2001,  
1419 Lacroix et al., 2020) applied to fCO<sub>2</sub>-based data products and inverse systems to isolate the anthropogenic  
1420 SO<sub>CEAN</sub> flux. Other possibly contributing factors are that the data-products potentially underestimate the winter  
1421 CO<sub>2</sub> outgassing south of the Polar Front (Bushinsky et al., 2019) and [potential](#) model biases. CO<sub>2</sub> fluxes from  
1422 this region are more sparsely sampled by all methods, especially in wintertime (Figure B1). [Dominant biases in](#)  
1423 [Earth System Models are related to mode water formation, stratification, and the chemical buffer capacity](#)  
1424 [\(Terhaar et al., 2021, Bourgeois et al., 2022, Terhaar et al., 2022\).](#)

Formatted: Outline numbered + Level: 4 + Numbering  
Style: 1, 2, 3, ... + Start at: 1 + Alignment: Left + Aligned at:  
0 cm + Indent at: 1.52 cm

1425 The interannual variability in the southern extra-tropics is low because of the dominance of ocean areas with  
1426 low variability compared to land areas. The split between land (SL<sub>AND</sub>-EL<sub>UC</sub>) and ocean (SO<sub>CEAN</sub>) shows a  
1427 substantial contribution to variability in the south coming from the land, with no consistency between the

1428 DGVMs and the inversions or among inversions. This is expected due to the difficulty of separating exactly the  
1429 land and oceanic fluxes when viewed from atmospheric observations alone. The  $SO_{CEAN}$  interannual variability  
1430 was found to be higher in the  $fCO_2$ -based data products (0.09 to 0.19  $GtC\ yr^{-1}$ ) compared to GOBMs (0.03 to  
1431 0.06  $GtC\ yr^{-1}$ ) in 1990-2021 (Figure B2). Model subsampling experiments recently illustrated that observation-  
1432 based products may overestimate decadal variability in the Southern Ocean carbon sink by 30% due to data  
1433 sparsity, based on one data product with the highest decadal variability (Gloege et al., 2021).

Formatted: Superscript

Formatted: Superscript

#### 1434 3.7.4.4 Tropical vs northern land uptake

1435 A continuing conundrum is the partitioning of the global atmosphere-land flux between the northern hemisphere  
1436 land and the tropical land (Stephens et al., 2017; Pan et al., 2011; Gaubert et al., 2019). It is of importance  
1437 because each region has its own history of land-use change, climate drivers, and impact of increasing  
1438 atmospheric  $CO_2$  and nitrogen deposition. Quantifying the magnitude of each sink is a prerequisite to  
1439 understanding how each individual driver impacts the tropical and mid/high-latitude carbon balance.

1440 We define the North-South (N-S) difference as net atmosphere-land flux north of  $30^\circ N$  minus the net  
1441 atmosphere-land flux south of  $30^\circ N$ . For the inversions, the N-S difference ranges from 0.1  $GtC\ yr^{-1}$  to 2.9  $GtC$   
1442  $yr^{-1}$  across this year's inversion ensemble with a preference across models for either a smaller Northern land  
1443 sink with a near neutral tropical land flux (medium N-S difference), or a large Northern land sink and a tropical  
1444 land source (large N-S difference).

1445 In the ensemble of DGVMs the N-S difference is  $0.6 \pm 0.5\ GtC\ yr^{-1}$ , a much narrower range than the one from  
1446 inversions. Only two DGVMs have a N-S difference larger than 1.0  $GtC\ yr^{-1}$ . The larger agreement across  
1447 DGVMs than across inversions is to be expected as there is no correlation between Northern and Tropical land  
1448 sinks in the DGVMs as opposed to the inversions where the sum of the two regions being well-constrained leads  
1449 to an anti-correlation between these two regions. The much smaller spread in the N-S difference between the  
1450 DGVMs could help to scrutinise the inverse systems further. For example, a large northern land sink and a  
1451 tropical land source in an inversion would suggest a large sensitivity to  $CO_2$  fertilisation (the dominant factor  
1452 driving the land sinks) for Northern ecosystems, which would be not mirrored by tropical ecosystems. Such a  
1453 combination could be hard to reconcile with the process understanding gained from the DGVMs ensembles and  
1454 independent measurements (e.g. Free Air  $CO_2$  Enrichment experiments). Such investigations will be further  
1455 pursued in the upcoming assessment from REgional Carbon Cycle Assessment and Processes (RECCAP2; Ciais  
1456 et al., 2020).

### 1457 3.8 Closing the Global Carbon Cycle

#### 1458 3.8.1 Partitioning of Cumulative Emissions and Sink Fluxes

1459 The global carbon budget over the historical period (1850-2021) is shown in Figure 3.

1460 Emissions during the period 1850-2021 amounted to  $670 \pm 65\ GtC$  and were partitioned among the atmosphere  
1461 ( $275 \pm 5\ GtC$ ; 41%), ocean ( $175 \pm 35\ GtC$ ; 26%), and the land ( $210 \pm 45\ GtC$ ; 31%). The cumulative land sink  
1462 is almost equal to the cumulative land-use emissions ( $200 \pm 60\ GtC$ ), making the global land nearly neutral over  
1463 the whole 1850-2021 period.

Formatted: Outline numbered + Level: 2 + Numbering  
Style: 1, 2, 3, ... + Start at: 1 + Alignment: Left + Aligned at:  
0 cm + Indent at: 1.02 cm

Formatted: Outline numbered + Level: 3 + Numbering  
Style: 1, 2, 3, ... + Start at: 1 + Alignment: Left + Aligned at:  
0 cm + Indent at: 1.27 cm

1464 The use of nearly independent estimates for the individual terms of the global carbon budget shows a cumulative  
1465 budget imbalance of 15 GtC (2% of total emissions) during 1850-2021 (Figure 3, Table 8), which, if correct,  
1466 suggests that emissions could be slightly too high by the same proportion (2%) or that the combined land and  
1467 ocean sinks are slightly underestimated (by about 3%), although these are well within the uncertainty range of  
1468 each component of the budget. Nevertheless, part of the imbalance could originate from the estimation of  
1469 significant increase in  $E_{FOS}$  and  $E_{LUC}$  between the mid 1920s and the mid 1960s which is unmatched by a similar  
1470 growth in atmospheric  $CO_2$  concentration as recorded in ice cores (Figure 3). However, the known loss of  
1471 additional sink capacity of 30-40 GtC (over the 1850-2020 period) due to reduced forest cover has not been  
1472 accounted for in our method and would exacerbate the budget imbalance (see Appendix D.4).

Deleted: Section 2.7

Deleted: ).

1473 For the more recent 1960-2021 period where direct atmospheric  $CO_2$  measurements are available, total  
1474 emissions ( $E_{FOS} + E_{LUC}$ ) amounted to  $470 \pm 50$  GtC, of which  $385 \pm 20$  GtC (82%) were caused by fossil  $CO_2$   
1475 emissions, and  $85 \pm 45$  GtC (18%) by land-use change (Table 8). The total emissions were partitioned among  
1476 the atmosphere ( $210 \pm 5$  GtC; 45%), ocean ( $120 \pm 25$  GtC; 26%), and the land ( $145 \pm 30$  GtC; 30%), with a near  
1477 zero ( $-5$  GtC) unattributed budget imbalance. All components except land-use change emissions have  
1478 significantly grown since 1960, with important interannual variability in the growth rate in atmospheric  $CO_2$   
1479 concentration and in the land  $CO_2$  sink (Figure 4), and some decadal variability in all terms (Table 6).  
1480 Differences with previous budget releases are documented in Figure B5.

1481 The global carbon budget averaged over the last decade (2012-2021) is shown in Figure 2, Figure 14 (right  
1482 panel) and Table 6. For this period, 89% of the total emissions ( $E_{FOS} + E_{LUC}$ ) were from fossil  $CO_2$  emissions  
1483 ( $E_{FOS}$ ), and 11% from land-use change ( $E_{LUC}$ ). The total emissions were partitioned among the atmosphere  
1484 (48%), ocean (26%) and land (29%), with a near-zero unattributed budget imbalance ( $\sim 3\%$ ). For single years,  
1485 the budget imbalance can be larger (Figure 4). For 2021, the combination of our estimated sources ( $10.9 \pm 0.9$   
1486  $GtC\ yr^{-1}$ ) and sinks ( $11.6 \pm 1.0\ GtC\ yr^{-1}$ ) leads to a  $B_{IM}$  of  $-0.6$  GtC, suggesting a slight underestimation of the  
1487 anthropogenic sources, and/or an overestimation of the combined land and ocean sinks

Formatted: Font: (Default) Gungsuh

Formatted: Font: (Default) Gungsuh

### 1488 3.8.2 Carbon Budget Imbalance trend and variability

Formatted: Outline numbered + Level: 3 + Numbering  
Style: 1, 2, 3, ... + Start at: 1 + Alignment: Left + Aligned at:  
0 cm + Indent at: 1.27 cm

1489 The carbon budget imbalance ( $B_{IM}$ ; Eq. 1, Figure 4) quantifies the mismatch between the estimated total  
1490 emissions and the estimated changes in the atmosphere, land, and ocean reservoirs. The mean budget imbalance  
1491 from 1960 to 2021 is very small ( $4.6$  GtC over the period, i.e. average of  $0.07\ GtC\ yr^{-1}$ ) and shows no trend over  
1492 the full time series (Figure 4). The process models (GOBMs and DGVMs) and data-products have been selected  
1493 to match observational constraints in the 1990s, but no further constraints have been applied to their  
1494 representation of trend and variability. Therefore, the near-zero mean and trend in the budget imbalance is seen  
1495 as evidence of a coherent community understanding of the emissions and their partitioning on those time scales  
1496 (Figure 4). However, the budget imbalance shows substantial variability of the order of  $\pm 1\ GtC\ yr^{-1}$ , particularly  
1497 over semi-decadal time scales, although most of the variability is within the uncertainty of the estimates. The  
1498 positive carbon imbalance during the 1960s, and early 1990s, indicates that either the emissions were  
1499 overestimated, or the sinks were underestimated during these periods. The reverse is true for the 1970s, and to a  
1500 lower extent for the 1980s and 2012-2021 period (Figure 4, Table 6).

1503 We cannot attribute the cause of the variability in the budget imbalance with our analysis, we only note that the  
1504 budget imbalance is unlikely to be explained by errors or biases in the emissions alone because of its large semi-  
1505 decadal variability component, a variability that is untypical of emissions and has not changed in the past 60  
1506 years despite a near tripling in emissions (Figure 4). Errors in  $S_{\text{LAND}}$  and  $S_{\text{OCEAN}}$  are more likely to be the main  
1507 cause for the budget imbalance, especially on interannual to semi-decadal timescales. For example,  
1508 underestimation of the  $S_{\text{LAND}}$  by DGVMs has been reported following the eruption of Mount Pinatubo in 1991  
1509 possibly due to missing responses to changes in diffuse radiation (Mercado et al., 2009). Although since  
1510 GCB2021 we accounted for aerosol effects on solar radiation quantity and quality (diffuse vs direct), most  
1511 DGVMs only used the former as input (i.e., total solar radiation) (Table A1). Thus, the ensemble mean may not  
1512 capture the full effects of volcanic eruptions, i.e. associated with high light scattering sulphate aerosols, on the  
1513 land carbon sink (O’Sullivan et al., 2021). DGVMs are suspected to overestimate the land sink in response to  
1514 the wet decade of the 1970s (Sitch et al., 2008). Quasi-decadal variability in the ocean sink has also been  
1515 reported, with all methods agreeing on a smaller than expected ocean  $\text{CO}_2$  sink in the 1990s and a larger than  
1516 expected sink in the 2000s (Figure 10; Landschützer et al., 2016, DeVries et al., 2019, Hauck et al., 2020,  
1517 McKinley et al., 2020). Errors in sink estimates could also be driven by errors in the climatic forcing data,  
1518 particularly precipitation for  $S_{\text{LAND}}$  and wind for  $S_{\text{OCEAN}}$ . Also, the  $B_{\text{IM}}$  shows substantial departure from zero on  
1519 yearly time scales (Figure 4e), highlighting unresolved variability of the carbon cycle, likely in the land sink  
1520 ( $S_{\text{LAND}}$ ), given its large year to year variability (Figure 4d and 8).

1521 Both the budget imbalance ( $B_{\text{IM}}$ , Table 6) and the residual land sink from the global budget ( $E_{\text{FOS}}+E_{\text{LUC}}-G_{\text{ATM}}-$   
1522  $S_{\text{OCEAN}}$ , Table 5) include an error term due to the inconsistencies that arises from using  $E_{\text{LUC}}$  from bookkeeping  
1523 models, and  $S_{\text{LAND}}$  from DGVMs, most notably the loss of additional sink capacity (see section 2.7 [and](#)  
1524 [Appendix D.4](#)). Other differences include a better accounting of land use changes practices and processes in  
1525 bookkeeping models than in DGVMs, or the bookkeeping models error of having present-day observed carbon  
1526 densities fixed in the past. That the budget imbalance shows no clear trend towards larger values over time is an  
1527 indication that these inconsistencies probably play a minor role compared to other errors in  $S_{\text{LAND}}$  or  $S_{\text{OCEAN}}$ .  
1528 Although the budget imbalance is near zero for the recent decades, it could be due to compensation of errors.  
1529 We cannot exclude an overestimation of  $\text{CO}_2$  emissions, particularly from land-use change, given their large  
1530 uncertainty, as has been suggested elsewhere (Piao et al., 2018), combined with an underestimate of the sinks. A  
1531 larger DGVM ( $S_{\text{LAND}}-E_{\text{LUC}}$ ) over the extra-tropics would reconcile model results with inversion estimates for  
1532 fluxes in the total land during the past decade (Figure 13; Table 5). Likewise, a larger  $S_{\text{OCEAN}}$  is also possible  
1533 given the higher estimates from the data-products (see section 3.1.2, Figure 10 and Figure 13), the  
1534 underestimation of interior ocean anthropogenic carbon accumulation in the GOBMs (section 3.5.5), and the  
1535 recently suggested upward adjustments of the ocean carbon sink in Earth System Models (Terhaar et al., 2022),  
1536 and in data-products, here related to a potential temperature bias and skin effects (Watson et al., 2020, Dong et  
1537 al., 2022, Figure 10). If  $S_{\text{OCEAN}}$  were to be based on data-products alone, with all data-products including this  
1538 adjustment, this would result in a 2012-2021  $S_{\text{OCEAN}}$  of  $3.8 \text{ GtC yr}^{-1}$  (Dong et al., 2022) or  $>4 \text{ GtC yr}^{-1}$  (Watson  
1539 et al., 2020), i.e., outside of the range supported by the atmospheric inversions and with an implied negative  $B_{\text{IM}}$   
1540 of more than  $-1 \text{ GtC yr}^{-1}$  indicating that a closure of the budget could only be achieved with either anthropogenic  
1541 emissions being significantly larger and/or the net land sink being substantially smaller than estimated here.

1542 More integrated use of observations in the Global Carbon Budget, either on their own or for further constraining  
1543 model results, should help resolve some of the budget imbalance (Peters et al., 2017).

1544

#### 1545 4 Tracking progress towards mitigation targets

1546 The average growth in global fossil CO<sub>2</sub> emissions peaked at +3% per year during the 2000s, driven by the rapid  
1547 growth in emissions in China. In the last decade, however, the global growth rate has slowly declined, reaching  
1548 a low +0.5% per year over 2012-2021 (including the 2020 global decline and the 2021 emissions rebound).

1549 While this slowdown in global fossil CO<sub>2</sub> emissions growth is welcome, it is far from the emission decrease  
1550 needed to be consistent with the temperature goals of the Paris Agreement.

1551 Since the 1990s, the average growth rate of fossil CO<sub>2</sub> emissions has continuously declined across the group of  
1552 developed countries of the Organisation for Economic Co-operation and Development (OECD), with emissions  
1553 peaking in around 2005 and now declining at around 1% yr<sup>-1</sup> (Le Quéré et al., 2021). In the decade 2012-2021,  
1554 territorial fossil CO<sub>2</sub> emissions decreased significantly (at the 95% confidence level) in 24 countries whose  
1555 economies grew significantly (also at the 95% confidence level): Belgium, Croatia, Czech Republic, Denmark,  
1556 Estonia, Finland, France, Germany, Hong Kong, Israel, Italy, Japan, Luxembourg, Malta, Mexico, Netherlands,  
1557 Norway, Singapore, Slovenia, Sweden, Switzerland, United Kingdom, USA, and Uruguay (updated from Le  
1558 Quéré et al., 2019). Altogether, these 24 countries emitted 2.4 GtC yr<sup>-1</sup> (8.8 GtCO<sub>2</sub> yr<sup>-1</sup>) on average over the last  
1559 decade, about one quarter of world CO<sub>2</sub> fossil emissions. Consumption-based emissions also fell significantly  
1560 during the final decade for which estimates are available (2011-2020) in 15 of these countries: Belgium,  
1561 Denmark, Estonia, Finland, France, Germany, Hong Kong, Israel, Japan, Luxembourg, Mexico, Netherlands,  
1562 Singapore, Sweden, United Kingdom, and Uruguay. Figure 15 shows that the emission declines in the USA and  
1563 the EU27 are primarily driven by increased decarbonisation (CO<sub>2</sub> emissions per unit energy) in the last decade  
1564 compared to the previous, with smaller contributions in the EU27 from slightly weaker economic growth and  
1565 slightly larger declines in energy per GDP. These countries have stable or declining energy use and so  
1566 decarbonisation policies replace existing fossil fuel infrastructure (Le Quéré et al. 2019).

1567 In contrast, fossil CO<sub>2</sub> emissions continue to grow in non-OECD countries, although the growth rate has slowed  
1568 from almost 6% yr<sup>-1</sup> during the 2000s to less than 2% yr<sup>-1</sup> in the last decade. Representing 47% of non-OECD  
1569 emissions in 2021, a large part of this slowdown is due to China, which has seen emissions growth decline from  
1570 nearly 10% yr<sup>-1</sup> in the 2000s to 1.5% yr<sup>-1</sup> in the last decade. Excluding China, non-OECD emissions grew at  
1571 3.3% yr<sup>-1</sup> in the 2000s compared to 1.6% yr<sup>-1</sup> in the last decade. Figure 15 shows that, compared to the previous  
1572 decade, China has had weaker economic growth in the last decade and a higher decarbonisation rate, with more  
1573 rapid declines in energy per GDP that are now back to levels seen during the 1990s. India and the rest of the  
1574 world have strong economic growth that is not offset by decarbonisation or declines in energy per GDP, driving  
1575 up fossil CO<sub>2</sub> emissions. Despite the high deployment of renewables in some countries (e.g., India), fossil  
1576 energy sources continue to grow to meet growing energy demand (Le Quéré et al. 2019).

1577 Globally, fossil CO<sub>2</sub> emissions growth is slowing, and this is due to the emergence of climate policy (Eskander  
1578 and Fankhauser 2020; Le Quere et al 2019) and technological change, which is leading to a shift from coal to  
1579 gas and growth in renewable energies, and reduced expansion of coal capacity. At the aggregated global level,

Formatted: Outline numbered + Level: 1 + Numbering  
Style: 1, 2, 3, ... + Start at: 1 + Alignment: Left + Aligned at:  
0 cm + Indent at: 0.76 cm

Formatted: Subscript

1580 decarbonisation shows a strong and growing signal in the last decade, with smaller contributions from lower  
1581 economic growth and declines in energy per GDP. Despite the slowing growth in global fossil CO<sub>2</sub> emissions,  
1582 emissions are still growing, far from the reductions needed to meet the ambitious climate goals of the UNFCCC  
1583 Paris agreement.

1584 We update the remaining carbon budget assessed by the IPCC AR6 (Canadell et al., 2021), accounting for the  
1585 2020 to 2022 estimated emissions from fossil fuel combustion (E<sub>FOS</sub>) and land use changes (E<sub>LUC</sub>). From  
1586 January 2023, the remaining carbon (50% likelihood) for limiting global warming to 1.5°C, 1.7°C and 2°C is  
1587 estimated to amount to 105, 200, and 335 GtC (380, 730, 1230 GtCO<sub>2</sub>). These numbers include an uncertainty  
1588 based on model spread (as in IPCC AR6), which is reflected through the percent likelihood of exceeding the  
1589 given temperature threshold. These remaining amounts correspond respectively to about 9, 18 and 30 years from  
1590 the beginning of 2023, at the 2022 level of total CO<sub>2</sub> emissions. Reaching net zero CO<sub>2</sub> emissions by 2050  
1591 entails cutting total anthropogenic CO<sub>2</sub> emissions by about 0.4 GtC (1.4 GtCO<sub>2</sub>) each year on average,  
1592 comparable to the decrease observed in 2020 during the COVID-19 pandemic.

1593

## 1594 5 Discussion

1595 Each year when the global carbon budget is published, each flux component is updated for all previous years to  
1596 consider corrections that are the result of further scrutiny and verification of the underlying data in the primary  
1597 input data sets. Annual estimates may be updated with improvements in data quality and timeliness (e.g., to  
1598 eliminate the need for extrapolation of forcing data such as land-use). Of all terms in the global budget, only the  
1599 fossil CO<sub>2</sub> emissions and the growth rate in atmospheric CO<sub>2</sub> concentration are based primarily on empirical  
1600 inputs supporting annual estimates in this carbon budget. The carbon budget imbalance, yet an imperfect  
1601 measure, provides a strong indication of the limitations in observations in understanding and representing  
1602 processes in models, and/or in the integration of the carbon budget components.

1603 The persistent unexplained variability in the carbon budget imbalance limits our ability to verify reported  
1604 emissions (Peters et al., 2017) and suggests we do not yet have a complete understanding of the underlying  
1605 carbon cycle dynamics on annual to decadal timescales. Resolving most of this unexplained variability should  
1606 be possible through different and complementary approaches. First, as intended with our annual updates, the  
1607 imbalance as an error term is reduced by improvements of individual components of the global carbon budget  
1608 that follow from improving the underlying data and statistics and by improving the models through the  
1609 resolution of some of the key uncertainties detailed in Table 10. Second, additional clues to the origin and  
1610 processes responsible for the variability in the budget imbalance could be obtained through a closer scrutiny of  
1611 carbon variability in light of other Earth system data (e.g., heat balance, water balance), and the use of a wider  
1612 range of biogeochemical observations to better understand the land-ocean partitioning of the carbon imbalance  
1613 (e.g. oxygen, carbon isotopes). Finally, additional information could also be obtained through higher resolution  
1614 and process knowledge at the regional level, and through the introduction of inferred fluxes such as those based  
1615 on satellite CO<sub>2</sub> retrievals. The limit of the resolution of the carbon budget imbalance is yet unclear, but most  
1616 certainly not yet reached given the possibilities for improvements that lie ahead.

Formatted: Font: 10 pt

Formatted: Indent: Left: 0 cm, First line: 0 cm, Outline numbered + Level: 1 + Numbering Style: 1, 2, 3, ... + Start at: 1 + Alignment: Left + Aligned at: 0 cm + Indent at: 0.76 cm

1617 Estimates of global fossil CO<sub>2</sub> emissions from different datasets are in relatively good agreement when the  
1618 different system boundaries of these datasets are considered (Andrew, 2020a). But while estimates of E<sub>FOS</sub> are  
1619 derived from reported activity data requiring much fewer complex transformations than some other components  
1620 of the budget, uncertainties remain, and one reason for the apparently low variation between datasets is  
1621 precisely the reliance on the same underlying reported energy data. The budget excludes some sources of fossil  
1622 CO<sub>2</sub> emissions, which available evidence suggests are relatively small (<1%). We have added emissions from  
1623 lime production in China and the US, but these are still absent in most other non-Annex I countries, and before  
1624 1990 in other Annex I countries.

1625 Estimates of E<sub>LUC</sub> suffer from a range of intertwined issues, including the poor quality of historical land-cover  
1626 and land-use change maps, the rudimentary representation of management processes in most models, and the  
1627 confusion in methodologies and boundary conditions used across methods (e.g., Armeth et al., 2017; Pongratz et  
1628 al., 2014, see also [Appendix D.4](#) on the loss of sink capacity; Bastos et al., 2021). Uncertainties in current and  
1629 historical carbon stocks in soils and vegetation also add uncertainty in the E<sub>LUC</sub> estimates. Unless a major effort  
1630 to resolve these issues is made, little progress is expected in the resolution of E<sub>LUC</sub>. This is particularly  
1631 concerning given the growing importance of E<sub>LUC</sub> for climate mitigation strategies, and the large issues in the  
1632 quantification of the cumulative emissions over the historical period that arise from large uncertainties in E<sub>LUC</sub>.

1633 By adding the DGVMs estimates of CO<sub>2</sub> fluxes due to environmental change from countries' managed forest  
1634 areas (part of S<sub>LAND</sub> in this budget) to the budget E<sub>LUC</sub> estimate, we successfully reconciled the large gap  
1635 between our E<sub>LUC</sub> estimate and the land use flux from NGHGs using the approach described in Grassi et al.  
1636 (2021) for future scenario and in Grassi et al. (2022b) using data from the Global Carbon Budget 2021. The  
1637 updated data presented here can be used as potential adjustment in the policy context, e.g., to help assessing the  
1638 collective countries' progress towards the goal of the Paris Agreement and avoiding double-accounting for the  
1639 sink in managed forests. In the absence of this adjustment, collective progress would hence appear better than it  
1640 is (Grassi et al. 2021). The need of such adjustment whenever a comparison between LULUCF fluxes reported  
1641 by countries and the global emission estimates of the IPCC is attempted is recommended also in the recent  
1642 UNFCCC Synthesis report for the first Global Stocktake (UNFCCC, 2022). However, this adjustment should be  
1643 seen as a short-term and pragmatic fix based on existing data, rather than a definitive solution to bridge the  
1644 differences between global models and national inventories. Additional steps are needed to understand and  
1645 reconcile the remaining differences, some of which are relevant at the country level (Grassi, et al. 2022b,  
1646 Schwingshackl, et al., *subm.*).

1647 The comparison of GOBMs, data products and inversions highlights substantial discrepancy in the Southern  
1648 Ocean (Figure 13, Hauck et al., 2020). A large part of the uncertainty in the mean fluxes stems from the regional  
1649 distribution of the river flux adjustment term. The current distribution (Aumont et al., 2001) is based on one  
1650 model study yielding the largest riverine outgassing flux south of 20°S, whereas a recent study, also based on  
1651 one model, simulates the largest share of the outgassing to occur in the tropics (Lacroix et al., 2020). The long-  
1652 standing sparse data coverage of fCO<sub>2</sub> observations in the Southern compared to the Northern Hemisphere (e.g.,  
1653 Takahashi et al., 2009) continues to exist (Bakker et al., 2016, 2022, Figure B1) and to lead to substantially  
1654 higher uncertainty in the SO<sub>CEAN</sub> estimate for the Southern Hemisphere (Watson et al., 2020, Gloege et al.,  
1655 2021). This discrepancy, which also hampers model improvement, points to the need for increased high-quality

Deleted: Section 2.7

Deleted:

1658 fCO<sub>2</sub> observations especially in the Southern Ocean. At the same time, model uncertainty is illustrated by the  
1659 large spread of individual GOBM estimates (indicated by shading in Figure 13) and highlights the need for  
1660 model improvement. The diverging trends in *SOCEAN* from different methods is a matter of concern, which is  
1661 unresolved. The assessment of the net land-atmosphere exchange from DGVMs and atmospheric inversions also  
1662 shows substantial discrepancy, particularly for the estimate of the total land flux over the northern extra-tropic.  
1663 This discrepancy highlights the difficulty to quantify complex processes (CO<sub>2</sub> fertilisation, nitrogen deposition  
1664 and fertilisers, climate change and variability, land management, etc.) that collectively determine the net land  
1665 CO<sub>2</sub> flux. Resolving the differences in the Northern Hemisphere land sink will require the consideration and  
1666 inclusion of larger volumes of observations.

1667 We provide metrics for the evaluation of the ocean and land models and the atmospheric inversions (Figs. B2 to  
1668 B4). These metrics expand the use of observations in the global carbon budget, helping 1) to support  
1669 improvements in the ocean and land carbon models that produce the sink estimates, and 2) to constrain the  
1670 representation of key underlying processes in the models and to allocate the regional partitioning of the CO<sub>2</sub>  
1671 fluxes. However, GOBMs skills have changed little since the introduction of the ocean model evaluation. The  
1672 additional simulation allows for direct comparison with interior ocean anthropogenic carbon estimates and  
1673 suggests that the models underestimate anthropogenic carbon uptake and storage. This is an initial step towards  
1674 the introduction of a broader range of observations that we hope will support continued improvements in the  
1675 annual estimates of the global carbon budget.

1676 We assessed before that a sustained decrease of -1% in global emissions could be detected at the 66%  
1677 likelihood level after a decade only (Peters et al., 2017). Similarly, a change in behaviour of the land and/or  
1678 ocean carbon sink would take as long to detect, and much longer if it emerges more slowly. To continue  
1679 reducing the carbon imbalance on annual to decadal time scales, regionalising the carbon budget, and integrating  
1680 multiple variables are powerful ways to shorten the detection limit and ensure the research community can  
1681 rapidly identify issues of concern in the evolution of the global carbon cycle under the current rapid and  
1682 unprecedented changing environmental conditions.

1683

## 1684 6 Conclusions

1685 The estimation of global CO<sub>2</sub> emissions and sinks is a major effort by the carbon cycle research community that  
1686 requires a careful compilation and synthesis of measurements, statistical estimates, and model results. The  
1687 delivery of an annual carbon budget serves two purposes. First, there is a large demand for up-to-date  
1688 information on the state of the anthropogenic perturbation of the climate system and its underpinning causes. A  
1689 broad stakeholder community relies on the data sets associated with the annual carbon budget including  
1690 scientists, policy makers, businesses, journalists, and non-governmental organisations engaged in adapting to  
1691 and mitigating human-driven climate change. Second, over the last decades we have seen unprecedented  
1692 changes in the human and biophysical environments (e.g., changes in the growth of fossil fuel emissions, impact  
1693 of COVID-19 pandemic, Earth's warming, and strength of the carbon sinks), which call for frequent  
1694 assessments of the state of the planet, a better quantification of the causes of changes in the contemporary global  
1695 carbon cycle, and an improved capacity to anticipate its evolution in the future. Building this scientific

Formatted: Indent: Left: 0 cm, First line: 0 cm, Outline numbered + Level: 1 + Numbering Style: 1, 2, 3, ... + Start at: 1 + Alignment: Left + Aligned at: 0 cm + Indent at: 0.76 cm

1696 understanding to meet the extraordinary climate mitigation challenge requires frequent, robust, transparent, and  
1697 traceable data sets and methods that can be scrutinised and replicated. This paper via 'living data' helps to keep  
1698 track of new budget updates.

1699

## 1700 7 **Data availability**

1701 The data presented here are made available in the belief that their wide dissemination will lead to greater  
1702 understanding and new scientific insights of how the carbon cycle works, how humans are altering it, and how  
1703 we can mitigate the resulting human-driven climate change. Full contact details and information on how to cite  
1704 the data shown here are given at the top of each page in the accompanying database and summarised in Table 2.

1705 The accompanying database includes [three](#) Excel files organised in the following spreadsheets:

1706 File [Global\\_Carbon\\_Budget\\_2022v0.1.xlsx](#) includes the following:

- 1707 1. Summary
- 1708 2. The global carbon budget (1959-2021);
- 1709 3. The historical global carbon budget (1750-2021);
- 1710 4. Global CO<sub>2</sub> emissions from fossil fuels and cement production by fuel type, and the per-capita emissions  
1711 (1850-2021);
- 1712 5. CO<sub>2</sub> emissions from land-use change from the individual [bookkeeping models](#) (1959-2021);
- 1713 6. Ocean CO<sub>2</sub> sink from the individual ocean models and fCO<sub>2</sub>-based products (1959-2021);
- 1714 7. Terrestrial CO<sub>2</sub> sink from the individual DGVMs (1959-2021);
- 1715 8. Cement carbonation CO<sub>2</sub> sink (1959-2021).

1716 File [National Fossil Carbon Emissions 2022v0.1.xlsx](#) includes the following:

- 1717 1. Summary
- 1718 2. Territorial country CO<sub>2</sub> emissions from fossil [fuels and cement production](#) (1850-2021);
- 1719 3. Consumption country CO<sub>2</sub> emissions from fossil [fuels and cement production](#) and emissions transfer from  
1720 the international trade of goods and services (1990-2020) using CDIAC/UNFCCC data as reference;
- 1721 4. Emissions transfers (Consumption minus territorial emissions; 1990-2020);
- 1722 5. Country definitions.

1723 File [National LandUseChange Carbon Emissions 2022v0.1.xlsx](#) includes the following:

- 1724 1. [Summary](#)
- 1725 2. [Territorial country CO<sub>2</sub> emissions from Land Use Change \(1850-2021\) from three bookkeeping models;](#)

1726

Formatted: Font: 10 pt

Formatted: Indent: Left: 0 cm, First line: 0 cm, Outline numbered + Level: 1 + Numbering Style: 1, 2, 3, ... + Start at: 1 + Alignment: Left + Aligned at: 0 cm + Indent at: 0.76 cm

Deleted: two

Formatted: Indent: Left: 0.12 cm, Outline numbered + Level: 4 + Numbering Style: 1, 2, 3, ... + Start at: 1 + Alignment: Left + Aligned at: 4.44 cm + Indent at: 5.08 cm

Formatted: Indent: Left: 0.12 cm, Space Before: 6 pt, Outline numbered + Level: 4 + Numbering Style: 1, 2, 3, ... + Start at: 1 + Alignment: Left + Aligned at: 4.44 cm + Indent at: 5.08 cm

Deleted: methods and

Formatted: Indent: Left: 0.12 cm, Outline numbered + Level: 4 + Numbering Style: 1, 2, 3, ... + Start at: 1 + Alignment: Left + Aligned at: 4.44 cm + Indent at: 5.08 cm

Formatted: Subscript

Deleted: ¶

Formatted: Font colour: Auto

Formatted: Font colour: Auto

Deleted: CO<sub>2</sub> emissions

Deleted: CO<sub>2</sub> emissions

1732 All three spreadsheets are published by the Integrated Carbon Observation System (ICOS) Carbon Portal and  
1733 are available at <https://doi.org/10.18160/GCP-2022> (Friedlingstein et al., 2022b). National emissions data are  
1734 also available from the Global Carbon Atlas (<http://www.globalcarbonatlas.org/>, last access: 25 September  
1735 2022) and from Our World in Data (<https://ourworldindata.org/co2-emissions>, last access: 25 September 2022).

Deleted: ¶  
Both

## 1737 8 Author contributions

1738 PF, MOS, MWJ, RMA, LGr, JH, CLQ, ITL, AO, GPP, WP, JP, CIS, and SS designed the study, conducted the  
1739 analysis, and wrote the paper with input from JGC, PC and RBJ. RMA, GPP and JIK produced the fossil fuel  
1740 emissions and their uncertainties and analysed the emissions data. MH and GM provided fossil fuel emission  
1741 data. JP, TGa, CIS and RAH provided the bookkeeping land-use change emissions with synthesis by JP and  
1742 CIS. JH, LB, ÖG, NG, TI, KL, NMa, LR, JS, RS, HiT, and ReW provided an update of the global ocean  
1743 biogeochemical models, MG, LGl, LGr, YI, AJ, ChR, JDS, and JZ provided an update of the ocean fCO<sub>2</sub> data  
1744 products, with synthesis on both streams by JH, LGr and NMa. SRA, NRB, MB, HCB, MC, WE, RAF, TGk,  
1745 KK, NL, NMe, NMM, DRM, SN, TO, DP, KP, ChR, IS, TS, AJS, CoS, ST, TT, BT, RiW, CW, AW provided  
1746 ocean fCO<sub>2</sub> measurements for the year 2021, with synthesis by AO and KO. AA, VKA, SF, AKJ, EK, DK, JK,  
1747 MJM, MOS, BP, QS, HaT, APW, WY, XY, and SZ provided an update of the Dynamic Global Vegetation  
1748 Models, with synthesis by SS and MOS. WP, ITL, FC, JL, YN, PIP, ChR, XT, and BZ provided an updated  
1749 atmospheric inversion, WP, FC, and ITL developed the protocol and produced the evaluation. RMA provided  
1750 predictions of the 2022 emissions and atmospheric CO<sub>2</sub> growth rate. PL provided the predictions of the 2022  
1751 ocean and land sinks. LPC, GCH, KKG, TMR and GRvdW provided forcing data for land-use change. RA, GG,  
1752 FT, and CY provided data for the land-use change NGHGI mapping. PPT provided key atmospheric CO<sub>2</sub> data.  
1753 MWJ produced the model atmospheric CO<sub>2</sub> forcing and the atmospheric CO<sub>2</sub> growth rate. MOS and NB  
1754 produced the aerosol diffuse radiative forcing for the DGVMs. IH provided the climate forcing data for the  
1755 DGVMs. ER provided the evaluation of the DGVMs. MWJ provided the emissions prior for use in the inversion  
1756 systems. ZL provided seasonal emissions data for most recent years for the emission prior. MWJ and MOS  
1757 developed the new data management pipeline which automates many aspects of the data collation, analysis,  
1758 plotting and synthesis. PF, MOS and MMJ coordinated the effort, revised all figures, tables, text and/or numbers  
1759 to ensure the update was clear from the 2021 edition and in line with the [globalcarbonatlas.org](http://www.globalcarbonatlas.org).

Formatted: Indent: Left: 0 cm, First line: 0 cm, Outline  
numbered + Level: 1 + Numbering Style: 1, 2, 3, ... + Start  
at: 1 + Alignment: Left + Aligned at: 0 cm + Indent at: 0.76  
cm

1761 **Competing interests.** The authors declare that they have no conflict of interest.

1762

1765 **9 Acknowledgements**

1766 We thank all people and institutions who provided the data used in this global carbon budget 2022 and the Global  
1767 Carbon Project members for their input throughout the development of this publication. We thank Nigel Hawtin  
1768 for producing Figure 2 and Figure 14. We thank Thomas Hawes for technical support with the data management  
1769 pipeline. We thank Ed Dlugokencky for providing atmospheric CO<sub>2</sub> measurements. We thank Ian G. C. Ashton,  
1770 Fatemeh Chegini, Trang T. Chau, Sam Ditkovsky, Christian Ethé, Amanda R. Fay, Lonnie Goddijn-Murphy,  
1771 T. Holding, Fabrice Lacroix, Enhui Liao, Galen A. McKinley, Shijie Shu, Richard Sims, Jade Skye, Andrew J.  
1772 Watson, David Willis, and David K. Woolf for their involvement in the development, use and analysis of the  
1773 models and data-products used here. Daniel Kennedy thanks all the scientists, software engineers, and  
1774 administrators who contributed to the development of CESM2. We thank Joe Salisbury, Doug Vandemark,  
1775 Christopher W. Hunt, and Peter Landschützer who contributed to the provision of surface ocean CO<sub>2</sub> observations  
1776 for the year 2021 (see Table A5). We also thank Benjamin Pfeil, Rocio Castaño-Primo, and Stephen D. Jones of  
1777 the Ocean Thematic Centre of the EU Integrated Carbon Observation System (ICOS) Research Infrastructure,  
1778 Eugene Burger of NOAA's Pacific Marine Environmental Laboratory and Alex Kozyr of NOAA's National  
1779 Centers for Environmental Information, for their contribution to surface ocean CO<sub>2</sub> data and metadata  
1780 management. This is PMEL contribution 5434. We thank the scientists, institutions, and funding agencies  
1781 responsible for the collection and quality control of the data in SOCAT as well as the International Ocean Carbon  
1782 Coordination Project (IOCCP), the Surface Ocean Lower Atmosphere Study (SOLAS) and the Integrated Marine  
1783 Biosphere Research (IMBeR) program for their support. We thank data providers ObsPack GLOBALVIEWplus  
1784 v7.0 and NRT v7.2 for atmospheric CO<sub>2</sub> observations. We thank the individuals and institutions that provided the  
1785 databases used for the model evaluations used here. We thank Fortunat Joos, Samar Khatiwala and Timothy  
1786 DeVries for providing historical data. Matthew J. McGrath thanks the whole ORCHIDEE group. Ian Harris thanks  
1787 the Japan Meteorological Agency (JMA) for producing the Japanese 55-year Reanalysis (JRA-55). Anthony P.  
1788 Walker thanks ORNL which is managed by UT-Battelle, LLC, for the DOE under contract DE-AC05-1008  
1789 00OR22725. Yosuke Niwa thanks CSIRO, EC, EMPA, FMI, IPEN, JMA, LSCE, NCAR, NIES, NILU, NIWA,  
1790 NOAA, SIO, and TU/NIPR for providing data for NISMON-CO<sub>2</sub>. Xiangjun Tian thanks Zhe Jin, Yilong Wang,  
1791 Tao Wang and Shilong Piao for their contributions to the GONGGA inversion system. Bo Zheng thanks the  
1792 comments and suggestions from Philippe Ciais and Frédéric Chevallier. Frédéric Chevallier thanks Marine  
1793 Remaud who maintained the atmospheric transport model for the CAMS inversion. Paul I. Palmer thanks Liang  
1794 Feng and acknowledges ongoing support from the National Centre for Earth Observation. Junjie Liu thanks the

Formatted: Indent: Left: 0 cm, First line: 0 cm, Outline numbered + Level: 1 + Numbering Style: 1, 2, 3, ... + Start at: 1 + Alignment: Left + Aligned at: 0 cm + Indent at: 0.76 cm

1795 Jet Propulsion Laboratory, California Institute of Technology. Wiley Evans thanks the Tula Foundation for  
1796 funding support. Australian ocean CO<sub>2</sub> data were sourced from Australia's Integrated Marine Observing System  
1797 (IMOS); IMOS is enabled by the National Collaborative Research Infrastructure Strategy (NCRIS). Margot  
1798 Cronin thanks Anthony English, Clynt Gregory and Gordon Furey (P&O Maritime Services) for their support.  
1799 Nathalie Lefèvre thanks the crew of the Cap San Lorenzo and the US IMAGO of IRD Brest for technical support.  
1800 Henry C. Bittig is grateful for the skillful technical support of M. Glockzin and B. Sadkowiak. Meike Becker and  
1801 Are Olsen thank Sparebanken Vest/Agenda Vestlandet for their support for the observations on the Statsraad  
1802 Lehmkuhl. Thanos Gkritzalis thanks the personnel and crew of Simon Stevin. Matthew W. Jones thanks Anthony  
1803 J. De-Gol for his technical and conceptual assistance with the development of GCP-GridFED. FAOSTAT is  
1804 funded by FAO member states through their contributions to the FAO Regular Programme, data contributions by  
1805 national experts are greatly acknowledged. The views expressed in this paper are the authors' only and do not  
1806 necessarily reflect those of FAO. Finally, we thank all funders who have supported the individual and joint  
1807 contributions to this work (see Table A9), as well as the reviewers of this manuscript and previous versions, and  
1808 the many researchers who have provided feedback.

1809

## 1810 **References**

- 1811 Ahlström, A., Raupach, M. R., Schurgers, G., Smith, B., Ameth, A., Jung, M., Reichstein, M., Canadell, J. G.,  
1812 Friedlingstein, P., Jain, A. K., Kato, E., Poulter, B., Sitch, S., Stocker, B. D., Viovy, N., Wang, Y. P., Wiltshire,  
1813 A., Zaehle, S., and Zeng, N.: The dominant role of semi-arid ecosystems in the trend and variability of the land  
1814 CO<sub>2</sub> sink, 348, 895–899, <https://doi.org/10.1126/science.aaa1668>, 2015.
- 1815 Amador-Jiménez, M., Millner, N., Palmer, C., Pennington, R. T., and Sileci, L.: The Unintended Impact of  
1816 Colombia's Covid-19 Lockdown on Forest Fires, *Environ Resource Econ*, 76, 1081–1105,  
1817 <https://doi.org/10.1007/s10640-020-00501-5>, 2020.
- 1818 Amante, C. and Eakins, B. W.: ETOPO1 Global Relief Model converted to PanMap layer format,  
1819 <https://doi.org/10.1594/PANGAEA.769615>, 2009.
- 1820 Andela, N., Morton, D. C., Giglio, L., Chen, Y., van der Werf, G. R., Kasibhatla, P. S., DeFries, R. S., Collatz,  
1821 G. J., Hantson, S., Kloster, S., Bachelet, D., Forrest, M., Lasslop, G., Li, F., Mangeon, S., Melton, J. R., Yue, C.,  
1822 and Randerson, J. T.: A human-driven decline in global burned area, *Science*, 356, 1356–1362,  
1823 <https://doi.org/10.1126/science.aal4108>, 2017.
- 1824 Andres, R. J., Boden, T. A., Bréon, F.-M., Ciais, P., Davis, S., Erickson, D., Gregg, J. S., Jacobson, A., Marland,  
1825 G., Miller, J., Oda, T., Olivier, J. G. J., Raupach, M. R., Rayner, P., and Treanton, K.: A synthesis of carbon  
1826 dioxide emissions from fossil-fuel combustion, *Biogeosciences*, 9, 1845–1871, <https://doi.org/10.5194/bg-9->

Formatted: Indent: Left: 0.63 cm, Hanging: 0.63 cm

- 1827 1845-2012, 2012.
- 1828 Andres, R. J., Boden, T. A., and Higdon, D.: A new evaluation of the uncertainty associated with CDIAC  
1829 estimates of fossil fuel carbon dioxide emission, *Tellus B: Chemical and Physical Meteorology*, 66, 23616,  
1830 <https://doi.org/10.3402/tellusb.v66.23616>, 2014.
- 1831 Andrew, R. M.: A comparison of estimates of global carbon dioxide emissions from fossil carbon sources, *Earth  
1832 Syst. Sci. Data*, 12, 1437–1465, <https://doi.org/10.5194/essd-12-1437-2020>, 2020a.
- 1833 Andrew, R. M.: Timely estimates of India’s annual and monthly fossil CO<sub>2</sub> emissions, *Earth Syst. Sci. Data*, 12,  
1834 2411–2421, <https://doi.org/10.5194/essd-12-2411-2020>, 2020b.
- 1835 Andrew, R. M.: Towards near real-time, monthly fossil CO<sub>2</sub> emissions estimates for the European Union with  
1836 current-year projections, *Atmospheric Pollution Research*, 101229, <https://doi.org/10.1016/j.apr.2021.101229>,  
1837 2021.
- 1838 Andrew, R. M. and Peters, G. P.: A multi-region input–output table based on the global trade analysis project  
1839 database (GTAP-MRIO), *Economic Systems Research*, 25, 99–121,  
1840 <https://doi.org/10.1080/09535314.2012.761953>, 2013.
- 1841 Andrew, R. M. and Peters, G. P.: The Global Carbon Project’s fossil CO<sub>2</sub> emissions dataset (2021v34),  
1842 <https://doi.org/10.5281/ZENODO.5569235>, 2021.
- 1843 Angelsen, A. and Kaimowitz, D.: Rethinking the Causes of Deforestation: Lessons from Economic Models,  
1844 *World Bank Res. Obs.*, 14, 73–98, <https://doi.org/10.1093/wbro/14.1.73>, 1999.
- 1845 Aragão, L. E. O. C., Anderson, L. O., Fonseca, M. G., Rosan, T. M., Vedovato, L. B., Wagner, F. H., Silva, C.  
1846 V. J., Silva Junior, C. H. L., Arai, E., Aguiar, A. P., Barlow, J., Berenguer, E., Deeter, M. N., Domingues, L. G.,  
1847 Gatti, L., Gloor, M., Malhi, Y., Marengo, J. A., Miller, J. B., Phillips, O. L., and Saatchi, S.: 21st Century  
1848 drought-related fires counteract the decline of Amazon deforestation carbon emissions, *Nat Commun*, 9, 536,  
1849 <https://doi.org/10.1038/s41467-017-02771-y>, 2018.
- 1850 Archer, D., Eby, M., Brovkin, V., Ridgwell, A., Cao, L., Mikolajewicz, U., Caldeira, K., Matsumoto, K.,  
1851 Munhoven, G., Montenegro, A., and Tokos, K.: Atmospheric Lifetime of Fossil Fuel Carbon Dioxide, *Annu.  
1852 Rev. Earth Planet. Sci.*, 37, 117–134, <https://doi.org/10.1146/annurev.earth.031208.100206>, 2009.
- 1853 Armeth, A., Sitch, S., Pongratz, J., Stocker, B. D., Ciais, P., Poulter, B., Bayer, A. D., Bondeau, A., Calle, L.,  
1854 Chini, L. P., Gasser, T., Fader, M., Friedlingstein, P., Kato, E., Li, W., Lindeskog, M., Nabel, J. E. M. S., Pugh,  
1855 T. A. M., Robertson, E., Viovy, N., Yue, C., and Zaehle, S.: Historical carbon dioxide emissions caused by  
1856 land-use changes are possibly larger than assumed, *Nature Geosci*, 10, 79–84, <https://doi.org/10.1038/ngeo2882>,  
1857 2017.
- 1858 Arora, V. K., Boer, G. J., Christian, J. R., Curry, C. L., Denman, K. L., Zahariev, K., Flato, G. M., Scinocca, J.  
1859 F., Merryfield, W. J., and Lee, W. G.: The Effect of Terrestrial Photosynthesis Down Regulation on the  
1860 Twentieth-Century Carbon Budget Simulated with the CCCma Earth System Model, 22, 6066–6088,

- 1861 <https://doi.org/10.1175/2009JCLI3037.1>, 2009.
- 1862 Asaadi, A., Arora, V. K., Melton, J. R., and Bartlett, P.: An improved parameterization of leaf area index (LAI)  
 1863 seasonality in the Canadian Land Surface Scheme (CLASS) and Canadian Terrestrial Ecosystem Model  
 1864 (CTEM) modelling framework, 15, 6885–6907, <https://doi.org/10.5194/bg-15-6885-2018>, 2018.
- 1865 Aumont, O., Orr, J. C., Monfray, P., Ludwig, W., Amiotte-Suchet, P., and Probst, J.-L.: Riverine-driven  
 1866 interhemispheric transport of carbon, *Global Biogeochem. Cycles*, 15, 393–405,  
 1867 <https://doi.org/10.1029/1999GB001238>, 2001.
- 1868 Aumont, O., Ethé, C., Tagliabue, A., Bopp, L., and Gehlen, M.: PISCES-v2: an ocean biogeochemical model  
 1869 for carbon and ecosystem studies, 8, 2465–2513, <https://doi.org/10.5194/gmd-8-2465-2015>, 2015.
- 1870 Avitabile, V., Herold, M., Heuvelink, G. B. M., Lewis, S. L., Phillips, O. L., Asner, G. P., Armston, J., Ashton,  
 1871 P. S., Banin, L., Bayol, N., Berry, N. J., Boeckx, P., de Jong, B. H. J., DeVries, B., Girardin, C. A. J., Kearsley,  
 1872 E., Lindsell, J. A., Lopez-Gonzalez, G., Lucas, R., Malhi, Y., Morel, A., Mitchard, E. T. A., Nagy, L., Qie, L.,  
 1873 Quinones, M. J., Ryan, C. M., Ferry, S. J. W., Sunderland, T., Laurin, G. V., Gatti, R. C., Valentini, R.,  
 1874 Verbeeck, H., Wijaya, A., and Willcock, S.: An integrated pan-tropical biomass map using multiple reference  
 1875 datasets, *Glob Change Biol*, 22, 1406–1420, <https://doi.org/10.1111/gcb.13139>, 2016.
- 1876 Baccini, A., Walker, W., Carvalho, L., Farina, M., Sulla-Menashe, D., and Houghton, R. A.: Tropical forests are  
 1877 a net carbon source based on aboveground measurements of gain and loss, *Science*, 358, 230–234,  
 1878 <https://doi.org/10.1126/science.aam5962>, 2017.
- 1879 Bakker, D. C. E., Pfeil, B., Landa, C. S., Metz, N., O'Brien, K. M., Olsen, A., Smith, K., Cosca, C., Harasawa,  
 1880 S., Jones, S. D., Nakaoka, S., Nojiri, Y., Schuster, U., Steinhoff, T., Sweeney, C., Takahashi, T., Tilbrook, B.,  
 1881 Wada, C., Wanninkhof, R., Alin, S. R., Balestrini, C. F., Barbero, L., Bates, N. R., Bianchi, A. A., Bonou, F.,  
 1882 Boutin, J., Bozec, Y., Burger, E. F., Cai, W.-J., Castle, R. D., Chen, L., Chierici, M., Currie, K., Evans, W.,  
 1883 Featherstone, C., Feely, R. A., Fransson, A., Goyet, C., Greenwood, N., Gregor, L., Hankin, S., Hardman-  
 1884 Mountford, N. J., Harlay, J., Hauck, J., Hoppema, M., Humphreys, M. P., Hunt, C. W., Huss, B., Ibáñez, J. S.  
 1885 P., Johannessen, T., Keeling, R., Kitidis, V., Körtzinger, A., Kozyr, A., Krasakopoulou, E., Kuwata, A.,  
 1886 Landschützer, P., Lauvset, S. K., Lefèvre, N., Lo Monaco, C., Manke, A., Mathis, J. T., Merlivat, L., Millero, F.  
 1887 J., Monteiro, P. M. S., Munro, D. R., Murata, A., Newberger, T., Omar, A. M., Ono, T., Paterson, K., Pearce,  
 1888 D., Pierrot, D., Robbins, L. L., Saito, S., Salisbury, J., Schlitzer, R., Schneider, B., Schweitzer, R., Sieger, R.,  
 1889 Skjelvan, I., Sullivan, K. F., Sutherland, S. C., Sutton, A. J., Tadokoro, K., Telszewski, M., Tuma, M., van  
 1890 Heuven, S. M. A. C., Vandemark, D., Ward, B., Watson, A. J., and Xu, S.: A multi-decade record of high-  
 1891 quality CO<sub>2</sub> data in version 3 of the Surface Ocean CO<sub>2</sub> Atlas (SOCAT), *Earth Syst. Sci. Data*, 8, 383–413,  
 1892 <https://doi.org/10.5194/essd-8-383-2016>, 2016.
- 1893 Bakker, Dorothee C. E.; Alin, Simone R.; Becker, Meike; Bittig, Henry C.; Castaño-Primo, Rocío; Feely,  
 1894 Richard A.; Gkritzalis, Thanos; Kadono, Koji; Kozyr, Alex; Lauvset, Siv K.; Metzl, Nicolas; Munro, David R.;  
 1895 Nakaoka, Shin-ichiro; Nojiri, Yukihiro; O'Brien, Kevin M.; Olsen, Are; Pfeil, Benjamin; Pierrot, Denis;  
 1896 Steinhoff, Tobias; Sullivan, Kevin F.; Sutton, Adrienne J.; Sweeney, Colm; Tilbrook, Bronte; Wada, Chisato;

- 1897 Wanninkhof, Rik; Willstrand Wranne, Anna; Akl, John; Apelthun, Lisa B.; Bates, Nicholas; Beatty, Cory M.;  
 1898 Burger, Eugene F.; Cai, Wei-Jun; Cosca, Catherine E.; Corredor, Jorge E.; Cronin, Margot; Cross, Jessica N.;  
 1899 De Carlo, Eric H.; DeGrandpre, Michael D.; Emerson, Steven; Enright, Matt P.; Enyo, Kazutaka; Evans, Wiley;  
 1900 Frangoulis, Constantin; Fransson, Agneta; García-Ibáñez, Maribel I.; Gehrung, Martina; Giannoudi, Louisa;  
 1901 Glockzin, Michael; Hales, Burke; Howden, Stephan D.; Hunt, Christopher W.; Ibáñez, J. Severino P.; Jones,  
 1902 Steve D.; Kamb, Linus; Körtzinger, Arne; Landa, Camilla S.; Landschützer, Peter; Lefèvre, Nathalie; Lo  
 1903 Monaco, Claire; Macovei, Vlad A.; Maenner Jones, Stacy; Meinig, Christian; Millero, Frank J.; Monacci,  
 1904 Natalie M.; Mordy, Calvin; Morell, Julio M.; Murata, Akihiko; Musielewicz, Sylvia; Neill, Craig; Newberger,  
 1905 Tim; Nomura, Daiki; Ohman, Mark; Ono, Tsuneo; Passmore, Abe; Petersen, Wilhelm; Petihakis, George;  
 1906 Perivoliotis, Leonidas; Plueddemann, Albert J.; Rehder, Gregor; Reynaud, Thierry; Rodriguez, Carmen; Ross,  
 1907 Andrew; Rutgersson, Anna; Sabine, Christopher L.; Salisbury, Joseph E.; Schlitzer, Reiner; Send, Uwe;  
 1908 Skjelvan, Ingunn; Stamatakis, Natalia; Sutherland, Stewart C.; Sweeney, Colm; Tadokoro, Kazuaki; Tanhua,  
 1909 Toste; Telszewski, Maciej; Trull, Tom; Vandemark, Douglas; van Ooijen, Erik; Voynova, Yoana G.; Wang,  
 1910 Hongjie; Weller, Robert A.; Whitehead, Chris; Wilson, Doug (2022). Surface Ocean CO2 Atlas Database  
 1911 Version 2022 (SOCATv2022) (NCEI Accession 0253659). NOAA National Centers for Environmental  
 1912 Information. <https://doi.org/10.25921/1h9f-nb73>.
- 1913 Ballantyne, A. P., Alden, C. B., Miller, J. B., Tans, P. P., and White, J. W. C.: Increase in observed net carbon  
 1914 dioxide uptake by land and oceans during the past 50 years, *Nature*, 488, 70–72,  
 1915 <https://doi.org/10.1038/nature11299>, 2012.
- 1916 Ballantyne, A. P., Andres, R., Houghton, R., Stocker, B. D., Wanninkhof, R., Anderegg, W., Cooper, L. A.,  
 1917 DeGrandpre, M., Tans, P. P., Miller, J. B., Alden, C., and White, J. W. C.: Audit of the global carbon budget:  
 1918 estimate errors and their impact on uptake uncertainty, *Biogeosciences*, 12, 2565–2584,  
 1919 <https://doi.org/10.5194/bg-12-2565-2015>, 2015.
- 1920 Bastos, A., O’Sullivan, M., Ciais, P., Makowski, D., Sitch, S., Friedlingstein, P., Chevallier, F., Rödenbeck, C.,  
 1921 Pongratz, J., Luijkx, I. T., Patra, P. K., Peylin, P., Canadell, J. G., Lauerwald, R., Li, W., Smith, N. E., Peters,  
 1922 W., Goll, D. S., Jain, A. K., Kato, E., Lienert, S., Lombardozzi, D. L., Haverd, V., Nabel, J. E. M. S., Poulter,  
 1923 B., Tian, H., Walker, A. P., and Zaehle, S.: Sources of Uncertainty in Regional and Global Terrestrial CO<sub>2</sub>  
 1924 Exchange Estimates, *Global Biogeochem. Cycles*, 34, <https://doi.org/10.1029/2019GB006393>, 2020.
- 1925 Bastos, A., Hartung, K., Nützel, T. B., Nabel, J. E. M. S., Houghton, R. A., and Pongratz, J.: Comparison of  
 1926 uncertainties in land-use change fluxes from bookkeeping model parameterisation, *ESD*, 12, 745–762,  
 1927 <https://doi.org/10.5194/esd-12-745-2021>, 2021.
- 1928 Basu, S., Baker, D. F., Chevallier, F., Patra, P. K., Liu, J., and Miller, J. B.: The impact of transport model  
 1929 differences on CO<sub>2</sub> surface flux estimates from OCO-2 retrievals of column average CO<sub>2</sub>, *Atmos. Chem. Phys.*,  
 1930 18, 7189–7215, <https://doi.org/10.5194/acp-18-7189-2018>, 2018.
- 1931 Bauer, J. E., Cai, W.-J., Raymond, P. A., Bianchi, T. S., Hopkinson, C. S., and Regnier, P. A. G.: The changing  
 1932 carbon cycle of the coastal ocean, *Nature*, 504, 61–70, <https://doi.org/10.1038/nature12857>, 2013.

- 1933 Beckman, J. and Countryman, A. M.: The Importance of Agriculture in the Economy: Impacts from COVID-19,  
1934 103, 1595–1611, <https://doi.org/10.1111/ajae.12212>, 2021.
- 1935 Bellouin, N., Rae, J., Jones, A., Johnson, C., Haywood, J., and Boucher, O.: Aerosol forcing in the Climate  
1936 Model Intercomparison Project (CMIP5) simulations by HadGEM2-ES and the role of ammonium nitrate, 116,  
1937 <https://doi.org/10.1029/2011JD016074>, 2011.
- 1938 Bennington, V., Gloege, L., and McKinley, G. A.: Variability in the Global Ocean Carbon Sink From 1959 to  
1939 2020 by Correcting Models with Observations, *Geophys. Res. Lett.*, 49, e2022GL098632,  
1940 <https://doi.org/10.1029/2022GL098632>, 2022.
- 1941 Berthet, S., Séférian, R., Bricaud, C., Chevallier, M., Voldoire, A., and Ethé, C.: Evaluation of an Online Grid-  
1942 Coarsening Algorithm in a Global Eddy-Admitting Ocean Biogeochemical Model, 11, 1759–1783,  
1943 <https://doi.org/10.1029/2019MS001644>, 2019.
- 1944 Bourgeois, T., Goris, N., Schwinger, J., and Tjiputra, J. F.: Stratification constrains future heat and carbon  
1945 uptake in the Southern Ocean between 30°S and 55°S, *Nat. Commun.*, 13, 340, [https://doi.org/10.1038/s41467-](https://doi.org/10.1038/s41467-022-27979-5)  
1946 [022-27979-5](https://doi.org/10.1038/s41467-022-27979-5), 2022.
- 1947 Brancalion, P. H. S., Broadbent, E. N., de-Miguel, S., Cardil, A., Rosa, M. R., Almeida, C. T., Almeida, D. R.  
1948 A., Chakravarty, S., Zhou, M., Gamarra, J. G. P., Liang, J., Crouzeilles, R., Hérault, B., Aragão, L. E. O. C.,  
1949 Silva, C. A., and Almeida-Zambrano, A. M.: Emerging threats linking tropical deforestation and the COVID-19  
1950 pandemic, *Perspectives in Ecology and Conservation*, 18, 243–246,  
1951 <https://doi.org/10.1016/j.pecon.2020.09.006>, 2020.
- 1952 Brienen, R. J. W., Phillips, O. L., Feldpausch, T. R., Gloor, E., Baker, T. R., Lloyd, J., Lopez-Gonzalez, G.,  
1953 Monteagudo-Mendoza, A., Malhi, Y., Lewis, S. L., Vásquez Martínez, R., Alexiades, M., Álvarez Dávila, E.,  
1954 Alvarez-Loayza, P., Andrade, A., Aragão, L. E. O. C., Araujo-Murakami, A., Arets, E. J. M. M., Arroyo, L.,  
1955 Aymard C., G. A., Bánki, O. S., Baraloto, C., Barroso, J., Bonal, D., Boot, R. G. A., Camargo, J. L. C., Castilho,  
1956 C. V., Chama, V., Chao, K. J., Chave, J., Comiskey, J. A., Cornejo Valverde, F., da Costa, L., de Oliveira, E. A.,  
1957 Di Fiore, A., Erwin, T. L., Fauset, S., Forsthofer, M., Galbraith, D. R., Grahame, E. S., Groot, N., Hérault, B.,  
1958 Higuchi, N., Honorio Coronado, E. N., Keeling, H., Killeen, T. J., Laurance, W. F., Laurance, S., Licona, J.,  
1959 Magnussen, W. E., Marimon, B. S., Marimon-Junior, B. H., Mendoza, C., Neill, D. A., Nogueira, E. M., Núñez,  
1960 P., Pallqui Camacho, N. C., Parada, A., Pardo-Molina, G., Peacock, J., Peña-Claros, M., Pickavance, G. C.,  
1961 Pitman, N. C. A., Poorter, L., Prieto, A., Quesada, C. A., Ramírez, F., Ramírez-Angulo, H., Restrepo, Z.,  
1962 Roopsind, A., Rudas, A., Salomão, R. P., Schwarz, M., Silva, N., Silva-Espejo, J. E., Silveira, M., Stropp, J.,  
1963 Talbot, J., ter Steege, H., Teran-Aguilar, J., Terborgh, J., Thomas-Caesar, R., Toledo, M., Torello-Raventos, M.,  
1964 Umetsu, R. K., van der Heijden, G. M. F., van der Hout, P., Guimarães Vieira, I. C., Vieira, S. A., Vilanova, E.,  
1965 Vos, V. A., and Zagt, R. J.: Long-term decline of the Amazon carbon sink, 519, 344–348,  
1966 <https://doi.org/10.1038/nature14283>, 2015.
- 1967 Broecker, W. S.: Ocean chemistry during glacial time, *Geochimica et Cosmochimica Acta*, 46, 1689–1705,  
1968 [https://doi.org/10.1016/0016-7037\(82\)90110-7](https://doi.org/10.1016/0016-7037(82)90110-7), 1982.

Deleted: .

Deleted: <https://doi.org/10.1038/s41467-022-27979-5>,

- 1971 Bruno, M. and Joos, F.: Terrestrial carbon storage during the past 200 years: A Monte Carlo Analysis of CO<sub>2</sub>  
 1972 data from ice core and atmospheric measurements, *Global Biogeochem. Cycles*, 11, 111–124,  
 1973 <https://doi.org/10.1029/96GB03611>, 1997.
- 1974 Buitenhuis, E. T., Hashioka, T., and Quéré, C. L.: Combined constraints on global ocean primary production  
 1975 using observations and models: OCEAN PRIMARY PRODUCTION, *Global Biogeochem. Cycles*, 27, 847–  
 1976 858, <https://doi.org/10.1002/gbc.20074>, 2013.
- 1977 Burton, C., Betts, R., Cardoso, M., Feldpausch, T. R., Harper, A., Jones, C. D., Kelley, D. I., Robertson, E., and  
 1978 Wiltshire, A.: Representation of fire, land-use change and vegetation dynamics in the Joint UK Land  
 1979 Environment Simulator vn4.9 (JULES), *Geosci. Model Dev.*, 12, 179–193, [https://doi.org/10.5194/gmd-12-179-](https://doi.org/10.5194/gmd-12-179-2019)  
 1980 2019, 2019.
- 1981 Bushinsky, S. M., Landschützer, P., Rödenbeck, C., Gray, A. R., Baker, D., Mazloff, M. R., Resplandy, L.,  
 1982 Johnson, K. S., and Sarmiento, J. L.: Reassessing Southern Ocean Air-Sea CO<sub>2</sub> Flux Estimates With the  
 1983 Addition of Biogeochemical Float Observations, *Global Biogeochem. Cycles*, 33, 1370–1388,  
 1984 <https://doi.org/10.1029/2019GB006176>, 2019.
- 1985 Canadell, J. G., Le Quere, C., Raupach, M. R., Field, C. B., Buitenhuis, E. T., Ciais, P., Conway, T. J., Gillett,  
 1986 N. P., Houghton, R. A., and Marland, G.: Contributions to accelerating atmospheric CO<sub>2</sub> growth from economic  
 1987 activity, carbon intensity, and efficiency of natural sinks, *Proceedings of the National Academy of Sciences*,  
 1988 104, 18866–18870, <https://doi.org/10.1073/pnas.0702737104>, 2007.
- 1989 Canadell, J. G., Monteiro, P. M. S., Costa, M. H., Cotrim da Cunha, L., Cox, P. M., Eliseev, A. V., Henson, S.,  
 1990 Ishii, M., Jaccard, S., Koven, C., Lohila, A., Patra, P. K., Piao, S., Rogelj, J., Syampungani, S., Zaehle, S., and  
 1991 Zickfeld, K.: Global Carbon and other Biogeochemical Cycles and Feedbacks. In: *Climate Change 2021: The*  
 1992 *Physical Science Basis. Contribution of Working Group I to the Sixth Assessment Report of the*  
 1993 *Intergovernmental Panel on Climate Change* [Masson-Delmotte, V., P. Zhai, A. Pirani, S. L. Connors, C. Péan,  
 1994 S. Berger, N. Caud, Y. Chen, L. Goldfarb, M. I. Gomis, M. Huang, K. Leitzell, E. Lonnoy, J.B.R. Matthews, T.  
 1995 K. Maycock, T. Waterfield, O. Yelekçi, R. Yu and B. Zhou (eds.)]. Cambridge University Press, 2021.
- 1996 Cao, Z., Myers, R. J., Lupton, R. C., Duan, H., Sacchi, R., Zhou, N., Reed Miller, T., Cullen, J. M., Ge, Q., and  
 1997 Liu, G.: The sponge effect and carbon emission mitigation potentials of the global cement cycle, *Nat Commun.*,  
 1998 11, 3777, <https://doi.org/10.1038/s41467-020-17583-w>, 2020.
- 1999 Carbon Monitor: CO<sub>2</sub> Emissions Variation, available at: <https://carbonmonitor.org/>, last access: 25 September  
 2000 2022., 2022.
- 2001 Chatfield, C.: The Holt-Winters Forecasting Procedure, 27, 264–279, <https://doi.org/10.2307/2347162>, 1978.
- 2002 Chau, T. T. T., Gehlen, M., and Chevallier, F.: QUALITY INFORMATION DOCUMENT for Global Ocean  
 2003 Surface Carbon Product MULTIOBS\_GLO\_BIO\_CARBON\_SURFACE\_REP\_015\_008, Le Laboratoire des  
 2004 Sciences du Climat et de l'Environnement, 2020.

2005 Chau, T. T. T., Gehlen, M., and Chevallier, F.: A seamless ensemble-based reconstruction of surface ocean  
2006  $p\text{CO}_2$  and air–sea  $\text{CO}_2$  fluxes over the global coastal and open oceans, *Biogeosciences*, 19, 1087–1109,  
2007 <https://doi.org/10.5194/bg-19-1087-2022>, 2022.

2008 Chevallier, F.: On the parallelization of atmospheric inversions of  $\text{CO}_2$  surface fluxes within a variational  
2009 framework, 6, 783–790, <https://doi.org/10.5194/gmd-6-783-2013>, 2013.

2010 Chevallier, F., Fisher, M., Peylin, P., Serrar, S., Bousquet, P., Bréon, F.-M., Chédin, A., and Ciais, P.: Inferring  
2011  $\text{CO}_2$  sources and sinks from satellite observations: Method and application to TOVS data, *J. Geophys. Res.*,  
2012 110, D24309, <https://doi.org/10.1029/2005JD006390>, 2005.

2013 Chevallier, F., Remaud, M., O'Dell, C. W., Baker, D., Peylin, P., and Cozic, A.: Objective evaluation of  
2014 surface- and satellite-driven carbon dioxide atmospheric inversions, *Atmos. Chem. Phys.*, 19, 14233–14251,  
2015 <https://doi.org/10.5194/acp-19-14233-2019>, 2019.

2016 Chini, L., Hurtt, G., Sahajpal, R., Frohling, S., Klein Goldewijk, K., Sitch, S., Ganzenmüller, R., Ma, L., Ott, L.,  
2017 Pongratz, J., and Poulter, B.: Land-use harmonization datasets for annual global carbon budgets, 13, 4175–4189,  
2018 <https://doi.org/10.5194/essd-13-4175-2021>, 2021.

2019 Ciais, P., Sabine, C., Bala, G., Bopp, L., Brovkin, V., Canadell, J. G., Chhabra, A., DeFries, R., Galloway, J.,  
2020 Heimann, M., Jones, C., Le Quéré, C., Myneni, R., Piao, S., Thornton, P., Willem, J., Friedlingstein, P., and  
2021 Munhoven, G.: Carbon and Other Biogeochemical Cycles, in *Climate Change 2013: The Physical Science  
2022 Basis, Contribution of Working Group I to the Fifth Assessment Report of the Intergovernmental Panel on  
2023 Climate Change*, edited by: Intergovernmental Panel on Climate Change, Cambridge University Press,  
2024 Cambridge, UK, 465–570, 2013.

2025 Ciais, P., Tan, J., Wang, X., Roedenbeck, C., Chevallier, F., Piao, S.-L., Moriarty, R., Broquet, G., Le Quéré, C.,  
2026 Canadell, J. G., Peng, S., Poulter, B., Liu, Z., and Tans, P.: Five decades of northern land carbon uptake  
2027 revealed by the interhemispheric  $\text{CO}_2$  gradient, *Nature*, 568, 221–225, [https://doi.org/10.1038/s41586-019-  
1078-6](https://doi.org/10.1038/s41586-019-<br/>
2028 1078-6), 2019.

2029 Ciais, P., Bastos, A., Chevallier, F., Lauerwald, R., Poulter, B., Canadell, P., Hugelius, G., Jackson, R. B., Jain,  
2030 A., Jones, M., Kondo, M., Luijkx, I. T., Patra, P. K., Peters, W., Pongratz, J., Petrescu, A. M. R., Piao, S., Qiu,  
2031 C., Von Randow, C., Regnier, P., Saunois, M., Scholes, R., Shvidenko, A., Tian, H., Yang, H., Wang, X., and  
2032 Zheng, B.: Definitions and methods to estimate regional land carbon fluxes for the second phase of the REgional  
2033 Carbon Cycle Assessment and Processes Project (RECCAP-2), *Geosci. Model Dev.*, 15, 1289–1316,  
2034 <https://doi.org/10.5194/gmd-15-1289-2022>, 2022.

2035 Collier, N., Hoffman, F. M., Lawrence, D. M., Keppel-Aleks, G., Koven, C. D., Riley, W. J., Mu, M., and  
2036 Randerson, J. T.: The International Land Model Benchmarking (ILAMB) System: Design, Theory, and  
2037 Implementation, *J. Adv. Model. Earth Syst.*, 10, 2731–2754, <https://doi.org/10.1029/2018MS001354>, 2018.

2038 Conchedda, G. and Tubiello, F. N.: Drainage of organic soils and GHG emissions: Validation with country data,  
2039 *Biosphere – Biogeosciences*, <https://doi.org/10.5194/essd-2020-202>, 2020.

Deleted: 1–46

Deleted: 2020-259, 2020

2042 Cooper, D. J., Watson, A. J., and Ling, R. D.: Variation of pCO<sub>2</sub> along a North Atlantic shipping route (U.K. to  
2043 the Caribbean): A year of automated observations, *Marine Chemistry*, 60, 147–164,  
2044 [https://doi.org/10.1016/S0304-4203\(97\)00082-0](https://doi.org/10.1016/S0304-4203(97)00082-0), 1998.

2045 Cox, A., Vermeulen, A., Manning, A., Beyersdorf, A., Zahn, A., Manning, A., Watson, A., Karion, A., Hensen,  
2046 A., Arlyn Andrews, Frumau, A., Colomb, A., Scheeren, B., Law, B., Baier, B., Munger, B., Paplawsky, B.,  
2047 Viner, B., Stephens, B., Daube, B., Labuschagne, C., Myhre, C. L., Hanson, C., Miller, C. E., Plass-Duelmer,  
2048 C., Plass-Duelmer, C., Gerbig, C., Sloop, C. D., Sweeney, C., Kubistin, D., Goto, D., Jaffe, D., Say, D., Van  
2049 Dinter, D., Bowling, D., Lam, D. H. Y., Dickon Young, Worthy, D., Dlugokencky, E., Kozlova, E., Gloor, E.,  
2050 Cuevas, E., Reyes-Sanchez, E., Hintsa, E., Kort, E., Morgan, E., Obersteiner, F., Apadula, F., Francois Gheusi,  
2051 Meinhardt, F., Moore, F., Vitkova, G., Chen, G., Bentz, G., Manca, G., Brailsford, G., Forster, G., Boenisch, H.,  
2052 Riris, H., Meijer, H., Timas, H., Matsueda, H., Huilin Chen, Levin, I., Lehner, I., Mammarella, I., Bartyzel, J.,  
2053 Abshire, J. B., Elkins, J. W., Levula, J., Jaroslaw Necki, Pichon, J. M., Peischl, J., Müller-Williams, J., Turnbull,  
2054 J., Miller, J. B., Lee, J., Lin, J., Josep-Anton Morgui, DiGangi, J. P., Hatakka, J., Coletta, J. D., Worsley, J.,  
2055 Holst, J., Kominkova, K., McKain, K., Saito, K., Aikin, K., Davis, K., Thoning, K., Tørseth, K., Haszpra, L.,  
2056 Mitchell, L., Gatti, L. V., Emmenegger, L., Lukasz Chmura, Merchant, L., Sha, M. K., Delmotte, M., et al.:  
2057 Multi-laboratory compilation of atmospheric carbon dioxide data for the period 1957-2019;  
2058 `obspack_co2_1_GLOBALVIEWplus_v6.1_2021-03-01`, <https://doi.org/10.25925/20201204>, 2021.

2059 Cox, P. M., Pearson, D., Booth, B. B., Friedlingstein, P., Huntingford, C., Jones, C. D., and Luke, C. M.:  
2060 Sensitivity of tropical carbon to climate change constrained by carbon dioxide variability, *Nature*, 494, 341–344,  
2061 <https://doi.org/10.1038/nature11882>, 2013.

2062 Crippa, M., Janssens-Maenhout, G., Guizzardi, D., Van Dingenen, R., and Dentener, F.: Contribution and  
2063 uncertainty of sectorial and regional emissions to regional and global PM<sub>2.5</sub> health impacts, 19, 5165–5186,  
2064 <https://doi.org/10.5194/acp-19-5165-2019>, 2019.

2065 Dai, A. and Trenberth, K. E.: Estimates of Freshwater Discharge from Continents: Latitudinal and Seasonal  
2066 Variations, 3, 660–687, [https://doi.org/10.1175/1525-7541\(2002\)003<0660:EOFDFC>2.0.CO;2](https://doi.org/10.1175/1525-7541(2002)003<0660:EOFDFC>2.0.CO;2), 2002.

2067 Davis, S. J. and Caldeira, K.: Consumption-based accounting of CO<sub>2</sub> emissions, *Proceedings of the National  
2068 Academy of Sciences*, 107, 5687–5692, <https://doi.org/10.1073/pnas.0906974107>, 2010.

2069 De Kauwe, M. G., Disney, M. I., Quaife, T., Lewis, P., and Williams, M.: An assessment of the MODIS  
2070 collection 5 leaf area index product for a region of mixed coniferous forest, *Remote Sensing of Environment*,  
2071 115, 767–780, <https://doi.org/10.1016/j.rse.2010.11.004>, 2011.

2072 De Kauwe, M. G., Medlyn, B. E., Zaehle, S., Walker, A. P., Dietze, M. C., Wang, Y.-P., Luo, Y., Jain, A. K.,  
2073 El-Masri, B., Hickler, T., Wårlind, D., Weng, E., Parton, W. J., Thornton, P. E., Wang, S., Prentice, I. C., Asao,  
2074 S., Smith, B., McCarthy, H. R., Iversen, C. M., Hanson, P. J., Warren, J. M., Oren, R., and Norby, R. J.: Where  
2075 does the carbon go? A model–data intercomparison of vegetation carbon allocation and turnover processes at  
2076 two temperate forest free-air CO<sub>2</sub> enrichment sites, *New Phytol.*, 203, 883–899,  
2077 <https://doi.org/10.1111/nph.12847>, 2014.

2078 Decharme, B., Delire, C., Minvielle, M., Colin, J., Vergnes, J.-P., Alias, A., Saint-Martin, D., Séférian, R.,  
2079 Sénési, S., and Voldoire, A.: Recent Changes in the ISBA-CTRIP Land Surface System for Use in the CNRM-  
2080 CM6 Climate Model and in Global Off-Line Hydrological Applications, 11, 1207–1252,  
2081 <https://doi.org/10.1029/2018MS001545>, 2019.

2082 Delire, C., Séférian, R., Decharme, B., Alkama, R., Calvet, J.-C., Carrer, D., Gibelin, A.-L., Joetzier, E., Morel,  
2083 X., Rocher, M., and Tzanos, D.: The Global Land Carbon Cycle Simulated With ISBA-CTRIP: Improvements  
2084 Over the Last Decade, 12, e2019MS001886, <https://doi.org/10.1029/2019MS001886>, 2020.

2085 Denman, K. L., Brasseur, G., Chidthaisong, A., Ciais, P., Cox, P. M., Dickinson, R. E., Hauglustaine, D.,  
2086 Heinze, C., Holland, E., Jacob, D., Lohmann, U., Ramachandran, S., Leite da Silva Dias, P., Wofsy, S. C., and  
2087 Zhang, X.: Couplings Between Changes in the Climate System and Biogeochemistry, in: *Climate Change 2007:  
2088 The Physical Science Basis. Contribution of Working Group I to the Fourth Assessment Report of the  
2089 Intergovernmental Panel on Climate Change*, edited by: Solomon, S., Qin, D., Manning, M., Marquis, M.,  
2090 Averyt, K., Tignor, M. M. B., Miller, H. L., and Chen, Z. L., Cambridge University Press, Cambridge, UK and  
2091 New York, USA, 499–587, 2007.

2092 Denning, A. S., Fung, I. Y., and Randall, D.: Latitudinal gradient of atmospheric CO<sub>2</sub> due to seasonal exchange  
2093 with land biota, *Nature*, 376, 240–243, <https://doi.org/10.1038/376240a0>, 1995.

2094 Denvil-Sommer, A., Gehlen, M., Vrac, M., and Mejia, C.: LSCE-FFNN-v1: a two-step neural network model  
2095 for the reconstruction of surface ocean pCO<sub>2</sub> over the global ocean, 12, 2091–2105,  
2096 <https://doi.org/10.5194/gmd-12-2091-2019>, 2019.

2097 DeVries, T.: The oceanic anthropogenic CO<sub>2</sub> sink: Storage, air-sea fluxes, and transports over the industrial  
2098 era, *Global Biogeochem. Cycles*, 28, 631–647, <https://doi.org/10.1002/2013GB004739>, 2014.

2099 DeVries, T., Holzer, M., and Primeau, F.: Recent increase in oceanic carbon uptake driven by weaker upper-  
2100 ocean overturning, *Nature*, 542, 215–218, <https://doi.org/10.1038/nature21068>, 2017.

2101 DeVries, T., Quéré, C. L., Andrews, O., Berthet, S., Hauck, J., Ilyina, T., Landschützer, P., Lenton, A., Lima, I.  
2102 D., Nowicki, M., Schwinger, J., and Séférian, R.: Decadal trends in the ocean carbon sink, *PNAS*, 116, 11646–  
2103 11651, <https://doi.org/10.1073/pnas.1900371116>, 2019.

2104 Di Sarra, A. G., Karion, A., Arlyn Andrews, Colomb, A., Scheeren, B., Viner, B., Myhre, C. L., Miller, C. E.,  
2105 Plass-Duelmer, C., Plass-Duelmer, C., Sloop, C. D., Sweeney, C., Kubistin, D., Jaffe, D., Dlugokencky, E.,  
2106 Vitkova, G., Manca, G., Huilin Chen, Lehner, I., Mammarella, I., Pichon, J. M., Müller-Williams, J., Miller, J.  
2107 B., Lee, J., Hatakka, J., Holst, J., Kominkova, K., McKain, K., Thoning, K., Tørseth, K., Emmenegger, L., Sha,  
2108 M. K., Delmotte, M., Fischer, M. L., Schumacher, M., Leuenberger, M., Steinbacher, M., De Mazière, M.,  
2109 Lindauer, M., Mölder, M., Heliasz, M., Marek, M. V., Ramonet, M., Lopez, M., Laurent, O., Hermanssen, O.,  
2110 Trisolino, P., Cristofanelli, P., Smith, P., Bakwin, P., Bergamaschi, P., Keronen, P., Tans, P., Piacentino, S.,  
2111 Biraud, S. C., Conil, S., De Wekker, S., Biermann, T., Laurila, T., Aalto, T., and Kazan, V.: Multi-laboratory  
2112 compilation of atmospheric carbon dioxide data for the years 2020-2021; *obspace\_co2\_1\_NRT\_v6.1.1\_2021-*  
2113 *05-17*, <https://doi.org/10.25925/20210517>, 2021.

2114 Dickson, A. G., Sabine, C. L., and Christian, J. R.: Guide to best practices for ocean CO<sub>2</sub> measurement. Sidney,  
 2115 British Columbia, North Pacific Marine Science Organization, 191pp. (PICES Special Publication 3; IOCCP  
 2116 Report 8). DOI: <https://doi.org/10.25607/OBP-1342>, 2007.

2117 Dlugokencky, E. and Tans, P.: Trends in atmospheric carbon dioxide, National Oceanic and Atmospheric  
 2118 Administration, [Global Monitoring Laboratory \(NOAA/GML\)](https://www.gml.noaa.gov/gmd/ccgg/trends/global.html), available at:  
 2119 <http://www.gml.noaa.gov/gmd/ccgg/trends/global.html>, accessed: 16 November 2020., 2020.

2120 Dlugokencky, E. and Tans, P.: Trends in atmospheric carbon dioxide, National Oceanic and Atmospheric  
 2121 Administration, [Global Monitoring Laboratory \(NOAA/GML\)](https://www.gml.noaa.gov/gmd/ccgg/trends/global.html), available at:  
 2122 <http://www.gml.noaa.gov/gmd/ccgg/trends/global.html>, last access: 25 September 2022., 2022.

2123 Doney, S. C., Lima, I., Feely, R. A., Glover, D. M., Lindsay, K., Mahowald, N., Moore, J. K., and Wanninkhof,  
 2124 R.: Mechanisms governing interannual variability in upper-ocean inorganic carbon system and air–sea CO<sub>2</sub>  
 2125 fluxes: Physical climate and atmospheric dust, *Deep Sea Research Part II: Topical Studies in Oceanography*, 56,  
 2126 640–655, <https://doi.org/10.1016/j.dsr2.2008.12.006>, 2009.

2127 Dong, Y., Bakker, D. C. E., Bell, T. G., Huang, B., Landschützer, P., Liss, P. S., and Yang, M.: Update on the  
 2128 Temperature Corrections of Global Air–Sea CO<sub>2</sub> Flux Estimates, *Glob. Biogeochem. Cycles*, 36,  
 2129 e2022GB007360, <https://doi.org/10.1029/2022GB007360>, 2022.

2130 Dou, X., Wang, Y., Ciaia, P., Chevallier, F., Davis, S. J., Crippa, M., Janssens-Maenhout, G., Guizzardi, D.,  
 2131 Solazzo, E., Yan, F., Huo, D., Zheng, B., Zhu, B., Cui, D., Ke, P., Sun, T., Wang, H., Zhang, Q., Gentine, P.,  
 2132 Deng, Z., and Liu, Z.: Near-real-time global gridded daily CO<sub>2</sub> emissions, *The Innovation*, 3, 100182,  
 2133 <https://doi.org/10.1016/j.xinn.2021.100182>, 2022.

2134 Duce, R. A., LaRoche, J., Altieri, K., Arrigo, K. R., Baker, A. R., Capone, D. G., Cornell, S., Dentener, F.,  
 2135 Galloway, J., Ganeshram, R. S., Geider, R. J., Jickells, T., Kuypers, M. M., Langlois, R., Liss, P. S., Liu, S. M.,  
 2136 Middelburg, J. J., Moore, C. M., Nickovic, S., Oschlies, A., Pedersen, T., Prospero, J., Schlitzer, R., Seitzinger,  
 2137 S., Sorensen, L. L., Uematsu, M., Ulloa, O., Voss, M., Ward, B., and Zamora, L.: Impacts of Atmospheric  
 2138 Anthropogenic Nitrogen on the Open Ocean, *Science*, 320, 893–897, <https://doi.org/10.1126/science.1150369>,  
 2139 2008.

2140 Dufour, C. O., Sommer, J. L., Gehlen, M., Orr, J. C., Molines, J., Simeon, J., and Barnier, B.: Eddy  
 2141 compensation and controls of the enhanced sea-to-air CO<sub>2</sub> flux during positive phases of the Southern Annular  
 2142 Mode, *Global Biogeochem. Cycles*, 27, 950–961, <https://doi.org/10.1002/gbc.20090>, 2013.

2143 Eakins, B. W. and Sharman, G. F.: National Geophysical Data Center: Volumes of the World’s Oceans from  
 2144 ETOPO1, available at: [https://www.ngdc.noaa.gov/mgg/global/etopo1\\_ocean\\_volumes.html](https://www.ngdc.noaa.gov/mgg/global/etopo1_ocean_volumes.html), last access: 25  
 2145 September 2022, U.S. Department of Commerce, 2010.

2146 Eggleston, H. S., Buendia, L., Miwa, K., Ngara, T., and Tanabe, K.: Volume 4: Agriculture, forestry and land  
 2147 use. in: 2006 IPCC guidelines for national greenhouse gas inventories., 2006.

2148 EIA: U.S. Energy Information Administration: Short-Term Energy Outlook, available at:

Deleted: Earth System Research

Deleted: ESRL

Deleted: esrl

Deleted: Earth System Research

Deleted: ESRL

Deleted: esrl

- 2155 <http://www.eia.gov/forecasts/steo/outlook>, last access: 25 September 2022., 2022.
- 2156 Erb, K.-H., Kastner, T., Luysaert, S., Houghton, R. A., Kuemmerle, T., Olofsson, P., and Haberl, H.: Bias in  
2157 the attribution of forest carbon sinks, *Nature Clim Change*, 3, 854–856, <https://doi.org/10.1038/nclimate2004>,  
2158 2013.
- 2159 Erb, K.-H., Kastner, T., Plutzer, C., Bais, A. L. S., Carvalhais, N., Fetzel, T., Gingrich, S., Haberl, H., Lauk, C.,  
2160 Niederscheider, M., Pongratz, J., Thurner, M., and Luysaert, S.: Unexpectedly large impact of forest  
2161 management and grazing on global vegetation biomass, *Nature*, 553, 73–76,  
2162 <https://doi.org/10.1038/nature25138>, 2018.
- 2163 Eskander, S. M. S. U. and Fankhauser, S.: Reduction in greenhouse gas emissions from national climate  
2164 legislation, *Nat. Clim. Chang.*, 10, 750–756, <https://doi.org/10.1038/s41558-020-0831-z>, 2020.
- 2165 Etheridge, D. M., Steele, L. P., Langenfelds, R. L., Francey, R. J., Barnola, J.-M., and Morgan, V. I.: Natural  
2166 and anthropogenic changes in atmospheric CO<sub>2</sub> over the last 1000 years from air in Antarctic ice and firn, *J.*  
2167 *Geophys. Res.*, 101, 4115–4128, <https://doi.org/10.1029/95JD03410>, 1996.
- 2168 Eyring, V., Bony, S., Meehl, G. A., Senior, C. A., Stevens, B., Stouffer, R. J., and Taylor, K. E.: Overview of  
2169 the Coupled Model Intercomparison Project Phase 6 (CMIP6) experimental design and organization, *Geosci.*  
2170 *Model Dev.*, 9, 1937–1958, <https://doi.org/10.5194/gmd-9-1937-2016>, 2016.
- 2171 FAO: Global Forest Resources Assessment 2020: Main report, FAO, Rome, Italy, 184 pp.,  
2172 <https://doi.org/10.4060/ca9825en>, 2020.
- 2173 FAO: FAOSTAT Statistical Database, domains Climate Change, available at:  
2174 <http://www.fao.org/faostat/en/#data/GT>, last access: 25 September 2022, 2021.
- 2175 FAOSTAT: FAOSTAT: Food and Agriculture Organization Statistics Division, available at:  
2176 <http://faostat.fao.org/>, last access: 25 September 2022), 2021.
- 2177 FAO/UNEP: Food and Agriculture Organisation / United Nations Environment Programme: The state of food  
2178 and agriculture 1981, available at: <https://www.fao.org/3/ap661e/ap661e.pdf>, last access: 25 September 2022,  
2179 1981.
- 2180 Fan, L., Wigneron, J.-P., Ciais, P., Chave, J., Brandt, M., Fensholt, R., Saatchi, S. S., Bastos, A., Al-Yaari, A.,  
2181 Hufkens, K., Qin, Y., Xiao, X., Chen, C., Myneni, R. B., Fernandez-Moran, R., Mialon, A., Rodriguez-  
2182 Fernandez, N. J., Kerr, Y., Tian, F., and Peñuelas, J.: Satellite-observed pantropical carbon dynamics, *Nat.*  
2183 *Plants*, 5, 944–951, <https://doi.org/10.1038/s41477-019-0478-9>, 2019.
- 2184 Fay, A. R. and McKinley, G. A.: Global open-ocean biomes: mean and temporal variability, 6, 273–284,  
2185 <https://doi.org/10.5194/essd-6-273-2014>, 2014.
- 2186 Fay, A. R., Gregor, L., Landschützer, P., McKinley, G. A., Gruber, N., Gehlen, M., Iida, Y., Laruelle, G. G.,  
2187 Rödenbeck, C., and Zeng, J.: Harmonization of global surface ocean pCO<sub>2</sub> mapped products and their flux

2188 calculations; an improved estimate of the ocean carbon sink, 1–32, <https://doi.org/10.5194/essd-2021-16>, 2021a.

2189 Fay, A. R., Gregor, L., Landschützer, P., McKinley, G. A., Gruber, N., Gehlen, M., Iida, Y., Laruelle, G. G.,  
 2190 Rödenbeck, C., Roobaert, A., and Zeng, J.: SeaFlux: harmonization of air–sea CO<sub>2</sub> fluxes from surface pCO<sub>2</sub>  
 2191 data products using a standardized approach, 13, 4693–4710, <https://doi.org/10.5194/essd-13-4693-2021>, 2021b.

2192 Feng, L., Palmer, P. I., Bosch, H., and Dance, S.: Estimating surface CO<sub>2</sub> fluxes from space-borne CO<sub>2</sub> dry air  
 2193 mole fraction observations using an ensemble Kalman Filter, 15, 2009.

2194 Feng, L., Palmer, P. I., Parker, R. J., Deutscher, N. M., Feist, D. G., Kivi, R., Morino, I., and Sussmann, R.:  
 2195 Estimates of European uptake of CO<sub>2</sub> inferred from GOSAT XCO<sub>2</sub> retrievals: sensitivity to measurement bias  
 2196 inside and outside Europe, *Atmos. Chem. Phys.*, 16, 1289–1302, <https://doi.org/10.5194/acp-16-1289-2016>,  
 2197 2016.

2198 Feng, Y., Zeng, Z., Searchinger, T. D., Ziegler, A. D., Wu, J., Wang, D., He, X., Elsen, P. R., Ciais, P., Xu, R.,  
 2199 Guo, Z., Peng, L., Tao, Y., Spracklen, D. V., Holden, J., Liu, X., Zheng, Y., Xu, P., Chen, J., Jiang, X., Song,  
 2200 X.-P., Lakshmi, V., Wood, E. F., and Zheng, C.: Doubling of annual forest carbon loss over the tropics during  
 2201 the early twenty-first century, *Nat. Sustain.*, 1–8, <https://doi.org/10.1038/s41893-022-00854-3>, 2022.

2202 Friedlingstein, P., Houghton, R. A., Marland, G., Hackler, J., Boden, T. A., Conway, T. J., Canadell, J. G.,  
 2203 Raupach, M. R., Ciais, P., and Le Quéré, C.: Update on CO<sub>2</sub> emissions, *Nature Geosci*, 3, 811–812,  
 2204 <https://doi.org/10.1038/ngeo1022>, 2010.

2205 Friedlingstein, P., Andrew, R. M., Rogelj, J., Peters, G. P., Canadell, J. G., Knutti, R., Luderer, G., Raupach, M.  
 2206 R., Schaeffer, M., van Vuuren, D. P., and Le Quéré, C.: Persistent growth of CO<sub>2</sub> emissions and implications  
 2207 for reaching climate targets, *Nature Geosci*, 7, 709–715, <https://doi.org/10.1038/ngeo2248>, 2014.

2208 Friedlingstein, P., Jones, M. W., O’Sullivan, M., Andrew, R. M., Hauck, J., Peters, G. P., Peters, W., Pongratz,  
 2209 J., Sitoh, S., Le Quéré, C., Bakker, D. C. E., Canadell, J. G., Ciais, P., Jackson, R. B., Anthoni, P., Barbero, L.,  
 2210 Bastos, A., Bastrikov, V., Becker, M., Bopp, L., Buitenhuis, E., Chandra, N., Chevallier, F., Chini, L. P., Currie,  
 2211 K. I., Feely, R. A., Gehlen, M., Gilfillan, D., Gkritzalis, T., Goll, D. S., Gruber, N., Gutekunst, S., Harris, I.,  
 2212 Haverd, V., Houghton, R. A., Hurtt, G., Ilyina, T., Jain, A. K., Joetzjer, E., Kaplan, J. O., Kato, E., Klein  
 2213 Goldewijk, K., Korsbakken, J. I., Landschützer, P., Lauvset, S. K., Lefèvre, N., Lenton, A., Lienert, S.,  
 2214 Lombardozi, D., Marland, G., McGuire, P. C., Melton, J. R., Metzl, N., Munro, D. R., Nabel, J. E. M. S.,  
 2215 Nakaoka, S.-I., Neill, C., Omar, A. M., Ono, T., Peregon, A., Pierrot, D., Poulter, B., Rehder, G., Resplandy, L.,  
 2216 Robertson, E., Rödenbeck, C., Séférian, R., Schwinger, J., Smith, N., Tans, P. P., Tian, H., Tilbrook, B.,  
 2217 Tubiello, F. N., van der Werf, G. R., Wiltshire, A. J., and Zaehle, S.: Global Carbon Budget 2019, *Earth Syst.*  
 2218 *Sci. Data*, 11, 1783–1838, <https://doi.org/10.5194/essd-11-1783-2019>, 2019.

2219 Friedlingstein, P., O’Sullivan, M., Jones, M. W., Andrew, R. M., Hauck, J., Olsen, A., Peters, G. P., Peters, W.,  
 2220 Pongratz, J., Sitoh, S., Le Quéré, C., Canadell, J. G., Ciais, P., Jackson, R. B., Alin, S., Aragão, L. E. O. C.,  
 2221 Armeth, A., Arora, V., Bates, N. R., Becker, M., Benoit-Cattin, A., Bittig, H. C., Bopp, L., Bultan, S., Chandra,  
 2222 N., Chevallier, F., Chini, L. P., Evans, W., Florentie, L., Forster, P. M., Gasser, T., Gehlen, M., Gilfillan, D.,  
 2223 Gkritzalis, T., Gregor, L., Gruber, N., Harris, I., Hartung, K., Haverd, V., Houghton, R. A., Ilyina, T., Jain, A.

2224 K., Joetzier, E., Kadono, K., Kato, E., Kitidis, V., Korsbakken, J. I., Landschützer, P., Lefèvre, N., Lenton, A.,  
2225 Lienert, S., Liu, Z., Lombardozzi, D., Marland, G., Metz, N., Munro, D. R., Nabel, J. E. M. S., Nakaoka, S.-I.,  
2226 Niwa, Y., O'Brien, K., Ono, T., Palmer, P. I., Pierrot, D., Poulter, B., Resplandy, L., Robertson, E., Rödenbeck,  
2227 C., Schwinger, J., Séférian, R., Skjelvan, I., Smith, A. J. P., Sutton, A. J., Tanhua, T., Tans, P. P., Tian, H.,  
2228 Tilbrook, B., van der Werf, G., Vuichard, N., Walker, A. P., Wanninkhof, R., Watson, A. J., Willis, D.,  
2229 Wiltshire, A. J., Yuan, W., Yue, X., and Zaehle, S.: Global Carbon Budget 2020, *Earth Syst. Sci. Data*, 12,  
2230 3269–3340, <https://doi.org/10.5194/essd-12-3269-2020>, 2020.

2231 Friedlingstein, P., Jones, M. W., O'Sullivan, M., Andrew, R. M., Bakker, D. C. E., Hauck, J., Le Quéré, C.,  
2232 Peters, G. P., Peters, W., Pongratz, J., Sitch, S., Canadell, J. G., Ciais, P., Jackson, R. B., Alin, S. R., Anthoni,  
2233 P., Bates, N. R., Becker, M., Bellouin, N., Bopp, L., Chau, T. T. T., Chevallier, F., Chini, L. P., Cronin, M.,  
2234 Currie, K. I., Decharme, B., Djeutchouang, L. M., Dou, X., Evans, W., Feely, R. A., Feng, L., Gasser, T.,  
2235 Gilfillan, D., Gkritzalis, T., Grassi, G., Gregor, L., Gruber, N., Gürses, Ö., Harris, I., Houghton, R. A., Hurtt, G.  
2236 C., Iida, Y., Ilyina, T., Luijckx, I. T., Jain, A., Jones, S. D., Kato, E., Kennedy, D., Klein Goldewijk, K., Knauer,  
2237 J., Korsbakken, J. I., Körtzinger, A., Landschützer, P., Lauvset, S. K., Lefèvre, N., Lienert, S., Liu, J., Marland,  
2238 G., McGuire, P. C., Melton, J. R., Munro, D. R., Nabel, J. E. M. S., Nakaoka, S.-I., Niwa, Y., Ono, T., Pierrot,  
2239 D., Poulter, B., Rehder, G., Resplandy, L., Robertson, E., Rödenbeck, C., Rosan, T. M., Schwinger, J.,  
2240 Schwingshackl, C., Séférian, R., Sutton, A. J., Sweeney, C., Tanhua, T., Tans, P. P., Tian, H., Tilbrook, B.,  
2241 Tubiello, F., van der Werf, G. R., Vuichard, N., Wada, C., Wanninkhof, R., Watson, A. J., Willis, D., Wiltshire,  
2242 A. J., Yuan, W., Yue, C., Yue, X., Zaehle, S., and Zeng, J.: Global Carbon Budget 2021, *Earth Syst. Sci. Data*,  
2243 14, 1917–2005, <https://doi.org/10.5194/essd-14-1917-2022>, 2022a.

2244 Friedlingstein, P., O'Sullivan, M., Jones, M. W., Andrew, R. M., Gregor, L., Hauck, L., Le Quéré, C., Luijckx, I.  
2245 T., Olsen, A., Peters, G. P., Peters, W., Pongratz, J., Schwingshackl, C., Sitch, S., Canadell, J. G., Ciais, P.,  
2246 Jackson, R. B., Alin, S., Alkama, R., Arneeth, A., Arora, V. K., Bates, N. R., Becker, M., Bellouin, N., Bittig, H.  
2247 C., Bopp, L., Chevallier, F., Chini, L. P., Cronin, M., Evans, W., Falk, S., Feely, R. A., Gasser, T., Gehlen, M.,  
2248 Gkritzalis, T., Gloege, L., Grassi, G., Gruber, N., Gürses, Ö., Harris, I., Hefner, M., Houghton, R. A., Hurtt, G.  
2249 C., Iida, Y., Ilyina, T., Jain, A. T., Jersild, A., Kadono, K., Kato, E., Kennedy, D., Klein Goldewijk, K., Knauer,  
2250 J., Korsbakken, J. I., Landschützer, P., Lefèvre, N., Lindsay, Keith., Liu, J., Marland, G., Mayot, N., McGrath,  
2251 M. J., Metz, N., Monacci, N. M., Munro, D. R., Nakaoka, S.-I., Niwa, Y., O'Brien, K., Ono, T., Palmer, P. I.,  
2252 Pan, N., Pierrot, D., Pockock, K., Poulter, B., Resplandy, L., Robertson, E., Rödenbeck, C., Rodriguez, C.,  
2253 Rosan, T. M., Schwinger, J., Séférian, R., Shutler, J. D., Skjelvan, I., Steinhoff, T., Sun, Q., Sutton, A. J.,  
2254 Sweeney, C., Takao, S., Tanhua, T., Tans, P. P., Tian, X., Tian, H., Tilbrook, B., Tsujino, H., Tubiello, F., van  
2255 der Werf, G. R., Walker, A. P., Wanninkhof, R., Whitehead, C., Wranne, A., Wright, R. M., Yuan, W., Yue, C.,  
2256 Yue, X., Zaehle, S., Zeng, J., Zheng, B. and Zhu, L.: Supplemental data of the Global Carbon Budget 2022,  
2257 ICOS-ERIC Carbon Portal, <https://doi.org/10.18160/GCP-2022>, 2022b.

2258 Ganzenmüller, R., Bultan, S., Winkler, K., Fuchs, R., Zabel, F., and Pongratz, J.: Land-use change emissions  
2259 based on high-resolution activity data substantially lower than previously estimated, *Environ. Res. Lett.*, 17,  
2260 064050, <https://doi.org/10.1088/1748-9326/ac70d8>, 2022.

2261 Gasser, T. and Ciais, P.: A theoretical framework for the net land-to-atmosphere CO<sub>2</sub> flux and its implications

2262 in the definition of "emissions from land-use change", *Earth Syst. Dynam.*, 4, 171–186,  
 2263 <https://doi.org/10.5194/esd-4-171-2013>, 2013.

2264 Gasser, T., Crepin, L., Quilcaille, Y., Houghton, R. A., Ciais, P., and Obersteiner, M.: Historical CO<sub>2</sub> emissions  
 2265 from land use and land cover change and their uncertainty, *Biogeosciences*, 17, 4075–4101,  
 2266 <https://doi.org/10.5194/bg-17-4075-2020>, 2020.

2267 Gaubert, B., Stephens, B. B., Basu, S., Chevallier, F., Deng, F., Kort, E. A., Patra, P. K., Peters, W., Rödenbeck,  
 2268 C., Saeki, T., Schimel, D., Van der Laan-Luijkx, I., Wofsy, S., and Yin, Y.: Global atmospheric CO<sub>2</sub> inverse  
 2269 models converging on neutral tropical land exchange, but disagreeing on fossil fuel and atmospheric growth  
 2270 rate, *Biogeosciences*, 16, 117–134, <https://doi.org/10.5194/bg-16-117-2019>, 2019.

2271 Gaubert, B., Emmons, L. K., Raeder, K., Tilmes, S., Miyazaki, K., Arellano Jr., A. F., Elguindi, N., Granier, C.,  
 2272 Tang, W., Barré, J., Worden, H. M., Buchholz, R. R., Edwards, D. P., Franke, P., Anderson, J. L., Saunio, M.,  
 2273 Schroeder, J., Woo, J.-H., Simpson, I. J., Blake, D. R., Meinardi, S., Wennberg, P. O., Crounse, J., Teng, A.,  
 2274 Kim, M., Dickerson, R. R., He, H., Ren, X., Pusede, S. E., and Diskin, G. S.: Correcting model biases of CO in  
 2275 East Asia: impact on oxidant distributions during KORUS-AQ, 20, 14617–14647, [https://doi.org/10.5194/acp-](https://doi.org/10.5194/acp-20-14617-2020)  
 2276 [20-14617-2020](https://doi.org/10.5194/acp-20-14617-2020), 2020.

2277 GCCA, 2021. Concrete Future: The GCCA 2050 Cement and Concrete Industry Roadmap for Net Zero  
 2278 Concrete, available at: <https://gccassociation.org/concretefuture/>, last access: 2 August 2022.

2279 Giglio, L., Schroeder, W., and Justice, C. O.: The collection 6 MODIS active fire detection algorithm and fire  
 2280 products, *Remote Sensing of Environment*, 178, 31–41, <https://doi.org/10.1016/j.rse.2016.02.054>, 2016.

2281 Gilfillan, D. and Marland, G.: CDIAC-FF: global and national CO<sub>2</sub> emissions from fossil fuel combustion and  
 2282 cement manufacture: 1751–2017, 13, 1667–1680, <https://doi.org/10.5194/essd-13-1667-2021>, 2021.

2283 Gloege, L., McKinley, G. A., Landschützer, P., Fay, A. R., Frölicher, T. L., Fyfe, J. C., Ilyina, T., Jones, S.,  
 2284 Lovenduski, N. S., Rodgers, K. B., Schlunegger, S., and Takano, Y.: Quantifying Errors in Observationally  
 2285 Based Estimates of Ocean Carbon Sink Variability, 35, e2020GB006788,  
 2286 <https://doi.org/10.1029/2020GB006788>, 2021.

2287 Gloege, L., Yan, M., Zheng, T., and McKinley, G. A.: Improved Quantification of Ocean Carbon Uptake by  
 2288 Using Machine Learning to Merge Global Models and pCO<sub>2</sub> Data, *J. Adv. Model. Earth Syst.*, 14,  
 2289 e2021MS002620, <https://doi.org/10.1029/2021MS002620>, 2022.

2290 Goddijn-Murphy, L. M., Woolf, D. K., Land, P. E., Shutler, J. D., and Donlon, C.: The OceanFlux Greenhouse  
 2291 Gases methodology for deriving a sea surface climatology of CO<sub>2</sub> fugacity in support of air–sea gas flux  
 2292 studies, 11, 519–541, <https://doi.org/10.5194/os-11-519-2015>, 2015.

2293 Golar, G., Malik, A., Muis, H., Herman, A., Nurudin, N., and Lukman, L.: The social-economic impact of  
 2294 COVID-19 pandemic: implications for potential forest degradation, *Heliyon*, 6, e05354,  
 2295 <https://doi.org/10.1016/j.heliyon.2020.e05354>, 2020.

2296 Goris, N., Tjiputra, J. F., Olsen, A., Schwinger, J., Lauvset, S. K., [and](#) Jeansson, E.: Constraining Projection-  
2297 Based Estimates of the Future North Atlantic Carbon Uptake, *J. Clim.*, 31, 3959–3978,  
2298 <https://doi.org/10.1175/JCLI-D-17-0564.1>, 2018.

2299 Grassi, G., House, J., Kurz, W. A., Cescatti, A., Houghton, R. A., Peters, G. P., Sanz, M. J., Viñas, R. A.,  
2300 Alkama, R., Arneth, A., Bondeau, A., Dentener, F., Fader, M., Federici, S., Friedlingstein, P., Jain, A. K., Kato,  
2301 E., Koven, C. D., Lee, D., Nabel, J. E. M. S., Nassikas, A. A., Perugini, L., Rossi, S., Sitch, S., Viovy, N.,  
2302 Wiltshire, A., and Zaehle, S.: Reconciling global-model estimates and country reporting of anthropogenic forest  
2303 CO2 sinks, *Nature Clim Change*, 8, 914–920, <https://doi.org/10.1038/s41558-018-0283-x>, 2018.

2304 Grassi, G., Stehfest, E., Rogelj, J., van Vuuren, D., Cescatti, A., House, J., Nabuurs, G.-J., Rossi, S., Alkama,  
2305 R., Viñas, R. A., Calvin, K., Ceccherini, G., Federici, S., Fujimori, S., Gusti, M., Hasegawa, T., Havlik, P.,  
2306 Humpenöder, F., Korosuo, A., Perugini, L., Tubiello, F. N., and Popp, A.: Critical adjustment of land mitigation  
2307 pathways for assessing countries' climate progress, *Nat. Clim. Chang.*, 11, 425–434,  
2308 <https://doi.org/10.1038/s41558-021-01033-6>, 2021.

2309 Grassi, G., Conchedda, G., Federici, S., Abad Viñas, R., Korosuo, A., Melo, J., Rossi, S., Sandker, M.,  
2310 Somogyi, Z., and Tubiello, F. N.: *Carbon fluxes from land 2000–2020: bringing clarity on countries' reporting*,  
2311 *Biogeosciences and biodiversity*, <https://doi.org/10.5194/essd-2022-104>, 2022a.

2312 Grassi, G., Schwingshackl, C., Gasser, T., Houghton, R. A., Sitch, S., Canadell, J. G., Cescatti, A., Ciais, P.,  
2313 Federici, S., Friedlingstein, P., Kurz, W. A., Sanz Sanchez, M. J., Abad Viñas, R., Alkama, R., Ceccherini, G.,  
2314 Kato, E., Kennedy, D., Knauer, J., Korosuo, A., McGrath, M. J., Nabel, J., Poulter, B., Rossi, S., Walker, A. P.,  
2315 Yuan, W., Yue, X., and Pongratz, J.: Mapping land-use fluxes for 2001–2020 from global models to national  
2316 inventories, *ESSD – Land/Land Cover and Land Use*, <https://doi.org/10.5194/essd-2022-245>, 2022b.

2317 Gregg, J. S., Andres, R. J., and Marland, G.: China: Emissions pattern of the world leader in CO2 emissions  
2318 from fossil fuel consumption and cement production, *Geophys. Res. Lett.*, 35, L08806,  
2319 <https://doi.org/10.1029/2007GL032887>, 2008.

2320 Gregor, L. and Gruber, N.: OceanSODA-ETHZ: a global gridded data set of the surface ocean carbonate system  
2321 for seasonal to decadal studies of ocean acidification, 13, 777–808, <https://doi.org/10.5194/essd-13-777-2021>,  
2322 2021.

2323 Gregor, L., Lebehot, A. D., Kok, S., and Scheel Monteiro, P. M.: A comparative assessment of the uncertainties  
2324 of global surface ocean CO2 estimates using a machine-learning ensemble (CSIR-ML6 version 2019a) – have  
2325 we hit the wall?, 12, 5113–5136, <https://doi.org/10.5194/gmd-12-5113-2019>, 2019.

2326 Gruber, N., Gloor, M., Mikaloff Fletcher, S. E., Doney, S. C., Dutkiewicz, S., Follows, M. J., Gerber, M.,  
2327 Jacobson, A. R., Joos, F., Lindsay, K., Menemenlis, D., Mouchet, A., Müller, S. A., Sarmiento, J. L., and  
2328 Takahashi, T.: Oceanic sources, sinks, and transport of atmospheric CO2, 23,  
2329 <https://doi.org/10.1029/2008GB003349>, 2009.

2330 Gruber, N., Clement, D., Carter, B. R., Feely, R. A., van Heuven, S., Hoppema, M., Ishii, M., Key, R. M.,

Deleted: &

Deleted: Journal of Climate,

Deleted: (10),

Deleted: -

Deleted: . Retrieved Sep 25, 2022, from <https://journals.ametsoc.org/view/journals/clim/31/10/jcli-d-17-0564.1.xml>,

Deleted: N.: Carbon Fluxes from Land 2000–2020: Bringing Clarity on Countries' Reporting, *Earth System Science Data*, April. <https://doi.org/https://doi.org/10.5194/essd-2022-104>,

Deleted: Earth Syst. Sci. Data Discuss. [preprint],

Deleted: , in review

2343 Kozyr, A., Lauvset, S. K., Lo Monaco, C., Mathis, J. T., Murata, A., Olsen, A., Perez, F. F., Sabine, C. L.,  
 2344 Tanhua, T., and Wanninkhof, R.: The oceanic sink for anthropogenic CO<sub>2</sub> from 1994 to 2007, 363, 1193–1199,  
 2345 <https://doi.org/10.1126/science.aau5153>, 2019.

2346 Gruère, G. and Brooks, J.: Viewpoint: Characterising early agricultural and food policy responses to the  
 2347 outbreak of COVID-19, *Food Policy*, 100, 102017, <https://doi.org/10.1016/j.foodpol.2020.102017>, 2021.

2348 Guan, D., Liu, Z., Geng, Y., Lindner, S., and Hubacek, K.: The gigatonne gap in China’s carbon dioxide  
 2349 inventories, *Nature Clim Change*, 2, 672–675, <https://doi.org/10.1038/nclimate1560>, 2012.

2350 [Gulev, S. K., Thorne, P. W., Ahn, J., Dentener, F. J., Domingues, C. M., Gerland, S., Gong, D. S., Kaufman, S.,](#)  
 2351 [Nnamchi, H. C., Quaas, J., Rivera, J. A., Sathyendranath, S., Smith, S. J., Trewin, B., von Shuckmann, K., and](#)  
 2352 [Vose, R. S.: Changing State of the Climate System. In: Climate Change 2021: The Physical Science Basis.](#)  
 2353 [Contribution of Working Group I to the Sixth Assessment Report of the Intergovernmental Panel on Climate](#)  
 2354 [Change \[Masson-Delmotte, V., Zhai, P., Pirani, A., Connors, S. L., Péan, C., Berger, S., Caud, N., Chen, Y.,](#)  
 2355 [Goldfarb, L., Gomis, M. I., Huang, M., Leitzell, K., Lonnoy, E., Matthews, J.B.R., Maycock, T.K., Waterfield,](#)  
 2356 [T., Yelekci, O., Yu, R. and Zhou, B. \(eds.\)\]. Cambridge University Press, Cambridge, United Kingdom and](#)  
 2357 [New York, NY, USA, pp. 287–422, doi:10.1017/9781009157896.004, 2021.](#)

2358 Guo, R., Wang, J., Bing, L., Tong, D., Ciais, P., Davis, S. J., Andrew, R. M., Xi, F., and Liu, Z.: Global CO<sub>2</sub>  
 2359 uptake by cement from 1930 to 2019, 13, 1791–1805, <https://doi.org/10.5194/essd-13-1791-2021>, 2021.

2360 Gütschow, J., Jeffery, M. L., Gieseke, R., Gebel, R., Stevens, D., Krapp, M., and Rocha, M.: The PRIMAP-hist  
 2361 national historical emissions time series, 8, 571–603, <https://doi.org/10.5194/essd-8-571-2016>, 2016.

2362 Gütschow, J., Günther, A., and Pflüger, M.: The PRIMAP-hist national historical emissions time series (1750-  
 2363 2019) v2.3.1, <https://doi.org/10.5281/zenodo.5494497>, 2021.

2364 Hall, B. D., Crotwell, A. M., Kitzis, D. R., Mefford, T., Miller, B. R., Schibig, M. F., and Tans, P. P.: Revision  
 2365 of the World Meteorological Organization Global Atmosphere Watch (WMO/GAW) CO<sub>2</sub> calibration scale, 14,  
 2366 3015–3032, <https://doi.org/10.5194/amt-14-3015-2021>, 2021.

2367 Hansen, M. C., Potapov, P. V., Moore, R., Hancher, M., Turubanova, S. A., Tyukavina, A., Thau, D., Stehman,  
 2368 S. V., Goetz, S. J., Loveland, T. R., Kommareddy, A., Egorov, A., Chini, L., Justice, C. O., and Townshend, J.  
 2369 R. G.: High-Resolution Global Maps of 21st-Century Forest Cover Change, *Science*, 342, 850–853,  
 2370 <https://doi.org/10.1126/science.1244693>, 2013.

2371 Hansis, E., Davis, S. J., and Pongratz, J.: Relevance of methodological choices for accounting of land use  
 2372 change carbon fluxes, *Global Biogeochem. Cycles*, 29, 1230–1246, <https://doi.org/10.1002/2014GB004997>,  
 2373 2015.

2374 Harris, I., Jones, P. D., Osborn, T. J., and Lister, D. H.: Updated high-resolution grids of monthly climatic  
 2375 observations - the CRU TS3.10 Dataset, *Int. J. Climatol.*, 34, 623–642, <https://doi.org/10.1002/joc.3711>, 2014.

2376 Harris, I., Osborn, T. J., Jones, P., and Lister, D.: Version 4 of the CRU TS monthly high-resolution gridded

Moved (insertion) [3]

Moved (insertion) [4]

Moved (insertion) [5]

Moved (insertion) [6]

2377 multivariate climate dataset, *Sci Data*, 7, 109, <https://doi.org/10.1038/s41597-020-0453-3>, 2020.

2378 Hauck, J., Zeising, M., Le Quéré, C., Gruber, N., Bakker, D. C. E., Bopp, L., Chau, T. T. T., Gürses, Ö., Ilyina,  
 2379 T., Landschützer, P., Lenton, A., Resplandy, L., Rödenbeck, C., Schwinger, J., and Séférian, R.: Consistency  
 2380 and Challenges in the Ocean Carbon Sink Estimate for the Global Carbon Budget, *Front. Mar. Sci.*, 7, 571720,  
 2381 <https://doi.org/10.3389/fmars.2020.571720>, 2020.

2382 Haverd, V., Smith, B., Nieradzki, L., Briggs, P. R., Woodgate, W., Trudinger, C. M., Canadell, J. G., and Cuntz,  
 2383 M.: A new version of the CABLE land surface model (Subversion revision r4601) incorporating land use and  
 2384 land cover change, woody vegetation demography, and a novel optimisation-based approach to plant  
 2385 coordination of photosynthesis, *Geosci. Model Dev.*, 11, 2995–3026, [https://doi.org/10.5194/gmd-11-2995-](https://doi.org/10.5194/gmd-11-2995-2018)  
 2386 2018, 2018.

2387 Heinimann, A., Mertz, O., Frohling, S., Christensen, A. E., Hurni, K., Sedano, F., Chini, L. P., Sahajpal, R.,  
 2388 Hansen, M., and Hurr, G.: A global view of shifting cultivation: Recent, current, and future extent, *PLOS ONE*,  
 2389 12, e0184479, <https://doi.org/10.1371/journal.pone.0184479>, 2017.

2390 Hertwich, E. G. and Peters, G. P.: Carbon Footprint of Nations: A Global, Trade-Linked Analysis, *Environ. Sci.*  
 2391 *Technol.*, 43, 6414–6420, <https://doi.org/10.1021/es803496a>, 2009.

2392 Hickler, T., Smith, B., Prentice, I. C., Mjöfors, K., Miller, P., Arneth, A., and Sykes, M. T.: CO<sub>2</sub> fertilization in  
 2393 temperate FACE experiments not representative of boreal and tropical forests, 14, 1531–1542,  
 2394 <https://doi.org/10.1111/j.1365-2486.2008.01598.x>, 2008.

2395 Ho, D. T., Wanninkhof, R., Schlosser, P., Ullman, D. S., Hebert, D., and Sullivan, K. F.: Toward a universal  
 2396 relationship between wind speed and gas exchange: Gas transfer velocities measured with 3He/SF<sub>6</sub> during the  
 2397 Southern Ocean Gas Exchange Experiment, 116, <https://doi.org/10.1029/2010JC006854>, 2011.

2398 Hoesly, R. M., Smith, S. J., Feng, L., Klimont, Z., Janssens-Maenhout, G., Pitkanen, T., Seibert, J. J., Vu, L.,  
 2399 Andres, R. J., Bolt, R. M., Bond, T. C., Dawidowski, L., Kholod, N., Kurokawa, J., Li, M., Liu, L., Lu, Z.,  
 2400 Moura, M. C. P., O'Rourke, P. R., and Zhang, Q.: Historical (1750–2014) anthropogenic emissions of reactive  
 2401 gases and aerosols from the Community Emissions Data System (CEDS), *Geosci. Model Dev.*, 11, 369–408,  
 2402 <https://doi.org/10.5194/gmd-11-369-2018>, 2018.

2403 Hong, C., Burney, J. A., Pongratz, J., Nabel, J. E. M. S., Mueller, N. D., Jackson, R. B., and Davis, S. J.: Global  
 2404 and regional drivers of land-use emissions in 1961–2017, 589, 554–561, [https://doi.org/10.1038/s41586-020-](https://doi.org/10.1038/s41586-020-03138-y)  
 2405 03138-y, 2021.

2406 Hooijer, A., Page, S., Canadell, J. G., Silvius, M., Kwadijk, J., Wösten, H., and Jauhiainen, J.: Current and  
 2407 future CO<sub>2</sub> emissions from drained peatlands in Southeast Asia, *Biogeosciences*, 7, 1505–1514,  
 2408 <https://doi.org/10.5194/bg-7-1505-2010>, 2010.

2409 Houghton, R. A.: Why are estimates of the terrestrial carbon balance so different?, 9, 500–509,  
 2410 <https://doi.org/10.1046/j.1365-2486.2003.00620.x>, 2003.

2411 Houghton, R. A. and Nassikas, A. A.: Global and regional fluxes of carbon from land use and land cover change  
2412 1850-2015: Carbon Emissions From Land Use, *Global Biogeochem. Cycles*, 31, 456–472,  
2413 <https://doi.org/10.1002/2016GB005546>, 2017.

2414 Houghton, R. A., House, J. I., Pongratz, J., van der Werf, G. R., DeFries, R. S., Hansen, M. C., Le Quéré, C.,  
2415 and Ramankutty, N.: Carbon emissions from land use and land-cover change, *Biogeosciences*, 9, 5125–5142,  
2416 <https://doi.org/10.5194/bg-9-5125-2012>, 2012.

2417 Hubau, W., Lewis, S. L., Phillips, O. L., Affum-Baffoe, K., Beeckman, H., Cuni-Sanchez, A., Daniels, A. K.,  
2418 Ewango, C. E. N., Fauset, S., Mukinzi, J. M., Sheil, D., Sonké, B., Sullivan, M. J. P., Sunderland, T. C. H.,  
2419 Taedoumg, H., Thomas, S. C., White, L. J. T., Abernethy, K. A., Adu-Bredu, S., Amani, C. A., Baker, T. R.,  
2420 Banin, L. F., Baya, F., Begne, S. K., Bennett, A. C., Benedet, F., Bitariho, R., Bocko, Y. E., Boeckx, P.,  
2421 Boundja, P., Brienen, R. J. W., Brncic, T., Chezeaux, E., Chuyong, G. B., Clark, C. J., Collins, M., Comiskey, J.,  
2422 A., Coomes, D. A., Dargie, G. C., de Haulleville, T., Kamdem, M. N. D., Doucet, J.-L., Esquivel-Muelbert, A.,  
2423 Feldpausch, T. R., Fofanah, A., Foli, E. G., Gilpin, M., Gloor, E., Gonmadje, C., Gourlet-Fleury, S., Hall, J. S.,  
2424 Hamilton, A. C., Harris, D. J., Hart, T. B., Hockemba, M. B. N., Hladik, A., Ifo, S. A., Jeffery, K. J., Jucker, T.,  
2425 Yakusu, E. K., Kearsley, E., Kenfack, D., Koch, A., Leal, M. E., Levesley, A., Lindsell, J. A., Lisingo, J.,  
2426 Lopez-Gonzalez, G., Lovett, J. C., Makana, J.-R., Malhi, Y., Marshall, A. R., Martin, J., Martin, E. H., Mbayu,  
2427 F. M., Medjibe, V. P., Mihindou, V., Mitchard, E. T. A., Moore, S., Munishi, P. K. T., Bengone, N. N., Ojo, L.,  
2428 Ondo, F. E., Peh, K. S.-H., Pickavance, G. C., Poulsen, A. D., Poulsen, J. R., Qie, L., Reitsma, J., Rovero, F.,  
2429 Swaine, M. D., Talbot, J., Taplin, J., Taylor, D. M., Thomas, D. W., Toirambe, B., Mukendi, J. T., Tuagben, D.,  
2430 Umunay, P. M., et al.: Asynchronous carbon sink saturation in African and Amazonian tropical forests, 579, 80–  
2431 87, <https://doi.org/10.1038/s41586-020-2035-0>, 2020.

2432 Hugelius, G., Bockheim, J. G., Camill, P., Elberling, B., Grosse, G., Harden, J. W., Johnson, K., Jorgenson, T.,  
2433 Koven, C. D., Kuhry, P., Michaelson, G., Mishra, U., Palmtag, J., Ping, C.-L., O'Donnell, J., Schirmermeister, L.,  
2434 Schuur, E. A. G., Sheng, Y., Smith, L. C., Strauss, J., and Yu, Z.: A new data set for estimating organic carbon  
2435 storage to 3 m depth in soils of the northern circumpolar permafrost region, *Earth Syst. Sci. Data*, 5, 393–402,  
2436 <https://doi.org/10.5194/essd-5-393-2013>, 2013.

2437 Humphrey, V., Zscheischler, J., Ciais, P., Gudmundsson, L., Sitch, S., and Seneviratne, S. I.: Sensitivity of  
2438 atmospheric CO<sub>2</sub> growth rate to observed changes in terrestrial water storage, 560, 628–631,  
2439 <https://doi.org/10.1038/s41586-018-0424-4>, 2018.

2440 Humphrey, V., Berg, A., Ciais, P., Gentine, P., Jung, M., Reichstein, M., Seneviratne, S. I., and Frankenberg,  
2441 C.: Soil moisture–atmosphere feedback dominates land carbon uptake variability, 592, 65–69,  
2442 <https://doi.org/10.1038/s41586-021-03325-5>, 2021.

2443 Huntzinger, D. N., Michalak, A. M., Schwalm, C., Ciais, P., King, A. W., Fang, Y., Schaefer, K., Wei, Y.,  
2444 Cook, R. B., Fisher, J. B., Hayes, D., Huang, M., Ito, A., Jain, A. K., Lei, H., Lu, C., Maignan, F., Mao, J.,  
2445 Parazoo, N., Peng, S., Poulter, B., Ricciuto, D., Shi, X., Tian, H., Wang, W., Zeng, N., and Zhao, F.:  
2446 Uncertainty in the response of terrestrial carbon sink to environmental drivers undermines carbon-climate  
2447 feedback predictions, *Sci Rep*, 7, 4765, <https://doi.org/10.1038/s41598-017-03818-2>, 2017.

2448 Hurtt, G., Chini, L., Sahajpal, R., Frolking, S., Bodirsky, B. L., Calvin, K., Doelman, J., Fisk, J., Fujimori, S.,  
2449 Klein Goldewijk, K., Hasegawa, T., Havlik, P., Heinemann, A., Humpenöder, F., Jungclaus, J., Kaplan, J.,  
2450 Krisztin, T., Lawrence, D., Lawrence, P., Mertz, O., Pongratz, J., Popp, A., Riahi, K., Shevliakova, E., Stehfest,  
2451 E., Thornton, P., van Vuuren, D., and Zhang, X.: input4MIPs.CMIP6.CMIP.UofMD.UofMD-landState-2-1-h,  
2452 <https://doi.org/10.22033/ESGF/input4MIPs.1127>, 2017.

2453 Hurtt, G. C., Chini, L. P., Frolking, S., Betts, R. A., Feddema, J., Fischer, G., Fisk, J. P., Hibbard, K., Houghton,  
2454 R. A., Janetos, A., Jones, C. D., Kindermann, G., Kinoshita, T., Klein Goldewijk, K., Riahi, K., Shevliakova, E.,  
2455 Smith, S., Stehfest, E., Thomson, A., Thornton, P., van Vuuren, D. P., and Wang, Y. P.: Harmonization of land-  
2456 use scenarios for the period 1500–2100: 600 years of global gridded annual land-use transitions, wood harvest,  
2457 and resulting secondary lands, *Climatic Change*, 109, 117–161, <https://doi.org/10.1007/s10584-011-0153-2>,  
2458 2011.

2459 Hurtt, G. C., Chini, L., Sahajpal, R., Frolking, S., Bodirsky, B. L., Calvin, K., Doelman, J. C., Fisk, J., Fujimori,  
2460 S., Klein Goldewijk, K., Hasegawa, T., Havlik, P., Heinemann, A., Humpenöder, F., Jungclaus, J., Kaplan, J. O.,  
2461 Kennedy, J., Krisztin, T., Lawrence, D., Lawrence, P., Ma, L., Mertz, O., Pongratz, J., Popp, A., Poulter, B.,  
2462 Riahi, K., Shevliakova, E., Stehfest, E., Thornton, P., Tubiello, F. N., van Vuuren, D. P., and Zhang, X.:  
2463 Harmonization of global land use change and management for the period 850–2100 (LUH2) for CMIP6, *Geosci.*  
2464 *Model Dev.*, 13, 5425–5464, <https://doi.org/10.5194/gmd-13-5425-2020>, 2020.

2465 IEA: International Energy Agency: Global Energy Review, available at: [https://www.iea.org/reports/global-](https://www.iea.org/reports/global-energy-review-2021)  
2466 [energy-review-2021](https://www.iea.org/reports/global-energy-review-2021), last access: 25 September 2022, 2021a.

2467 IEA: International Energy Agency: World Energy Outlook, available at: [https://www.iea.org/reports/world-](https://www.iea.org/reports/world-energy-outlook-2021)  
2468 [energy-outlook-2021](https://www.iea.org/reports/world-energy-outlook-2021), last access: 25 September 2022, 2021b.

2469 IEA/OECD: International Energy Agency/Organisation for Economic Cooperation and Development: CO2  
2470 emissions from fuel combustion, available at: [https://webstore.iea.org/co2-emissions-from-fuel-combustion-](https://webstore.iea.org/co2-emissions-from-fuel-combustion-2019-highlights)  
2471 [2019-highlights](https://webstore.iea.org/co2-emissions-from-fuel-combustion-2019-highlights), last access: 25 September 2022, 2019.

2472 Iida, Y., Kojima, A., Takatani, Y., Nakano, T., Sugimoto, H., Midorikawa, T., and Ishii, M.: Trends in pCO2  
2473 and sea–air CO2 flux over the global open oceans for the last two decades, *J Oceanogr*, 71, 637–661,  
2474 <https://doi.org/10.1007/s10872-015-0306-4>, 2015.

2475 Iida, Y., Takatani, Y., Kojima, A., and Ishii, M.: Global trends of ocean CO2 sink and ocean acidification: an  
2476 observation-based reconstruction of surface ocean inorganic carbon variables, *J Oceanogr*, 77, 323–358,  
2477 <https://doi.org/10.1007/s10872-020-00571-5>, 2021.

2478 Ilyina, T., Six, K. D., Segschneider, J., Maier-Reimer, E., Li, H., and Núñez-Riboni, I.: Global ocean  
2479 biogeochemistry model HAMOCC: Model architecture and performance as component of the MPI-Earth system  
2480 model in different CMIP5 experimental realizations: The Model Hamoccc within Mpi-Esm in Cmpip5, *J. Adv.*  
2481 *Model. Earth Syst.*, 5, 287–315, <https://doi.org/10.1029/2012MS000178>, 2013.

2482 IMF: International Monetary Fund: World Economic Outlook, available at: <http://www.imf.org>, last access: 25

2483 September 2022, 2022.

2484 Inness, A., Ades, M., Agustí-Panareda, A., Barré, J., Benedictow, A., Blechschmidt, A.-M., Dominguez, J. J.,  
 2485 Engelen, R., Eskes, H., Flemming, J., Huijnen, V., Jones, L., Kipling, Z., Massart, S., Parrington, M., Peuch, V.-  
 2486 H., Razinger, M., Remy, S., Schulz, M., and Suttie, M.: The CAMS reanalysis of atmospheric composition, 19,  
 2487 3515–3556, <https://doi.org/10.5194/acp-19-3515-2019>, 2019.

2488 IPCC: Summary for Policymakers. In: Climate Change 2021: The Physical Science Basis. Contribution of  
 2489 Working Group I to the Sixth Assessment Report of the Intergovernmental Panel on Climate Change [Masson-  
 2490 Delmotte, V., P. Zhai, A. Pirani, S.L. Connors, C. Péan, S. Berger, N. Caud, Y. Chen, L. Goldfarb, M.I. Gomis,  
 2491 M. Huang, K. Leitzell, E. Lonnoy, J.B.R. Matthews, T.K. Maycock, T. Waterfield, O. Yelekçi, R. Yu, and B.  
 2492 Zhou (eds.)]. Cambridge University Press, 2021.

2493 Ito, A. and Inatomi, M.: Use of a process-based model for assessing the methane budgets of global terrestrial  
 2494 ecosystems and evaluation of uncertainty, 9, 759–773, <https://doi.org/10.5194/bg-9-759-2012>, 2012.

2495 Jackson, R. B., Canadell, J. G., Le Quéré, C., Andrew, R. M., Korsbakken, J. I., Peters, G. P., and Nakicenovic,  
 2496 N.: Reaching peak emissions, *Nature Clim Change*, 6, 7–10, <https://doi.org/10.1038/nclimate2892>, 2016.

2497 Jackson, R. B., Le Quéré, C., Andrew, R. M., Canadell, J. G., Korsbakken, J. I., Liu, Z., Peters, G. P., and  
 2498 Zheng, B.: Global energy growth is outpacing decarbonization, *Environ. Res. Lett.*, 13, 120401,  
 2499 <https://doi.org/10.1088/1748-9326/aaf303>, 2018.

2500 Jackson, R. B., Friedlingstein, P., Andrew, R. M., Canadell, J. G., Le Quéré, C., and Peters, G. P.: Persistent  
 2501 fossil fuel growth threatens the Paris Agreement and planetary health, *Environ. Res. Lett.*, 14, 121001,  
 2502 <https://doi.org/10.1088/1748-9326/ab57b3>, 2019.

2503 Jackson, R. B., Friedlingstein, P., Quéré, C. L., Abernethy, S., Andrew, R. M., Canadell, J. G., Ciais, P., Davis,  
 2504 S. J., Deng, Z., Liu, Z., Korsbakken, J. I., and Peters, G. P.: Global fossil carbon emissions rebound near pre-  
 2505 COVID-19 levels, *Environ. Res. Lett.*, 17, 031001, <https://doi.org/10.1088/1748-9326/ac55b6>, 2022.

2506 Jacobson, A. R., Mikaloff Fletcher, S. E., Gruber, N., Sarmiento, J. L., and Gloor, M.: A joint atmosphere-ocean  
 2507 inversion for surface fluxes of carbon dioxide: 1. Methods and global-scale fluxes: JOINT INVERSION-  
 2508 METHODS AND GLOBAL FLUXES, *Global Biogeochem. Cycles*, 21,  
 2509 <https://doi.org/10.1029/2005GB002556>, 2007.

2510 Jähne, B.: Air-Sea Gas Exchange, in: Encyclopedia of Ocean Sciences, Elsevier, 1–13,  
 2511 <https://doi.org/10.1016/B978-0-12-409548-9.11613-6>, 2019.

2512 Jähne, B. and Haußecker, H.: Air-water gas exchange, *Annu. Rev. Fluid Mech.*, 30, 443–468,  
 2513 <https://doi.org/10.1146/annurev.fluid.30.1.443>, 1998.

2514 Jain, A. K., Meiyappan, P., Song, Y., and House, J. I.: CO2 emissions from land-use change affected more by  
 2515 nitrogen cycle, than by the choice of land-cover data, 19, 2893–2906, <https://doi.org/10.1111/gcb.12207>, 2013.

Deleted: sea gas exchange. Elements of Physical Oceanography: A Derivative of the

Deleted: 160–169. <https://doi.org/10.1016/B978-0-12-409548-9.11613-6>.

Deleted: , Haussecker

Deleted: Annual reviews of fluid mechanics,

Deleted: :

Deleted: <https://www.annualreviews.org/doi/10.1146/annurev.fluid.30.1.443>.

2525 Janssens-Maenhout, G., Crippa, M., Guizzardi, D., Muntean, M., Schaaf, E., Dentener, F., Bergamaschi, P.,  
2526 Pagliari, V., Olivier, J. G. J., Peters, J. A. H. W., van Aardenne, J. A., Monni, S., Doering, U., Petrescu, A. M.  
2527 R., Solazzo, E., and Oreggioni, G. D.: EDGAR v4.3.2 Global Atlas of the three major greenhouse gas emissions  
2528 for the period 1970–2012, *Earth Syst. Sci. Data*, 11, 959–1002, <https://doi.org/10.5194/essd-11-959-2019>, 2019.

2529 Jin, Z., Wang, T., Zhang, H., Wang, Y., Ding, J., and Tian, X.: Constraint of satellite CO<sub>2</sub> retrieval on the global  
2530 carbon cycle from a Chinese atmospheric inversion system, under review, *Sci. China Earth Sci.*, 2022.

2531 JODI: Joint Organisations Data Initiative, available at: <https://www.jodidata.org>, last access: 25 September  
2532 2022, 2022.

2533 Jones, M. W., Andrew, R. M., Peters, G. P., Janssens-Maenhout, G., De-Gol, A. J., Ciais, P., Patra, P. K.,  
2534 Chevallier, F., and Le Quéré, C.: Gridded fossil CO<sub>2</sub> emissions and related O<sub>2</sub> combustion consistent with  
2535 national inventories 1959–2018, *Sci Data*, 8, 2, <https://doi.org/10.1038/s41597-020-00779-6>, 2021.

2536 Jones, M. W., Andrew, R. M., Peters, G. P., Janssens-Maenhout, G., De-Gol, A. J., Dou, X., Liu, Z., Pickers, P.,  
2537 Ciais, P., Patra, P. K., Chevallier, F., and Le Quéré, C.: Gridded fossil CO<sub>2</sub> emissions and related O<sub>2</sub>  
2538 combustion consistent with national inventories 1959–2021, <https://doi.org/10.5281/zenodo.4277266>, 2022.

2539 Joos, F. and Spahni, R.: Rates of change in natural and anthropogenic radiative forcing over the past 20,000  
2540 years, *Proceedings of the National Academy of Sciences*, 105, 1425–1430,  
2541 <https://doi.org/10.1073/pnas.0707386105>, 2008.

2542 Joos, F., Spahni, R., Stocker, B. D., Lienert, S., Müller, J., Fischer, H., Schmitt, J., Prentice, I. C., Otto-Bliesner,  
2543 B., and Liu, Z.: N<sub>2</sub>O changes from the Last Glacial Maximum to the preindustrial – Part 2: terrestrial N<sub>2</sub>O  
2544 emissions and carbon–nitrogen cycle interactions, *Biogeosciences*, 17, 3511–3543, [https://doi.org/10.5194/bg-](https://doi.org/10.5194/bg-17-3511-2020)  
2545 17-3511-2020, 2020.

2546 Jung, M., Reichstein, M., Ciais, P., Seneviratne, S. I., Sheffield, J., Goulden, M. L., Bonan, G., Cescatti, A.,  
2547 Chen, J., de Jeu, R., Dolman, A. J., Eugster, W., Gerten, D., Gianelle, D., Gobron, N., Heinke, J., Kimball, J.,  
2548 Law, B. E., Montagnani, L., Mu, Q., Mueller, B., Oleson, K., Papale, D., Richardson, A. D., Rouspard, O.,  
2549 Running, S., Tomelleri, E., Viovy, N., Weber, U., Williams, C., Wood, E., Zaehle, S., and Zhang, K.: Recent  
2550 decline in the global land evapotranspiration trend due to limited moisture supply, *Nature*, 467, 951–954,  
2551 <https://doi.org/10.1038/nature09396>, 2010.

2552 Jung, M., Reichstein, M., Schwalm, C. R., Huntingford, C., Sitch, S., Ahlström, A., Arneth, A., Camps-Valls,  
2553 G., Ciais, P., Friedlingstein, P., Gans, F., Ichii, K., Jain, A. K., Kato, E., Papale, D., Poulter, B., Raduly, B.,  
2554 Rödenbeck, C., Tramontana, G., Viovy, N., Wang, Y.-P., Weber, U., Zaehle, S., and Zeng, N.: Compensatory  
2555 water effects link yearly global land CO<sub>2</sub> sink changes to temperature, *Nature*, 541, 516–520,  
2556 <https://doi.org/10.1038/nature20780>, 2017.

2557 Kalnay, E., Kanamitsu, M., Kistler, R., Collins, W., Deaven, D., Gandin, L., Iredell, M., Saha, S., White, G.,  
2558 Woollen, J., Zhu, Y., Chelliah, M., Ebisuzaki, W., Higgins, W., Janowiak, J., Mo, K. C., Ropelewski, C., Wang,  
2559 J., Leetmaa, A., Reynolds, R., Jenne, R., and Joseph, D.: The NCEP/NCAR 40-Year Reanalysis Project, 77,

2560 437–472, [https://doi.org/10.1175/1520-0477\(1996\)077<0437:TNYRP>2.0.CO;2](https://doi.org/10.1175/1520-0477(1996)077<0437:TNYRP>2.0.CO;2), 1996.

2561 Kato, E., Kinoshita, T., Ito, A., Kawamiya, M., and Yamagata, Y.: Evaluation of spatially explicit emission  
 2562 scenario of land-use change and biomass burning using a process-based biogeochemical model, 8, 104–122,  
 2563 <https://doi.org/10.1080/1747423X.2011.628705>, 2013.

2564 Keeling, C. D., Bacastow, R. B., Bainbridge, A. E., Ekdahl, C. A., Guenther, P. R., Waterman, L. S., and Chin,  
 2565 J. F. S.: Atmospheric carbon dioxide variations at Mauna Loa Observatory, Hawaii, 28, 538–551,  
 2566 <https://doi.org/10.1111/j.2153-3490.1976.tb00701.x>, 1976.

2567 Keeling, R. F. and Manning, A. C.: 5.15 - Studies of Recent Changes in Atmospheric O<sub>2</sub> Content, in: Treatise  
 2568 on Geochemistry (Second Edition), edited by: Holland, H. D. and Turekian, K. K., Elsevier, Oxford, 385–404,  
 2569 <https://doi.org/10.1016/B978-0-08-095975-7.00420-4>, 2014.

2570 Keppler, L. and Landschützer, P.: Regional Wind Variability Modulates the Southern Ocean Carbon Sink, *Sci*  
 2571 *Rep*, 9, 7384, <https://doi.org/10.1038/s41598-019-43826-y>, 2019.

2572 Khatiwala, S., Primeau, F., and Hall, T.: Reconstruction of the history of anthropogenic CO<sub>2</sub> concentrations in  
 2573 the ocean, *Nature*, 462, 346–349, <https://doi.org/10.1038/nature08526>, 2009.

2574 Khatiwala, S., Tanhua, T., Mikaloff Fletcher, S., Gerber, M., Doney, S. C., Graven, H. D., Gruber, N.,  
 2575 McKinley, G. A., Murata, A., Ríos, A. F., and Sabine, C. L.: Global ocean storage of anthropogenic carbon,  
 2576 *Biogeosciences*, 10, 2169–2191, <https://doi.org/10.5194/bg-10-2169-2013>, 2013.

2577 Klein Goldewijk, K., Beusen, A., Doelman, J., and Stehfest, E.: Anthropogenic land use estimates for the  
 2578 Holocene – HYDE 3.2, *Earth Syst. Sci. Data*, 9, 927–953, <https://doi.org/10.5194/essd-9-927-2017>, 2017a.

2579 Klein Goldewijk, K., Dekker, S. C., and van Zanden, J. L.: Per-capita estimations of long-term historical land  
 2580 use and the consequences for global change research, *Journal of Land Use Science*, 1747423X.2017.1354938,  
 2581 <https://doi.org/10.1080/1747423X.2017.1354938>, 2017b.

2582 Kobayashi, S., Ota, Y., Harada, Y., Ebata, A., Moriya, M., Onoda, H., Onogi, K., Kamahori, H., Kobayashi, C.,  
 2583 Endo, H., Miyaoka, K., and Takahashi, K.: The JRA-55 Reanalysis: General Specifications and Basic  
 2584 Characteristics, *Journal of the Meteorological Society of Japan*, 93, 5–48, <https://doi.org/10.2151/jmsj.2015-001>, 2015.

2586 Kong, Y., Zheng, B., Zhang, Q., and He, K.: Global and regional carbon budget for 2015–2020 inferred from  
 2587 OCO-2 based on an ensemble Kalman filter coupled with GEOS-Chem, *Atmospheric Chem. Phys.*, 22, 10769–  
 2588 10788, <https://doi.org/10.5194/acp-22-10769-2022>, 2022.

2589 Korsbakken, J. I., Peters, G. P., and Andrew, R. M.: Uncertainties around reductions in China’s coal use and  
 2590 CO<sub>2</sub> emissions, *Nature Clim Change*, 6, 687–690, <https://doi.org/10.1038/nclimate2963>, 2016.

2591 Krinner, G., Viovy, N., de Noblet-Ducoudré, N., Ogée, J., Polcher, J., Friedlingstein, P., Ciais, P., Sitch, S., and  
 2592 Prentice, I. C.: A dynamic global vegetation model for studies of the coupled atmosphere-biosphere system:

2593 DVGM for coupled climate studies, *Global Biogeochem. Cycles*, 19, <https://doi.org/10.1029/2003GB002199>,  
2594 2005.

2595 Lacroix, F., Ilyina, T., and Hartmann, J.: Oceanic CO<sub>2</sub> outgassing and biological production hotspots induced  
2596 by pre-industrial river loads of nutrients and carbon in a global modeling approach, *Biogeosciences*, 17, 55–88,  
2597 <https://doi.org/10.5194/bg-17-55-2020>, 2020.

2598 Lacroix, F., Ilyina, T., Mathis, M., Laruelle, G. G., and Regnier, P.: Historical increases in land-derived nutrient  
2599 inputs may alleviate effects of a changing physical climate on the oceanic carbon cycle, *Glob Change Biol*, 27,  
2600 5491–5513, <https://doi.org/10.1111/gcb.15822>, 2021.

2601 Landschützer, P., Gruber, N., Bakker, D. C. E., Schuster, U., Nakaoka, S., Payne, M. R., Sasse, T. P., and Zeng,  
2602 J.: A neural network-based estimate of the seasonal to inter-annual variability of the Atlantic Ocean carbon sink,  
2603 *Biogeosciences*, 10, 7793–7815, <https://doi.org/10.5194/bg-10-7793-2013>, 2013.

2604 Landschützer, P., Gruber, N., Bakker, D. C. E., and Schuster, U.: Recent variability of the global ocean carbon  
2605 sink, *Global Biogeochem. Cycles*, 28, 927–949, <https://doi.org/10.1002/2014GB004853>, 2014.

2606 Landschützer, P., Gruber, N., Haumann, F. A., Rödenbeck, C., Bakker, D. C. E., van Heuven, S., Hoppema, M.,  
2607 Metzl, N., Sweeney, C., Takahashi, T., Tilbrook, B., and Wanninkhof, R.: The reinvigoration of the Southern  
2608 Ocean carbon sink, *Science*, 349, 1221–1224, <https://doi.org/10.1126/science.aab2620>, 2015.

2609 Landschützer, P., Gruber, N., and Bakker, D. C. E.: Decadal variations and trends of the global ocean carbon  
2610 sink: decadal air-sea CO<sub>2</sub> flux variability, *Global Biogeochem. Cycles*, 30, 1396–1417,  
2611 <https://doi.org/10.1002/2015GB005359>, 2016.

2612 Landschützer, P., Laruelle, G. G., Roobaert, A., and Regnier, P.: A uniform pCO<sub>2</sub> climatology combining open  
2613 and coastal oceans, 12, 2537–2553, <https://doi.org/10.5194/essd-12-2537-2020>, 2020.

2614 Lang, F., Ackermann, L., Huang, Y., Truong, S. C. H., Siems, S. T., and Manton, M. J.: A climatology of open  
2615 and closed mesoscale cellular convection over the Southern Ocean derived from Himawari-8 observations, 1–  
2616 27, <https://doi.org/10.5194/acp-2021-681>, 2021.

2617 Lasslop, G., Reichstein, M., Papale, D., Richardson, A. D., Arneeth, A., Barr, A., Stoy, P., and Wohlfahrt, G.:  
2618 Separation of net ecosystem exchange into assimilation and respiration using a light response curve approach:  
2619 critical issues and global evaluation: Separation of NEE into GPP and RECO, 16, 187–208,  
2620 <https://doi.org/10.1111/j.1365-2486.2009.02041.x>, 2010.

2621 Lawrence, D. M., Fisher, R. A., Koven, C. D., Oleson, K. W., Swenson, S. C., Bonan, G., Collier, N., Ghimire,  
2622 B., van Kampenhou, L., Kennedy, D., Kluzek, E., Lawrence, P. J., Li, F., Li, H., Lombardozzi, D., Riley, W. J.,  
2623 Sacks, W. J., Shi, M., Vertenstein, M., Wieder, W. R., Xu, C., Ali, A. A., Badger, A. M., Bisht, G., van den  
2624 Broeke, M., Brunke, M. A., Burns, S. P., Buzan, J., Clark, M., Craig, A., Dahlin, K., Drewniak, B., Fisher, J. B.,  
2625 Flanner, M., Fox, A. M., Gentine, P., Hoffman, F., Keppel-Aleks, G., Knox, R., Kumar, S., Lenaerts, J., Leung,  
2626 L. R., Lipscomb, W. H., Lu, Y., Pandey, A., Pelletier, J. D., Perket, J., Randerson, J. T., Ricciuto, D. M.,

2627 Sanderson, B. M., Slater, A., Subin, Z. M., Tang, J., Thomas, R. Q., Val Martin, M., and Zeng, X.: The  
2628 Community Land Model Version 5: Description of New Features, Benchmarking, and Impact of Forcing  
2629 Uncertainty, 11, 4245–4287, <https://doi.org/10.1029/2018MS001583>, 2019.

2630 Le Quéré, C., Rödenbeck, C., Buitenhuis, E. T., Conway, T. J., Langenfelds, R., Gomez, A., Labuschagne, C.,  
2631 Ramonet, M., Nakazawa, T., Metz, N., Gillett, N., and Heimann, M.: Saturation of the Southern Ocean CO<sub>2</sub>  
2632 Sink Due to Recent Climate Change, 316, 1735–1738, <https://doi.org/10.1126/science.1136188>, 2007.

2633 Le Quéré, C., Raupach, M. R., Canadell, J. G., Marland, G., Bopp, L., Ciais, P., Conway, T. J., Doney, S. C.,  
2634 Feely, R. A., Foster, P., Friedlingstein, P., Gurney, K., Houghton, R. A., House, J. I., Huntingford, C., Levy, P.  
2635 E., Lomas, M. R., Majkut, J., Metz, N., Ometto, J. P., Peters, G. P., Prentice, I. C., Randerson, J. T., Running,  
2636 S. W., Sarmiento, J. L., Schuster, U., Sitch, S., Takahashi, T., Viovy, N., van der Werf, G. R., and Woodward,  
2637 F. I.: Trends in the sources and sinks of carbon dioxide, *Nature Geosci*, 2, 831–836,  
2638 <https://doi.org/10.1038/ngco689>, 2009.

2639 Le Quéré, C., Andres, R. J., Boden, T., Conway, T., Houghton, R. A., House, J. I., Marland, G., Peters, G. P.,  
2640 van der Werf, G. R., Ahlström, A., Andrew, R. M., Bopp, L., Canadell, J. G., Ciais, P., Doney, S. C., Enright,  
2641 C., Friedlingstein, P., Huntingford, C., Jain, A. K., Jourdain, C., Kato, E., Keeling, R. F., Klein Goldewijk, K.,  
2642 Levis, S., Levy, P., Lomas, M., Poulter, B., Raupach, M. R., Schwinger, J., Sitch, S., Stocker, B. D., Viovy, N.,  
2643 Zaehle, S., and Zeng, N.: The global carbon budget 1959–2011, *Earth Syst. Sci. Data*, 5, 165–185,  
2644 <https://doi.org/10.5194/essd-5-165-2013>, 2013.

2645 Le Quéré, C., Peters, G. P., Andres, R. J., Andrew, R. M., Boden, T. A., Ciais, P., Friedlingstein, P., Houghton,  
2646 R. A., Marland, G., Moriarty, R., Sitch, S., Tans, P., Armeth, A., Arvanitis, A., Bakker, D. C. E., Bopp, L.,  
2647 Canadell, J. G., Chini, L. P., Doney, S. C., Harper, A., Harris, I., House, J. I., Jain, A. K., Jones, S. D., Kato, E.,  
2648 Keeling, R. F., Klein Goldewijk, K., Körtzinger, A., Koven, C., Lefèvre, N., Maignan, F., Omar, A., Ono, T.,  
2649 Park, G.-H., Pfeil, B., Poulter, B., Raupach, M. R., Regnier, P., Rödenbeck, C., Saito, S., Schwinger, J.,  
2650 Segschneider, J., Stocker, B. D., Takahashi, T., Tilbrook, B., van Heuven, S., Viovy, N., Wanninkhof, R.,  
2651 Wiltshire, A., and Zaehle, S.: Global carbon budget 2013, *Earth Syst. Sci. Data*, 6, 235–263,  
2652 <https://doi.org/10.5194/essd-6-235-2014>, 2014.

2653 Le Quéré, C., Moriarty, R., Andrew, R. M., Peters, G. P., Ciais, P., Friedlingstein, P., Jones, S. D., Sitch, S.,  
2654 Tans, P., Armeth, A., Boden, T. A., Bopp, L., Bozec, Y., Canadell, J. G., Chini, L. P., Chevallier, F., Cosca, C.  
2655 E., Harris, I., Hoppema, M., Houghton, R. A., House, J. I., Jain, A. K., Johannessen, T., Kato, E., Keeling, R. F.,  
2656 Kitidis, V., Klein Goldewijk, K., Koven, C., Landa, C. S., Landschützer, P., Lenton, A., Lima, I. D., Marland,  
2657 G., Mathis, J. T., Metz, N., Nojiri, Y., Olsen, A., Ono, T., Peng, S., Peters, W., Pfeil, B., Poulter, B., Raupach,  
2658 M. R., Regnier, P., Rödenbeck, C., Saito, S., Salisbury, J. E., Schuster, U., Schwinger, J., Séférian, R.,  
2659 Segschneider, J., Steinhoff, T., Stocker, B. D., Sutton, A. J., Takahashi, T., Tilbrook, B., van der Werf, G. R.,  
2660 Viovy, N., Wang, Y.-P., Wanninkhof, R., Wiltshire, A., and Zeng, N.: Global carbon budget 2014, *Earth Syst.  
2661 Sci. Data*, 7, 47–85, <https://doi.org/10.5194/essd-7-47-2015>, 2015a.

2662 Le Quéré, C., Moriarty, R., Andrew, R. M., Canadell, J. G., Sitch, S., Korsbakken, J. I., Friedlingstein, P.,  
2663 Peters, G. P., Andres, R. J., Boden, T. A., Houghton, R. A., House, J. I., Keeling, R. F., Tans, P., Armeth, A.,

2664 Bakker, D. C. E., Barbero, L., Bopp, L., Chang, J., Chevallier, F., Chini, L. P., Ciais, P., Fader, M., Feely, R. A.,  
2665 Gkritzalis, T., Harris, I., Hauck, J., Ilyina, T., Jain, A. K., Kato, E., Kitidis, V., Klein Goldewijk, K., Koven, C.,  
2666 Landschützer, P., Lauvset, S. K., Lefèvre, N., Lenton, A., Lima, I. D., Metzl, N., Millero, F., Munro, D. R.,  
2667 Murata, A., Nabel, J. E. M. S., Nakaoka, S., Nojiri, Y., O'Brien, K., Olsen, A., Ono, T., Pérez, F. F., Pfeil, B.,  
2668 Pierrot, D., Poulter, B., Rehder, G., Rödenbeck, C., Saito, S., Schuster, U., Schwinger, J., Séférian, R.,  
2669 Steinhoff, T., Stocker, B. D., Sutton, A. J., Takahashi, T., Tilbrook, B., van der Laan-Luijkx, I. T., van der Werf,  
2670 G. R., van Heuven, S., Vandemark, D., Viovy, N., Wiltshire, A., Zaehle, S., and Zeng, N.: Global Carbon  
2671 Budget 2015, *Earth Syst. Sci. Data*, 7, 349–396, <https://doi.org/10.5194/essd-7-349-2015>, 2015b.

2672 Le Quéré, C., Andrew, R. M., Canadell, J. G., Sitch, S., Korsbakken, J. I., Peters, G. P., Manning, A. C., Boden,  
2673 T. A., Tans, P. P., Houghton, R. A., Keeling, R. F., Alin, S., Andrews, O. D., Anthoni, P., Barbero, L., Bopp, L.,  
2674 Chevallier, F., Chini, L. P., Ciais, P., Currie, K., Delire, C., Doney, S. C., Friedlingstein, P., Gkritzalis, T.,  
2675 Harris, I., Hauck, J., Haverd, V., Hoppema, M., Klein Goldewijk, K., Jain, A. K., Kato, E., Körtzinger, A.,  
2676 Landschützer, P., Lefèvre, N., Lenton, A., Lienert, S., Lombardozi, D., Melton, J. R., Metzl, N., Millero, F.,  
2677 Monteiro, P. M. S., Munro, D. R., Nabel, J. E. M. S., Nakaoka, S., O'Brien, K., Olsen, A., Omar, A. M., Ono,  
2678 T., Pierrot, D., Poulter, B., Rödenbeck, C., Salisbury, J., Schuster, U., Schwinger, J., Séférian, R., Skjelvan, I.,  
2679 Stocker, B. D., Sutton, A. J., Takahashi, T., Tian, H., Tilbrook, B., van der Laan-Luijkx, I. T., van der Werf, G.  
2680 R., Viovy, N., Walker, A. P., Wiltshire, A. J., and Zaehle, S.: Global Carbon Budget 2016, *Earth Syst. Sci. Data*,  
2681 8, 605–649, <https://doi.org/10.5194/essd-8-605-2016>, 2016.

2682 Le Quéré, C., Andrew, R. M., Friedlingstein, P., Sitch, S., Pongratz, J., Manning, A. C., Korsbakken, J. I.,  
2683 Peters, G. P., Canadell, J. G., Jackson, R. B., Boden, T. A., Tans, P. P., Andrews, O. D., Arora, V. K., Bakker,  
2684 D. C. E., Barbero, L., Becker, M., Betts, R. A., Bopp, L., Chevallier, F., Chini, L. P., Ciais, P., Cosca, C. E.,  
2685 Cross, J., Currie, K., Gasser, T., Harris, I., Hauck, J., Haverd, V., Houghton, R. A., Hunt, C. W., Hurtt, G.,  
2686 Ilyina, T., Jain, A. K., Kato, E., Kautz, M., Keeling, R. F., Klein Goldewijk, K., Körtzinger, A., Landschützer,  
2687 P., Lefèvre, N., Lenton, A., Lienert, S., Lima, I., Lombardozi, D., Metzl, N., Millero, F., Monteiro, P. M. S.,  
2688 Munro, D. R., Nabel, J. E. M. S., Nakaoka, S., Nojiri, Y., Padin, X. A., Peregon, A., Pfeil, B., Pierrot, D.,  
2689 Poulter, B., Rehder, G., Reimer, J., Rödenbeck, C., Schwinger, J., Séférian, R., Skjelvan, I., Stocker, B. D.,  
2690 Tian, H., Tilbrook, B., Tubiello, F. N., van der Laan-Luijkx, I. T., van der Werf, G. R., van Heuven, S., Viovy,  
2691 N., Vuichard, N., Walker, A. P., Watson, A. J., Wiltshire, A. J., Zaehle, S., and Zhu, D.: Global Carbon Budget  
2692 2017, *Earth Syst. Sci. Data*, 10, 405–448, <https://doi.org/10.5194/essd-10-405-2018>, 2018a.

2693 Le Quéré, C., Andrew, R. M., Friedlingstein, P., Sitch, S., Hauck, J., Pongratz, J., Pickers, P. A., Korsbakken, J.  
2694 I., Peters, G. P., Canadell, J. G., Arneeth, A., Arora, V. K., Barbero, L., Bastos, A., Bopp, L., Chevallier, F.,  
2695 Chini, L. P., Ciais, P., Doney, S. C., Gkritzalis, T., Goll, D. S., Harris, I., Haverd, V., Hoffman, F. M.,  
2696 Hoppema, M., Houghton, R. A., Hurtt, G., Ilyina, T., Jain, A. K., Johannessen, T., Jones, C. D., Kato, E.,  
2697 Keeling, R. F., Klein Goldewijk, K., Landschützer, P., Lefèvre, N., Lienert, S., Liu, Z., Lombardozi, D., Metzl,  
2698 N., Munro, D. R., Nabel, J. E. M. S., Nakaoka, S., Neill, C., Olsen, A., Ono, T., Patra, P., Peregon, A., Peters,  
2699 W., Peylin, P., Pfeil, B., Pierrot, D., Poulter, B., Rehder, G., Resplandy, L., Robertson, E., Rocher, M.,  
2700 Rödenbeck, C., Schuster, U., Schwinger, J., Séférian, R., Skjelvan, I., Steinhoff, T., Sutton, A., Tans, P. P.,  
2701 Tian, H., Tilbrook, B., Tubiello, F. N., van der Laan-Luijkx, I. T., van der Werf, G. R., Viovy, N., Walker, A.  
2702 P., Wiltshire, A. J., Wright, R., Zaehle, S., and Zheng, B.: Global Carbon Budget 2018, *Earth Syst. Sci. Data*,

2703 10, 2141–2194, <https://doi.org/10.5194/essd-10-2141-2018>, 2018b.

2704 Le Quéré, C., Korsbakken, J. I., Wilson, C., Tosun, J., Andrew, R., Andres, R. J., Canadell, J. G., Jordan, A.,  
 2705 Peters, G. P., and van Vuuren, D. P.: Drivers of declining CO<sub>2</sub> emissions in 18 developed economies, *Nat.*  
 2706 *Clim. Chang.*, 9, 213–217, <https://doi.org/10.1038/s41558-019-0419-7>, 2019.

2707 Le Quéré, C., Peters, G. P., Friedlingstein, P., Andrew, R. M., Canadell, J. G., Davis, S. J., Jackson, R. B., and  
 2708 Jones, M. W.: Fossil CO<sub>2</sub> emissions in the post-COVID-19 era, *Nat. Clim. Chang.*, 11, 197–199,  
 2709 <https://doi.org/10.1038/s41558-021-01001-0>, 2021.

2710 Li, H. and Ilyina, T.: Current and Future Decadal Trends in the Oceanic Carbon Uptake Are Dominated by  
 2711 Internal Variability, *Geophys. Res. Lett.*, 45, 916–925, <https://doi.org/10.1002/2017GL075370>, 2018.

2712 Li, W., Ciais, P., Peng, S., Yue, C., Wang, Y., Thurner, M., Saatchi, S. S., Arneeth, A., Avitabile, V., Carvalhais,  
 2713 N., Harper, A. B., Kato, E., Koven, C., Liu, Y. Y., Nabel, J. E. M. S., Pan, Y., Pongratz, J., Poulter, B., Pugh, T.  
 2714 A. M., Santoro, M., Sitch, S., Stocker, B. D., Viovy, N., Wiltshire, A., Yousefpour, R., and Zaehle, S.: Land-use  
 2715 and land-cover change carbon emissions between 1901 and 2012 constrained by biomass observations,  
 2716 *Biogeosciences*, 14, 5053–5067, <https://doi.org/10.5194/bg-14-5053-2017>, 2017.

2717 Liao, E., Resplandy, L., Liu, J., and Bowman, K. W.: Amplification of the Ocean Carbon Sink During El Niños:  
 2718 Role of Poleward Ekman Transport and Influence on Atmospheric CO<sub>2</sub>, 34, e2020GB006574,  
 2719 <https://doi.org/10.1029/2020GB006574>, 2020.

2720 Lienert, S. and Joos, F.: A Bayesian ensemble data assimilation to constrain model parameters and land-use  
 2721 carbon emissions, *Biogeosciences*, 15, 2909–2930, <https://doi.org/10.5194/bg-15-2909-2018>, 2018.

2722 Liu, J., Baskaran, L., Bowman, K., Schimel, D., Bloom, A. A., Parazoo, N. C., Oda, T., Carroll, D.,  
 2723 Menemenlis, D., Joiner, J., Commane, R., Daube, B., Gatti, L. V., McKain, K., Miller, J., Stephens, B. B.,  
 2724 Sweeney, C., and Wofsy, S.: Carbon Monitoring System Flux Net Biosphere Exchange 2020 (CMS-Flux NBE  
 2725 2020), 13, 299–330, <https://doi.org/10.5194/essd-13-299-2021>, 2021.

2726 Liu, Z., Guan, D., Wei, W., Davis, S. J., Ciais, P., Bai, J., Peng, S., Zhang, Q., Hubacek, K., Marland, G.,  
 2727 Andres, R. J., Crawford-Brown, D., Lin, J., Zhao, H., Hong, C., Boden, T. A., Feng, K., Peters, G. P., Xi, F.,  
 2728 Liu, J., Li, Y., Zhao, Y., Zeng, N., and He, K.: Reduced carbon emission estimates from fossil fuel combustion  
 2729 and cement production in China, *Nature*, 524, 335–338, <https://doi.org/10.1038/nature14677>, 2015.

2730 Liu, Z., Ciais, P., Deng, Z., Davis, S. J., Zheng, B., Wang, Y., Cui, D., Zhu, B., Dou, X., Ke, P., Sun, T., Guo,  
 2731 R., Zhong, H., Boucher, O., Bréon, F.-M., Lu, C., Guo, R., Xue, J., Boucher, E., Tanaka, K., and Chevallier, F.:  
 2732 Carbon Monitor, a near-real-time daily dataset of global CO<sub>2</sub> emission from fossil fuel and cement production,  
 2733 *Sci Data*, 7, 392, <https://doi.org/10.1038/s41597-020-00708-7>, 2020a.

2734 Liu, Z., Ciais, P., Deng, Z., Lei, R., Davis, S. J., Feng, S., Zheng, B., Cui, D., Dou, X., Zhu, B., Guo, R., Ke, P.,  
 2735 Sun, T., Lu, C., He, P., Wang, Y., Yue, X., Wang, Y., Lei, Y., Zhou, H., Cai, Z., Wu, Y., Guo, R., Han, T., Xue,  
 2736 J., Boucher, O., Boucher, E., Chevallier, F., Tanaka, K., Wei, Y., Zhong, H., Kang, C., Zhang, N., Chen, B., Xi,

2737 F., Liu, M., Bréon, F.-M., Lu, Y., Zhang, Q., Guan, D., Gong, P., Kammen, D. M., He, K., and Schellnhuber, H.  
2738 J.: Near-real-time monitoring of global CO<sub>2</sub> emissions reveals the effects of the COVID-19 pandemic, *Nat*  
2739 *Commun*, 11, 5172, <https://doi.org/10.1038/s41467-020-18922-7>, 2020b.

2740 Long, M. C., Moore, J. K., Lindsay, K., Levy, M., Doney, S. C., Luo, J. Y., et al., 2021. Simulations with the  
2741 Marine Biogeochemistry Library (MARBL). *Journal of Advances in Modeling Earth Systems*, 13,  
2742 e2021MS002647, <https://doi.org/10.1029/2021MS002647>.

2743 Ma, L., Hurtt, G. C., Chini, L. P., Sahajpal, R., Pongratz, J., Frohling, S., Stehfest, E., Klein Goldewijk, K.,  
2744 O’Leary, D., and Doelman, J. C.: Global rules for translating land-use change (LUH2) to land-cover change for  
2745 CMIP6 using GLM2, *Geosci. Model Dev.*, 13, 3203–3220, <https://doi.org/10.5194/gmd-13-3203-2020>, 2020.

2746 Maki, T., Ikegami, M., Fujita, T., Hirahara, T., Yamada, K., Mori, K., Takeuchi, A., Tsutsumi, Y., Suda, K., and  
2747 Conway, T. J.: New technique to analyse global distributions of CO<sub>2</sub> concentrations and fluxes from non-  
2748 processed observational data, 62, 797–809, <https://doi.org/10.1111/j.1600-0889.2010.00488.x>, 2010.

2749 MapBiomas: MapBiomas Collection 6, available at: <https://plataforma.brasil.mapbiomas.org/>, last access: 25  
2750 September 2022, 2022.

2751 Marland, G.: Uncertainties in Accounting for CO<sub>2</sub> From Fossil Fuels, 12, 136–139,  
2752 <https://doi.org/10.1111/j.1530-9290.2008.00014.x>, 2008.

2753 Marland, G., Hamal, K., and Jonas, M.: How Uncertain Are Estimates of CO<sub>2</sub> Emissions?, 13, 4–7,  
2754 <https://doi.org/10.1111/j.1530-9290.2009.00108.x>, 2009.

2755 Masarie, K. A. and Tans, P. P.: Extension and integration of atmospheric carbon dioxide data into a globally  
2756 consistent measurement record, *J. Geophys. Res.*, 100, 11593, <https://doi.org/10.1029/95JD00859>, 1995.

2757 Mather, A.: The transition from deforestation to reforestation in Europe., 35–52, 2001.

2758 Matricardi, E. A. T., Skole, D. L., Costa, O. B., Pedloski, M. A., Samek, J. H., and Miguel, E. P.: Long-term  
2759 forest degradation surpasses deforestation in the Brazilian Amazon, 369, 1378–1382,  
2760 <https://doi.org/10.1126/science.abb3021>, 2020.

2761 Mauritsen, T., Bader, J., Becker, T., Behrens, J., Bittner, M., Brokopf, R., Brovkin, V., Claussen, M., Crueger,  
2762 T., Esch, M., Fast, I., Fiedler, S., Fläschner, D., Gayler, V., Giorgetta, M., Goll, D. S., Haak, H., Hagemann, S.,  
2763 Hedemann, C., Hohenegger, C., Ilyina, T., Jahns, T., Jiménez-de-la-Cuesta, D., Jungclaus, J., Kleinen, T.,  
2764 Kloster, S., Kracher, D., Kinne, S., Kleberg, D., Lasslop, G., Kornbluh, L., Marotzke, J., Matei, D., Meraner,  
2765 K., Mikolajewicz, U., Modali, K., Möbis, B., Müller, W. A., Nabel, J. E. M. S., Nam, C. C. W., Notz, D.,  
2766 Nyawira, S.-S., Paulsen, H., Peters, K., Pincus, R., Pohlmann, H., Pongratz, J., Popp, M., Raddatz, T. J., Rast,  
2767 S., Redler, R., Reick, C. H., Rohrschneider, T., Schemann, V., Schmidt, H., Schnur, R., Schulzweida, U., Six,  
2768 K. D., Stein, L., Stemmler, I., Stevens, B., von Storch, J.-S., Tian, F., Voigt, A., Vrese, P., Wieners, K.-H.,  
2769 Wilkenskjaeld, S., Winkler, A., and Roeckner, E.: Developments in the MPI-M Earth System Model version 1.2  
2770 (MPI-ESM1.2) and Its Response to Increasing CO<sub>2</sub>, 11, 998–1038, <https://doi.org/10.1029/2018MS001400>,

2771 2019.

2772 McGrath, M. J., Luysaert, S., Meyfroidt, P., Kaplan, J. O., Bürgi, M., Chen, Y., Erb, K., Gimmi, U.,  
2773 McInerney, D., Naudts, K., Otto, J., Pasztor, F., Ryder, J., Schelhaas, M.-J., and Valade, A.: Reconstructing  
2774 European forest management from 1600 to 2010, *12*, 4291–4316, <https://doi.org/10.5194/bg-12-4291-2015>,  
2775 2015.

2776 McKinley, G. A., Pilcher, D. J., Fay, A. R., Lindsay, K., Long, M. C., and Lovenduski, N. S.: Timescales for  
2777 detection of trends in the ocean carbon sink, *Nature*, *530*, 469–472, <https://doi.org/10.1038/nature16958>, 2016.

2778 McKinley, G. A., Fay, A. R., Eddebbar, Y. A., Gloege, L., and Lovenduski, N. S.: External Forcing Explains  
2779 Recent Decadal Variability of the Ocean Carbon Sink, *AGU Advances*, *1*,  
2780 <https://doi.org/10.1029/2019AV000149>, 2020.

2781 McNeil, B. I.: Anthropogenic CO<sub>2</sub> Uptake by the Ocean Based on the Global Chlorofluorocarbon Data Set, *299*,  
2782 235–239, <https://doi.org/10.1126/science.1077429>, 2003.

2783 Meiyappan, P., Jain, A. K., and House, J. I.: Increased influence of nitrogen limitation on CO<sub>2</sub> emissions from  
2784 future land use and land use change, *Global Biogeochem. Cycles*, *29*, 1524–1548,  
2785 <https://doi.org/10.1002/2015GB005086>, 2015.

2786 Melton, J. R., Arora, V. K., Wisernig-Cojoc, E., Seiler, C., Fortier, M., Chan, E., and Teckentrup, L.: CLASSIC  
2787 v1.0: the open-source community successor to the Canadian Land Surface Scheme (CLASS) and the Canadian  
2788 Terrestrial Ecosystem Model (CTEM) – Part 1: Model framework and site-level performance, *Geosci. Model  
2789 Dev.*, *13*, 2825–2850, <https://doi.org/10.5194/gmd-13-2825-2020>, 2020.

2790 Mercado, L. M., Bellouin, N., Sitch, S., Boucher, O., Huntingford, C., Wild, M., and Cox, P. M.: Impact of  
2791 changes in diffuse radiation on the global land carbon sink, *Nature*, *458*, 1014–1017,  
2792 <https://doi.org/10.1038/nature07949>, 2009.

2793 Merchant, C. J., Embury, O., Bulgin, C. E., Block, T., Corlett, G. K., Fiedler, E., Good, S. A., Mittaz, J.,  
2794 Rayner, N. A., Berry, D., Eastwood, S., Taylor, M., Tsushima, Y., Waterfall, A., Wilson, R., and Donlon, C.:  
2795 Satellite-based time-series of sea-surface temperature since 1981 for climate applications, *Sci. Data*, *6*, 223,  
2796 <https://doi.org/10.1038/s41597-019-0236-x>, 2019.

2797 Mikaloff Fletcher, S. E., Gruber, N., Jacobson, A. R., Doney, S. C., Dutkiewicz, S., Gerber, M., Follows, M.,  
2798 Joos, F., Lindsay, K., Menemenlis, D., Mouchet, A., Müller, S. A., and Sarmiento, J. L.: Inverse estimates of  
2799 anthropogenic CO<sub>2</sub> uptake, transport, and storage by the ocean: air-sea exchange of anthropogenic carbon,  
2800 *Global Biogeochem. Cycles*, *20*, <https://doi.org/10.1029/2005GB002530>, 2006.

2801 Müller, J. and Joos, F.: Committed and projected future changes in global peatlands – continued transient model  
2802 simulations since the Last Glacial Maximum, *Biogeosciences*, *18*, 3657–3687, <https://doi.org/10.5194/bg-18-3657-2021>, 2021.

2804 Myneni, R. B., Ramakrishna, R., Nemani, R., and Running, S. W.: Estimation of global leaf area index and

2805 absorbed par using radiative transfer models, *IEEE Trans. Geosci. Remote Sensing*, 35, 1380–1393,  
2806 <https://doi.org/10.1109/36.649788>, 1997.

2807 Naegler, T.: Reconciliation of excess 14C-constrained global CO<sub>2</sub> piston velocity estimates, 61, 372–384,  
2808 <https://doi.org/10.1111/j.1600-0889.2008.00408.x>, 2009.

2809 Nakamura, T., Yamazaki, K., Iwamoto, K., Honda, M., Miyoshi, Y., Ogawa, Y., and Ukita, J.: A negative phase  
2810 shift of the winter AO/NAO due to the recent Arctic sea-ice reduction in late autumn, 120, 3209–3227,  
2811 <https://doi.org/10.1002/2014JD022848>, 2015.

2812 Nakano, H., Tsujino, H., Hirabara, M., Yasuda, T., Motoi, T., Ishii, M., and Yamanaka, G.: Uptake mechanism  
2813 of anthropogenic CO<sub>2</sub> in the Kuroshio Extension region in an ocean general circulation model, *J. Oceanogr.*, 67,  
2814 765–783, <https://doi.org/10.1007/s10872-011-0075-7>, 2011.

2815 Narayanan, B., Aguiar, A., and McDougall, R.: Global Trade, Assistance, and Production: The GTAP 9 Data  
2816 Base, *Cent. Glob. Trade Anal. Purdue Univ.*, available at: [https://](https://www.gtap.agecon.purdue.edu/databases/v9/default.asp)  
2817 [www.gtap.agecon.purdue.edu/databases/v9/default.asp](https://www.gtap.agecon.purdue.edu/databases/v9/default.asp), last access: 25 September 2022, 2015.

2818 NBS: National Bureau of Statistics of China: Statistical Communiqué of the People’s Republic of China on the  
2819 2021 National Economic and Social Development, available at:  
2820 [http://www.stats.gov.cn/english/PressRelease/202202/t20220227\\_1827963.html](http://www.stats.gov.cn/english/PressRelease/202202/t20220227_1827963.html), last access: 25 September  
2821 2022, 2022.

2822 NCEP: National Centers for Environmental Prediction. ONI Index. Cold & Warm Episodes by Season, available  
2823 at: [https://origin.cpc.ncep.noaa.gov/products/analysis\\_monitoring/ensostuff/ONI\\_v5.php](https://origin.cpc.ncep.noaa.gov/products/analysis_monitoring/ensostuff/ONI_v5.php), last access: 25  
2824 September 2022, 2022.

2825 Nightingale, P. D., Liss, P. S., and Schlosser, P.: Measurements of air-sea gas transfer during an open ocean  
2826 algal bloom, 27, 2117–2120, <https://doi.org/10.1029/2000GL011541>, 2000.

2827 Niwa, Y., Ishijima, K., Ito, A., and Iida, Y.: Toward a long-term atmospheric CO<sub>2</sub> inversion for elucidating  
2828 natural carbon fluxes: technical notes of NISMOM-CO<sub>2</sub> v2021.1, *Prog. Earth Planet Sci.*, 9, 42,  
2829 <https://doi.org/10.1186/s40645-022-00502-6>, 2022.

2830 Niwa, Y., Langenfelds, R., Krummel, P., Loh, Z., Worthy, Doug, Hatakka, Juha, Aalto, Tuula, Ramonet,  
2831 Michel, Delmotte, Marc, Schmidt, Martina, Gheusi, Francois, Mihalopoulos, N., Morgui, J.A., Andrews, Arlyn,  
2832 Dlugokencky, Ed, Lee, John, Sweeney, Colm, Thoning, Kirk, Tans, Pieter, De Wekker, Stephan, Fischer, Marc  
2833 L., Jaffe, Dan, McKain, Kathryn, Viner, Brian, Miller, John B., Karion, Anna, Miller, Charles, Sloop,  
2834 Christopher D., Saito, Kazuyuki, Aoki, Shuji, Morimoto, Shinji, Goto, Daisuke, Steinbacher, Martin, Myhre,  
2835 Cathrine Lund, Hermanssen, Ove, Stephens, Britton, Keeling, Ralph, Afshar, Sara, Paplawsky, Bill, Cox, Adam,  
2836 Walker, Stephen, Schuldt, Kenneth, Mukai, Hitoshi, Machida, Toshinobu, Sasakawa, Motoki, Nomura, Shohei,  
2837 Ito, Akihiko, Iida, Yosuke, and Jones, Matthew W.: Long-term global CO<sub>2</sub> fluxes estimated by NICAM-based  
2838 Inverse Simulation for Monitoring CO<sub>2</sub> (NISMOM-CO<sub>2</sub>) (ver.2022.1), <https://doi.org/10.17595/20201127.001>,  
2839 2020.

2840 Obermeier, W. A., Nabel, J. E. M. S., Loughran, T., Hartung, K., Bastos, A., Havermann, F., Anthoni, P.,  
2841 Arneth, A., Goll, D. S., Lienert, S., Lombardozi, D., Luyssaert, S., McGuire, P. C., Melton, J. R., Poulter, B.,  
2842 Sitch, S., Sullivan, M. O., Tian, H., Walker, A. P., Wiltshire, A. J., Zaehle, S., and Pongratz, J.: Modelled land  
2843 use and land cover change emissions – a spatio-temporal comparison of different approaches, *12*, 635–670,  
2844 <https://doi.org/10.5194/esd-12-635-2021>, 2021.

2845 O'Rourke, P. R., Smith, S. J., Mott, A., Ahsan, H., McDuffie, E. E., Crippa, M., Klimont, Z., McDonald, B.,  
2846 Wang, S., Nicholson, M. B., Feng, L., and Hoesly, R. M.: CEDS v\_2021\_04\_21 Release Emission Data,  
2847 <https://doi.org/10.5281/zenodo.4741285>, 2021.

2848 Orr, J. C., Najjar, R. G., Aumont, O., Bopp, L., Bullister, J. L., Danabasoglu, G., Doney, S. C., Dunne, J. P.,  
2849 Dutay, J.-C., Graven, H., Griffies, S. M., John, J. G., Joos, F., Levin, I., Lindsay, K., Matear, R. J., McKinley,  
2850 G. A., Mouchet, A., Oschlies, A., Romanou, A., Schlitzer, R., Tagliabue, A., Tanhua, T., and Yool, A.:  
2851 Biogeochemical protocols and diagnostics for the CMIP6 Ocean Model Intercomparison Project (OMIP), *10*,  
2852 2169–2199, <https://doi.org/10.5194/gmd-10-2169-2017>, 2017.

2853 O'Sullivan, M., Zhang, Y., Bellouin, N., Harris, I., Mercado, L. M., Sitch, S., Ciais, P., and Friedlingstein, P.:  
2854 Aerosol–light interactions reduce the carbon budget imbalance, *Environ. Res. Lett.*, *16*, 124072,  
2855 <https://doi.org/10.1088/1748-9326/ac3b77>, 2021.

2856 O'Sullivan, M., Friedlingstein, P., Sitch, S., Anthoni, P., Arneth, A., Arora, V. K., Bastrikov, V., Delire, C.,  
2857 Goll, D. S., Jain, A., Kato, E., Kennedy, D., Knauer, J., Lienert, S., Lombardozi, D., McGuire, P. C., Melton, J.  
2858 R., Nabel, J. E. M. S., Pongratz, J., Poulter, B., Séférian, R., Tian, H., Vuichard, N., Walker, A. P., Yuan, W.,  
2859 Yue, X., and Zaehle, S.: Process-oriented analysis of dominant sources of uncertainty in the land carbon sink,  
2860 *Nat. Commun.*, *13*, 4781, <https://doi.org/10.1038/s41467-022-32416-8>, 2022.

2861 Palmer, P. I., Feng, L., Baker, D., Chevallier, F., Bösch, H., and Somkuti, P.: Net carbon emissions from  
2862 African biosphere dominate pan-tropical atmospheric CO<sub>2</sub> signal, *Nat Commun*, *10*, 3344,  
2863 <https://doi.org/10.1038/s41467-019-11097-w>, 2019.

2864 Pan, Y., Birdsey, R. A., Fang, J., Houghton, R., Kauppi, P. E., Kurz, W. A., Phillips, O. L., Shvidenko, A.,  
2865 Lewis, S. L., Canadell, J. G., Ciais, P., Jackson, R. B., Pacala, S. W., McGuire, A. D., Piao, S., Rautiainen, A.,  
2866 Sitch, S., and Hayes, D.: A Large and Persistent Carbon Sink in the World's Forests, *Science*, *333*, 988–993,  
2867 <https://doi.org/10.1126/science.1201609>, 2011.

2868 Patra, P. K., Takigawa, M., Watanabe, S., Chandra, N., Ishijima, K., and Yamashita, Y.: Improved Chemical  
2869 Tracer Simulation by MIROC4.0-based Atmospheric Chemistry-Transport Model (MIROC4-ACTM), *SOLA*,  
2870 *14*, 91–96, <https://doi.org/10.2151/sola.2018-016>, 2018.

2871 Pendrill, F., Persson, U. M., Godar, J., Kastner, T., Moran, D., Schmidt, S., and Wood, R.: Agricultural and  
2872 forestry trade drives large share of tropical deforestation emissions, *Global Environmental Change*, *56*, 1–10,  
2873 <https://doi.org/10.1016/j.gloenvcha.2019.03.002>, 2019.

2874 Peters, G. P., Andrew, R., and Lennox, J.: Constructing an environmentally-extended multi-regional input–

2875 output table using the GTAP database, *Economic Systems Research*, 23, 131–152,  
2876 <https://doi.org/10.1080/09535314.2011.563234>, 2011a.

2877 Peters, G. P., Minx, J. C., Weber, C. L., and Edenhofer, O.: Growth in emission transfers via international trade  
2878 from 1990 to 2008, *Proceedings of the National Academy of Sciences*, 108, 8903–8908,  
2879 <https://doi.org/10.1073/pnas.1006388108>, 2011b.

2880 Peters, G. P., Davis, S. J., and Andrew, R.: A synthesis of carbon in international trade, *Biogeosciences*, 9,  
2881 3247–3276, <https://doi.org/10.5194/bg-9-3247-2012>, 2012a.

2882 Peters, G. P., Marland, G., Le Quéré, C., Boden, T., Canadell, J. G., and Raupach, M. R.: Rapid growth in CO<sub>2</sub>  
2883 emissions after the 2008–2009 global financial crisis, *Nature Clim Change*, 2, 2–4,  
2884 <https://doi.org/10.1038/nclimate1332>, 2012b.

2885 Peters, G. P., Andrew, R. M., Boden, T., Canadell, J. G., Ciais, P., Le Quéré, C., Marland, G., Raupach, M. R.,  
2886 and Wilson, C.: The challenge to keep global warming below 2 °C, *Nature Clim Change*, 3, 4–6,  
2887 <https://doi.org/10.1038/nclimate1783>, 2013.

2888 Peters, G. P., Le Quéré, C., Andrew, R. M., Canadell, J. G., Friedlingstein, P., Ilyina, T., Jackson, R. B., Joos,  
2889 F., Korsbakken, J. I., McKinley, G. A., Sitch, S., and Tans, P.: Towards real-time verification of CO<sub>2</sub> emissions,  
2890 *Nature Clim Change*, 7, 848–850, <https://doi.org/10.1038/s41558-017-0013-9>, 2017.

2891 Peters, G. P., Andrew, R. M., Canadell, J. G., Friedlingstein, P., Jackson, R. B., Korsbakken, J. I., Le Quéré, C.,  
2892 and Peregon, A.: Carbon dioxide emissions continue to grow amidst slowly emerging climate policies, *Nat.*  
2893 *Clim. Chang.*, 10, 3–6, <https://doi.org/10.1038/s41558-019-0659-6>, 2020.

2894 Petrescu, A. M. R., Peters, G. P., Janssens-Maenhout, G., Ciais, P., Tubiello, F. N., Grassi, G., Nabuurs, G.-J.,  
2895 Leip, A., Carmona-García, G., Winiwarter, W., Höglund-Isaksson, L., Günther, D., Solazzo, E., Kiesow, A.,  
2896 Bastos, A., Pongratz, J., Nabel, J. E. M. S., Conchedda, G., Pilli, R., Andrew, R. M., Schelhaas, M.-J., and  
2897 Dolman, A. J.: European anthropogenic AFOLU greenhouse gas emissions: a review and benchmark data, *Earth*  
2898 *Syst. Sci. Data*, 12, 961–1001, <https://doi.org/10.5194/essd-12-961-2020>, 2020.

2899 Pfeil, B., Olsen, A., Bakker, D. C. E., Hankin, S., Koyuk, H., Kozyr, A., Malczyk, J., Manke, A., Metzl, N.,  
2900 Sabine, C. L., Akl, J., Alin, S. R., Bates, N., Bellerby, R. G. J., Borges, A., Boutin, J., Brown, P. J., Cai, W.-J.,  
2901 Chavez, F. P., Chen, A., Cosca, C., Fassbender, A. J., Feely, R. A., González-Dávila, M., Goyet, C., Hales, B.,  
2902 Hardman-Mountford, N., Heinze, C., Hood, M., Hoppema, M., Hunt, C. W., Hydes, D., Ishii, M., Johannessen,  
2903 T., Jones, S. D., Key, R. M., Körtzinger, A., Landschützer, P., Lauvset, S. K., Lefèvre, N., Lenton, A.,  
2904 Lourantou, A., Merlivat, L., Midorikawa, T., Mintrop, L., Miyazaki, C., Murata, A., Nakadate, A., Nakano, Y.,  
2905 Nakaoka, S., Nojiri, Y., Omar, A. M., Padin, X. A., Park, G.-H., Paterson, K., Perez, F. F., Pierrot, D., Poisson,  
2906 A., Ríos, A. F., Santana-Casiano, J. M., Salisbury, J., Sarma, V. V. S. S., Schlitzer, R., Schneider, B., Schuster,  
2907 U., Sieger, R., Skjelvan, I., Steinhoff, T., Suzuki, T., Takahashi, T., Tedesco, K., Telszewski, M., Thomas, H.,  
2908 Tilbrook, B., Tjiputra, J., Vandemark, D., Veness, T., Wanninkhof, R., Watson, A. J., Weiss, R., Wong, C. S.,  
2909 and Yoshikawa-Inoue, H.: A uniform, quality controlled Surface Ocean CO<sub>2</sub> Atlas (SOCAT), *Earth Syst. Sci.*  
2910 *Data*, 5, 125–143, <https://doi.org/10.5194/essd-5-125-2013>, 2013.

2911 Piao, S., Ciais, P., Friedlingstein, P., de Noblet-Ducoudré, N., Cadule, P., Viovy, N., and Wang, T.:  
2912 Spatiotemporal patterns of terrestrial carbon cycle during the 20th century, 23,  
2913 <https://doi.org/10.1029/2008GB003339>, 2009.

2914 Piao, S., Huang, M., Liu, Z., Wang, X., Ciais, P., Canadell, J. G., Wang, K., Bastos, A., Friedlingstein, P.,  
2915 Houghton, R. A., Le Quéré, C., Liu, Y., Myneni, R. B., Peng, S., Pongratz, J., Sitch, S., Yan, T., Wang, Y., Zhu,  
2916 Z., Wu, D., and Wang, T.: Lower land-use emissions responsible for increased net land carbon sink during the  
2917 slow warming period, *Nature Geosci*, 11, 739–743, <https://doi.org/10.1038/s41561-018-0204-7>, 2018.

2918 Pongratz, J., Reick, C. H., Houghton, R. A., and House, J. I.: Terminology as a key uncertainty in net land use  
2919 and land cover change carbon flux estimates, *Earth Syst. Dynam.*, 5, 177–195, [https://doi.org/10.5194/esd-5-](https://doi.org/10.5194/esd-5-177-2014)  
2920 177-2014, 2014.

2921 Potapov, P., Hansen, M. C., Laestadius, L., Turubanova, S., Yaroshenko, A., Thies, C., Smith, W., Zhuravleva,  
2922 I., Komarova, A., Minnemeyer, S., and Esipova, E.: The last frontiers of wilderness: Tracking loss of intact  
2923 forest landscapes from 2000 to 2013, 3, e1600821, <https://doi.org/10.1126/sciadv.1600821>, 2017.

2924 Poulter, B., Frank, D. C., Hodson, E. L., and Zimmermann, N. E.: Impacts of land cover and climate data  
2925 selection on understanding terrestrial carbon dynamics and the CO<sub>2</sub> airborne fraction, *Biogeosciences*, 8, 2027–  
2926 2036, <https://doi.org/10.5194/bg-8-2027-2011>, 2011.

2927 Poulter, B., Freeborn, P. H., Jolly, W. M., and Varner, J. M.: COVID-19 lockdowns drive decline in active fires  
2928 in southeastern United States, *PNAS*, 118, <https://doi.org/10.1073/pnas.2105666118>, 2021.

2929 Prather, M.: Interactive comment on “Carbon dioxide and climate impulse response functions for the  
2930 computation of greenhouse gas metrics: a multi-model analysis” by F. Joos et al., 6, 2012.

2931 Prentice, I. C., Farquhar, G. D., Fasham, M. J. R., Goulden, M. L., Heimann, M., Jaramillo, V. J., Kheshgi, H.  
2932 S., Le Quéré, C., Scholes, R. J., and Wallace, D. W. R.: The Carbon Cycle and Atmospheric Carbon Dioxide, in  
2933 *Climate Change 2001: The Scientific Basis. Contribution of Working Group I to the Third Assessment Report*  
2934 *of the Intergovernmental Panel on Climate Change*, edited by: Houghton, J. T., Ding, Y., Griggs, D. J., Noguer,  
2935 M., van der Linden, P. J., Dai, X., Maskell, K., and Johnson, C. A., Cambridge University Press, Cambridge,  
2936 United Kingdom and New York, NY, USA, 183–237, 2001.

2937 Price, J. T. and Warren, R.: Literature Review of the Potential of “Blue Carbon” Activities to Reduce Emissions,  
2938 available at: [https://avoid-net-uk.cc.ic.ac.uk/wp-content/uploads/delightful-downloads/2016/03/Literature-](https://avoid-net-uk.cc.ic.ac.uk/wp-content/uploads/delightful-downloads/2016/03/Literature-review-of-the-potential-of-blue-carbon-activities-to-reduce-emissions-AVOID2-WPE2.pdf)  
2939 [review-of-the-potential-of-blue-carbon-activities-to-reduce-emissions-AVOID2-WPE2.pdf](https://avoid-net-uk.cc.ic.ac.uk/wp-content/uploads/delightful-downloads/2016/03/Literature-review-of-the-potential-of-blue-carbon-activities-to-reduce-emissions-AVOID2-WPE2.pdf), last access: 25  
2940 September 2022, 2016.

2941 Qin, Y., Xiao, X., Wigneron, J.-P., Ciais, P., Brandt, M., Fan, L., Li, X., Crowell, S., Wu, X., Doughty, R.,  
2942 Zhang, Y., Liu, F., Sitch, S., and Moore, B.: Carbon loss from forest degradation exceeds that from  
2943 deforestation in the Brazilian Amazon, *Nat. Clim. Chang.*, 11, 442–448, [https://doi.org/10.1038/s41558-021-](https://doi.org/10.1038/s41558-021-01026-5)  
2944 01026-5, 2021.

2945 Qiu, C., Ciais, P., Zhu, D., Guenet, B., Peng, S., Petrescu, A. M. R., Lauerwald, R., Makowski, D., Gallego-  
2946 Sala, A. V., Charman, D. J., and Brewer, S. C.: Large historical carbon emissions from cultivated northern  
2947 peatlands, 7, eabf1332, <https://doi.org/10.1126/sciadv.abf1332>, 2021.

2948 Raupach, M. R., Marland, G., Ciais, P., Le Quere, C., Canadell, J. G., Klepper, G., and Field, C. B.: Global and  
2949 regional drivers of accelerating CO<sub>2</sub> emissions, *Proceedings of the National Academy of Sciences*, 104, 10288–  
2950 10293, <https://doi.org/10.1073/pnas.0700609104>, 2007.

2951 Regnier, P., Friedlingstein, P., Ciais, P., Mackenzie, F. T., Gruber, N., Janssens, I. A., Laruelle, G. G.,  
2952 Lauerwald, R., Luysaert, S., Andersson, A. J., Arndt, S., Arnosti, C., Borges, A. V., Dale, A. W., Gallego-Sala,  
2953 A., Goddérís, Y., Goossens, N., Hartmann, J., Heinze, C., Ilyina, T., Joos, F., LaRowe, D. E., Leifeld, J.,  
2954 Meysman, F. J. R., Munhoven, G., Raymond, P. A., Spahni, R., Suntharalingam, P., and Thullner, M.:  
2955 Anthropogenic perturbation of the carbon fluxes from land to ocean, *Nature Geosci*, 6, 597–607,  
2956 <https://doi.org/10.1038/ngco1830>, 2013.

2957 Regnier, P., Resplandy, L., Najjar, R. G., and Ciais, P.: The land-to-ocean loops of the global carbon cycle,  
2958 *Nature*, 603, 401–410, <https://doi.org/10.1038/s41586-021-04339-9>, 2022.

2959 Reick, C. H., Gayler, V., Goll, D., Hagemann, S., Heidkamp, M., Nabel, J. E. M. S., Raddatz, T., Roeckner, E.,  
2960 Schnur, R., and Wilkenskjaeld, S.: JSBACH 3 - The land component of the MPI Earth System Model:  
2961 documentation of version 3.2, <https://doi.org/10.17617/2.3279802>, 2021.

2962 Remaud, M., Chevallier, F., Cozic, A., Lin, X., and Bousquet, P.: On the impact of recent developments of the  
2963 LMDz atmospheric general circulation model on the simulation of CO<sub>2</sub> transport, 11, 4489,  
2964 <https://doi.org/10.5194/gmd-11-4489-2018>, 2018.

2965 Resplandy, L., Keeling, R. F., Rödenbeck, C., Stephens, B. B., Khatriwala, S., Rodgers, K. B., Long, M. C.,  
2966 Bopp, L., and Tans, P. P.: Revision of global carbon fluxes based on a reassessment of oceanic and riverine  
2967 carbon transport, *Nature Geosci*, 11, 504–509, <https://doi.org/10.1038/s41561-018-0151-3>, 2018.

2968 Reynolds, R. W., Rayner, N. A., Smith, T. M., Stokes, D. C., and Wang, W.: An Improved In Situ and Satellite  
2969 SST Analysis for Climate, *J. Clim.*, 15, 1609–1625, [https://doi.org/10.1175/1520-0442\(2002\)015<1609:AIISAS>2.0.CO;2](https://doi.org/10.1175/1520-0442(2002)015<1609:AIISAS>2.0.CO;2), 2002.

2971 Rhein, M., Rintoul, S. R., Aoki, S., Campos, E., Chambers, D., Feely, R. A., Gulev, S., Johnson, G. C., Josey, S.  
2972 A., Kostianoy, A., Mauritzen, C., Roemmich, D., and Talley, L. D.: *Observations: Ocean*, edited by: Stocker, T.  
2973 F., Qin, D., Plattner, G.-K., Tignor, M., Allen, S. K., Boschung, J., Nauels, A., Xia, Y., Bex, V., and Midgley, P.  
2974 M., Cambridge University Press, 255–316, 2013.

2975 Rödenbeck, C., Houweling, S., Gloor, M., and Heimann, M.: CO<sub>2</sub> flux history 1982–2001 inferred from  
2976 atmospheric data using a global inversion of atmospheric transport, 46, 2003.

2977 Rödenbeck, C., Keeling, R. F., Bakker, D. C. E., Metzl, N., Olsen, A., Sabine, C., and Heimann, M.: Global  
2978 surface-ocean pCO<sub>2</sub> and sea–air CO<sub>2</sub> flux variability from an observation-driven ocean mixed-layer scheme, 9,

2979 193–216, <https://doi.org/10.5194/os-9-193-2013>, 2013.

2980 Rödenbeck, C., Bakker, D. C. E., Metzl, N., Olsen, A., Sabine, C., Cassar, N., Reum, F., Keeling, R. F., and  
 2981 Heimann, M.: Interannual sea–air CO<sub>2</sub> flux variability from an observation-driven ocean mixed-layer scheme,  
 2982 11, 4599–4613, <https://doi.org/10.5194/bg-11-4599-2014>, 2014.

2983 Rödenbeck, C., Bakker, D. C. E., Gruber, N., Iida, Y., Jacobson, A. R., Jones, S., Landschützer, P., Metzl, N.,  
 2984 Nakaoka, S., Olsen, A., Park, G.-H., Peylin, P., Rodgers, K. B., Sasse, T. P., Schuster, U., Shutler, J. D.,  
 2985 Valsala, V., Wanninkhof, R., and Zeng, J.: Data-based estimates of the ocean carbon sink variability – first  
 2986 results of the Surface Ocean CO<sub>2</sub> Mapping intercomparison (SOCOM), *Biogeosciences*, 12, 7251–7278,  
 2987 <https://doi.org/10.5194/bg-12-7251-2015>, 2015.

2988 Rödenbeck, C., Zaehle, S., Keeling, R., and Heimann, M.: History of El Niño impacts on the global carbon  
 2989 cycle 1957–2017: a quantification from atmospheric CO<sub>2</sub> data, 373, 20170303,  
 2990 <https://doi.org/10.1098/rstb.2017.0303>, 2018.

2991 Rödenbeck, C., DeVries, T., Hauck, J., Le Quéré, C., and Keeling, R. F.: Data-based estimates of interannual  
 2992 sea–air CO<sub>2</sub> flux variations 1957–2020 and their relation to environmental drivers, *Biogeosciences*, 19, 2627–  
 2993 2652, <https://doi.org/10.5194/bg-19-2627-2022>, 2022.

2994 Roobaert, A., Laruelle, G. G., Landschützer, P., and Regnier, P.: Uncertainty in the global oceanic CO<sub>2</sub> uptake  
 2995 induced by wind forcing: quantification and spatial analysis, 15, 1701–1720, <https://doi.org/10.5194/bg-15-1701-2018>, 2018.

2997 Rosan, T. M., Klein Goldewijk, K., Ganzenmüller, R., O’Sullivan, M., Pongratz, J., Mercado, L. M., Aragao, L.  
 2998 E. O. C., Heinrich, V., Randow, C. V., Wiltshire, A., Tubiello, F. N., Bastos, A., Friedlingstein, P., and Sitch,  
 2999 S.: A multi-data assessment of land use and land cover emissions from Brazil during 2000–2019, *Environ. Res.  
 3000 Lett.*, 16, 074004, <https://doi.org/10.1088/1748-9326/ac08c3>, 2021.

3001 Rypdal, K., Paciorek, N., Eggleston, S., Goodwin, J., Irving, W., Penman, J., and Woodfield, M.: Volume 1:  
 3002 Introduction to the 2006 Guidelines in: 2006 IPCC guidelines for national greenhouse gas inventories., 2006.

3003 Saatchi, S. S., Harris, N. L., Brown, S., Lefsky, M., Mitchard, E. T. A., Salas, W., Zutta, B. R., Buermann, W.,  
 3004 Lewis, S. L., Hagen, S., Petrova, S., White, L., Silman, M., and Morel, A.: Benchmark map of forest carbon  
 3005 stocks in tropical regions across three continents, *Proceedings of the National Academy of Sciences*, 108, 9899–  
 3006 9904, <https://doi.org/10.1073/pnas.1019576108>, 2011.

3007 Sabine, C. L., Feely, R. A., Gruber, N., Key, R. M., Lee, K., Bullister, J. L., Wanninkhof, R., Wong, C. S.,  
 3008 Wallace, D. W. R., Tilbrook, B., Millero, F. J., Peng, T.-H., Kozyr, A., Ono, T., and Rios, A. F.: The Oceanic  
 3009 Sink for Anthropogenic CO<sub>2</sub>, 305, 367–371, <https://doi.org/10.1126/science.1097403>, 2004.

3010 Sarmiento, J. L., Orr, J. C., and Siegenthaler, U.: A perturbation simulation of CO<sub>2</sub> uptake in an ocean general  
 3011 circulation model, 97, 3621–3645, <https://doi.org/10.1029/91JC02849>, 1992.

3012 Sato, M., Hansen, J. E., McCormick, M. P., and Pollack, J. B.: Stratospheric aerosol optical depths, 1850–1990,

Formatted: Not Superscript/ Subscript

3013 98, 22987–22994, <https://doi.org/10.1029/93JD02553>, 1993.

3014 Saunois, M., Stavert, A. R., Poulter, B., Bousquet, P., Canadell, J. G., Jackson, R. B., Raymond, P. A.,  
3015 Dlugokencky, E. J., Houweling, S., Patra, P. K., Ciais, P., Arora, V. K., Bastviken, D., Bergamaschi, P., Blake,  
3016 D. R., Brailsford, G., Bruhwiler, L., Carlson, K. M., Carrol, M., Castaldi, S., Chandra, N., Crevoisier, C., Crill,  
3017 P. M., Covey, K., Curry, C. L., Etiope, G., Frankenberg, C., Gedney, N., Hegglin, M. I., Höglund-Isaksson, L.,  
3018 Hugelius, G., Ishizawa, M., Ito, A., Janssens-Maenhout, G., Jensen, K. M., Joos, F., Kleinen, T., Krummel, P.  
3019 B., Langenfelds, R. L., Laruelle, G. G., Liu, L., Machida, T., Maksyutov, S., McDonald, K. C., McNorton, J.,  
3020 Miller, P. A., Melton, J. R., Morino, I., Müller, J., Murguia-Flores, F., Naik, V., Niwa, Y., Noce, S., O’Doherty,  
3021 S., Parker, R. J., Peng, C., Peng, S., Peters, G. P., Prigent, C., Prinn, R., Ramonet, M., Regnier, P., Riley, W. J.,  
3022 Rosentreter, J. A., Segers, A., Simpson, I. J., Shi, H., Smith, S. J., Steele, L. P., Thornton, B. F., Tian, H.,  
3023 Tohjima, Y., Tubiello, F. N., Tsuruta, A., Viovy, N., Voulgarakis, A., Weber, T. S., van Weele, M., van der  
3024 Werf, G. R., Weiss, R. F., Worthy, D., Wunch, D., Yin, Y., Yoshida, Y., Zhang, W., Zhang, Z., Zhao, Y.,  
3025 Zheng, B., Zhu, Q., Zhu, Q., and Zhuang, Q.: The Global Methane Budget 2000–2017, *Earth Syst. Sci. Data*, 12,  
3026 1561–1623, <https://doi.org/10.5194/essd-12-1561-2020>, 2020.

3027 Schimel, D., Alves, D., Enting, I. G., Heimann, M., Joos, F., Raynaud, D., Wigley, T., Prater, M., Derwent, R.,  
3028 Ehhalt, D., Fraser, P., Sanhueza, E., Zhou, X., Jonas, P., Charlson, R., Rodhe, H., Sadasivan, S., Shine, K. P.,  
3029 Fouquart, Y., Ramaswamy, V., Solomon, S., Srinivasan, J., Albritton, D., Derwent, R., Isaksen, I., Lal, M., and  
3030 Wuebbles, D.: Radiative Forcing of Climate Change, in: *Climate Change 1995 The Science of Climate Change*,  
3031 Contribution of Working Group I to the Second Assessment Report of the Intergovernmental Panel on Climate  
3032 Change, edited by: Houghton, J. T., Meira Rilho, L. G., Callander, B. A., Harris, N., Kattenberg, A., and  
3033 Maskell, K., Cambridge University Press, Cambridge, United Kingdom and New York, NY, USA, 1995.

3034 Schimel, D., Stephens, B. B., and Fisher, J. B.: Effect of increasing CO<sub>2</sub> on the terrestrial carbon cycle, *Proc*  
3035 *Natl Acad Sci USA*, 112, 436–441, <https://doi.org/10.1073/pnas.1407302112>, 2015.

3036 Schourup-Kristensen, V., Sidorenko, D., Wolf-Gladrow, D. A., and Völker, C.: A skill assessment of the  
3037 biogeochemical model REcoM2 coupled to the Finite Element Sea Ice–Ocean Model (FESOM 1.3), *Geosci.*  
3038 *Model Dev.*, 7, 2769–2802, <https://doi.org/10.5194/gmd-7-2769-2014>, 2014.

3039 Schuh, A. E., Jacobson, A. R., Basu, S., Weir, B., Baker, D., Bowman, K., Chevallier, F., Crowell, S., Davis, K.  
3040 J., Deng, F., Denning, S., Feng, L., Jones, D., Liu, J., and Palmer, P. I.: Quantifying the Impact of Atmospheric  
3041 Transport Uncertainty on CO<sub>2</sub> Surface Flux Estimates, *Global Biogeochem. Cycles*, 33, 484–500,  
3042 <https://doi.org/10.1029/2018GB006086>, 2019.

3043 Schuldt et al. Multi-laboratory compilation of atmospheric carbon dioxide data for the period 1957–2020.  
3044 <https://doi.org/10.25925/20210801>

3045 Schuldt et al. Multi-laboratory compilation of atmospheric carbon dioxide data for the period 2021–2022.  
3046 <http://doi.org/10.25925/20220624>

3047 Schwinger, J., Goris, N., Tjiputra, J. F., Kriest, I., Bentsen, M., Bethke, I., Ilicak, M., Assmann, K. M., and  
3048 Heinze, C.: Evaluation of NorESM-OC (versions 1 and 1.2), the ocean carbon-cycle stand-alone configuration

Field Code Changed

Deleted:

3050 of the Norwegian Earth System Model (NorESM1), *Geosci. Model Dev.*, 9, 2589–2622,  
3051 <https://doi.org/10.5194/gmd-9-2589-2016>, 2016.

3052 Schwingshackl, C., Obermeier, W., Bultan, S., Grassi, G., Canadell, J. G., Friedlingstein, P., Gasser, T.,  
3053 Houghton, R. A., Kurz, W. A., Sitch, S., and Pongratz, J.: Separating natural and land-use CO<sub>2</sub> fluxes at  
3054 country-level to reconcile land-based mitigation estimates, submitted, *One Earth*, 2022.

3055 Séférian, R., Nabat, P., Michou, M., Saint-Martin, D., Voldoire, A., Colin, J., Decharme, B., Delire, C., Berthet,  
3056 S., Chevallier, M., Sénési, S., Franchisteguy, L., Vial, J., Mallet, M., Joetzjer, E., Geoffroy, O., Guérémy, J.-F.,  
3057 Moine, M.-P., Msadek, R., Ribes, A., Rocher, M., Roehrig, R., Salas-y-Méla, D., Sanchez, E., Terray, L.,  
3058 Valcke, S., Waldman, R., Aumont, O., Bopp, L., Deshayes, J., Éthé, C., and Madec, G.: Evaluation of CNRM  
3059 Earth System Model, CNRM-ESM2-1: Role of Earth System Processes in Present-Day and Future Climate,  
3060 *Journal of Advances in Modeling Earth Systems*, 11, 4182–4227, <https://doi.org/10.1029/2019MS001791>, 2019.

3061 Seiler, C., Melton, J. R., Arora, V. K., Sitch, S., Friedlingstein, P., Anthoni, P., Goll, D., Jain, A. K., Joetzjer, E.,  
3062 Lienert, S., Lombardozi, D., Luyssaert, S., Nabel, J. E. M. S., Tian, H., Vuichard, N., Walker, A. P., Yuan, W.,  
3063 [and Zaehle, S.: Are Terrestrial Biosphere Models Fit for Simulating the Global Land Carbon Sink? J. Adv.](#)  
3064 [Model, Earth Syst.](#), 14, e2021MS002946, <https://doi.org/10.1029/2021MS002946>, 2022.

3065 Sellar, A. A., Jones, C. G., Mulcahy, J. P., Tang, Y., Yool, A., Wiltshire, A., O'Connor, F. M., Stringer, M.,  
3066 Hill, R., Palmieri, J., Woodward, S., Mora, L., Kuhlbrodt, T., Rumbold, S. T., Kelley, D. I., Ellis, R., Johnson,  
3067 C. E., Walton, J., Abraham, N. L., Andrews, M. B., Andrews, T., Archibald, A. T., Berthou, S., Burke, E.,  
3068 Blockley, E., Carslaw, K., Dalvi, M., Edwards, J., Folberth, G. A., Gedney, N., Griffiths, P. T., Harper, A. B.,  
3069 Hendry, M. A., Hewitt, A. J., Johnson, B., Jones, A., Jones, C. D., Keeble, J., Liddicoat, S., Morgenstern, O.,  
3070 Parker, R. J., Predoi, V., Robertson, E., Siahann, A., Smith, R. S., Swaminathan, R., Woodhouse, M. T., Zeng,  
3071 G., and Zerroukat, M.: UKESM1: Description and Evaluation of the U.K. Earth System Model, *J. Adv. Model.*  
3072 *Earth Syst.*, 11, 4513–4558, <https://doi.org/10.1029/2019MS001739>, 2019.

3073 Shu, S., Jain, A. K., Koven, C. D., and Mishra, U.: Estimation of Permafrost SOC Stock and Turnover Time  
3074 Using a Land Surface Model With Vertical Heterogeneity of Permafrost Soils, 34, e2020GB006585,  
3075 <https://doi.org/10.1029/2020GB006585>, 2020.

3076 [Sitch, S., Huntingford, C., Gedney, N., Levy, P. E., Lomas, M., Piao, S. L., Betts, R., Ciais, P., Cox, P.,](#)  
3077 [Friedlingstein, P., Jones, C. D., Prentice, I. C., and Woodward, F. I.: Evaluation of the terrestrial carbon cycle,](#)  
3078 [future plant geography and climate-carbon cycle feedbacks using five Dynamic Global Vegetation Models](#)  
3079 [\(DGVMs\): Uncertainty In Land Carbon Cycle Feedbacks](#), 14, 2015–2039, <https://doi.org/10.1111/j.1365->  
3080 [2486.2008.01626.x](#), 2008.

3081 Smith, B., Wårlind, D., Arneeth, A., Hickler, T., Leadley, P., Siltberg, J., and Zaehle, S.: Implications of  
3082 incorporating N cycling and N limitations on primary production in an individual-based dynamic vegetation  
3083 model, *Biogeosciences*, 11, 2027–2054, <https://doi.org/10.5194/bg-11-2027-2014>, 2014.

3084 Stephens, B. B., Gurney, K. R., Tans, P. P., Sweeney, C., Peters, W., Bruhwiler, L., Ciais, P., Ramonet, M.,  
3085 Bousquet, P., Nakazawa, T., Aoki, S., Machida, T., Inoue, G., Vinnichenko, N., Lloyd, J., Jordan, A., Heimann,

**Deleted:** terrestrial biosphere models fit

**Deleted:** simulating

**Deleted:** global land carbon sink? Journal of Advances in Modeling...

**Deleted:** Systems,

**Deleted:** <https://doi.org/10.1029/2021MS002946>.

**Moved up [4]:** H. L.,

**Moved up [5]:** L.,

**Moved up [3]:** M.,

**Moved up [6]:** O.,

**Deleted:** Silva Junior, C.

**Deleted:** Pessoa, A. C.

**Deleted:** Carvalho, N. S., Reis, J. B. C., Anderson, L.

**Deleted:** and Aragão, L. E. O. C.: The Brazilian Amazon deforestation rate in 2020 is the greatest of the decade, *Nat Ecol Evol*, 5, 144–145, <https://doi.org/10.1038/s41559-020-01368-x>, 2021.¶

3103 M., Shibistova, O., Langenfelds, R. L., Steele, L. P., Francey, R. J., and Denning, A. S.: Weak Northern and  
3104 Strong Tropical Land Carbon Uptake from Vertical Profiles of Atmospheric CO<sub>2</sub>, *Science*, 316, 1732–1735,  
3105 <https://doi.org/10.1126/science.1137004>, 2007.

3106 Stocker, T., Qin, D., and Plattner, G.-K.: *Climate Change 2013: The Physical Science Basis. Contribution of*  
3107 *Working Group I to the Fifth Assessment Report of the Intergovernmental Panel on Climate Change*, edited by:  
3108 Intergovernmental Panel on Climate Change, Cambridge University Press, Cambridge, 2013.

3109 Sweeney, C., Gloor, E., Jacobson, A. R., Key, R. M., McKinley, G., Sarmiento, J. L., and Wanninkhof, R.:  
3110 Constraining global air-sea gas exchange for CO<sub>2</sub> with recent bomb 14C measurements, 21,  
3111 <https://doi.org/10.1029/2006GB002784>, 2007.

3112 SX Coal: Monthly coal consumption estimates, <http://www.sxcoal.com/> (last access: 25 September 2022), 2022.

3113 Takahashi, T., Sutherland, S. C., Wanninkhof, R., Sweeney, C., Feely, R. A., Chipman, D. W., Hales, B.,  
3114 Friederich, G., Chavez, F., Sabine, C., Watson, A., Bakker, D. C. E., Schuster, U., Metzl, N., Yoshikawa-Inoue,  
3115 H., Ishii, M., Midorikawa, T., Nojiri, Y., Körtzinger, A., Steinhoff, T., Hoppema, M., Olafsson, J., Arnarson, T.  
3116 S., Tilbrook, B., Johannessen, T., Olsen, A., Bellerby, R., Wong, C. S., Delille, B., Bates, N. R., and de Baar, H.  
3117 J. W.: Climatological mean and decadal change in surface ocean pCO<sub>2</sub>, and net sea–air CO<sub>2</sub> flux over the  
3118 global oceans, *Deep Sea Research Part II: Topical Studies in Oceanography*, 56, 554–577,  
3119 <https://doi.org/10.1016/j.dsr2.2008.12.009>, 2009.

3120 Terhaar, J., Frölicher, T. L., and Joos, F.: Southern Ocean anthropogenic carbon sink constrained by sea surface  
3121 salinity, *Sci. Adv.*, 7, [eabd5964](https://doi.org/10.1126/sciadv.abd5964), <https://doi.org/10.1126/sciadv.abd5964>, 2021.

3122 Terhaar, J., Frölicher, T. L., and Joos, F.: Observation-constrained estimates of the global ocean carbon sink  
3123 from Earth system models, *Biogeosciences*, 19, 4431–4457, <https://doi.org/10.5194/bg-19-4431-2022>, 2022.

3124 Thomason, L. W., Ernest, N., Millán, L., Rieger, L., Bourassa, A., Vernier, J.-P., Manney, G., Luo, B.,  
3125 Arfeuille, F., and Peter, T.: A global space-based stratospheric aerosol climatology: 1979–2016, 10, 469–492,  
3126 <https://doi.org/10.5194/essd-10-469-2018>, 2018.

3127 Tian, H., Xu, X., Lu, C., Liu, M., Ren, W., Chen, G., Melillo, J., and Liu, J.: Net exchanges of CO<sub>2</sub>, CH<sub>4</sub>, and  
3128 N<sub>2</sub>O between China’s terrestrial ecosystems and the atmosphere and their contributions to global climate  
3129 warming, 116, <https://doi.org/10.1029/2010JG001393>, 2011.

3130 Tian, H., Chen, G., Lu, C., Xu, X., Hayes, D. J., Ren, W., Pan, S., Huntzinger, D. N., and Wofsy, S. C.: North  
3131 American terrestrial CO<sub>2</sub> uptake largely offset by CH<sub>4</sub> and N<sub>2</sub>O emissions: toward a full accounting of the  
3132 greenhouse gas budget, *Climatic Change*, 129, 413–426, <https://doi.org/10.1007/s10584-014-1072-9>, 2015.

3133 Todd-Brown, K. E. O., Randerson, J. T., Post, W. M., Hoffman, F. M., Tarnocai, C., Schuur, E. A. G., and  
3134 Allison, S. D.: Causes of variation in soil carbon simulations from CMIP5 Earth system models and comparison  
3135 with observations, *Biogeosciences*, 10, 1717–1736, <https://doi.org/10.5194/bg-10-1717-2013>, 2013.

3136 Tohjima, Y., Mukai, H., Machida, T., Hoshina, Y., and Nakaoka, S.-I.: Global carbon

Deleted: 5964–5992

Deleted: .

Formatted: Font: (Default) Gungsuh

3139 budgets estimated from atmospheric O<sub>2</sub>/N<sub>2</sub> and CO<sub>2</sub> observations in the western  
3140 Pacific region over a 15-year period, 19, 9269–9285, [https://doi.org/10.5194/acp-](https://doi.org/10.5194/acp-19-9269-2019)  
3141 19-9269-2019, 2019.

3142 Torero, M. and FAO: Impact of the Ukraine-Russia conflict on global food security and related matters under  
3143 the mandate of the Food and Agriculture Organization of the United Nations (FAO), available at:  
3144 <https://www.fao.org/3/njl164en/njl164en.pdf>, last access: 25 Sept 2022, 2022.

3145 Tubiello, F. N., Conchedda, G., Wanner, N., Federici, S., Rossi, S., and Grassi, G.: Carbon emissions and  
3146 removals from forests: new estimates, 1990–2020, *Earth Syst. Sci. Data*, 13, 1681–1691,  
3147 <https://doi.org/10.5194/essd-13-1681-2021>, 2021.

3148 Tyukavina, A., Potapov, P., Hansen, M. C., Pickens, A. H., Stehman, S. V., Turubanova, S., Parker, D., Zalles,  
3149 V., Lima, A., Kommareddy, I., Song, X.-P., Wang, L., and Harris, N.: Global Trends of Forest Loss Due to Fire  
3150 From 2001 to 2019, *Front. Remote Sens.*, 3, 2022.

3151 UN: United Nations Statistics Division: National Accounts Main Aggregates Database, available at:  
3152 <http://unstats.un.org/unsd/snaama/Introduction.asp>, last access: 25 September 2022, 2021.

3153 UNFCCC: Synthesis report for the technical assessment component of the first global stocktake, [available at:](https://unfccc.int/documents/461466)  
3154 <https://unfccc.int/documents/461466>, last access: 25 September 2022, 2022

3155 Urakawa, L. S., Tsujino, H., Nakano, H., Sakamoto, K., Yamanaka, G., and Toyoda, T.: The sensitivity of a  
3156 depth-coordinate model to diapycnal mixing induced by practical implementations of the isopycnal tracer  
3157 diffusion scheme, *Ocean Model.*, 154, 101693, <https://doi.org/10.1016/j.ocemod.2020.101693>, 2020.

3158 Vale, M. M., Berenguer, E., Argollo de Menezes, M., Viveiros de Castro, E. B., Pugliese de Siqueira, L., and  
3159 Portela, R. de C. Q.: The COVID-19 pandemic as an opportunity to weaken environmental protection in Brazil,  
3160 *Biological Conservation*, 255, 108994, <https://doi.org/10.1016/j.biocon.2021.108994>, 2021.

3161 van der Laan-Luijkx, I. T., van der Velde, I. R., van der Veen, E., Tsuruta, A., Stanislawski, K.,  
3162 Babenhauserheide, A., Zhang, H. F., Liu, Y., He, W., Chen, H., Masarie, K. A., Krol, M. C., and Peters, W.:  
3163 The CarbonTracker Data Assimilation Shell (CTDAS) v1.0: implementation and global carbon balance 2001–  
3164 2015, *Geosci. Model Dev.*, 10, 2785–2800, <https://doi.org/10.5194/gmd-10-2785-2017>, 2017.

3165 van der Velde, I. R., Miller, J. B., Schaefer, K., van der Werf, G. R., Krol, M. C., and Peters, W.: Terrestrial  
3166 cycling of <sup>13</sup>C<sub>2</sub>O<sub>2</sub> by photosynthesis, respiration, and biomass burning in SiBCASA, 11, 6553–6571,  
3167 <https://doi.org/10.5194/bg-11-6553-2014>, 2014.

3168 van der Velde, I. R., van der Werf, G. R., Houweling, S., Maasackers, J. D., Borsdorff, T., Landgraf, J., Tol, P.,  
3169 van Kempen, T. A., van Hees, R., Hoogveen, R., Veeffkind, J. P., and Aben, I.: Vast CO<sub>2</sub> release from  
3170 Australian fires in 2019–2020 constrained by satellite, 597, 366–369, [https://doi.org/10.1038/s41586-021-](https://doi.org/10.1038/s41586-021-03712-y)  
3171 03712-y, 2021.

3172 van der Werf, G. R., Randerson, J. T., Giglio, L., Collatz, G. J., Mu, M., Kasibhatla, P. S., Morton, D. C.,

Deleted: Frontiers in  
Deleted: Sensing,  
Deleted: <https://www.frontiersin.org/articles/10.3389/frsen.>  
Deleted: 825190

3177 DeFries, R. S., Jin, Y., and van Leeuwen, T. T.: Global fire emissions and the contribution of deforestation,  
3178 savanna, forest, agricultural, and peat fires (1997–2009), *Atmos. Chem. Phys.*, 10, 11707–11735,  
3179 <https://doi.org/10.5194/acp-10-11707-2010>, 2010.

3180 van der Werf, G. R., Randerson, J. T., Giglio, L., van Leeuwen, T. T., Chen, Y., Rogers, B. M., Mu, M., van  
3181 Marle, M. J. E., Morton, D. C., Collatz, G. J., Yokelson, R. J., and Kasibhatla, P. S.: Global fire emissions  
3182 estimates during 1997–2016, *Earth Syst. Sci. Data*, 9, 697–720, <https://doi.org/10.5194/essd-9-697-2017>, 2017.

3183 van Wees, D., van der Werf, G. R., Randerson, J. T., Andela, N., Chen, Y., and Morton, D. C.: The role of fire  
3184 in global forest loss dynamics, *Glob. Change Biol.*, 27, 2377–2391, <https://doi.org/10.1111/gcb.15591>, 2021.

3185 Vaittinada Ayar, P., Bopp, L., Christian, J. R., Ilyina, T., Krasting, J. P., Séférian, R., Tsujino, H., Watanabe,  
3186 M., Yool, A., and Tjiputra, J.: Contrasting projections of the ENSO-driven CO<sub>2</sub> flux variability in the equatorial  
3187 Pacific under high-warming scenario, *Earth Syst. Dynam.*, 13, 1097–1118, [https://doi.org/10.5194/esd-13-1097-](https://doi.org/10.5194/esd-13-1097-2022)  
3188 2022, 2022.

3189 Viovy, N.: CRUNCEP data set, available at:  
3190 [ftp://nacp.ornl.gov/synthesis/2009/frescati/temp/land\\_use\\_change/original/readme.htm](ftp://nacp.ornl.gov/synthesis/2009/frescati/temp/land_use_change/original/readme.htm), last access: 25  
3191 September 2022, 2016.

3192 Vuichard, N., Messina, P., Luyssaert, S., Guenet, B., Zaehle, S., Ghattas, J., Bastrikov, V., and Peylin, P.:  
3193 Accounting for carbon and nitrogen interactions in the global terrestrial ecosystem model ORCHIDEE (trunk  
3194 version, rev 4999): multi-scale evaluation of gross primary production, *Geosci. Model Dev.*, 12, 4751–4779,  
3195 <https://doi.org/10.5194/gmd-12-4751-2019>, 2019.

3196 Walker, A. P., Quaipe, T., Bodegom, P. M., De Kauwe, M. G., Keenan, T. F., Joiner, J., Lomas, M. R.,  
3197 MacBean, N., Xu, C., Yang, X., and Woodward, F. I.: The impact of alternative trait-scaling hypotheses for the  
3198 maximum photosynthetic carboxylation rate ( $V_{cmax}$ ) on global gross primary production, *New Phytol.*, 215,  
3199 1370–1386, <https://doi.org/10.1111/nph.14623>, 2017.

3200 Walker, A. P., De Kauwe, M. G., Bastos, A., Belmecheri, S., Georgiou, K., Keeling, R. F., McMahon, S. M.,  
3201 Medlyn, B. E., Moore, D. J. P., Norby, R. J., Zaehle, S., Anderson-Teixeira, K. J., Battipaglia, G., Brienen, R. J.  
3202 W., Cabugao, K. G., Cailleret, M., Campbell, E., Canadell, J. G., Ciais, P., Craig, M. E., Ellsworth, D. S.,  
3203 Farquhar, G. D., Fatichi, S., Fisher, J. B., Frank, D. C., Graven, H., Gu, L., Haverd, V., Heilman, K., Heimann,  
3204 M., Hungate, B. A., Iversen, C. M., Joos, F., Jiang, M., Keenan, T. F., Knauer, J., Körner, C., Leshyk, V. O.,  
3205 Leuzinger, S., Liu, Y., MacBean, N., Malhi, Y., McVicar, T. R., Penuelas, J., Pongratz, J., Powell, A. S., Riutta,  
3206 T., Sabot, M. E. B., Schleucher, J., Sitch, S., Smith, W. K., Sulman, B., Taylor, B., Terrer, C., Torn, M. S.,  
3207 Treseder, K. K., Trugman, A. T., Trumbore, S. E., van Mantgem, P. J., Voelker, S. L., Whelan, M. E., and  
3208 Zuidema, P. A.: Integrating the evidence for a terrestrial carbon sink caused by increasing atmospheric CO<sub>2</sub>,  
3209 229, 2413–2445, <https://doi.org/10.1111/nph.16866>, 2021.

3210 Wanninkhof, R.: Relationship between wind speed and gas exchange over the ocean, 97, 7373–7382,  
3211 <https://doi.org/10.1029/92JC00188>, 1992.

- 3212 Wanninkhof, R.: Relationship between wind speed and gas exchange over the ocean revisited, 12, 351–362,  
3213 <https://doi.org/10.4319/lom.2014.12.351>, 2014.
- 3214 Wanninkhof, R., Park, G.-H., Takahashi, T., Sweeney, C., Feely, R., Nojiri, Y., Gruber, N., Doney, S. C.,  
3215 McKinley, G. A., Lenton, A., Le Quéré, C., Heinze, C., Schwinger, J., Graven, H., and Khatiwala, S.: Global  
3216 ocean carbon uptake: magnitude, variability and trends, *Biogeosciences*, 10, 1983–2000,  
3217 <https://doi.org/10.5194/bg-10-1983-2013>, 2013.
- 3218 Watson, A. J., Schuster, U., Shutler, J. D., Holding, T., Ashton, I. G. C., Landschützer, P., Woolf, D. K., and  
3219 Goddijn-Murphy, L.: Revised estimates of ocean-atmosphere CO<sub>2</sub> flux are consistent with ocean carbon  
3220 inventory, *Nat Commun*, 11, 4422, <https://doi.org/10.1038/s41467-020-18203-3>, 2020.
- 3221 Watson, R. T., Rohde, H., Oeschger, H., and Siegenthaler, U.: Greenhouse Gases and Aerosols, in: *Climate  
3222 Change: The IPCC Scientific Assessment*. Intergovernmental Panel on Climate Change (IPCC), edited by:  
3223 Houghton, J. T., Jenkins, G. J., and Ephraums, J. J., Cambridge University Press, Cambridge, 140, 1990.
- 3224 Weiss, R. F. and Price, B. A.: Nitrous oxide solubility in water and seawater, *Marine Chemistry*, 8, 347–359,  
3225 [https://doi.org/10.1016/0304-4203\(80\)90024-9](https://doi.org/10.1016/0304-4203(80)90024-9), 1980.
- 3226 Wenzel, S., Cox, P. M., Eyring, V., and Friedlingstein, P.: Projected land photosynthesis constrained by changes  
3227 in the seasonal cycle of atmospheric CO<sub>2</sub>, *Nature*, 538, 499–501, <https://doi.org/10.1038/nature19772>, 2016.
- 3228 Wilkenskjeld, S., Kloster, S., Pongratz, J., Raddatz, T., and Reick, C. H.: Comparing the influence of net and  
3229 gross anthropogenic land-use and land-cover changes on the carbon cycle in the MPI-ESM, *Biogeosciences*, 11,  
3230 4817–4828, <https://doi.org/10.5194/bg-11-4817-2014>, 2014.
- 3231 Wiltshire, A. J., Burke, E. J., Chadburn, S. E., Jones, C. D., Cox, P. M., Davies-Barnard, T., Friedlingstein, P.,  
3232 Harper, A. B., Liddicoat, S., Sitch, S., and Zaehle, S.: JULES-CN: a coupled terrestrial carbon–nitrogen scheme  
3233 (JULES vn5.1), 14, 2161–2186, <https://doi.org/10.5194/gmd-14-2161-2021>, 2021.
- 3234 Woodward, F. I. and Lomas, M. R.: Vegetation dynamics – simulating responses to climatic change, *Biol. Rev.*,  
3235 79, 643–670, <https://doi.org/10.1017/S1464793103006419>, 2004.
- 3236 Wright, R. M., Le Quéré, C., Buitenhuis, E., Pitois, S., and Gibbons, M. J.: Role of jellyfish in the plankton  
3237 ecosystem revealed using a global ocean biogeochemical model, 18, 1291–1320, <https://doi.org/10.5194/bg-18-1291-2021>, 2021.
- 3239 Wunder, S., Kaimowitz, D., Jensen, S., and Feder, S.: Coronavirus, macroeconomy, and forests: What likely  
3240 impacts?, *For. Policy Econ.*, 131, 102536, <https://doi.org/10.1016/j.forpol.2021.102536>, 2021.
- 3241 Xi, F., Davis, S. J., Ciais, P., Crawford-Brown, D., Guan, D., Pade, C., Shi, T., Syddall, M., Lv, J., Ji, L., Bing,  
3242 L., Wang, J., Wei, W., Yang, K.-H., Lagerblad, B., Galan, I., Andrade, C., Zhang, Y., and Liu, Z.: Substantial  
3243 global carbon uptake by cement carbonation, *Nature Geosci*, 9, 880–883, <https://doi.org/10.1038/ngeo2840>,  
3244 2016.

3245 Xia, J., Chen, Y., Liang, S., Liu, D., and Yuan, W.: Global simulations of carbon allocation coefficients for  
3246 deciduous vegetation types, 67, 28016, <https://doi.org/10.3402/tellusb.v67.28016>, 2015.

3247 Yeager, S. G., Rosenbloom, N., Gnanville, A. A., Wu, X., Simpson, I., Li, H., Molina, M. J., Krumhardt, K.,  
3248 Mogen, S., Lindsay, K., Lombardozzi, D., Wieder, W., Kim, W. M., Richter, J. H., Long, M., Danabasoglu, G.,  
3249 Bailey, D., Holland, M., Lovenduski, N., Strand, W. G., and King, T.: The Seasonal-to-Multiyear Large  
3250 Ensemble (SMYLE) prediction system using the Community Earth System Model version 2, *Geoscientific  
3251 Model Development*, 15, 6451–6493, <https://doi.org/10.5194/gmd-15-6451-2022>, 2022.

3252 Yin, X.: Responses of leaf nitrogen concentration and specific leaf area to atmospheric CO<sub>2</sub> enrichment: a  
3253 retrospective synthesis across 62 species: Leaf response to atmospheric CO<sub>2</sub> enrichment, 8, 631–642,  
3254 <https://doi.org/10.1046/j.1365-2486.2002.00497.x>, 2002.

3255 Yu, Z., Ciais, P., Piao, S., Houghton, R. A., Lu, C., Tian, H., Agathokleous, E., Kattel, G. R., Sitch, S., Goll, D.,  
3256 Yue, X., Walker, A., Friedlingstein, P., Jain, A. K., Liu, S., and Zhou, G.: Forest expansion dominates China's  
3257 land carbon sink since 1980, *Nat. Commun.*, 13, 5374, <https://doi.org/10.1038/s41467-022-32961-2>, 2022.

3258 Yuan, W., Liu, D., Dong, W., Liu, S., Zhou, G., Yu, G., Zhao, T., Feng, J., Ma, Z., Chen, J., Chen, Y., Chen, S.,  
3259 Han, S., Huang, J., Li, L., Liu, H., Liu, S., Ma, M., Wang, Y., Xia, J., Xu, W., Zhang, Q., Zhao, X., and Zhao,  
3260 L.: Multiyear precipitation reduction strongly decreases carbon uptake over northern China, 119, 881–896,  
3261 <https://doi.org/10.1002/2014JG002608>, 2014.

3262 Yue, C., Ciais, P., Luysaert, S., Li, W., McGrath, M. J., Chang, J., and Peng, S.: Representing anthropogenic  
3263 gross land use change, wood harvest, and forest age dynamics in a global vegetation model ORCHIDEE-MICT  
3264 v8.4.2, 11, 409–428, <https://doi.org/10.5194/gmd-11-409-2018>, 2018.

3265 Yue, X. and Unger, N.: The Yale Interactive terrestrial Biosphere model version 1.0: description, evaluation and  
3266 implementation into NASA GISS ModelE2, *Geosci. Model Dev.*, 8, 2399–2417, <https://doi.org/10.5194/gmd-8-2399-2015>, 2015.

3267

3268 Zaehle, S. and Friend, A. D.: Carbon and nitrogen cycle dynamics in the O-CN land surface model: 1. Model  
3269 description, site-scale evaluation, and sensitivity to parameter estimates: Site-scale evaluation of a C-N model,  
3270 *Global Biogeochem. Cycles*, 24, <https://doi.org/10.1029/2009GB003521>, 2010.

3271 Zaehle, S., Ciais, P., Friend, A. D., and Prieur, V.: Carbon benefits of anthropogenic reactive nitrogen offset by  
3272 nitrous oxide emissions, *Nature Geosci.*, 4, 601–605, <https://doi.org/10.1038/ngeo1207>, 2011.

3273 Zaehle, S., Medlyn, B. E., De Kauwe, M. G., Walker, A. P., Dietze, M. C., Hickler, T., Luo, Y., Wang, Y.-P., El-Masri,  
3274 B., Thornton, P., Jain, A., Wang, S., Warland, D., Weng, E., Parton, W., Iversen, C. M., Gallet-Budynek, A.,  
3275 McCarthy, H., Finzi, A., Hanson, P. J., Prentice, I. C., Oren, R., and Norby, R. J.: Evaluation of 11 terrestrial  
3276 carbon–nitrogen cycle models against observations from two temperate Free-Air CO<sub>2</sub> Enrichment studies,  
3277 *New Phytol.*, 202, 803–822, <https://doi.org/10.1111/nph.12697>, 2014.

3278 Zeng, J., Nojiri, Y., Landschützer, P., Telszewski, M., and Nakaoka, S.: A Global Surface Ocean fCO<sub>2</sub> Climatology  
3279 Based on a Feed-Forward Neural Network, 31, 1838–1849, <https://doi.org/10.1175/JTECH-D-13-00137.1>,  
3280 2014.

3281 Zheng, B., Chevallier, F., Yin, Y., Ciais, P., Fortems-Cheiney, A., Deeter, M. N., Parker, R. J., Wang, Y., Worden, H.  
3282 M., and Zhao, Y.: Global atmospheric carbon monoxide budget 2000–2017 inferred from multi-species  
3283 atmospheric inversions, 26, 2019.

3284 Zheng, B., Ciais, P., Chevallier, F., Chuvieco, E., Chen, Y., and Yang, H.: Increasing forest fire emissions despite  
3285 the decline in global burned area, 7, eabh2646, <https://doi.org/10.1126/sciadv.abh2646>, 2021.

3286 Zscheischler, J., Mahecha, M. D., Avitabile, V., Calle, L., Carvalhais, N., Ciais, P., Gans, F., Gruber, N.,  
3287 Hartmann, J., Herold, M., Ichii, K., Jung, M., Landschützer, P., Laruelle, G. G., Lauerwald, R., Papale, D.,  
3288 Peylin, P., Poulter, B., Ray, D., Regnier, P., Rödenbeck, C., Roman-Cuesta, R. M., Schwalm, C., Tramontana,  
3289 G., Tyukavina, A., Valentini, R., van der Werf, G., West, T. O., Wolf, J. E., and Reichstein, M.: Reviews and  
3290 syntheses: An empirical spatiotemporal description of the global surface–atmosphere carbon fluxes:  
3291 opportunities and data limitations, *Biogeosciences*, 14, 3685–3703, <https://doi.org/10.5194/bg-14-3685-2017>,  
3292 2017.

3293

3294

3295

3296

3297

3298

3299 Tables

3300

Table 1. Factors used to convert carbon in various units (by convention, Unit 1 = Unit 2 × conversion).			
Unit 1	Unit 2	Conversion	Source
GtC (gigatonnes of carbon)	ppm (parts per million) (a)	2.124 (b)	Ballantyne et al. (2012)
GtC (gigatonnes of carbon)	PgC (petagrams of carbon)		1 SI unit conversion
GtCO <sub>2</sub> (gigatonnes of carbon dioxide)	GtC (gigatonnes of carbon)		3.664 44.01/12.011 in mass equivalent
GtC (gigatonnes of carbon)	MtC (megatonnes of carbon)		1000 SI unit conversion
(a) Measurements of atmospheric CO <sub>2</sub> concentration have units of dry-air mole fraction. 'ppm' is an abbreviation for micromole/mol, dry air.			
(b) The use of a factor of 2.124 assumes that all the atmosphere is well mixed within one year. In reality, only the troposphere is well mixed and the growth rate of CO <sub>2</sub> concentration in the less well-mixed stratosphere is not measured by sites from the NOAA network. Using a factor of 2.124 makes the approximation that the growth rate of CO <sub>2</sub> concentration in the stratosphere equals that of the troposphere on a yearly basis.			

Formatted Table

3301  
3302

3303

**Table 2.** How to cite the individual components of the global carbon budget presented here.

<b>Component</b>	<b>Primary reference</b>
Global fossil CO <sub>2</sub> emissions (EFOS), total and by fuel type	Updated from Andrew and Peters (2021)
National territorial fossil CO <sub>2</sub> emissions (EFOS)	Gilfillan and Marland (2022), UNFCCC (2022)
National consumption-based fossil CO <sub>2</sub> emissions (EFOS) by country (consumption)	Peters et al. (2011b) updated as described in this paper
Net land-use change flux (ELUC)	This paper (see Table 4 for individual model references).
Growth rate in atmospheric CO <sub>2</sub> concentration (GATM)	Dlugokencky and Tans (2022)
Ocean and land CO <sub>2</sub> sinks (SOCEAN and SLAND)	This paper (see Table 4 for individual model and data products references).

Formatted Table

3304

**Table 3.** Main methodological changes in the global carbon budget since 2018. Methodological changes introduced in one year are kept for the following years unless noted. Empty cells mean there were no methodological changes introduced that year. Table A7 lists methodological changes from the first global carbon budget publication up to 2017.

Publication year	Fossil fuel emissions		LUC emissions	Reservoirs			Uncertainty & other changes
	Global	Country (territorial)		Atmosphere	Ocean	Land	
2018 Le Quéré et al. (2018b) GCB2018	Revision in cement emissions; Projection includes EU-specific data	Aggregation of overseas territories into governing nations for total of 213 countries a	Average of two bookkeeping models; use of 16 DGVMs	Use of four atmospheric inversions	Based on seven models	Based on 16 models; revised atmospheric forcing from CRUNCEP to CRUJRA	Introduction of metrics for evaluation of individual models using observations
2019 Friedlingstein et al. (2019) GCB2019	Global emissions calculated as sum of all countries plus bunkers, rather than taken directly from CDIAC.		Average of two bookkeeping models; use of 15 DGVMs	Use of three atmospheric inversions	Based on nine models	Based on 16 models	
2020 Friedlingstein et al. (2020) GCB2020	Cement carbonation now included in the EFOS estimate, reducing EFOS by about 0.2GtC yr <sup>-1</sup> for the last decade	India's emissions from Andrew (2020: India); Corrections to Netherland Antilles and Aruba and Soviet emissions before 1950 as per Andrew (2020: CO <sub>2</sub> ); China's coal emissions in 2019 derived from official statistics, emissions now shown for EU27 instead of EU28. Projection for 2020 based on assessment of four approaches.	Average of three bookkeeping models; use of 17 DGVMs. Estimate of gross land use sources and sinks provided	Use of six atmospheric inversions	Based on nine models. River flux revised and partitioned NH, Tropics, SH	Based on 17 models	

Formatted: Numbering: Continuous

Formatted Table

2021	Projections are no longer an assessment of four approaches.	Official data included for a number of additional countries, new estimates for South Korea, added emissions from lime production in China.	ELUC estimate compared to the estimates adopted in national GHG inventories (NGHGI)		Average of means of eight models and means of seven data-products. Current year prediction of SOCEAN using a feed-forward neural network method	Current year prediction of SLAND using a feed-forward neural network method	
Friedlingstein et al. (2022a) GCB2021							
2022	This study		ELUC provided at country level. Decomposition into fluxes from deforestation, organic soils, <a href="#">re/afforestation and wood harvest</a> , and other transitions. Change in the methodology to derive LUC maps for Brazil to capture recent upturn in deforestation. <a href="#">Inclusion of two new datasets for peat drainage.</a>	Use of nine atmospheric inversions	Average of means of ten models and means of seven data-products	Based on 16 models. Change in the methodology to derive LUC maps for Brazil to capture recent upturn in deforestation	

Deleted: uptake in forests

3306  
3307

**Table 4. References for the process models, bookkeeping models, ocean data products, and atmospheric inversions. All models and products are updated with new data to the end of year 2021, and the atmospheric forcing for the DGVMs has been updated as described in [Appendix C.2.2](#).**

Model/data name	Reference	Change from Global Carbon Budget 2021 (Friedlingstein et al., 2022a)
<i>Bookkeeping models for land-use change emissions</i>		
BLUE	Hansis et al. (2015)	No change to model, but simulations performed with updated LUH2 forcing. Update in added peat drainage emissions (based on three spatially explicit datasets).
updated H&N2017	Houghton and Nassikas (2017)	Minor bug fix in the fuel harvest estimates, that was causing an overestimation of fuel sink. Update in added peat drainage emissions (based on three spatially explicit datasets).
OSCAR	Gasser et al. (2020)	No change to model, but land use forcing changed to LUH2-GCB2022 and FRA2020 (as used by H&N and extrapolated to 2021), both prescribed at higher spatial resolution (210 instead of 96 regions/countries). Constraining based on last year's budget data for SLAND over 1960-2021. Update in added peat drainage emissions (based on three spatially explicit datasets).
<i>Dynamic global vegetation models</i>		
CABLE-POP	Haverd et al. (2018)	changes in parameterisation. Diffuse fraction of incoming radiation read in as forcing.
CLASSIC	Melton et al. (2020) (a)	Minor bug fixes.
CLM5.0	Lawrence et al. (2019)	No change.
DLEM	Tian et al. (2015) (b)	No change.
IBIS	Yuan et al. (2014) (c)	No change.
ISAM	Meiyappan et al. (2015) (d)	No change.
JSBACH	Reick et al. (2021) (e)	No change.
JULES-ES	Wiltshire et al. (2021) (f)	Minor bug fixes. (Using JULES v6.3, suite u-co002)
LPJ-GUESS	Smith et al. (2014) (g)	No change.
LPJ	Poulter et al. (2011) (h)	No change.
LPX-Bern	Lienert and Joos (2018)	Following the results of Joos et al. (2018), we use modified parameter values which yield a more reasonable (lower) BNF, termed LPX v1.5. This parameter version has increased N immobilization and a stronger N limitation, than the previous version. The N <sub>2</sub> O Emissions were adjusted accordingly. The parameters

Formatted Table

Deleted: Section

Deleted: f)

Deleted: g)

Deleted: h)

Deleted: i)

		were obtained by running an ensemble simulation and imposing various observational constraints and subsequently adjusting N immobilization. For the methodology see Lienert et. al. (2018).
OCN	Zaehle and Friend (2010) <a href="#">(i)</a>	No change (uses r294).
ORCHIDEEv3	Vuichard et al. (2019) <a href="#">(j)</a>	No change (ORCHIDEE - V3; revision 7267)
SDGVM	Walker et al. (2017) <a href="#">(k)</a>	No change.
VISIT	Kato et al. (2013) <a href="#">(l)</a>	No change.
YIBs	Yue and Unger (2015)	No change.
<i>Global ocean biogeochemistry models</i>		
NEMO-PlankTOM12	Wright et al. (2021)	Minor bug fixes
MICOM-HAMOCC (NorESM-OCv1.2)	Schwinger et al. (2016)	No change.
MPIOM-HAMOCC6	Lacroix et al. (2021)	No change.
NEMO3.6-PISCESv2-gas (CNRM)	Berthet et al. (2019) <a href="#">(m)</a>	No change.
FESOM-2.1-REcoM2	Hauck et al. (2020) <a href="#">(n)</a>	Extended spin-up, minor bug fixes
MOM6-COBALT (Princeton)	Liao et al. (2020)	No change
CESM-ETHZ	Doney et al. (2009)	Changed salinity restoring in the surface ocean from 700 days to 300 days, except for the Southern Ocean south of 45S, where the restoring timescale was set to 60 days.
NEMO-PISCES (IPSL)	Aumont et al. (2015)	No change.
MRI-ESM2-1	Nakano et al. (2011), Urakawa et al. (2020)	New this year.
CESM2	Long et al. (2021) <a href="#">(o)</a>	New this year.
<i>ocean data products</i>		
MPI-SOMFFN	Landschützer et al. (2016)	update to SOCATv2022 measurements and timeperiod 1982-2021; The estimate now covers the full ocean domain as well as the Arctic Ocean extension described in: Landschützer, P., Laruelle, G. G., Roobaert, A., and Regnier, P.: A uniform pCO2

Deleted: j)

Deleted: k)

Deleted: l)

Deleted: m)

Deleted: n)

Deleted: o)

Deleted: p)

		climatology combining open and coastal oceans, Earth Syst. Sci. Data, 12, 2537–2553, <a href="https://doi.org/10.5194/essd-12-2537-2020">https://doi.org/10.5194/essd-12-2537-2020</a> , 2020.
Jena-MLS	Rödenbeck et al. (2022)	update to SOCATv2022 measurements, time period extended to 1957-2021
CMEMS-LSCE-FFNNv2	Chau et al. (2022)	Update to SOCATv2022 measurements and time period 1985-2021. The CMEMS-LSCE-FFNNv2 product now covers both the open ocean and coastal regions.
LDEO-HPD	Gloege et al. (2022) <a href="#">(p)</a>	New this year
UOEx-Watson	Watson et al. (2020)	Updated to SOCAT v2022 and OISSTv2.1, as recalculated by Holding et al.
NIES-NN	Zeng et al. (2014)	Updated to SOCAT v2022. Small changes in method (gas-exchange coefficient $\alpha = 0.271$ ; trend calculation 1990-2020, predictors include lon and lat)
JMA-MLR	Iida et al. (2021)	Updated to SOCATv2022 SST fields (MGDSST) updated
OS-ETHZ-GRaCER	Gregor and Gruber (2021)	No change
<i>Atmospheric inversions</i>		
CAMS	Chevallier et al. (2005) <a href="#">(q)</a>	Updated to WMOX2019 scale. Extension to year 2021, revision of the station list, update of the prior fluxes
CarbonTracker Europe (CTE)	van der Laan-Luijkx et al. (2017)	Updated to WMOX2019 scale. Biosphere prior fluxes from the SiB4 model instead of SiBCASA model. Extension to 2021.
Jena CarboScope	Rödenbeck et al. (2018) <a href="#">(r)</a>	Updated to WMOX2019 scale. Extension to 2021.
UoE in-situ	Feng et al., (2016) <a href="#">(s)</a>	Updated to WMOX2019 scale. Updated station list, and refined land-ocean map. Extension to 2021.
NISMON-CO2	Niwa et al., (2022) <a href="#">(t)</a>	Updated to WMOX2019 scale. Positive definite flux parameters and updated station list. Extension to 2021.
CMS-Flux	Liu et al., (2021)	Updated to WMOX2019 scale. Extension to 2021.
GONGGA	Jin et al. (2022 in review) <a href="#">(u)</a>	New this year.
THU	Kong et al. (2022)	New this year.
CAMS-Satellite	Chevallier et al. (2005) (r)	New this year.
(a) see also Asaadi et al. (2018).		
(b) see also Tian et al. (2011)		
(c) the dynamic carbon allocation scheme was presented by Xia et al. (2015)		
(d) see also Jain et al. (2013). Soil biogeochemistry is updated based on Shu et al. (2020)		

Deleted: q)

Deleted: r)

Deleted: s)

Deleted: t)

Deleted: u)

Deleted: v)

(e) see also [Mauritsen et al. \(2019\)](#).

(f) see also [Sellar et al. \(2019\)](#) and [Burton et al., \(2019\)](#). JULES-ES is the Earth System configuration of the Joint UK Land Environment Simulator as used in the UK Earth System Model (UKESM).

(g) to account for the differences between the derivation of shortwave radiation from CRU cloudiness and DSWRF from CRUJRA, the photosynthesis scaling parameter  $\alpha$  was modified (-15%) to yield similar results.

(h) compared to published version, decreased LPJ wood harvest efficiency so that 50 % of biomass was removed off-site compared to 85 % used in the 2012 budget. Residue management of managed grasslands increased so that 100 % of harvested grass enters the litter pool.

(i) see also [Zaehle et al. \(2011\)](#).

(j) see also [Zaehle and Friend \(2010\)](#) and [Krinner et al. \(2005\)](#).

(k) see also [Woodward and Lomas \(2004\)](#).

(l) see also [Ito and Inatomi \(2012\)](#).

(m) see also [Séférian et al. \(2019\)](#).

(n) see also [Schourup-Kristensen et al \(2014\)](#).

(o) see also [Yeager et al. \(2022\)](#).

(p) see also [Bennington et al. \(2022\)](#).

(q) see also [Remaud \(2018\)](#).

(r) see also [Rödenbeck et al. \(2003\)](#).

(s) see also [Feng et al. \(2009\)](#) and [Palmer et al. \(2019\)](#).

(t) see also [Niwa et al. \(2020\)](#).

(u) see also [Tian et al. \(2014\)](#).

- Deleted: Decharme
- Deleted: and Seferian et al. (2019)
- Moved (insertion) [7]
- Deleted: (f) see also Mauritsen et al. (2019)
- Moved up [7]: see also Sellar et al. (2019) and Burton et al., (2019). JULES-ES is the Earth System configuration of the Joint UK Land Environment Simulator as used in the UK Earth System Model (UKESM).
- Deleted: (g)
- Deleted: (h) to account for the differences between the derivation of shortwave radiation from CRU cloudiness and DSWRF from CRUJRA, the photosynthesis scaling parameter  $\alpha$  was modified (-15%) to yield similar results.
- Deleted: (i) compared to published version, decreased LPJ wood harvest efficiency so that 50 % of biomass was removed off-site compared to 85 % used in the 2012 budget. Residue management of managed grasslands increased so that 100 % of harvested grass enters the litter pool.
- Deleted: 2011.
- Deleted: Zaehle
- Deleted: Friend (2010) and Krinner et al. (2005)
- Deleted: Woodward
- Deleted: Lomas (2004)
- Deleted: Ito and Inatomi (2012).
- Deleted: Séférian
- Deleted: . (2019)
- Deleted: Schourup-Kristensen
- Deleted: (2014)
- Deleted: Yeager
- Deleted: Bennington et al. (2022)
- Deleted: Remaud (2018)
- Deleted: (s)
- Deleted: Rödenbeck
- Deleted: (2003)
- Deleted: Feng
- Deleted: (2009) and Palmer et al. (2019)
- Deleted: Niwa
- Deleted: 2020)
- Deleted: (v) see also Tian et al. (2014)



3400  
 3401  
 3402  
 3403  
 3404  
 3405  
 3406  
 3407  
 3408  
 3409  
 3410  
 3411  
 3412  
 3413  
 3414  
 3415

Formatted: Font: Bold

**Table 6. Decadal mean in the five components of the anthropogenic CO<sub>2</sub> budget for different periods, and last year available. All values are in GtC yr<sup>-1</sup>, and uncertainties are reported as ±1σ. Fossil CO<sub>2</sub> emissions include cement carbonation. The table also shows the budget imbalance (B<sub>IM</sub>), which provides a measure of the discrepancies among the nearly independent estimates. A positive imbalance means the emissions are overestimated and/or the sinks are too small. All values are rounded to the nearest 0.1 GtC and therefore columns do not necessarily add to zero.**

		<i>Mean (GtC/yr)</i>							
		1960s	1970s	1980s	1990s	2000s	2012-2021	2021	2022 (Projection)
Total emissions (EFOS + ELUC)	Fossil CO <sub>2</sub> emissions (EFOS)	3±0.2	4.7±0.2	5.5±0.3	6.3±0.3	7.7±0.4	9.6±0.5	9.9±0.5	10±0.5
	Land-use change emissions (ELUC)	1.5±0.2	1.2±0.2	1.3±0.2	1.5±0.2	1.4±0.2	1.2±0.2	1.1±0.2	1±0.7
	Total emissions	4.5±0.7	5.9±0.7	6.8±0.8	7.8±0.8	9.1±0.8	10.8±0.8	10.9±0.9	10.9±0.9
Partitioning	Growth rate in atmos CO <sub>2</sub> (GATM)	1.7±0.07	2.8±0.07	3.4±0.02	3.1±0.02	4±0.02	5.2±0.02	5.2±0.2	5.5±0.4
	Ocean sink (SOCEAN)	1.1±0.4	1.4±0.4	1.8±0.4	2.1±0.4	2.3±0.4	2.9±0.4	2.9±0.4	2.9±0.4
	Terrestrial sink (SLAND)	1.2±0.4	2.2±0.5	1.9±0.7	2.5±0.4	2.7±0.5	3.1±0.6	3.5±0.9	3.4±0.9

	1960s	1970s	1980s	1990s	2000s	2012-2021	2021	2022 (Projection)
Budget Imbalance (BIM+E FOS+E LUC- (GATM +SOCE AN+SL AND))	0.4	-0.4	-0.3	0.1	0.1	-0.3	-0.6	-0.9

\*Fossil emissions excluding the cement carbonation sink amount to 3.1±0.2 GtC/yr, 4.7±0.2 GtC/yr, 5.5±0.3 GtC/yr, 6.4±0.3 GtC/yr, 7.9±0.4 GtC/yr, and 9.8±0.5 GtC/yr for the decades 1960s to 2010s respectively and to 10.1±0.5 GtC/yr for 2021, and 10.2±0.5 GtC/yr for 2022.

3416

**Table 7.** Comparison of the projection with realised fossil CO2 emissions (EFOS). The ‘Actual’ values are first the estimate available using actual data, and the ‘Projected’ values refers to estimates made before the end of the year for each publication. Projections based on a different method from that described here during 2008-2014 are available in Le Quéré et al., (2016). All values are adjusted for leap years.

	World		China		USA		EU28 / EU27 (i)		India		Rest of World	
	Project ed	Actual	Proje cted	Actual	Proje cted	Actual	Proje cted	Actual	Proje cted	Actual	Proje cted	Actual
2015 (a)	-0.6% (-1.6 to 0.5)	0.06%	-3.9% (-4.6 to -1.1)	-0.7%	-1.5% (-5.5 to 0.3)	-2.5%	-	-	-	-	1.2% (-0.2 to 2.6)	1.2%
2016 (b)	-0.2% (-1.0 to +1.8)	0.20%	-0.5% (-3.8 to +1.3)	-0.3%	-1.7% (-4.0 to +0.6)	-2.1%	-	-	-	-	1.0% (-0.4 to +2.5)	1.3%
2017 (c)	2.0% (+0.8 to +3.0)	1.6%	3.5% (+0.7 to +5.4)	1.5%	-0.4% (-2.7 to +1.0)	-0.5%	-	-	2.00% (+0.2 to +3.8)	3.9%	1.6% (0.0 to +3.2)	1.9%
2018 (d)	2.7% (+1.8 to +3.7)	2.1%	4.7% (+2.0 to +7.4)	2.3%	2.5% (+0.5 to +4.5)	2.8%	-0.7% (-2.6 to +1.3)	-2.1%	6.3% (+4.3 to +8.3)	8.0%	1.8% (+0.5 to +3.0)	1.7%
2019 (e)	0.5% (-0.3 to +1.4)	0.1%	2.6% (+0.7 to +4.4)	2.2%	-2.4% (-4.7 to -0.1)	-2.6%	-1.7% (-5.1 to +1.8%)	-4.3%	1.8% (-0.7 to +3.7)	1.0%	0.5% (-0.8 to +1.8)	0.5%
2020 (f)	-6.7%	-5.4%	-1.7%	1.4%	-12.2%	-10.6%	-11.3% (EU27)	-10.9%	-9.1%	-7.3%	-7.4%	-7.0%
2021 (g)	4.8% (4.2 to 5.4%)	5.1%	4.3% (3.0 to 5.4%)	3.5%	6.8% (6.6 to 7.0%)	6.2%	6.3% (4.3 to 8.3%)	6.8%	11.2% (10.7 to 11.7%)	11.1%	3.2% (2.0 to 4.3%)	4.5%
2022 (h)	1.1% (0% to 1.7%)		-1.5% (-3.0 to 0.1%)		1.6% (-0.9 to 4.1%)		-1.0% (-2.9 to 1.0%)		5.6% (3.5 to 7.7%)		2.5% (0.1 to 2.3%)	

(a) Jackson et al. (2016) and Le Quéré et al. (2015a). (b) Le Quéré et al. (2016). (c) Le Quéré et al. (2018a). (d) Le Quéré et al. (2018b). (e) Friedlingstein et al., (2019), (f) Friedlingstein et al., (2020), (g) Friedlingstein et al., (2022a), (h) This study

(i) EU28 until 2019, EU27 from 2020

		1960s	1970s	1980s
Total emissions (EFOS + ELUC)	Fossil CO2 emissions (EFOS)	3±0.2	4.7±0.2	5.1±0.2
	Land-use change emissions (ELUC)	1.5±0.7	1.2±0.7	1.1±0.7
	Total emissions	4.5±0.7	5.9±0.7	6.2±0.7
Partitioning	Growth rate in annual CO2 (GATM)	1.7±0.07	2.8±0.07	3.0±0.07
	Ocean sink (SOCEAN)	1.1±0.4	1.4±0.4	1.5±0.4
	Terrestrial sink (SLAND)	1.2±0.4	2.2±0.5	2.3±0.5
Budget Imbalance	BIM=EFOS+ELUC-(GATM+SOCEAN+SLAND)	0.4	-0.4	-0.4

\*Fossil emissions excluding the cement carbonation sink amount and 9.8±0.5 GtC/yr for the decades 1960s to 2010s respectively!

**Deleted:** Section Break (Next Page)

**Formatted:** Numbering: Continuous

**Formatted Table**

**Formatted Table**

421  
422  
423  
424  
425  
426  
427  
428  
429

**Table 8. Cumulative CO<sub>2</sub> for different time periods in gigatonnes of carbon (GtC). Fossil CO<sub>2</sub> emissions include cement carbonation. The budget imbalance (B<sub>IM</sub>) provides a measure of the discrepancies among the nearly independent estimates. All values are rounded to the nearest 5 GtC and therefore columns do not necessarily add to zero. Uncertainties are reported as follows: E<sub>FOS</sub> is 5% of cumulative emissions; E<sub>LUC</sub> prior to 1959 is 1σ spread from the DGVMs, E<sub>LUC</sub> post-1959 is 0.7\*number of years (where 0.7 GtC/yr is the uncertainty on the annual ELUC flux estimate); G<sub>ATM</sub> uncertainty is held constant at 5 GtC for all time periods; S<sub>OCEAN</sub> uncertainty is 20% of the cumulative sink (20% relates to the annual uncertainty of 0.4 GtC/yr, which is ~20% of the current ocean sink); and S<sub>LAND</sub> is the 1σ spread from the DGVMs estimates.**

		<a href="#">1750-2021</a>	<a href="#">1850-2014</a>	<a href="#">1850-2021</a>	<a href="#">1960-2021</a>	<a href="#">1850-2022</a>
Emissions	<a href="#">Fossil CO2 emissions (EFOS)</a>	<a href="#">470±25</a>	<a href="#">400±20</a>	<a href="#">465±25</a>	<a href="#">385±20</a>	<a href="#">475±25</a>
	<a href="#">Land-use change emissions (ELUC)</a>	<a href="#">235±70</a>	<a href="#">195±60</a>	<a href="#">205±60</a>	<a href="#">85±45</a>	<a href="#">205±60</a>
	<a href="#">Total emissions</a>	<a href="#">700±75</a>	<a href="#">595±60</a>	<a href="#">670±65</a>	<a href="#">470±50</a>	<a href="#">680±65</a>
Partitioning	<a href="#">Growth rate in atmos CO2 (GATM)</a>	<a href="#">295±5</a>	<a href="#">235±5</a>	<a href="#">275±5</a>	<a href="#">210±5</a>	<a href="#">280±5</a>
	<a href="#">Ocean sink (SOCEAN)</a>	<a href="#">185±35</a>	<a href="#">155±30</a>	<a href="#">175±35</a>	<a href="#">120±25</a>	<a href="#">180±35</a>
	<a href="#">Terrestrial sink (SLAND)</a>	<a href="#">230±50</a>	<a href="#">185±40</a>	<a href="#">210±45</a>	<a href="#">145±30</a>	<a href="#">210±45</a>
Budget imbalance	<a href="#">BIM=EFOS+ELUC-(GATM+SOCEAN+SLAND)</a>	<a href="#">-5</a>	<a href="#">15</a>	<a href="#">15</a>	<a href="#">-5</a>	<a href="#">10</a>

430  
431  
432  
433

434  
435  
436

**Table 9: Mapping of global carbon cycle models' land flux definitions to the definition of the LULUCF net flux used in national Greenhouse Gas Inventories reported to UNFCCC. See Sec. C.2.3 and Tab. A8 for detail on methodology and comparison to other datasets.**

	2002-2011	2012-2021
ELUC from bookkeeping estimates (from Table 5)	1.4	1.2
SLAND on non-intact forest from DGVMs	-1.7	-1.8
ELUC plus SLAND on non-intact forests	-0.3	-0.6
National Greenhouse Gas Inventories	-0.4	-0.5

437  
438

		1750-2021
Emissions	Fossil CO2 emissions (EFOS)	470±25
	Land-use change emissions (ELUC)	235±70
	Total emissions	700±75
Partitioning	Growth rate in atmos CO2 (GATM)	295±5
	Ocean sink (SOCEAN)	185±35
	Terrestrial sink (SLAND)	230±50
Budget imbalance	BIM=EFOS+ELUC-(GATM+SOCEAN+SLAND)	-5

**Deleted:**

**Formatted: Font: 10 pt**

**Formatted Table**

**Table 10.** Major known sources of uncertainties in each component of the Global Carbon Budget, defined as input data or processes that have a demonstrated effect of at least  $\pm 0.3$  GtC yr<sup>-1</sup>.

Source of uncertainty	Time scale (years)	Location	Status	Evidence
Fossil CO <sub>2</sub> emissions (EFOS; Section 2.1)				
energy statistics	annual to decadal	global, but mainly China & major developing countries	see Sect. 2.1	(Korsbakken et al., 2016, Guan et al., 2012)
carbon content of coal	annual to decadal	global, but mainly China & major developing countries	see Sect. 2.1	(Liu et al., 2015)
system boundary	annual to decadal	all countries	see Sect. 2.1	(Andrew, 2020)
Net land-use change flux (ELUC; section 2.2)				
land-cover and land-use change statistics	continuous	global; in particular tropics	see Sect. 2.4	(Houghton et al., 2012, Gasser et al., 2020, Ganzenmüller et al., 2022, Yu et al. 2022)
sub-grid-scale transitions	annual to decadal	global	see Sect. 2.4, Table A1	(Wilkenskjeld et al., 2014)
vegetation biomass	annual to decadal	global; in particular tropics	see Sect. 2.4	(Houghton et al., 2012, Bastos et al., 2021)
forest degradation (fire, selective logging)	annual to decadal	tropics	see Sect. 3.2.2, Table A1	(Aragão et al., 2018, Qin et al., 2020)
wood and crop harvest	annual to decadal	global; SE Asia	see Table A1	(Arneth et al., 2017, Erb et al., 2018)
peat burning (a)	multi-decadal trend	global	see Table A1	(van der Werf et al., 2010, 2017)
loss of additional sink capacity	multi-decadal trend	global	not included; see Appendix D4	(Pongratz et al., 2014, Gasser et al., 2020; Obermeier et al., 2021)
Atmospheric growth rate (GATM; section 2.3) no demonstrated uncertainties larger than $\pm 0.3$ GtC yr <sup>-1</sup> (b)				
Ocean sink (SOCEAN; section 2.4)				
sparsity in surface fCO <sub>2</sub> observations	mean, decadal variability and trend	global, in particular southern hemisphere	see Sect 3.5.2	(Gloege et al., 2021, Denvil-Sommer et al., 2021, Bushinsky et al., 2019)
riverine carbon outgassing and its anthropogenic perturbation	annual to decadal	global, in particular partitioning between Tropics and South	see Sect. 2.4 (anthropogenic perturbations not included)	(Aumont et al., 2001, Resplandy et al., 2018, Lacroix et al., 2020)
Models underestimate interior ocean	annual to decadal	global	see Sect 3.5.5	(Friedlingstein et al., 2021, this study, see also Terhaar et al., 2022)

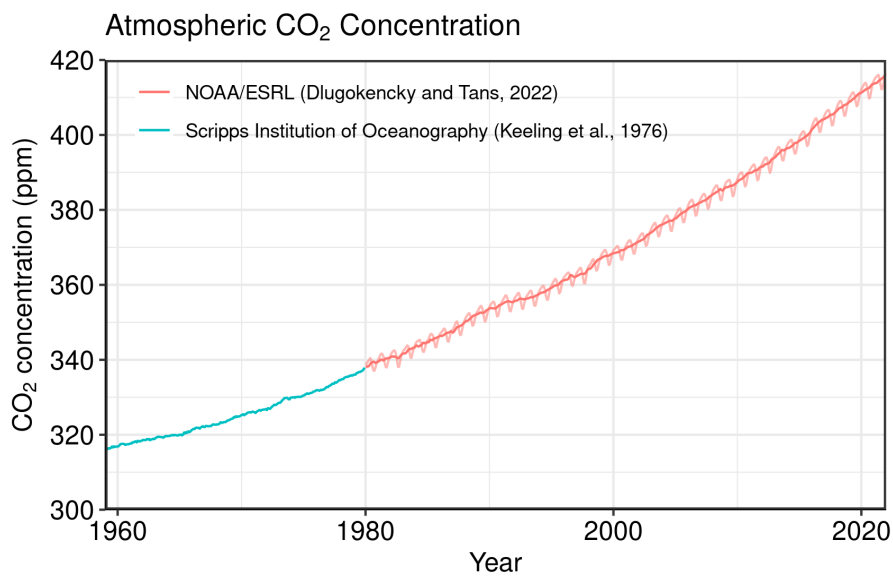
Formatted Table

anthropogenic carbon storage				
near-surface temperature and salinity gradients	mean on all time-scales	global	see Sect. 3.8.2	(Watson et al., 2020; Dong et al., 2022)
Land sink (SLAND; section 2.5)				
strength of CO2 fertilisation	multi-decadal trend	global	see Sect. 2.5	(Wenzel et al., 2016; Walker et al., 2021)
response to variability in temperature and rainfall	annual to decadal	global; in particular tropics	see Sect. 2.5	(Cox et al., 2013; Jung et al., 2017; Humphrey et al., 2018; 2021)
nutrient limitation and supply	annual to decadal	global		(Zaehle et al., 2014)
carbon allocation and tissue turnover rates	annual to decadal	global		(De Kauwe et al., 2014; O'Sullivan et al., 2022)
tree mortality	annual	global in particular tropics	see Sect. 2.5	(Hubau et al., 2021; Brienen et al., 2020)
response to diffuse radiation	annual	global	see Sect. 2.5	(Mercado et al., 2009; O'Sullivan et al., 2021)
(a) As result of interactions between land-use and climate				
(b) The uncertainties in GATM have been estimated as $\pm 0.2 \text{ GtC yr}^{-1}$ , although the conversion of the growth rate into a global annual flux assuming instantaneous mixing throughout the atmosphere introduces additional errors that have not yet been quantified.				

441

Figures and Captions

Formatted: Indent: Left: 0.63 cm, Hanging: 0.63 cm



442

443

444

445

446

447

448

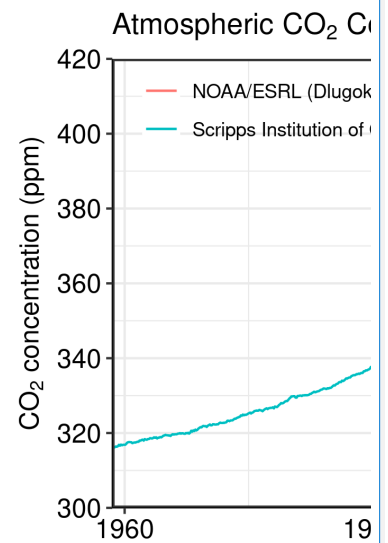
449

450

451

452

Figure 1. Surface average atmospheric CO<sub>2</sub> concentration (ppm). Since 1980, monthly data are from NOAA/GML (Dlugokencky and Tans, 2022) and are based on an average of direct atmospheric CO<sub>2</sub> measurements from multiple stations in the marine boundary layer (Masarie and Tans, 1995). The 1958-1979 monthly data are from the Scripps Institution of Oceanography, based on an average of direct atmospheric CO<sub>2</sub> measurements from the Mauna Loa and South Pole stations (Keeling et al., 1976). To account for the difference of mean CO<sub>2</sub> and seasonality between the NOAA/GML and the Scripps station networks used here, the Scripps surface average (from two stations) was de-seasonalised and adjusted to match the NOAA/GML surface average (from multiple stations) by adding the mean difference of 0.667 ppm, calculated here from overlapping data during 1980-2012.



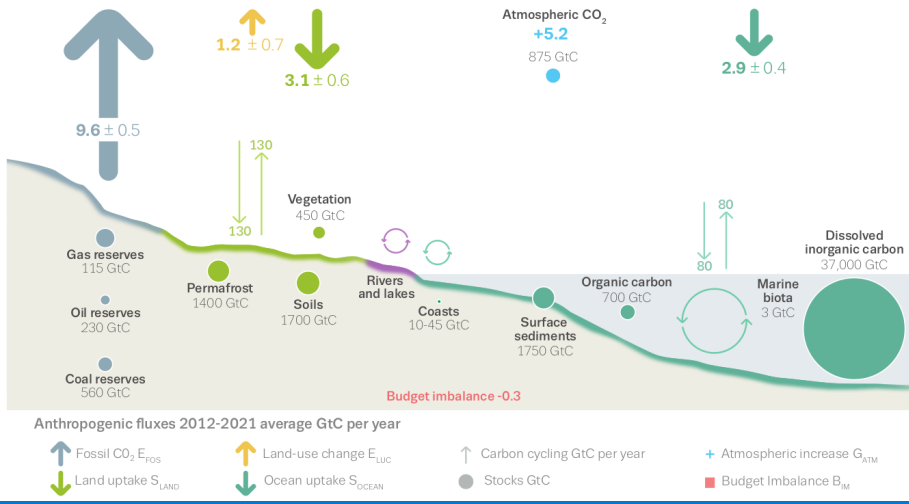
Deleted:

Deleted: ESRL

Deleted: ESRL

Deleted: ESRL

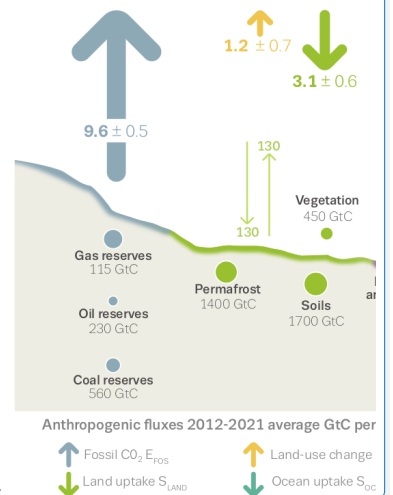
# The global carbon cycle



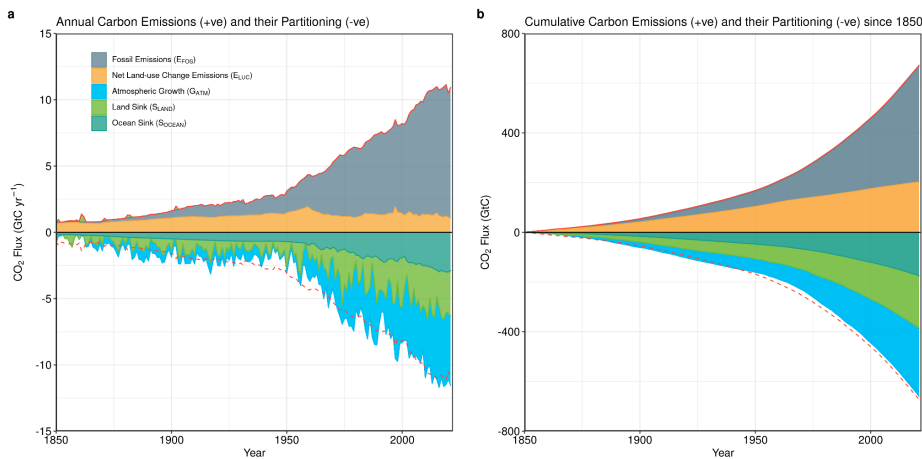
Formatted Table

Figure 2. Schematic representation of the overall perturbation of the global carbon cycle caused by anthropogenic activities, averaged globally for the decade 2012-2021. See legends for the corresponding arrows and units. The uncertainty in the atmospheric CO<sub>2</sub> growth rate is very small (±0.02 GtC yr<sup>-1</sup>) and is neglected for the figure. The anthropogenic perturbation occurs on top of an active carbon cycle, with fluxes and stocks represented in the background and taken from Canadell et al. (2021) for all numbers, except for the carbon stocks in coasts which is from a literature review of coastal marine sediments (Price and Warren, 2016).

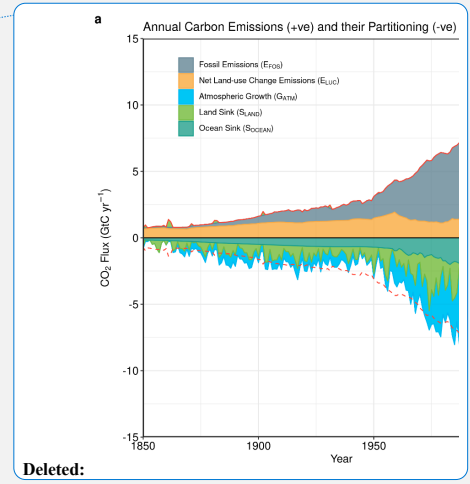
# The global carbon cycle



Deleted:  
Formatted: Not Superscript/ Subscript



**Figure 3. Combined components of the global carbon budget illustrated in Figure 2 as a function of time, for fossil CO<sub>2</sub> emissions ( $E_{FOS}$ , including a small sink from cement carbonation; grey) and emissions from land-use change ( $E_{LUC}$ ; brown), as well as their partitioning among the atmosphere ( $G_{ATM}$ ; cyan), ocean ( $S_{OCEAN}$ ; blue), and land ( $S_{LAND}$ ; green). Panel (a) shows annual estimates of each flux and panel (b) the cumulative flux (the sum of all prior annual fluxes) since the year 1850. The partitioning is based on nearly independent estimates from observations (for  $G_{ATM}$ ) and from process model ensembles constrained by data (for  $S_{OCEAN}$  and  $S_{LAND}$ ) and does not exactly add up to the sum of the emissions, resulting in a budget imbalance ( $BI_M$ ) which is represented by the difference between the bottom red line (mirroring total emissions) and the sum of carbon fluxes in the ocean, land, and atmosphere reservoirs. All data are in  $GtC\ yr^{-1}$  (panel a) and  $GtC$  (panel b). The  $E_{FOS}$  estimate is based on a mosaic of different datasets, and has an uncertainty of  $\pm 5\%$  ( $\pm 1\sigma$ ). The  $E_{LUC}$  estimate is from three bookkeeping models (Table 4) with uncertainty of  $\pm 0.7\ GtC\ yr^{-1}$ . The  $G_{ATM}$  estimates prior to 1959 are from Joos and Spahni (2008) with uncertainties equivalent to about  $\pm 0.1-0.15\ GtC\ yr^{-1}$  and from Dlugokencky and Tans (2022) since 1959 with uncertainties of about  $\pm 0.07\ GtC\ yr^{-1}$  during 1959-1979 and  $\pm 0.02\ GtC\ yr^{-1}$  since 1980. The  $S_{OCEAN}$  estimate is the average from Khatiwala et al. (2013) and DeVries (2014) with uncertainty of about  $\pm 30\%$  prior to 1959, and the average of an ensemble of models and an ensemble of  $fCO_2$  data products (Table 4) with uncertainties of about  $\pm 0.4\ GtC\ yr^{-1}$  since 1959. The  $S_{LAND}$  estimate is the average of an ensemble of models (Table 4) with uncertainties of about  $\pm 1\ GtC\ yr^{-1}$ . See the text for more details of each component and their uncertainties.**



Deleted:

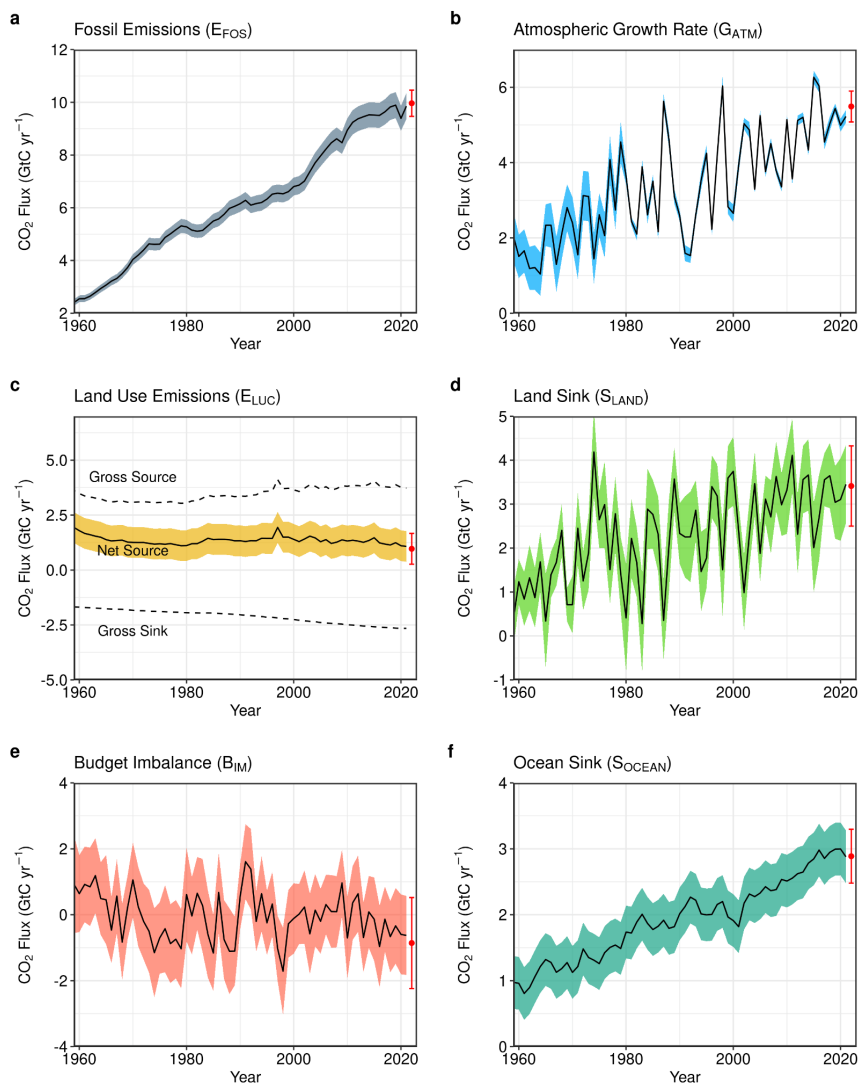
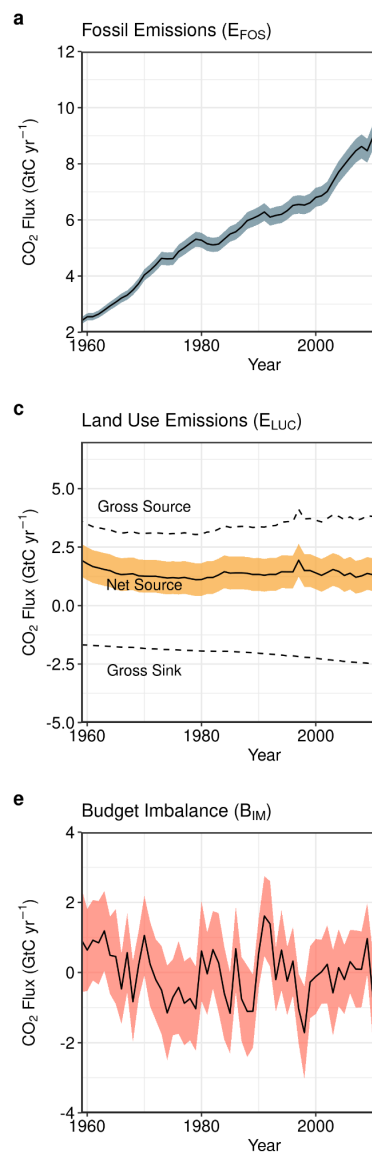


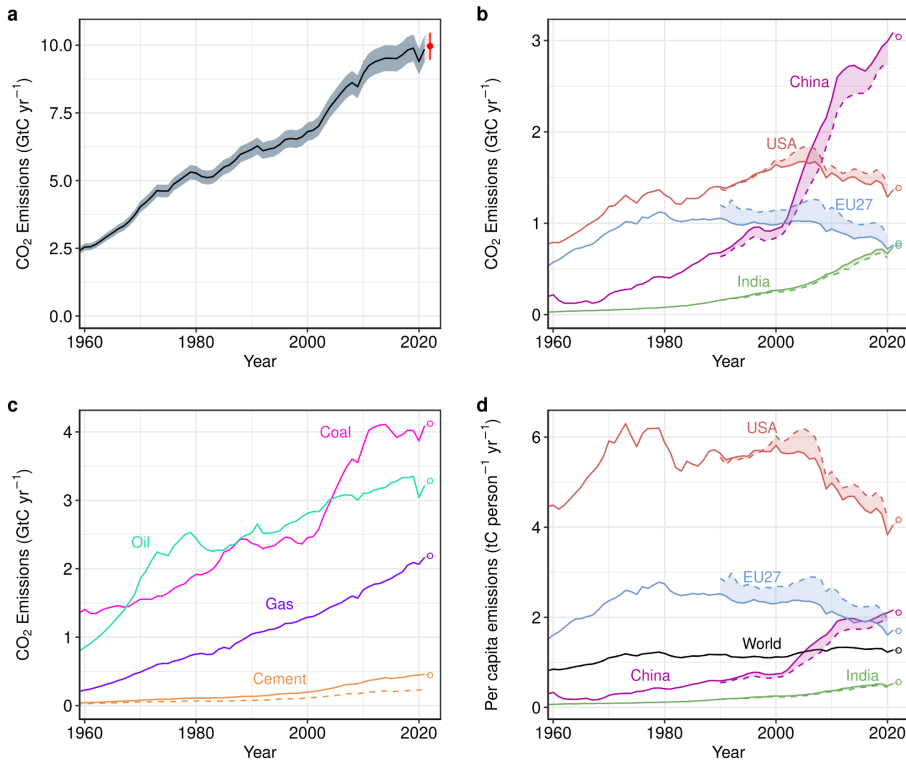
**Figure 4.** Components of the global carbon budget and their uncertainties as a function of time, presented individually for (a) fossil CO<sub>2</sub> and cement carbonation emissions ( $E_{FOS}$ ), (b) growth rate in atmospheric CO<sub>2</sub> concentration ( $G_{ATM}$ ), (c) emissions from land-use change ( $E_{LUC}$ ), (d) the land CO<sub>2</sub> sink ( $S_{LAND}$ ), (e) the ocean CO<sub>2</sub> sink ( $S_{OCEAN}$ ), (f) the budget imbalance that is not accounted for by the other terms. Positive values of  $S_{LAND}$  and  $S_{OCEAN}$  represent a flux from the atmosphere to land or the ocean. All data are in GtC yr<sup>-1</sup> with the uncertainty bounds representing  $\pm 1$  standard deviation in shaded colour. Data sources are as in Figure 3. The red dots indicate our projections for the year 2022 and the red error bars the uncertainty in the projections (see methods).

Formatted: Indent: Left: 1.27 cm



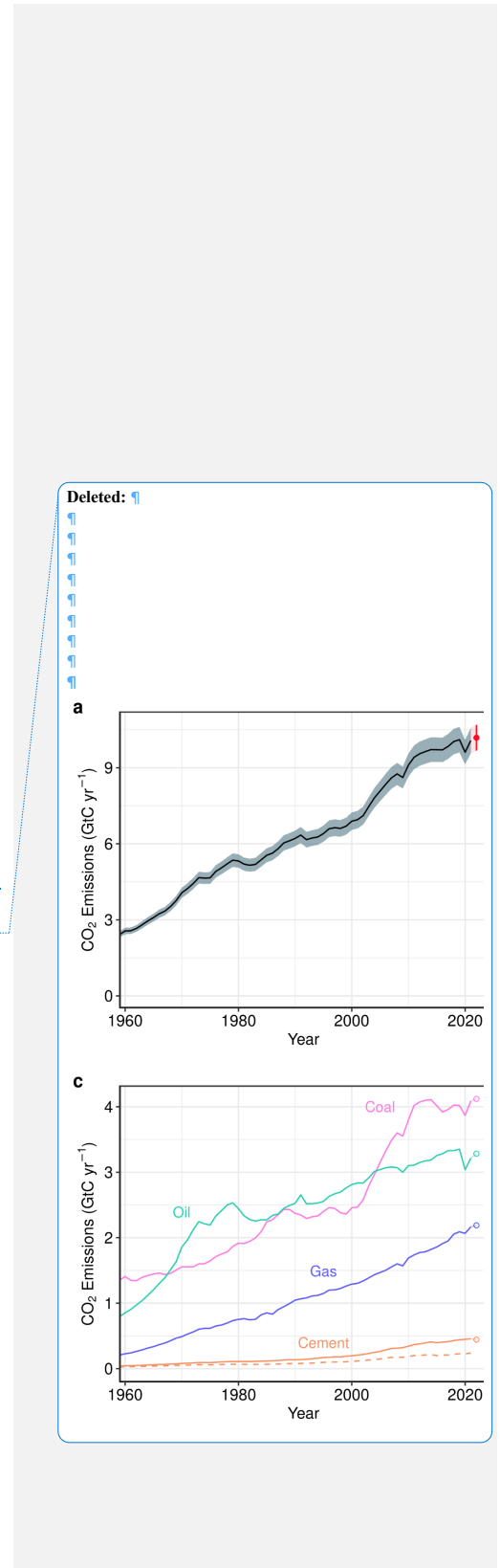
Deleted:

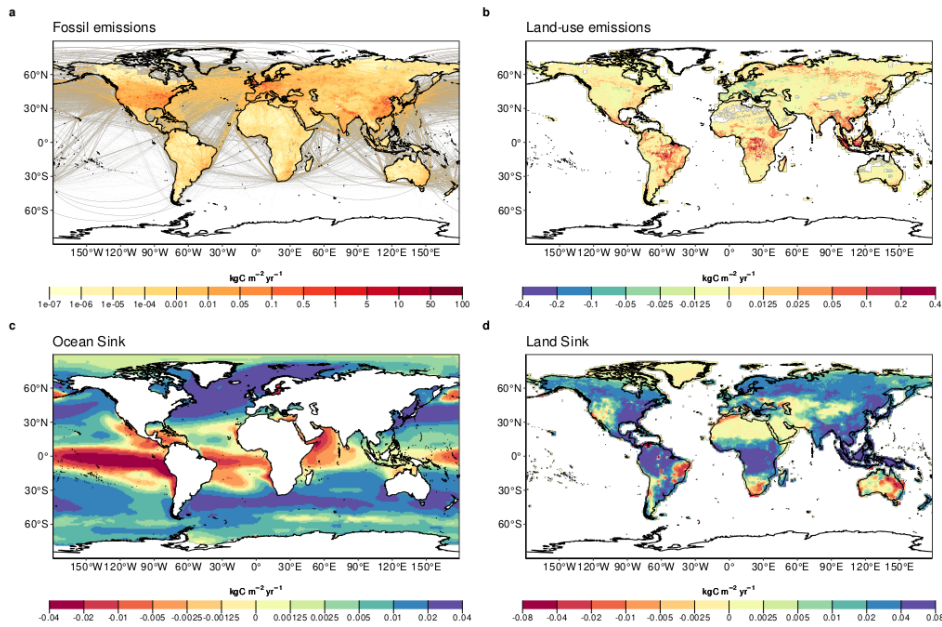
480  
481  
482  
483  
484  
485  
486  
487



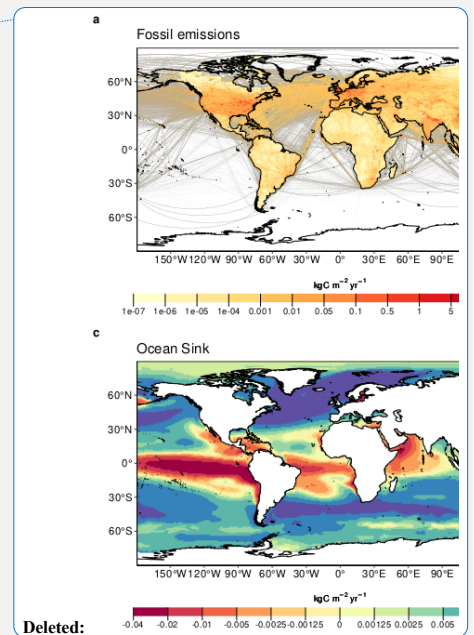
490  
491  
492  
493  
494  
495  
496  
497  
498  
499  
500

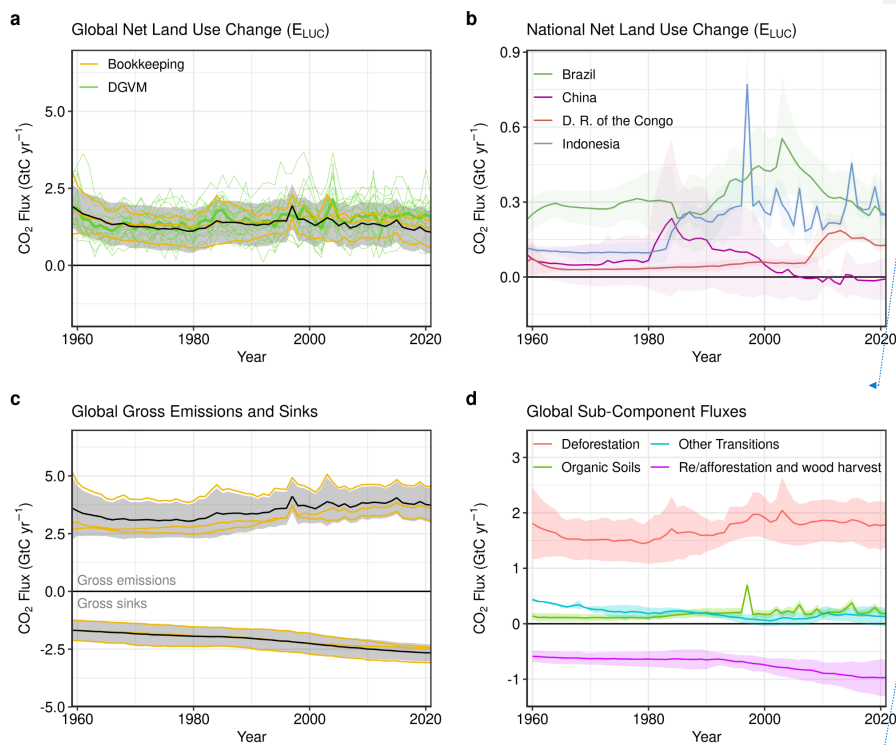
**Figure 5.** Fossil CO<sub>2</sub> emissions for (a) the globe, including an uncertainty of  $\pm 5\%$  (grey shading) and a projection through the year 2022 (red dot and uncertainty range), (b) territorial (solid lines) and consumption (dashed lines) emissions for the top three country emitters (USA, China, India) and for the European Union (EU27), (c) global emissions by fuel type, including coal, oil, gas, and cement, and cement minus cement carbonation (dashed), and (d) per-capita emissions the world and for the large emitters as in panel (b). Territorial emissions are primarily from a draft update of Gilfillan and Marland (2021) except for national data for Annex I countries for 1990-2020, which are reported to the UNFCCC as detailed in the text, as well as some improvements in individual countries, and extrapolated forward to 2021 using BP Energy Statistics. Consumption-based emissions are updated from Peters et al. (2011b). See Section 2.1 and Appendix C.1 for details of the calculations and data sources.





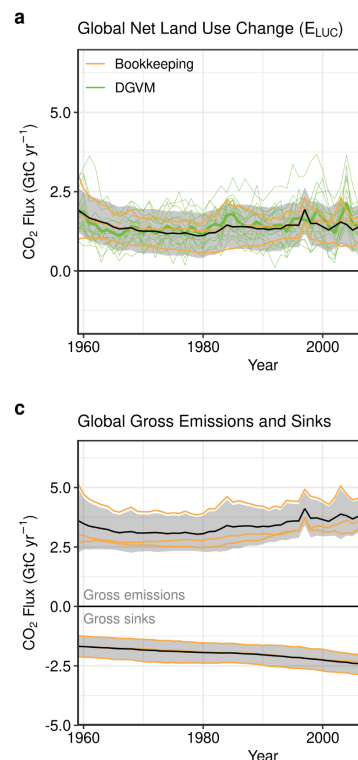
513 **Figure 6.** The 2012-2021 decadal mean components of the global carbon budget, presented for (a) fossil CO<sub>2</sub>
 514 emissions ( $E_{FOS}$ ), (b) land-use change emissions ( $E_{LUC}$ ), (c) the ocean CO<sub>2</sub> sink ( $S_{OCEAN}$ ), and (d) the land CO<sub>2</sub> sink
 515 ( $S_{LAND}$ ). Positive values for  $E_{FOS}$  and  $E_{LUC}$  represent a flux to the atmosphere, whereas positive values of  $S_{OCEAN}$  and
 516  $S_{LAND}$  represent a flux from the atmosphere to the ocean or the land. In all panels, yellow/red (green/blue) colours
 517 represent a flux from (into) the land/ocean to (from) the atmosphere. All units are in  $\text{kgC m}^{-2} \text{yr}^{-1}$ . Note the different
 518 scales in each panel.  $E_{FOS}$  data shown is from GCP-GridFEDv2022.2.  $E_{LUC}$  data shown is only from BLUE as the
 519 updated H&N2017 and OSCAR do not resolve gridded fluxes.  $S_{OCEAN}$  data shown is the average of GOBMs and
 520 data-products means, using GOBMs simulation A, no adjustment for bias and drift applied to the gridded fields
 521 (see Section 2.4).  $S_{LAND}$  data shown is the average of DGVMs for simulation S2 (see Section 2.5).





Formatted: Indent: Left: 1.27 cm

**Figure 7. Net CO<sub>2</sub> exchanges between the atmosphere and the terrestrial biosphere related to land use change.** (a) Net CO<sub>2</sub> emissions from land-use change ( $E_{LUC}$ ) with estimates from the three bookkeeping models (yellow lines) and the budget estimate (black with  $\pm 1\sigma$  uncertainty), which is the average of the three bookkeeping models. Estimates from individual DGVMs (narrow green lines) and the DGVM ensemble mean (thick green line) are also shown. (b) Net CO<sub>2</sub> emissions from land-use change from the four countries with largest cumulative emissions since 1959. Values shown are the average of the three bookkeeping models, with shaded regions as  $\pm 1\sigma$  uncertainty. (c) CO<sub>2</sub> gross sinks (negative, from regrowth after agricultural abandonment and wood harvesting) and gross sources (positive, from decaying material left dead on site, products after clearing of natural vegetation for agricultural purposes, wood harvesting, and, for BLUE, degradation from primary to secondary land through usage of natural vegetation as rangeland, and also from emissions from peat drainage and peat burning). Values are shown for the three bookkeeping models (yellow lines) and for their average (black with  $\pm 1\sigma$  uncertainty). The sum of the gross sinks and sources is  $E_{LUC}$  shown in panel (a). (d) Sources and sinks aggregated into four components that contribute to the net fluxes of CO<sub>2</sub>, including: (i) gross sources from deforestation; (ii) re/afforestation and wood harvest (i.e., the net flux on forest lands comprising slash and product decay following wood harvest; sinks due to regrowth after wood harvest or after abandonment, including reforestation and abandonment as parts of shifting cultivation cycles; afforestation), (iii) emissions from organic soils (peat drainage and peat fire, and (iv) sources and sinks related to other land use transitions. The scale of the fluxes shown is smaller than in panel (c) because the substantial gross sources and sinks from wood harvesting are accounted for as net flux under (ii). The sum of the component fluxes is  $E_{LUC}$  shown in panel (a).



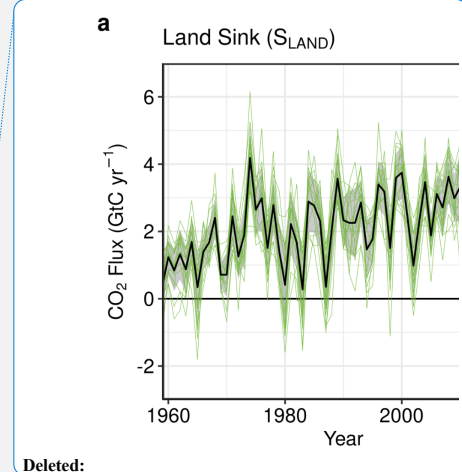
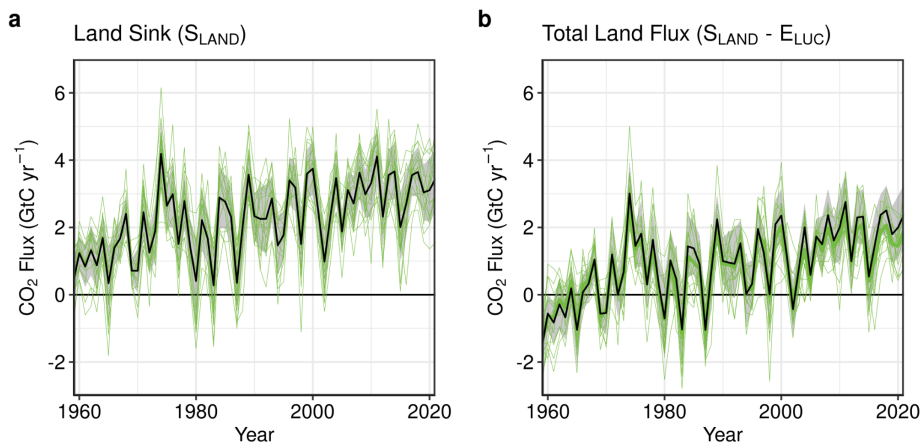
Deleted:

Deleted: .

Deleted: (

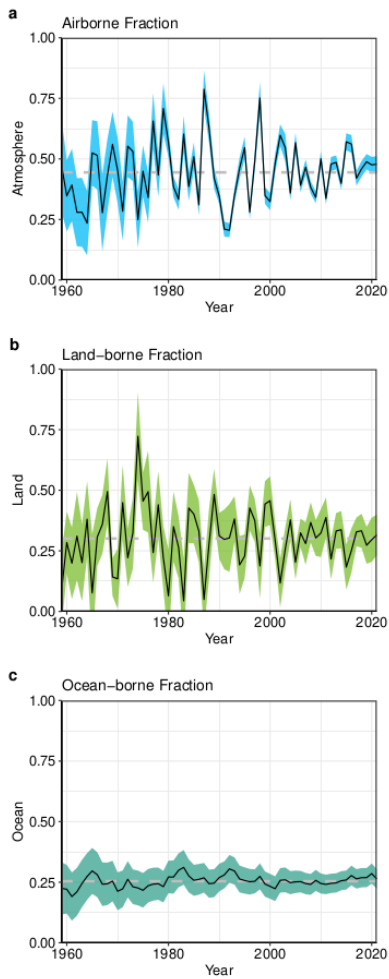
Deleted: in

524  
525  
526  
527  
528  
529  
530  
531  
532  
533  
534  
535  
536  
537  
538  
539  
540  
541  
542  
543  
544

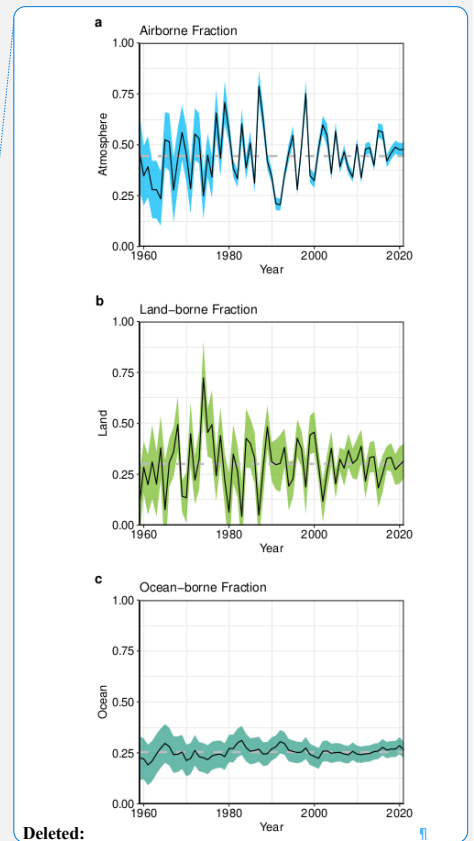


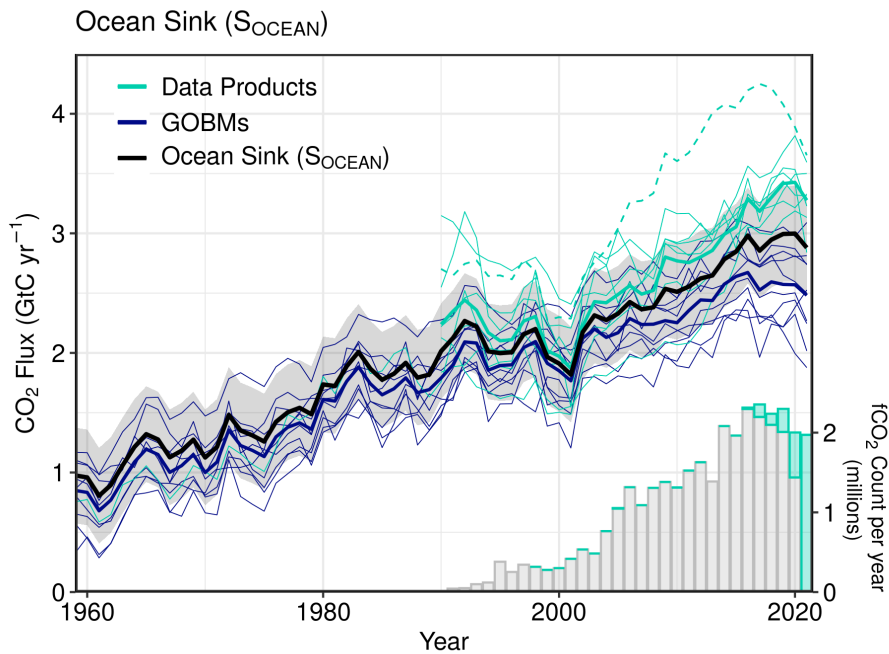
Formatted: Indent: Left: 1.9 cm

Figure 8: (a) The land CO<sub>2</sub> sink ( $S_{\text{LAND}}$ ) estimated by individual DGVMs estimates (green), as well as the budget estimate (black with  $\pm 1\sigma$  uncertainty), which is the average of all DGVMs. (b) Total atmosphere-land CO<sub>2</sub> fluxes ( $S_{\text{LAND}} - E_{\text{LUC}}$ ). The budget estimate of the total land flux (black with  $\pm 1\sigma$  uncertainty) combines the DGVM estimate of  $S_{\text{LAND}}$  from panel (a) with the bookkeeping estimate of  $E_{\text{LUC}}$  from Figure 7(a). Uncertainties are similarly propagated in quadrature from the budget estimates of  $S_{\text{LAND}}$  from panel (a) and  $E_{\text{LUC}}$  from Figure 7(a). DGVMs also provide estimates of  $E_{\text{LUC}}$  (see Figure 7(a)), which can be combined with their own estimates of the land sink. Hence panel (b) also includes an estimate for the total land flux for individual DGVMs (thin green lines) and their multi-model mean (thick green line).

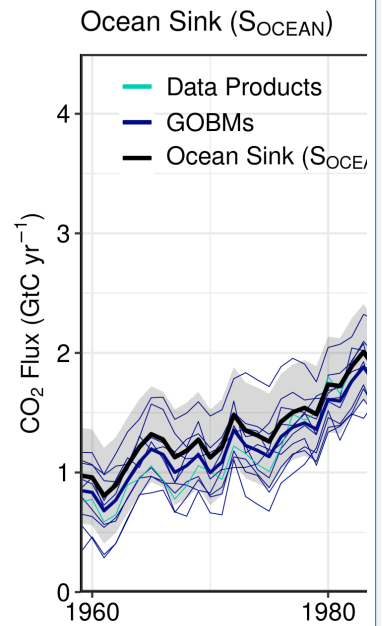


570  
571 **Figure 9.** The partitioning of total anthropogenic CO<sub>2</sub> emissions ( $E_{FOS} + E_{LUC}$ ) across (a) the atmosphere (airborne  
572 fraction), (b) land (land-borne fraction), and (c) ocean (ocean-borne fraction). Black lines represent the central  
573 estimate, and the coloured shading represents the uncertainty. The grey dashed lines represent the long-term  
574 average of the airborne (44%), land-borne (30%) and ocean-borne (25%) fractions during 1960-2021.





577  
 578 **Figure 10.** Comparison of the anthropogenic atmosphere-ocean CO<sub>2</sub> flux showing the budget values of S<sub>OCEAN</sub>  
 579 (black; with the uncertainty in grey shading), individual ocean models (royal blue), and the ocean fCO<sub>2</sub>-based data  
 580 products (cyan; with Watson et al. (2020) in dashed line as not used for ensemble mean). Only one data product  
 581 (Jena-MLS) extends back to 1959 (Rödenbeck et al., 2022). The fCO<sub>2</sub>-based data products were adjusted for the  
 582 pre-industrial ocean source of CO<sub>2</sub> from river input to the ocean, by subtracting a source of 0.65 GtC yr<sup>-1</sup> to  
 583 make them comparable to S<sub>OCEAN</sub> (see Section 2.4). Bar-plot in the lower right illustrates the number of fCO<sub>2</sub>  
 584 observations in the SOCAT v2022 database (Bakker et al., 2022). Grey bars indicate the number of data points in  
 585 SOCAT v2021, and coloured bars the newly added observations in v2022.



Deleted:  
 Deleted:  
 Deleted: 65

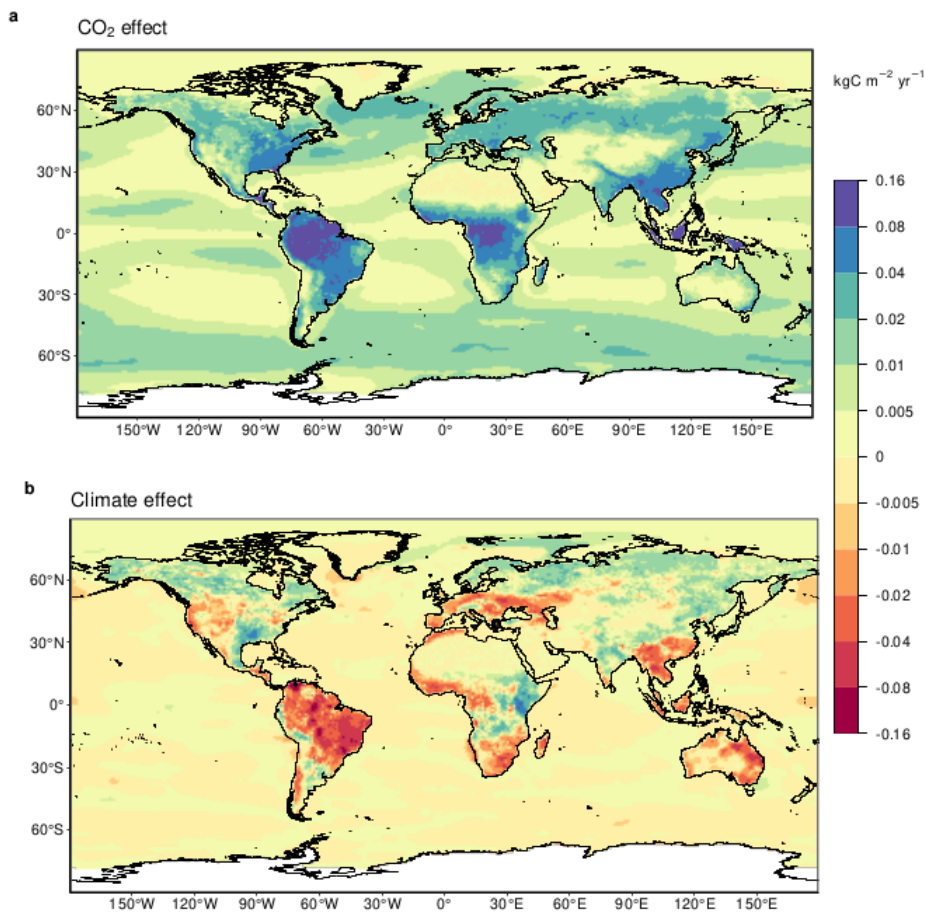


Figure 11. Attribution of the atmosphere-ocean ( $S_{\text{OCEAN}}$ ) and atmosphere-land ( $S_{\text{LAND}}$ )  $\text{CO}_2$  fluxes to (a) increasing atmospheric  $\text{CO}_2$  concentrations and (b) changes in climate, averaged over the previous decade 2012-2021. All data shown is from the processed-based GOBMs and DGVMs. The sum of ocean  $\text{CO}_2$  and climate effects will not equal the ocean sink shown in Figure 6 which includes the  $f\text{CO}_2$ -based data products. See Appendix C.3.2 and C.4.1 for attribution methodology. Units are in  $\text{kgC m}^{-2} \text{yr}^{-1}$  (note the non-linear colour scale).

Formatted: Indent: Left: 1.27 cm

593

594

595

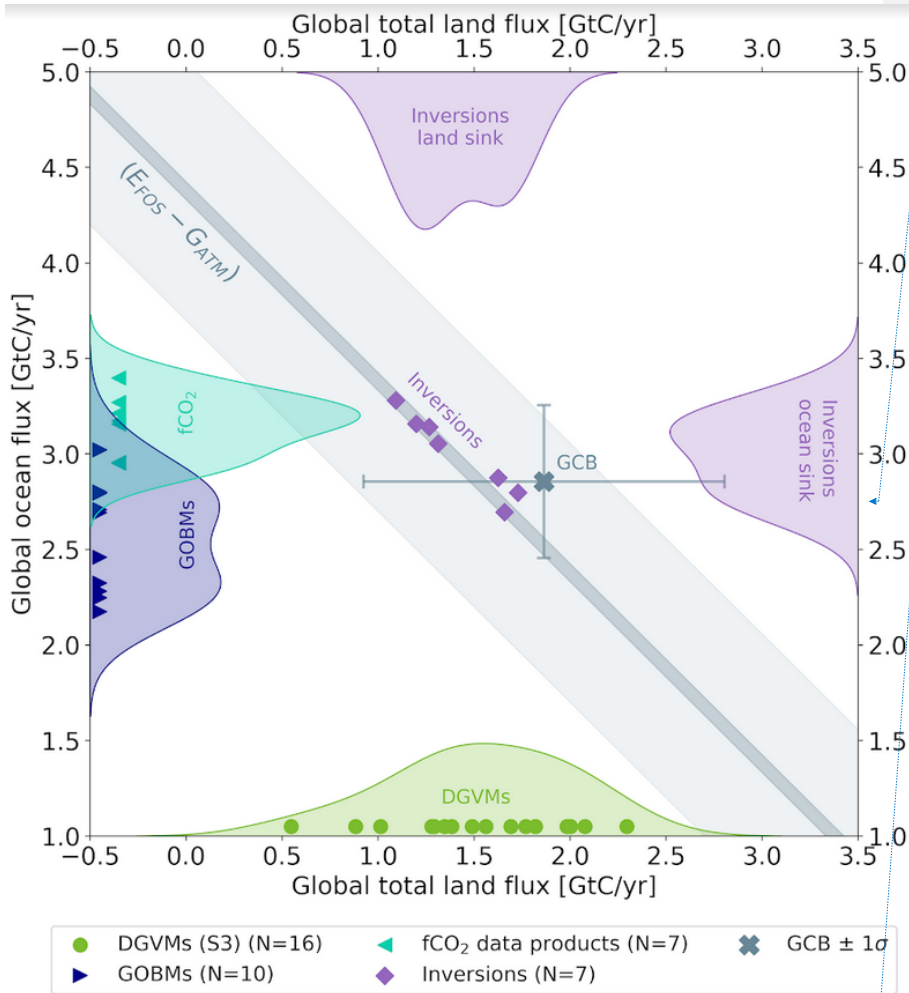
596

597

598

599

600



Formatted: Indent: Left: 1.27 cm

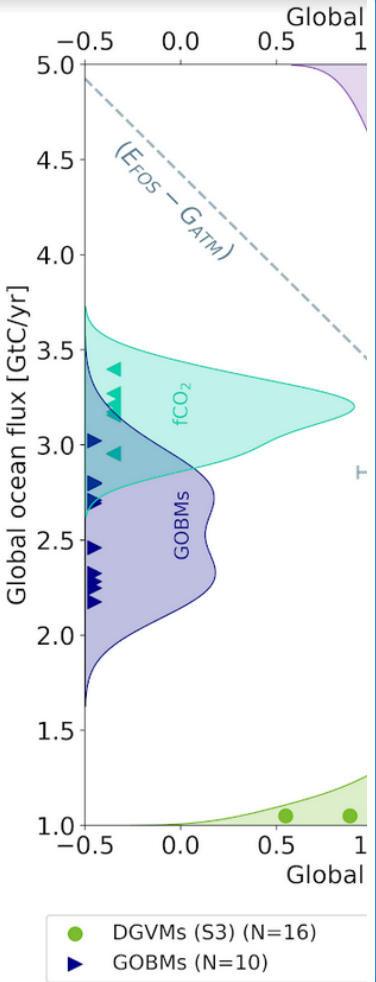
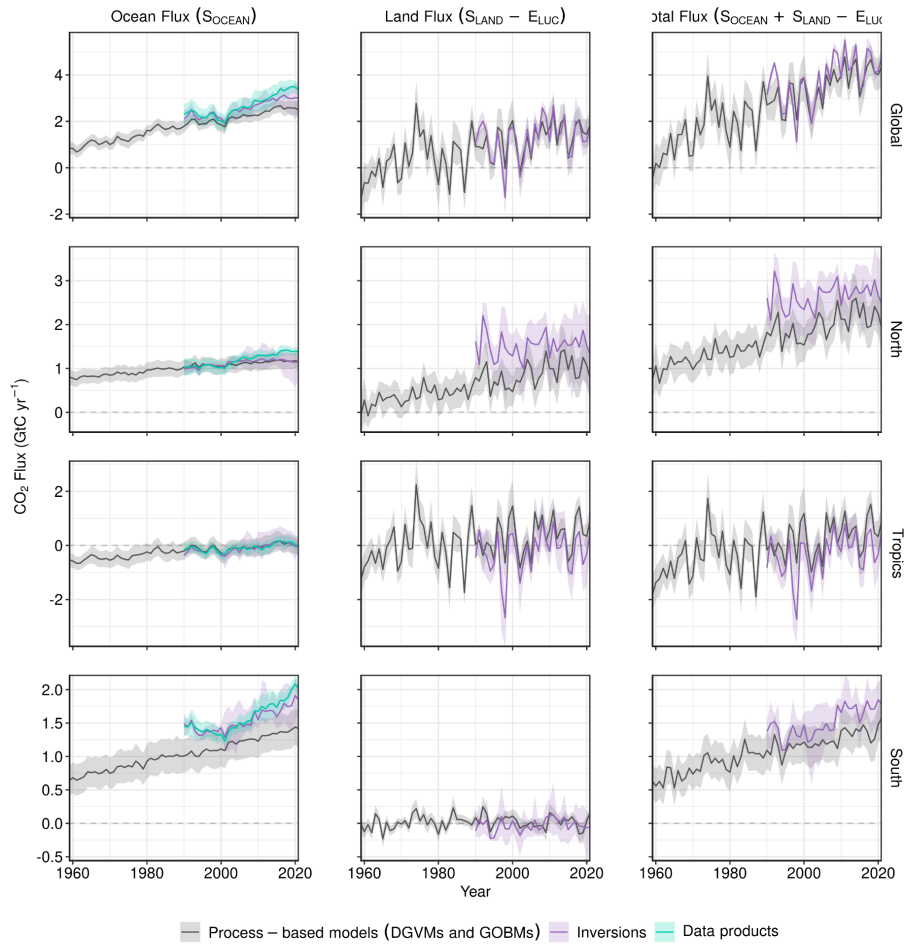


Figure 12. The 2012-2021 decadal mean net atmosphere-ocean and atmosphere-land fluxes derived from the ocean models and  $f\text{CO}_2$  products (y-axis, right and left pointing blue triangles respectively), and from the DGVMs (x-axis, green symbols), and the same fluxes estimated from the inversions (purple symbols on secondary x- and y-axis). The grey central point is the mean ( $\pm 1\sigma$ ) of  $S_{\text{OCEAN}}$  and  $(S_{\text{LAND}} - E_{\text{LUC}})$  as assessed in this budget. The shaded distributions show the density of the ensemble of individual estimates. The grey diagonal band represents the fossil fuel emissions minus the atmospheric growth rate from this budget ( $E_{\text{FOS}} - G_{\text{ATM}}$ ). Note that positive values are  $\text{CO}_2$  sinks.

Deleted:  
Formatted: Subscript  
Deleted: six

601  
602  
603  
604  
605  
606  
607  
608  
  
609  
610  
611

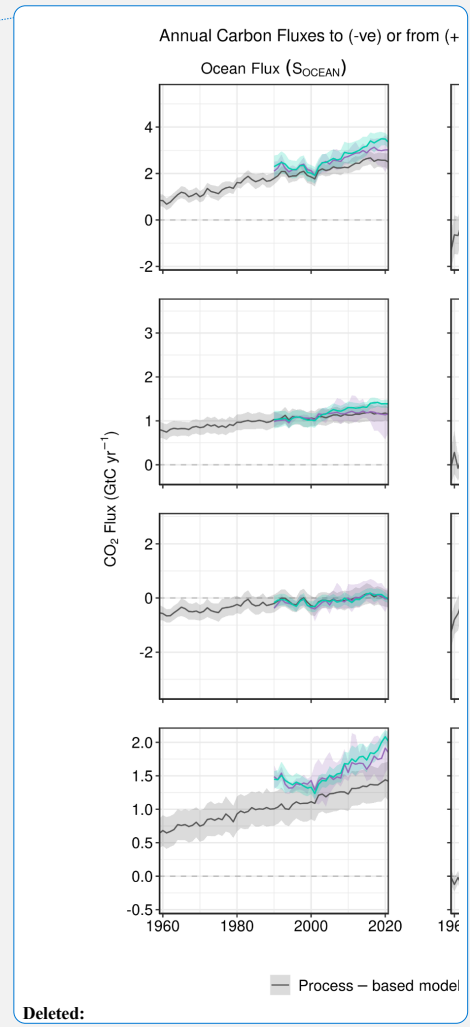
Annual Carbon Fluxes to (-ve) or from (+ve) the Atmosphere



614

615  
616  
617  
618  
619  
620  
621  
622  
623  
624  
625  
626  
627  
628  
629  
630  
631  
632

Figure 13. CO<sub>2</sub> fluxes between the atmosphere and the Earth's surface separated between land and oceans, globally and in three latitude bands. The ocean flux is  $S_{\text{OCEAN}}$  and the land flux is the net atmosphere-land fluxes from the DGVMs. The latitude bands are (top row) global, (2<sup>nd</sup> row) north (>30°N), (3<sup>rd</sup> row) tropics (30°S-30°N), and (bottom row) south (<30°S), and over ocean (left column), land (middle column), and total (right column). Estimates are shown for: process-based models (DGVMs for land, GOBMs for oceans); inversion systems (land and ocean); and fCO<sub>2</sub>-based data products (ocean only). Positive values indicate a flux from the atmosphere to the land or the ocean. Mean estimates from the combination of the process models for the land and oceans are shown (black line) with  $\pm 1$  standard deviation ( $1\sigma$ ) of the model ensemble (grey shading). For the total uncertainty in the process-based estimate of the total sink, uncertainties are summed in quadrature. Mean estimates from the atmospheric inversions are shown (purple lines) with their full spread (purple shading). Mean estimates from the fCO<sub>2</sub>-based data products are shown for the ocean domain (light blue lines) with their  $\pm 1\sigma$  spread (light blue shading). The global  $S_{\text{OCEAN}}$  (upper left) and the sum of  $S_{\text{OCEAN}}$  in all three regions represents the anthropogenic atmosphere-to-ocean flux based on the assumption that the preindustrial ocean sink was 0 GtC yr<sup>-1</sup> when riverine fluxes are not considered. This assumption does not hold at the regional level, where preindustrial fluxes can be significantly different from zero. Hence, the regional panels for  $S_{\text{OCEAN}}$  represent a combination of natural and anthropogenic fluxes. Bias-correction and area-weighting were only applied to global  $S_{\text{OCEAN}}$ ; hence the sum of the regions is slightly different from the global estimate (<0.05 GtC yr<sup>-1</sup>).

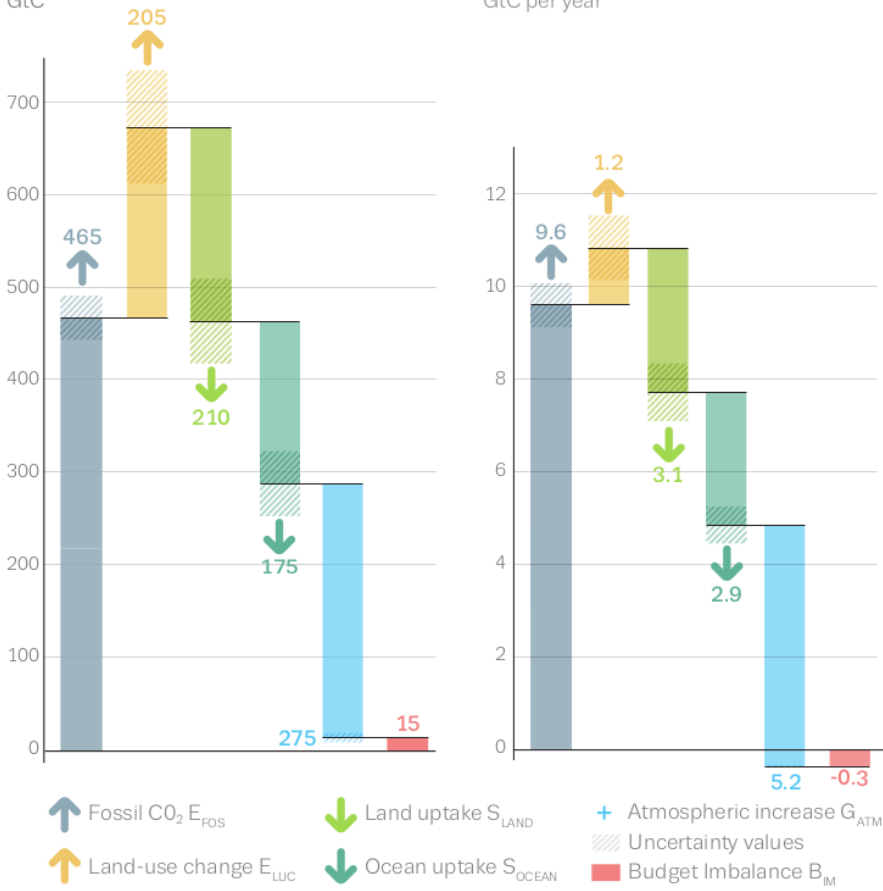


634

# Anthropogenic carbon flows

Cumulative changes 1850-2021  
GtC

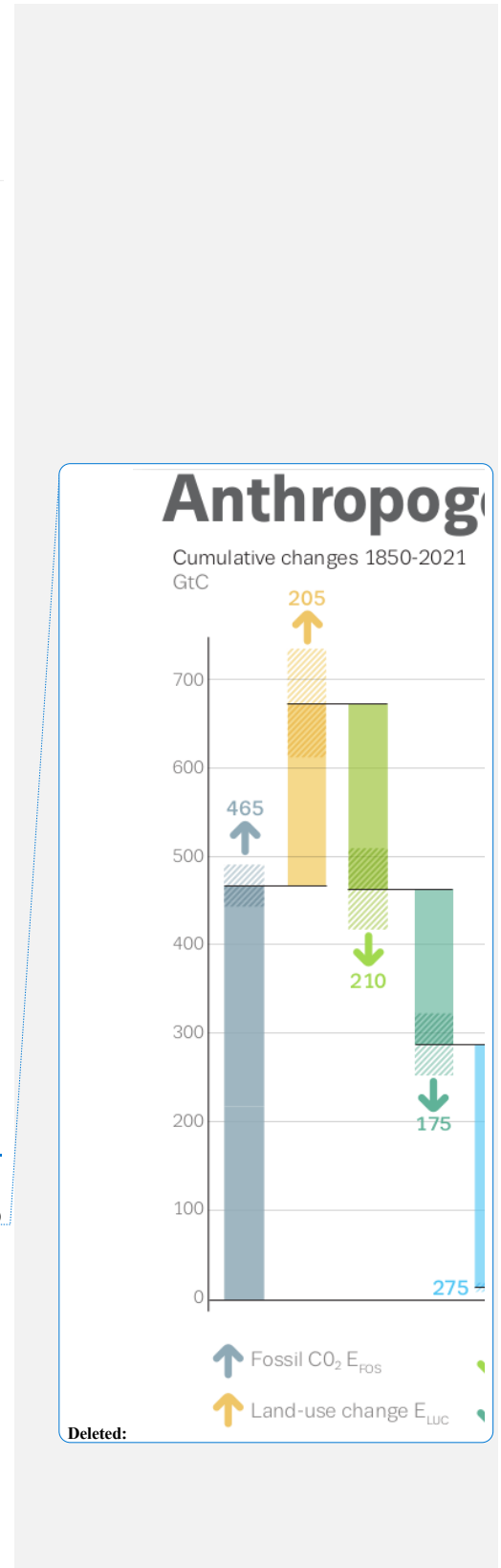
Mean fluxes 2012-2021  
GtC per year



635

636 **Figure 14. Cumulative changes over the 1850-2021 period (left) and average fluxes over the 2012-2021 period (right)**  
 637 **for the anthropogenic perturbation of the global carbon cycle. See the caption of Figure 3 for key information and**  
 638 **the methods in text for full details.**

639



641



642

643

644

645

646

647

648

649

650

651

652

**Figure 15. Kaya decomposition of the main drivers of fossil CO<sub>2</sub> emissions, considering population, GDP per person, Energy per GDP, and CO<sub>2</sub> emissions per energy, for China (top left), USA (top right), EU27 (middle left), India (middle right), Rest of the World (bottom left), and World (bottom right). Black dots are the annual fossil CO<sub>2</sub> emissions growth rate, coloured bars are the contributions from the different drivers. A general trend is that population and GDP growth put upward pressure on emissions, while energy per GDP and more recently CO<sub>2</sub> emissions per energy put downward pressure on emissions. Both the COVID-19 induced changes during 2020 and the recovery in 2021 led to a stark contrast to previous years, with different drivers in each region.**



654

## Appendix A. Supplementary Tables

Formatted: Indent: Left: 0.63 cm, Hanging: 0.63 cm

655

Table A1. Comparison of the processes included in the bookkeeping method and DGVMs in their estimates of ELUC and SLAND. See Table 4 for model references. All models include deforestation and forest regrowth after abandonment of agriculture (or from afforestation activities on agricultural land). Processes relevant for ELUC are only described for the DGVMs used with land-cover change in this study. [Here we use the term "DGVM" in the broadest sense in terms of global vegetation models which are able to dynamically adjust to imposed LULCC.](#)

Formatted Table

Formatted: Font: (Default) Calibri, 8 pt

	Bookkeeping Models				DGVMs														
	H&N	BLUE	OSCAR	CABLE-POP	CLASSIC	CLM5.0	DLEM	IBIS	ISAM	JSBACH	JULES-ES	LPJ-GUESS	LPJ	LPX-Berlin	OCNv2	ORCHIDEEv3	SDGVM	VISIT	YIBs
<b>Processes relevant for ELUC</b>																			
Wood harvest and forest degradation (a)	yes	yes	yes	yes	no	yes	yes	yes	yes	yes	no	yes	yes	no (d)	yes	yes	no	yes	no
Shifting cultivation / Subgrid scale transitions (b)	yes (b)	yes	yes	yes	no	yes	no	yes	no	yes	no	yes	yes	no (d)	no	no	no	yes	no
Cropland harvest (removed, R, or added to litter, L)	yes (R) (j)	yes (R) (j)	yes (R)	yes (R)	yes (L)	yes (R)	yes	yes (R)	yes	yes (R+L)	yes (R)	yes (R)	yes (L)	yes (R)	yes (R+L)	yes (R)	yes (R)	yes (R)	yes (L)
Peat fires	yes	yes	yes	no	no	yes	no	no	no	no	no	no	no	no	no	no	no	no	no
fire as a management tool	yes (j)	yes (j)	yes (h)	no	no	no	no	no	no	no	no	no	no	no	no	no	no	no	no
N fertilisation	yes (j)	yes (j)	yes (h)	no	no	yes	yes	no	yes	no	yes (i)	yes	no	yes	yes	yes	no	no	no
tillage	yes (j)	yes (j)	yes (h)	no	yes (g)	no	no	no	no	no	no	yes	no	no	no	yes (g)	no	no	no
irrigation	yes (j)	yes (j)	yes (h)	no	no	yes	yes	no	yes	no	no	yes	no	no	no	no	no	no	no
wetland drainage	yes (j)	yes (j)	yes (h)	no	no	no	no	no	yes	no	no	no	no	no	no	no	no	no	no
erosion	yes (j)	yes (j)	yes (h)	no	no	no	yes	no	no	no	no	no	no	no	no	no	no	yes	no
peat drainage	yes	yes	yes	no	no	no	no	no	no	no	no	no	no	no	no	no	no	no	no
Grazing and mowing Harvest (removed, r, or added to litter, l)	yes (r) (j)	yes (r) (j)	yes (r)	yes (r)	no	no	no	no	yes (r, l)	yes (l)	no	yes (r)	yes (l)	no	yes (r+l)	no	no	no	no
<b>Processes also relevant for SLAND (in addition to CO2 fertilisation and climate)</b>																			
Fire simulation and/or suppression	N.A.	N.A.	N.A.	no	yes	yes	no	yes	no	yes	yes	yes	yes	yes	no	no	yes	yes	no
Carbon-nitrogen interactions, including N deposition	N.A.	N.A.	N.A.	yes	no (f)	yes	yes	no	yes	yes	yes	yes	no	yes	yes	yes	yes (c)	no	no (f)
Separate treatment of direct and diffuse solar radiation	N.A.	N.A.	N.A.	yes	no	yes	no	no	no	no	yes	no	no	no	no	no	no	no	yes
(a) Refers to the routine harvest of established managed forests rather than pools of harvested products.																			
(b) No back- and forth-transitions between vegetation types at the country-level, but if forest loss based on FRA exceeded agricultural expansion based on FAO, then this amount of area was cleared for cropland and the same amount of area of old croplands abandoned.																			
(c) Limited. Nitrogen uptake is simulated as a function of soil C, and Vcmax is an empirical function of canopy N. Does not consider N deposition.																			
(d) Available but not active.																			
(e) Simple parameterization of nitrogen limitation based on Yin (2002; assessed on FACE experiments)																			
(f) Although C-N cycle interactions are not represented, the model includes a parameterization of down-regulation of photosynthesis as CO2 increases to emulate nutrient constraints (Arora et al., 2009)																			
(g) Tillage is represented over croplands by increased soil carbon decomposition rate and reduced humification of litter to soil carbon.																			
(h) as far as the DGVMs that OSCAR is calibrated to include it																			
(i) perfect fertilisation assumed, i.e. crops are not nitrogen limited and the implied fertiliser diagnosed																			
(j) Process captured implicitly by use of observed carbon densities.																			

Formatted Table

656

657

658

**Table A2. Comparison of the processes and model set up for the Global Ocean Biogeochemistry Models for their estimates of SOCEAN. See Table 4 for model references.**

	NEMO-PlankTOM12	NEMO-PISCES (IPSL)	MICOM-HAMOCC (NorESM1-OCv1.2)	MPIOM-HAMOCC6	FESOM-2.1-REcoM2	NEMO3.6-PISCESv2-gas (CNRM)	MOM6-COBALT (Princeton)	CESM-ETHZ	MRI-ESM2-1	CESM2
<b>Model specifics</b>										
Physical ocean model	NEMOv3.6-ORCA2	NEMOv3.6-eORCA1L75	MICOM (NorESM1-OCv1.2)	MPIOM	FESOM-2.1	NEMOv3.6-GELATov6-eORCA1L75	MOM6-SIS2	CESMv1.3 (ocean model based on POP2)	MRI.CO Mv4	CESM2-POP2
Biogeochemistry model	PlankTOM12	PISCESv2	HAMOCC (NorESM1-OCv1.2)	HAMOCC6	REcoM-2-M	PISCESv2-gas	COBALTV2	BEC (modified & extended)	NPZD	MARBL
Horizontal resolution	2° lon, 0.3 to 1.5° lat	1° lon, 0.3 to 1° lat	1° lon, 0.17 to 0.25 lat	1.5°	unstructured mesh, 20-120 km resolution (CORE mesh)	1° lon, 0.3 to 1° lat	0.5° lon, 0.25 to 0.5° lat	1.125° lon, 0.53° to 0.27° lat	1° lon, 0.3 to 0.5° lat	1.125° lon, 0.53° to 0.27° lat
Vertical resolution	31 levels	75 levels, 1m at the surface	51 isopycnic layers + 2 layers representing a bulk mixed layer	40 levels	46 levels, 10 m spacing in the top 100 m	75 levels, 1m at surface	75 levels hybrid coordinates, 2m at surface	60 levels	60 levels with 1-level bottom boundary layer	60 levels
Total ocean area on native grid (km <sup>2</sup> )	3.6080E+08	3.6270E+08	3.6006E+08	3.6598E+08	3.6435E+08	3.6270E+08	3.6111E+08	3.5926E+08	3.6141E+08	3.61E+08
Gas-exchange parameterization	Wanninkhof et al. 1992	Orr et al., 2017	Orr et al., 2017, but with a=0.337	Orr et al., 2017	Orr et al., 2017	Orr et al., 2017	Orr et al., 2017	Wanninkhof (1992, coefficient a scaled down to 0.31)	Orr et al., 2017	Orr et al., 2017
CO2 chemistry routines	Following Broecker et al. (1982)	mocsy	Following Dickson et al. 2007	Ilyina et al. (2013) adapted to comply with OMIP protocol (Orr et al., 2017)	mocsy	mocsy	mocsy	OCMIP2 (Orr et al.)	mocsy	OCMIP2 (Orr et al. 2017)
River input (PgC/yr) (organic/inorganic DIC)	0.723 / -	0.61 / -	0	0.77 / -	0 / 0	~0.611 / -	-0.07 / -0.15	0.33 / -	0 / 0	0.173/0.263
Net flux to sediment (PgC/yr) (organic/other)	0.723 / -	0.59 / -	around 0.54 / -	- / 0.44	0 / 0	~0.656 / -	-0.11 / -0.07 (CaCO3)	0.21 / -	0 / 0	0.345/0.110 (CaCO3)
<b>SPIN-UP procedure</b>										
Initialisation of carbon chemistry	GLODAPv1 (preindustrial DIC)	GLODAPv2 (preindustrial DIC)	GLODAPv1 (preindustrial DIC)	initialization from previous simulation	GLODAPv2 (preindustrial DIC)	GLODAPv2	GLODAPv2 (Alkalinity, DIC). DIC	GLODAPv2 (preindustrial DIC)	GLODAPv2 (preindustrial DIC)	GLODAPv2 (preindustrial DIC)

Formatted Table

Formatted Table

Formatted Table

							corrected to 1959 level (simulation A and C) and to pre-industrial level (simulation B and D) using Khatiwala et al 2009		DIC)	DIC)
Preindustrial spin-up prior to 1850	spin-up 1750-1947	spin-up starting in 1836 with 3 loops of JRA55	1000 year spin up	~2000 years	189 years	long spin-up (> 1000 years)	Other bgc tracers initialized from a GFDL-ESM2M spin-up (> 1000 years)	spinup 1655-1849	1661 years with xCO2 = 284.32	spinup 1653-1850, xCO2= 278
<b>Atmospheric forcing fields and CO2</b>										
Atmospheric forcing for (i) pre-industrial spin-up, (ii) spin-up 1850-1958 for simulation B, (iii) simulation B	looping NCEP year 1990 (i, ii, iii)	looping full JRA55 reanalysis	CORE-I (normal year) forcing (i, ii, iii)	OMIP climatology (i), NCEP year 1957 (ii,iii)	JRA55-do v.1.5.0 repeated year 1961 (i, ii, iii)	JRA55-do v1.5.0 full reanalysis (i) cycling year 1958 (ii,iii)	GFDL-ESM2M internal forcing (i), JRA55-do v1.5.0 repeat year 1959 (ii,iii)	COREv2 until 1835, from 1835-1850: JRA (i), normal year forcing created from JRA55-do version 1.3 (ii,iii)	JRA55-do v1.5.0 repeat year 1990/91 (i, ii, iii)	(i) repeating JRA 1958-2018 for spinup for A & D, repeating JRA 1990/1991 repeat year forcing for spinup for B & C, (ii) & (iii) JRA 1990/1991 repeat year forcing
Atmospheric CO2 for control spin-up 1850-1958 for simulation B, and for simulation B	constant 278ppm; converted to pCO2 with temperature formulation (Sarmiento et al., 1992)	xCO2 of 286.46ppm, converted to pCO2 with constant sea-level pressure and water vapour pressure	xCO2 of 278ppm, converted to pCO2 with sea-level pressure and water vapour pressure	xCO2 of 278ppm, no conversion to pCO2	xCO2 of 278ppm, converted to pCO2 with sea-level pressure and water vapour pressure	xCO2 of 286.46ppm, converted to pCO2 with constant sea-level pressure and water vapour pressure	xCO2 of 278ppm, converted to pCO2 with sea-level pressure and water vapour pressure	xCO2 = 287.4ppm, converted to pCO2 with atmospheric pressure, and water vapour pressure	xCO2 of 284.32ppm (CMIP6 piControl), converted to pCO2 with water vapour and sea-level pressure (JRA55-	xCO2= 278

									do repeat year 1990/91)	
Atmospheric forcing for historical spin-up 1850-1958 for simulation A (i) and for simulation A (ii)	1750-1947: looping NCEP year 1990; 1948-2021: NCEP	1836-1958 : looping full JRA55 reanalysis (i), JRA55-do-v1.4 then 1.5 for 2020-21 (ii)	CORE-I (normal year) forcing; from 1948 onwards NCEP-R1 with CORE-II corrections	NCEP 6 hourly cyclic forcing (10 years starting from 1948, i), 1948-2021: transient NCEP forcing	JRA55-do-v1.5.0 repeated year 1961 (i), transient JRA55-do-v1.5.0 (ii)	JRA55-do cycling year 1958 (i), JRA55-do-v1.5.0 (ii)	JRA55-do-v1.5 repeat year 1959 (i), v1.5.0 (1959-2019, v1.5.0.1b (2020), v1.5.0.1 (2020-2021; ii)	JRA55 version 1.3, repeat cycle between 1958-2018 (i), v1.3 (1959-2018), v.1.5.0.1 (2020-2021)	1653-1957: repeated cycle JRA55-do v1.5.0 1958-2018 (i), v1.5.0 (1958-2018), v1.5.0.1 (2019-2021; ii)	(i) repeating JRA 1958-2018, (ii) JRA 1958-2021
Atmospheric CO2 for historical spin-up 1850-1958 for simulation A (i) and simulation A (ii)	xCO2 provided by the GCB; converted to pCO2 temperature formulation (Sarmiento et al., 1992), monthly resolution (i, ii)	xCO2 as provided by the GCB, global mean, annual resolution, converted to pCO2 with sea-level pressure and water vapour pressure (i, ii)	xCO2 as provided by the GCB, converted to pCO2 with sea level pressure (taken from the atmospheric forcing) and water vapor correction (i, ii)	transient monthly xCO2 provided by GCB, no conversion (i, ii)	xCO2 as provided by the GCB, converted to pCO2 with sea-level pressure and water vapour pressure, global mean, monthly resolution (i, ii)	xCO2 as provided by the GCB, converted to pCO2 with constant sea-level pressure and water vapour pressure, global mean, yearly resolution (i, ii)	xCO2 at year 1959 level (315 ppm, i) and as provided by GCB (ii), both converted to pCO2 with sea-level pressure and water vapour pressure, global mean, yearly resolution (i, ii)	xCO2 as provided by the GCB, converted to pCO2 with locally determined atm. pressure, and water vapour pressure (i, ii)	xCO2 as provided for CMIP6 historical simulations, annual resolutions, annual resolution (i), and as provided by the GCB (ii), both converted to pCO2 with water vapour and sea-level pressure	annual global xCO2 provided by GCB, converted to equilibrium CO2* using atmospheric pressure and Weiss and Price (1980)

Table A3: Description of ocean data-products used for assessment of SOCEAN. See Table 4 for references.

	Jena-MLS	MPI-SOMFFN	CMEMS-LSCE-FFNN	Watson et al	NIES-NN	JMA-MLR	OS-ETHZ-GRACER	LDEO HPD
<b>Method</b>	Spatio-temporal interpolation (version oc_v2022). Spatio-temporal field of ocean-internal carbon sources/sinks is fit to the SOCATv2022 pCO <sub>2</sub> data. Includes a multi-linear regression against environmental drivers to bridge data gaps.	A feed-forward neural network (FFN) determines non-linear relationship between SOCAT pCO <sub>2</sub> measurements and environmental predictor data for 16 biogeochemical provinces (defined through a self-organizing map, SOM) and is used to fill the existing data gaps.	An ensemble of neural network models trained on 100 subsampled datasets from SOCAT and environmental predictors. The models are used to reconstruct sea surface fugacity of CO <sub>2</sub> and convert to air-sea CO <sub>2</sub> fluxes	Modified MPI-SOMFFN with SOCATv2022 pCO <sub>2</sub> database. Corrected to the subskin temperature of the ocean as measured by satellite (Goddijn-Murphy et al, 2015). Flux calculation corrected for the cool and salty surface skin. Monthly climatology for skin temperature correction derived from ESA CCI product for the period 2003 to 2011 (Merchant et al, 2019).	A feed forward neural network model trained on SOCAT 2021 fCO <sub>2</sub> and environmental predictor data. The fCO <sub>2</sub> was normalized to the reference year 2000 by a global fCO <sub>2</sub> trend: We fitted the dependence of fCO <sub>2</sub> on year by linear regression. We subtracted the trend from fCO <sub>2</sub> and used the neural network to model the nonlinear dependence of the residual on predictors. The trend was added to model predictions to reconstruct fCO <sub>2</sub> .	Fields of total alkalinity (TA) were estimated by using a multiple linear regressions (MLR) method based on GLODAPv2.2021 and satellite observation data. SOCATv2022 fCO <sub>2</sub> data were converted to dissolved inorganic carbon (DIC) with the TA. Fields of DIC were estimated by using a MLR method based on the DIC and satellite observation data	Geospatial Random Cluster Ensemble Regression is a two-step cluster-regression approach, where multiple clustering instances with slight variations are run to create an ensemble of estimates. We use K-means clustering and a combination of Gradient boosted trees and Feed-forward neural-networks to estimate SOCAT v2022 fCO <sub>2</sub> .	Based on fCO <sub>2</sub> -misfit between observed fCO <sub>2</sub> and eight of the ocean biogeochemical models used in this assessment. The eXtreme Gradient Boosting method links this misfit to environmental observations to reconstruct the model misfit across all space and time., which is then added back to model-based fCO <sub>2</sub> estimate. The final reconstruction of surface fCO <sub>2</sub> is the average across the eight reconstructions.
<b>Gas-exchange parameterization</b>	Wanninkhof 1992. Transfer coefficient k scaled to match a global mean transfer rate of 16.5 cm/hr by (Naegler, 2009)	Wanninkhof 1992. Transfer coefficient k scaled to match a global mean transfer rate of 16.5 cm/hr	Wanninkhof 2014. Transfer coefficient k scaled to match a global mean transfer rate of 16.5 cm/hr (Naegler, 2009)	Nightingale et al 2000	Wanninkhof, 2014. Transfer coefficient k scaled to match a global mean transfer rate of 16.5 cm/hr (Naegler, 2009)	Wanninkhof., 2014. Transfer coefficient k scaled to match a global mean transfer rate of 16.5 cm/hr (Naegler, 2009)	Wanninkhof 1992, averaged and scaled for three reanalysis wind data, to a global mean 16.5 cm/hr (after Naegler 2009; Fay & Gregor et al. 2021)	Wanninkhof 1992, averaged and scaled for three reanalysis wind data, to a global mean 16.5 cm/hr (after Naegler 2009; Fay & Gregor et al. 2021)
<b>Wind product</b>	JMA55-do reanalysis	ERA 5	ERA5	Mean and mean square winds monthly 1x1° from CCMP, 0.25x0.25° x 6-hourly,	ERA5	JRA55	JRA55, ERA5, NCEP1	JRA55, ERA5, CCMP2
<b>Spatial resolution</b>	2.5 degrees longitude x 2 degrees latitude	1x1 degree	1x1 degree	1x1 degree	1x1 degree	1x1 degree	1x1 degree	1x1 degree
<b>Temporal resolution</b>	daily	monthly	monthly	monthly	monthly	monthly	monthly	monthly

Formatted Table

Formatted Table

<b>Atmospheric CO2</b>	Spatially and temporally varying field based on atmospheric CO2 data from 169 stations (Jena CarboScope atmospheric inversion sEXTALL_v2021)	Spatially varying 1x1 degree atmospheric pCO2_wet calculated from the NOAA GMD, marine boundary layer xCO2 and NCEP sea level pressure with the moisture correction by Dickson et al 2007.	Spatially and monthly varying fields of atmospheric pCO2 computed from CO2 mole fraction (CO2 atmospheric inversion from the Copernicus Atmosphere Monitoring Service), and atmospheric dry-air pressure which is derived from monthly surface pressure (ERAS) and water vapour pressure fitted by Weiss and Price 1980	Atmospheric pCO2 (wet) calculated from NOAA marine boundary layer XCO2 and NCEP sea level pressure, with pH2O calculated from Cooper et al, 1998. 2021 XCO2 marine boundary values were not available at submission so we used preliminary values, estimated from 2020 values and increase at Mauna Loa.	NOAA Greenhouse Gas Marine Boundary Layer Reference. <a href="https://gml.noaa.gov/ccgg/mbi/mbi.html">https://gml.noaa.gov/ccgg/mbi/mbi.html</a>	Atmospheric xCO2 fields of JMA-GSAM inversion model (Maki et al. 2010; Nakamura et al. 2015) were used. They were converted to pCO2 by using JRA55 sea level pressure. 2021 xCO2 fields were not available at this stage, and we used global xCO2 increments from 2020 to 2021.	NOAA's marine boundary layer product for xCO2 is linearly interpolated onto a 1x1 degree grid and resampled from weekly to monthly. xCO2 is multiplied by ERA5 mean sea level pressure, where the latter corrected for water vapour pressure using Dickson et al. (2007). This results in monthly 1x1 degree pCO2atm.	NOAA's marine boundary layer product for xCO2 is linearly interpolated onto a 1x1 degree grid and resampled from weekly to monthly. xCO2 is multiplied by ERA5 mean sea level pressure, where the latter corrected for water vapour pressure using Dickson et al. (2007). This results in monthly 1x1 degree pCO2atm.
<b>Total ocean area on native grid (km2)</b>	3.63E+08	3.63E+08	3.50E+08	3.52E+08		3.10E+08 (2.98E+08 to 3.16E+08, depending on ice cover)	3.55E+08	3.61E+08
<b>method to extend product to full global ocean coverage</b>		Arctic and marginal seas added following Landschützer et al. (2020). No coastal cut.				Fay & Gregor et al. 2021	Method has near full coverage	Fay & Gregor et al. 2021. Gaps were filled with monthly climatology. Interannual variability was added to the climatology based on the temporal evolution of 5 products for years 1985 through 2020 and then only using this product for year 2021.

Deleted: ESRL

**Table A4.** Comparison of the inversion set up and input fields for the atmospheric inversions. Atmospheric inversions see the full CO<sub>2</sub> fluxes, including the anthropogenic and pre-industrial fluxes. Hence they need to be adjusted for the pre-industrial flux of CO<sub>2</sub> from the land to the ocean that is part of the natural carbon cycle before they can be compared with SOCEAN and SLAND from process models. See Table 4 for references.

	Copernicus Atmosphere Monitoring Service (CAMS)	Carbon-Tracker Europe (CTE)	Jena CarboScope	UoE	NISMON-CO <sub>2</sub>	CMS-Flux	GONGGA	THU	Copernicus Atmosphere Monitoring Service (CAMS) Satellite
<b>Version number</b>	v21r1	v2022	v2022	UoE v6.1b	v2022.1	v2022	v2022	v2022	FT21r2
<b>Observations</b>									
<b>Atmospheric observations</b>	Hourly resolution (well-mixed conditions) obspack GLOBALVIEWplus v7.0 (a) and NRT_v7.2(b), WDCGG, RAMCES and ICOS ATC	Hourly resolution (well-mixed conditions) obspack GLOBALVIEWplus v7.0 (a) and NRT_v7.2(b)	Flasks and hourly from various institutions (outliers removed by 2 $\sigma$ criterion)	Hourly resolution (well-mixed conditions) obspack GLOBALVIEWplus v7.0(a) and NRT_v7.2(b)	Hourly resolution (well-mixed conditions) obspack GLOBALVIEWplus v7.0(a) and NRT_v7.2(b)	ACOS-GOSAT v9r, OCO-2 v10 scaled to WMO 2019 standard and remote flask observations from ObsPack, GLOBALVIEWplus, v7.0(a) and NRT_v7.2(b)	OCO-2 v10r data that scaled to WMO 2019 standard	OCO-2 v10r data that scaled to WMO 2019 standard	bias-corrected ACOS GOSAT v9 over land until August 2024 + bias-corrected ACOS OCO-2 v10 over land, both rescaled to X2019
<b>Period covered</b>	1979-2021	2001-2021	1957-2021	2001-2021	1990-2021	2010-2021	2015-2021	2015-2021	2010-2021
<b>Prior fluxes</b>									
<b>Biosphere and fires</b>	ORCHIDEE, GFEDv4.1s	SiB4 and GFAS	Zero	CASA v1.0, climatology after 2016 and GFED4.0	VISIT and GFEDv4.1s	CARDAM OM	CASA and GFEDv4.1s	SiB4.2 and GFEDv4.1s	ORCHIDEE, GFEDv4.1s
<b>Ocean</b>	CMEMS-LSCE-FFNN 2021	CarboScope v2021	CarboScope v2022	Takahashi climatology	JMA global ocean mapping (Iida et al., 2015)	MOM6	Takahashi climatology	Takahashi climatology	CMEMS-LSCE-FFNN 2021
<b>Fossil fuels</b>	GridFED 2021.2(c) with an extrapolation to 2021 based on Carbonmonitor and NO <sub>2</sub>	GridFED 2021.3 + GridFED 2022.2 for 2021 (c)	GridFED v2022.2 (c)	GridFED 2022.1 (c)	GridFED v2022.2 (c)	GridFED2 022.2 (c)	GridFED 2021.3 (c) with an extrapolation to 2021 based on Carbonmonitor	GridFED v2022.1 (c)	GridFED 2021.2 (c) with an extrapolation to 2021 based on Carbonmonitor and NO <sub>2</sub>
<b>Transport and optimization</b>									
<b>Transport model</b>	LMDZ v6	TM5	TM3	GEOS-CHEM	NICAM-TM	GEOS-CHEM	GEOS-Chem v12.9.3	GEOS-CHEM	LMDZ v6

Formatted Table

<b>Weather forcing</b>	ECMWF	ECMWF	NCEP	MERRA	JRA55	MERRA	MERRA2	GEOS-FP	ECMWF
<b>Horizontal Resolution</b>	Global 3.75°x1.875°	Global 3°x2°; Europe 1°x1°, North America 1°x1°	Global 3.83°x5°	Global 4°x5°	Isocahedra l grid: ~225km	Global 4°x5°	Global 2°x2.5°	Global 4°x5°	Global 3.75°x1.875°
<b>Optimization</b>	Variational	Ensemble Kalman filter	Conjugate gradient (re-orthonormalization) (d)	Ensemble Kalman filter	Variational	Variational	Nonlinear least squares four-dimensional variational (NLS-4DVar)	Ensemble Kalman filter	Variational
<p>(a) <a href="https://doi.org/10.25925/20210801">https://doi.org/10.25925/20210801</a>. Schuldt et al. Multi-laboratory compilation of atmospheric carbon dioxide data for the period 1957-2020; obspack_co2_1_GLOBALVIEWplus_v7.0_2021-08-18; NOAA Earth System Research Laboratory, Global Monitoring Laboratory. <a href="http://doi.org/10.25925/20210801">http://doi.org/10.25925/20210801</a>.</p> <p>(b) <a href="http://doi.org/10.25925/20220624">http://doi.org/10.25925/20220624</a>. Schuldt et al. Multi-laboratory compilation of atmospheric carbon dioxide data for the period 2021-2022; obspack_co2_1_NRT_v7.2_2022-06-28; NOAA Earth System Research Laboratory, Global Monitoring Laboratory. <a href="http://doi.org/10.25925/20220624">http://doi.org/10.25925/20220624</a>.</p> <p>(c) GCP-GridFED v2021.2, v2021.3, v2022.1 and v2022.2 (Jones et al., 2022) are updates through the year 2021 of the GCP-GridFED dataset presented by Jones et al. (2021).</p> <p>(d) ocean prior not optimised</p>									

667  
668  
669  
670  
671  
672  
673  
674

**Table A5 Attribution of fCO<sub>2</sub> measurements for the year 2021 included in SOCATv2022 (Bakker et al., 2016, 2022) to inform ocean fCO<sub>2</sub>-based data products.**

Formatted Table

Platform Name	Regions	No. of measurements	Principal Investigators	No. of datasets	Platform Type
1 degree	North Atlantic, coastal	71,863	Tanhua, T.	1	Ship
Alawai_158W_21 N	Tropical Pacific	387	Sutton, A.; De Carlo, E. H.; Sabine, C.	1	Mooring
Atlantic Explorer	North Atlantic, tropical Atlantic, coastal	34,399	Bates, N. R.	16	Ship
Atlantic Sail	North Atlantic, coastal	27,496	Steinhoff, T.; Körtzinger, A.	7	Ship
BlueFin	Tropical Pacific	60,606	Alin, S. R.; Feely, R. A.	11	Ship
Cap San Lorenzo	North Atlantic, tropical Atlantic, coastal	44,281	Lefèvre, N.	7	Ship
CCE2_121W_34N	Coastal	1,333	Sutton, A.; Send, U.; Ohman, M.	1	Mooring
Celtic Explorer	North Atlantic, coastal	61,118	Cronin, M.	10	Ship
F.G. Walton Smith	Coastal	38,375	Rodriguez, C.; Millero, F. J.; Pierrot, D.; Wanninkhof, R.	14	Ship
Finnmaid	Coastal	223,438	Rehder, G.; Bittig, H. C.; Glockzin, M.	1	Ship
FRA56	Coastal	5,652	Tanhua, T.	1	Ship
G.O. Sars	Arctic, north Atlantic, coastal	82,607	Skjelvan, I.	9	Ship
GAKOA_149W_60 N	Coastal	402	Monacci, N.; Cross, J.; Musielewicz, S.; Sutton, A.	1	Mooring
Gordon Gunter	North Atlantic, coastal	36,058	Wanninkhof, R.; Pierrot, D.	6	Ship
Gulf Challenger	Coastal	6,375	Salisbury, J.; Vandemark, D.; Hunt, C. W.	6	Ship
Healy	Arctic, north Atlantic, coastal	28,998	Sweeney, C.; Newberger, T.; Sutherland, S. C.; Munro, D. R.	5	Ship
Henry B. Bigelow	North Atlantic, coastal	67,399	Wanninkhof, R.; Pierrot, D.	8	Ship
Heron Island	Coastal	989	Tilbrook, B.; Neill, C.; van Ooijen, E.; Passmore, A.; Black, J.	1	Mooring
Investigator	Southern Ocean, coastal, tropical Pacific, Indian Ocean	120,782	Tilbrook, B.; Akl, J.; Neill, C.	6	Ship
KC_BUOY	Coastal	2,860	Evans, W.; Pocock, K.	1	Mooring
Keifu Maru II	North Pacific, tropical Pacific, coastal	10,053	Kadono, K.	8	Ship
Laurence M. Gould	Southern Ocean	2,604	Sweeney, C.; Newberger, T.; Sutherland, S. C.; Munro, D. R.	1	Ship
Marion Dufresne	Indian Ocean, Southern Ocean, coastal	9,911	Lo Monaco, C.; Metzl, N.	1	Ship
Nathaniel B. Palmer	Southern Ocean	2,376	Sweeney, C.; Newberger, T.; Sutherland, S. C.; Munro, D. R.	1	Ship
New Century 2	North Pacific, tropical Pacific, north Atlantic, coastal	198,293	Nakaoka, S.-I.; Takao, S.	10	Ship
Newrest - Art and Fenetres	North Atlantic, tropical Atlantic, south Atlantic, coastal	17,699	Tanhua, T.	2	Ship
Quadra Island Field Station	Coastal	81,201	Evans, W.; Pocock, K.	1	Mooring
Ronald H. Brown	North Atlantic, coastal	31,661	Wanninkhof, R.; Pierrot, D.	3	Ship
Ryofu Maru III	North Pacific, tropical Pacific, coastal	10,464	Kadono, K.	8	Ship
Sea Explorer	Southern Ocean, north Atlantic, coastal, tropical Atlantic	37,027	Landshützer, P.; Tanhua, T.	2	Ship

Sikuliaq	Arctic, north Pacific, coastal	60,549	Sweeney, C.; Newberger, T.; Sutherland, S. C.; Munro, D. R.	13	Ship
Simon Stevin	Coastal	57,055	Gkritzalis, T.; Theetaert, H.; Cattrijsse, A.; T'Jampens, M.	11	Ship
Sitka Tribe of Alaska Environmental Research Laboratory	Coastal	19,086	Whitehead, C.; Evans, W.; Lanphier, K.; Peterson, W.; Kennedy, E.; Hales, B.	1	Mooring
SOFS_142E_46S	Southern Ocean	894	Sutton, A.; Trull, T.; Shadwick, E.	1	Mooring
Soyo Maru	Tropical Pacific, coastal	33,234	Ono, T.	3	Ship
Station M	North Atlantic	447	Skjelvan, I.	1	Mooring
Statsraad Lehmkuhl	North Atlantic, tropical Atlantic, coastal	47,881	Becker, M.; Olsen, A.	3	Ship
TAO125W_ON	Tropical Pacific	241	Sutton, A.	1	Mooring
Tavastland	Coastal	48,421	Willstrand Wranne, A.; Steinhoff, T.	17	Ship
Thomas G. Thompson	North Atlantic, tropical Atlantic, north Pacific, tropical Pacific, coastal	47,073	Alin, S. R.; Feely, R. A.	5	Ship
Trans Future 5	Southern Ocean, north Pacific, tropical Pacific, coastal	257,424	Nakaoka, S.-I.; Takao, S.	22	Ship
Tukuma Arctica	North Atlantic, coastal	70,033	Becker, M.; Olsen, A.	23	Ship
Wakatana Maru	North Pacific, coastal	13,392	Tadokoro, K.	2	Ship

**Table A6.** Aircraft measurement programs archived by Cooperative Global Atmospheric Data Integration Project (CGADIP; Schuldt et al. 2022a and 2022b) that contribute to the evaluation of the atmospheric inversions (Figure B4).

Site code	Measurement program name in Obstack	Specific doi	Data providers
AAO	Airborne Aerosol Observatory, Bondville, Illinois		Sweeney, C.; Dlugokencky, E.J.
ABOVE	Carbon in Arctic Reservoirs Vulnerability Experiment (CARVE)	<a href="https://doi.org/10.3334/ORNLDAAC/1404">https://doi.org/10.3334/ORNLDAAC/1404</a>	Sweeney, C., J.B. Miller, A. Karion, S.J. Dinardo, and C.E. Miller. 2016. CARVE: L2 Atmospheric Gas Concentrations, Airborne Flasks, Alaska, 2012-2015. ORNL DAAC, Oak Ridge, Tennessee, USA.
ACG	Alaska Coast Guard		Sweeney, C.; McKain, K.; Karion, A.; Dlugokencky, E.J.
ACT	Atmospheric Carbon and Transport - America		Sweeney, C.; Dlugokencky, E.J.; Baier, B.; Montzka, S.; Davis, K.
AIRCO RENOA A	NOAA AirCore		Colm Sweeney (NOAA) AND Bianca Baier (NOAA)
ALF	Alta Floresta		Gatti, L.V.; Gloor, E.; Miller, J.B.;
AOA	Aircraft Observation of Atmospheric trace gases by JMA		ghg_obs@met.kishou.go.jp
BGI	Bradgate, Iowa		Sweeney, C.; Dlugokencky, E.J.
BNE	Beaver Crossing, Nebraska		Sweeney, C.; Dlugokencky, E.J.
BRZ	Berezorechka, Russia		Sasakama, N.; Machida, T.
CAR	Briggsdale, Colorado		Sweeney, C.; Dlugokencky, E.J.
CMA	Cape May, New Jersey		Sweeney, C.; Dlugokencky, E.J.
CON	CONTRAIL (Comprehensive Observation Network for TRace gases by AirLiner)	<a href="http://dx.doi.org/10.17595/20180208.001">http://dx.doi.org/10.17595/20180208.001</a>	Machida, T.; Matsueda, H.; Sawa, Y. Niwa, Y.
CRV	Carbon in Arctic Reservoirs Vulnerability Experiment (CARVE)		Sweeney, C.; Karion, A.; Miller, J.B.; Miller, C.E.; Dlugokencky, E.J.
DND	Dahlen, North Dakota		Sweeney, C.; Dlugokencky, E.J.
ECO	East Coast Outflow		Sweeney, C.; McKain, K.
ESP	Estevan Point, British Columbia		Sweeney, C.; Dlugokencky, E.J.
ETL	East Trout Lake, Saskatchewan		Sweeney, C.; Dlugokencky, E.J.
FWI	Fairchild, Wisconsin		Sweeney, C.; Dlugokencky, E.J.
GSFC	NASA Goddard Space Flight Center Aircraft Campaign		Kawa, S.R.; Abshire, J.B.; Riris, H.
HAA	Molokai Island, Hawaii		Sweeney, C.; Dlugokencky, E.J.
HFM	Harvard University Aircraft Campaign		Wofsy, S.C.
HIL	Homer, Illinois		Sweeney, C.; Dlugokencky, E.J.
HIP	HIPPO (HIAPER Pole-to-Pole Observations)	<a href="https://doi.org/10.3334/CDIAC/HIPPO_010">https://doi.org/10.3334/CDIAC/HIPPO_010</a>	Wofsy, S.C.; Stephens, B.B.; Elkins, J.W.; Hintsa, E.J.; Moore, F.
IAGOS-CARIBI	In-service Aircraft for a Global Observing System		Obersteiner, F.; Boenisch, H.; Gehrlein, T.; Zahn, A.; Schuck, T.

Formatted Table

C			
INX	INFLUX (Indianapolis Flux Experiment)		Sweeney, C.; Dlugokencky, E.J.; Shepson, P.B.; Turnbull, J.
LEF	Park Falls, Wisconsin		Sweeney, C.; Dlugokencky, E.J.
NHA	Offshore Portsmouth, New Hampshire (Isles of Shoals)		Sweeney, C.; Dlugokencky, E.J.
OIL	Oglesby, Illinois		Sweeney, C.; Dlugokencky, E.J.
ORC	ORCAS (O2/N2 Ratio and CO2 Airborne Southern Ocean Study)	<a href="https://doi.org/10.5065/D6SB445X">https://doi.org/10.5065/D6SB445X</a>	Stephens, B.B., Sweeney, C., McKain, K., Kort, E.
PFA	Poker Flat, Alaska		Sweeney, C.; Dlugokencky, E.J.
RBA-B	Rio Branco		Gatti, L.V.; Gloor, E.; Miller, J.B.
RTA	Rarotonga		Sweeney, C.; Dlugokencky, E.J.
SCA	Charleston, South Carolina		Sweeney, C.; Dlugokencky, E.J.
SGP	Southern Great Plains, Oklahoma		Sweeney, C.; Dlugokencky, E.J.; Biraud, S.
TAB	Tabatinga		Gatti, L.V.; Gloor, E.; Miller, J.B.
TGC	Offshore Corpus Christi, Texas		Sweeney, C.; Dlugokencky, E.J.
THD	Trinidad Head, California		Sweeney, C.; Dlugokencky, E.J.
WBI	West Branch, Iowa		Sweeney, C.; Dlugokencky, E.J.

678  
679  
680  
681  
682  
683  
684  
685  
686  
687  
688  
689  
690  
691  
692

**Table A7.** Main methodological changes in the global carbon budget since first publication. Methodological changes introduced in one year are kept for the following years unless noted. Empty cells mean there were no methodological changes introduced that year.

Publication year	Fossil fuel emissions			LUC emissions	Reservoirs			Uncertainty & other changes
	Global	Country (territorial)	Country (consumption)		Atmosphere	Ocean	Land	
2006 (a)		Split in regions						
2007 (b)				ELUC based on FAO-FRA 2005; constant ELUC for 2006	1959-1979 data from Mauna Loa; data after 1980 from global average	Based on one ocean model tuned to reproduced observed 1990s sink		$\pm 1\sigma$ provided for all components
2008 (c)				Constant ELUC for 2007				
2009 (d)		Split between Annex B and non-Annex B	Results from an independent study discussed	Fire-based emission anomalies used for 2006-2008		Based on four ocean models normalised to observations with constant delta	First use of five DGVMs to compare with budget residual	
2010 (e)	Projection for current year based on GDP	Emissions for top emitters		ELUC updated with FAO-FRA 2010				
2011 (f)			Split between Annex B and non-Annex B					
2012 (g)		129 countries from 1959	129 countries and regions from 1990-2010 based on GTAP8.0	ELUC for 1997-2011 includes interannual anomalies from fire-based emissions	All years from global average	Based on 5 ocean models normalised to observations with ratio	Ten DGVMs available for SLAND; First use of four models to compare with ELUC	
2013 (h)		250 countries <sup>b</sup>	134 countries and regions 1990-2011 based on GTAP8.1, with detailed estimates for years 1997, 2001, 2004, and 2007	ELUC for 2012 estimated from 2001-2010 average		Based on six models compared with two data-products to year 2011	Coordinated DGVM experiments for SLAND and ELUC	Confidence levels; cumulative emissions; budget from 1750

Formatted Table

2014 (i)	Three years of BP data	Three years of BP data	Extended to 2012 with updated GDP data	ELUC for 1997-2013 includes interannual anomalies from fire-based emissions		Based on seven models	Based on ten models	Inclusion of breakdown of the sinks in three latitude bands and comparison with three atmospheric inversions
2015 (j)	Projection for current year based Jan-Aug data	National emissions from UNFCCC extended to 2014 also provided	Detailed estimates introduced for 2011 based on GTAP9			Based on eight models	Based on ten models with assessment of minimum realism	The decadal uncertainty for the DGVM ensemble mean now uses $\pm 1\sigma$ of the decadal spread across models
2016 (k)	Two years of BP data	Added three small countries; China's emissions from 1990 from BP data (this release only)		Preliminary ELUC using FRA-2015 shown for comparison; use of five DGVMs		Based on seven models	Based on fourteen models	Discussion of projection for full budget for current year
2017 (l)	Projection includes India-specific data			Average of two bookkeeping models; use of 12 DGVMs		Based on eight models that match the observed sink for the 1990s; no longer normalised	Based on 15 models that meet observation-based criteria (see Sect. 2.5)	Land multi-model average now used in main carbon budget, with the carbon imbalance presented separately; new table of key uncertainties
a Raupach et al. (2007)								
b Canadell et al. (2007)								
c GCP (2008)								
d Le Quéré et al. (2009)								
e Friedlingstein et al. (2010)								
f Peters et al. (2012b)								
g Le Quéré et al. (2013), Peters et al. (2013)								
h Le Quéré et al. (2014)								
i Le Quéré et al. (2015a)								
j Le Quéré et al. (2015b)								
k Le Quéré et al. (2016)								
l Le Quéré et al. (2018a)								

Formatted Table

3696

**Table A8: Mapping of global carbon cycle models' land flux definitions to the definition of the LULUCF net flux used in national reporting to UNFCCC. Non-intact lands are used here as proxy for "managed lands" in the country reporting, national Greenhouse Gas Inventories (NGHGI) are gap-filled (see Sec. C.2.3 for details). Where available, we provide independent estimates of certain fluxes for comparison. Units are GtC yr<sup>-1</sup>.**

			2002-2011	2012-2021
ELUC from bookkeeping estimates (from Tab. 5)			1.36	1.24
SLAND	Total (from Tab. 5)	from DGVMs	-2.85	-3.10
	in non-forest lands	from DGVMs	-0.74	-0.83
	in non-intact forest	from DGVMs	-1.67	-1.81
	in intact forests	from DGVMs	-0.44	-0.47
	in intact land	from ORCHIDEE-MICT	-1.34	-1.38
ELUC plus SLAND on non-intact lands	considering non-intact forests only	from bookkeeping ELUC and DGVMs	-0.31	-0.56
	considering all non-intact land	from ORCHIDEE-MICT	0.90	0.60
National Greenhouse Gas Inventories (LULUCF)			-0.37	-0.54
FAOSTAT (LULUCF)			0.39	0.24

3697

3698

Formatted: Numbering: Continuous

Formatted Table

Deleted: 80

**Table A9. Funding supporting the production of the various components of the global carbon budget in addition to the authors' supporting institutions (see also acknowledgements).**

Funder and grant number (where relevant)	Author Initials
Australia, Integrated Marine Observing System (IMOS)	BT
Australian National Environment Science Program (NESP)	JGC
Belgium, FWO (Flanders Research Foundation, contract GN I001821N)	TGk
BNP Paribas Foundation through Climate & Biodiversity initiative, philanthropic grant for developments of the Global Carbon Atlas	PC
Canada, Tula Foundation	WE, KP
China, National Natural Science Foundation (grant no. 41975155)	XY
China, National Natural Science Foundation (grant no. 42141020)	WY
China, National Natural Science Foundation of China (grant no. 41921005)	BZ
China, Scientific Research Start-up Funds (grant no. QD2021024C) from Tsinghua Shenzhen International Graduate School	BZ
China, Second Tibetan Plateau Scientific Expedition and Research Program (SQ2022QZKK0101)	XT
China, Young Elite Scientists Sponsorship Program by CAST (grant no. YESS20200135)	BZ
EC Copernicus Atmosphere Monitoring Service implemented by ECMWF	FC
EC Copernicus Marine Environment Monitoring Service implemented by Mercator Ocean	MG
EC H2020 (4C; grant no 821003)	PF, MOS, RMA, SS, GPP, PC, JIK, TI, LB, AJ, PL, LGr, NG, NMa, SZ
EC H2020 (CoCO2: grant no. 958927)	RMA, GPP, JIK
EC H2020 (COMFORT: grant no. 820989)	LGr, MG, NG
EC H2020 (CONSTRAIN: grant no 820829)	RS, TGa
EC H2020 (ESM2025 – Earth System Models for the Future; grant agreement No 101003536).	RS, TGa, TI, LB, BD
EC H2020 (JERICO-S3: grant no. 871153)	HCB
EC H2020 (VERIFY: grant no. 776810)	MWJ, RMA, GPP, PC, JIK, MJM
Efg International	TT, MG
European Space Agency Climate Change Initiative ESA-CCI RECCAP2 project 655 (ESRIN/4000123002/18/I-NB)	SS, PC
European Space Agency OceanSODA project (grant no. 4000137603/22/I-DT)	LGr, NG
France, French Oceanographic Fleet (FOF)	NMe
France, ICOS (Integrated Carbon Observation System) France	NL
France, Institut National des Sciences de l'Univers (INSU)	NMe
France, Institut polaire français Paul-Emile Victor(IPEV)	NMe
France, Institut de recherche français sur les ressources marines (IFREMER)	NMe
France, Institut de Recherche pour le Développement (IRD)	NL
France, Observatoire des sciences de l'univers Ecce-Terra (OSU at	NMe

Formatted Table

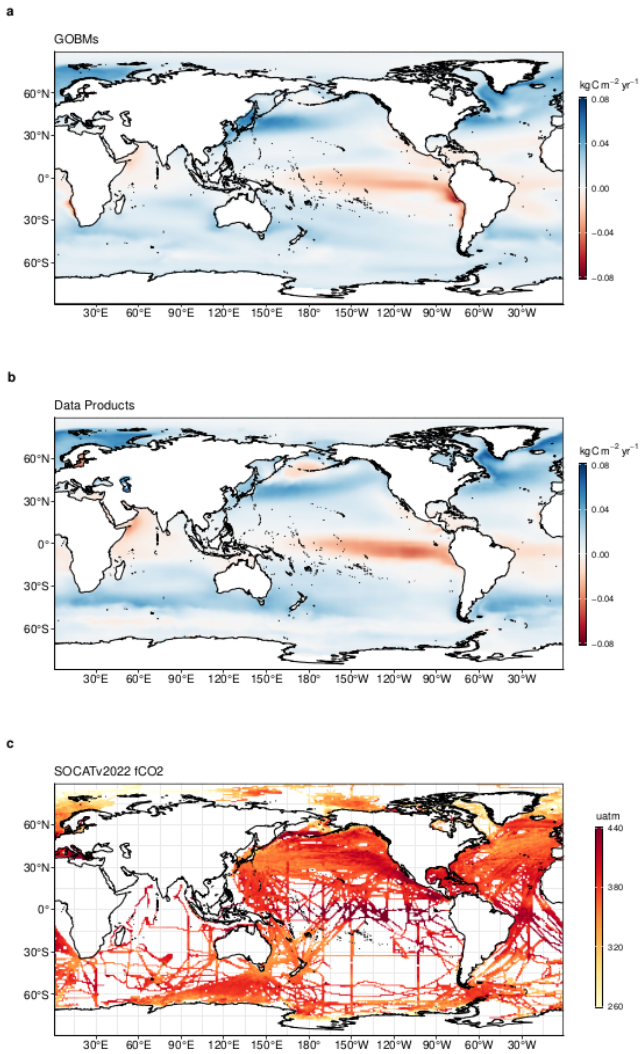
Sorbonne Université)	
Germany, Deutsche Forschungsgemeinschaft (DFG) under Germany's Excellence Strategy – EXC 2037 'Climate, Climatic Change, and Society' – Project Number: 390683824	TI
Germany, Federal Ministry for Education and Research (BMBF)	HCB
<a href="#">Germany, Federal Ministry for Education and Research (BMBF) under project "CDRSynTra" (01LS2101A)</a>	JP
Germany, German Federal Ministry of Education and Research under project "DArgo2025" (03F0857C)	TS
Germany, Helmholtz Association ATMO programme	AA
Germany, Helmholtz Young Investigator Group Marine Carbon and Ecosystem Feedbacks in the Earth System (MarESys), grant number VH-NG-1301	JH, OG
Germany, ICOS (Integrated Carbon Observation System) Germany	HCB
Hapag-Lloyd	TT, MG
Ireland, Marine Institute	MC
Japan, Environment Research and Technology Development Fund of the Ministry of the Environment (JPMEERF21S20810)	YN
Japan, Global Environmental Research Coordination System, Ministry of the Environment (grant number E1751)	SN, ST, TO
Japan, Environment Research and Technology Development Fund of the Ministry of the Environment (JPMEERF21S20800)	HT
Japan, Japan Meteorological Agency	KK
Kuehne + Nagel International AG	TT, MG
Mediterranean Shipping Company (MSc)	TT, MG
Monaco, Fondation Prince Albert II de Monaco	TT, MG
Monaco, Yacht Club de Monaco	TT, MG
Netherlands, ICOS (Integrated Carbon Observation System)	WP
Norway, Research Council of Norway (N-ICOS-2, grant no. 296012)	AO, MB, IS
Norway, Norwegian Research Council (grant no. 270061)	JS
Sweden, ICOS (Integrated Carbon Observation System)	AW
Sweden, Swedish Meteorological and Hydrological Institute	AW
Sweden, The Swedish Research Council	AW
Swiss National Science Foundation (grant no. 200020-200511)	QS
Tibet, Second Tibetan Plateau Scientific Expedition and Research Program (SQ2022QZKK0101)	TX
UK Royal Society (grant no. RP\R1\191063)	CLQ
UK, Natural Environment Research Council (SONATA: grant no. NE/P021417/1)	RW
UK, Natural Environmental Research Council (NE/R016518/1)	PIP
UK, Natural Environment Research Council (NE/V01417X/1)	MWJ
UK, Royal Society: The European Space Agency OCEANFLUX projects	JDS
UK Royal Society (grant no. RP\R1\191063)	CLQ

Formatted Table

USA, BIA Tribal Resilience	CW
USA, Cooperative Institute for Modeling the Earth System between the National Oceanic and Atmospheric Administration Geophysical Fluid Dynamics Laboratory and Princeton University and the High Meadows Environmental Institute	LR
USA, Cooperative Institute for Climate, Ocean, & Ecosystem Studies (CIOCES) under NOAA Cooperative Agreement NA20OAR4320271	KO
USA, Department of Energy, Biological and Environmental Research	APW
USA, Department of Energy, SciDac (DESC0012972)	GCH, LPC
USA, Energy Exascale Earth System Model (E3SM) project, Department of Energy, Office of Science, Office of Biological and Environmental Research	GCH, LPC
USA, EPA Indian General Assistance Program	CW
USA, NASA Carbon Monitoring System program and OCO Science team program (80NM0018F0583)	JL
USA, NASA Interdisciplinary Research in Earth Science (IDS) (80NSSC17K0348)	GCH, LPC, BP
USA, National Center for Atmospheric Research (NSF Cooperative Agreement No. 1852977)	DK
USA, National Oceanic and Atmospheric Administration, Ocean Acidification Program	DP, RW, SRA, RAF, AJS, NMM
USA, National Oceanic and Atmospheric Administration, Global Ocean Monitoring and Observing Program	DRM, CSw, NRB, CRodr, DP, RW, SRA, RAF, AJS
USA, National Science Foundation (grant number 1903722)	HT
USA, State of Alaska	NMM
<b>Computing resources</b>	
ADA HPC cluster at the University of East Anglia	MWJ
CAMS inversion was granted access to the HPC resources of TGCC under the allocation A0110102201	FC
Cheyenne supercomputer (doi:10.5065/D6RX99HX), were provided by the Computational and Information Systems Laboratory (CISL) at NCAR	DK
HPC cluster Aether at the University of Bremen, financed by DFG within the scope of the Excellence Initiative	ITL
MRI (FUJITSU Server PRIMERGY CX2550M5)	YN
NIES (SX-Aurora)	YN
NIES supercomputer system	EK

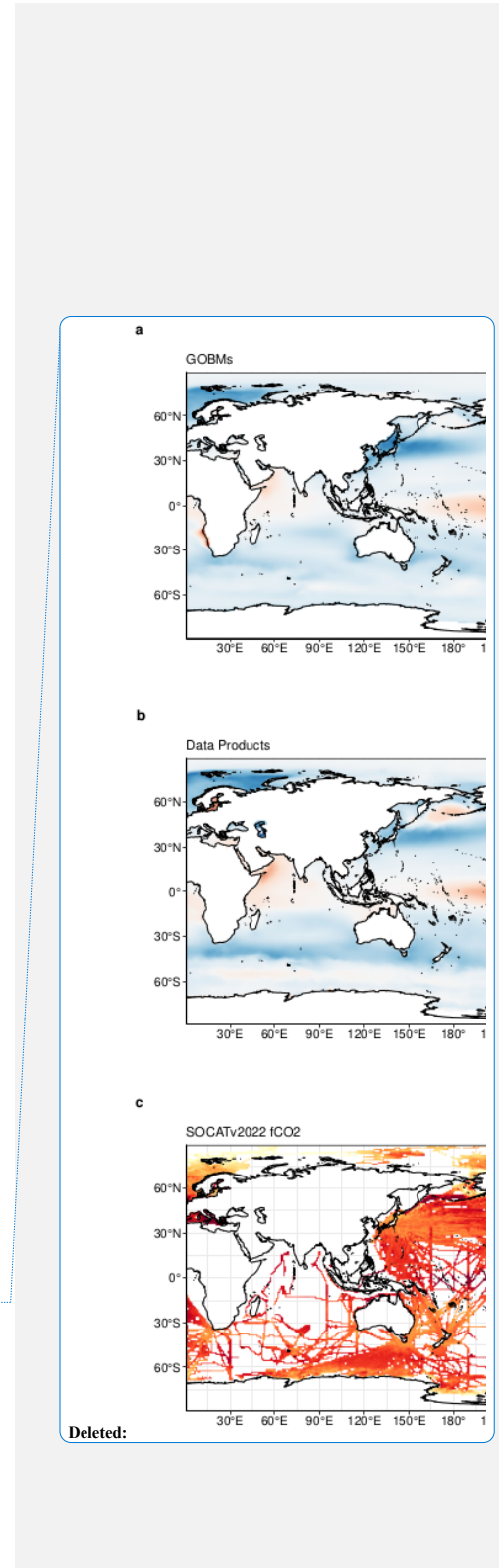
3701

**Deleted:** UNINETT Sigma2, National Infrastructure for High Performance Computing and Data Storage in Norway (NN2980K/NS2980K)  
JS... ... [1]

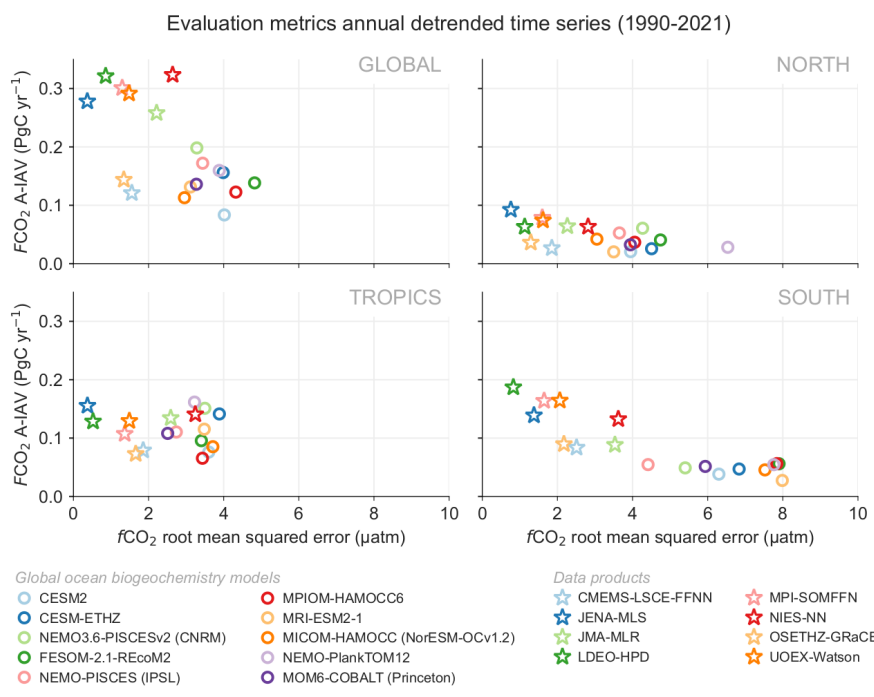


3707

3708 **Figure B1. Ensemble mean air-sea CO<sub>2</sub> flux from a) global ocean biogeochemistry models and b) fCO<sub>2</sub> based data products,**  
 3709 **averaged over 2012-2021 period (kg C m<sup>-2</sup> yr<sup>-1</sup>). Positive numbers indicate a flux into the ocean. c) gridded SOCAT v2022**  
 3710 **fCO<sub>2</sub> measurements, averaged over the 2012-2021 period (µatm). In (a) model simulation A is shown. The data-products**  
 3711 **represent the contemporary flux, i.e. including outgassing of riverine carbon, which is estimated to amount to 0.65 GtC yr<sup>-1</sup>**  
 3712 **globally.**

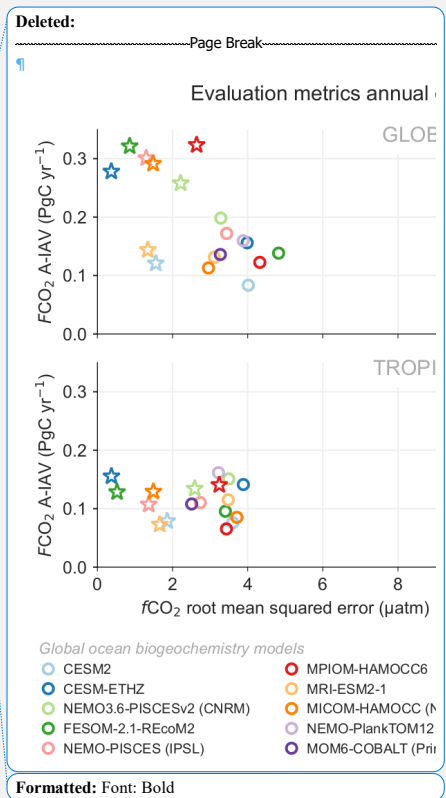


Deleted:

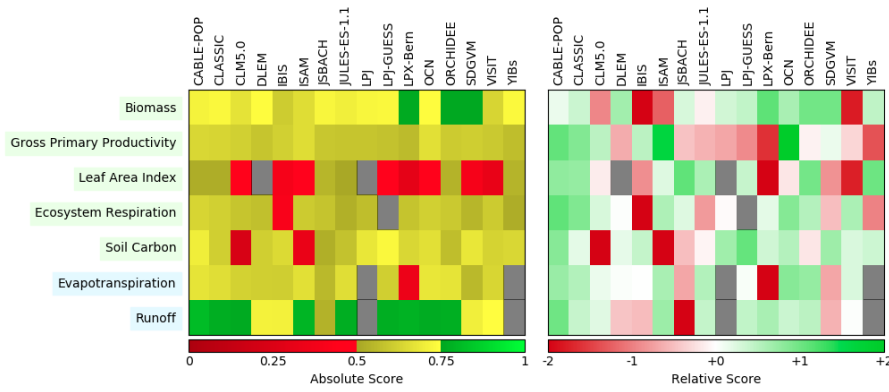


3714  
3715  
3716  
3717  
3718  
3719  
3720  
3721  
3722

**Figure B2.** Evaluation of the GOBMs and data products using the root mean squared error (RMSE) for the period 1990 to 2021, between the individual surface ocean fCO<sub>2</sub> mapping schemes and the SOCAT v2022 database. The y-axis shows the amplitude of the interannual variability of the air-sea CO<sub>2</sub> flux (A-IAV, taken as the standard deviation of the detrended annual time series). Results are presented for the globe, north (>30°N), tropics (30°S-30°N), and south (<30°S) for the GOBMs (see legend, circles) and for the fCO<sub>2</sub>-based data products (star symbols). The fCO<sub>2</sub>-based data products use the SOCAT database and therefore are not independent from the data (see section 2.4.1).

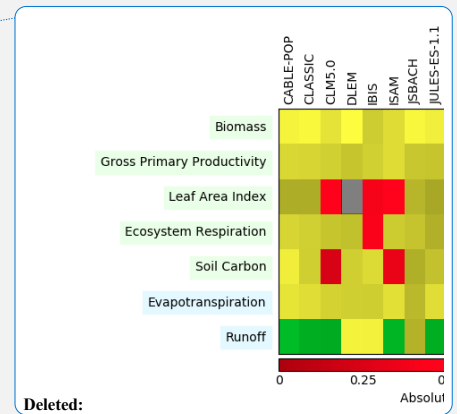


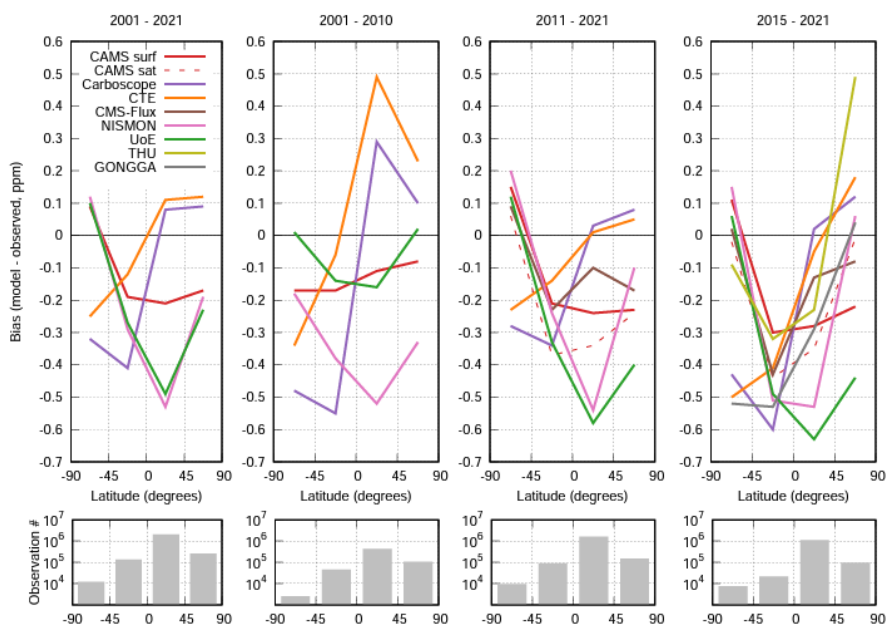
3727



3728 **Figure B3. Evaluation of the DGVMs using the International Land Model Benchmarking system (ILAMB; Collier et al.,**  
 3729 **2018) (left) absolute skill scores and (right) skill scores relative to other models. The benchmarking is done with observations**  
 3730 **for vegetation biomass (Saatchi et al., 2011; and GlobalCarbon unpublished data; Avitabile et al., 2016), GPP (Jung et al.,**  
 3731 **2010; Lasslop et al., 2010), leaf area index (De Kauwe et al., 2011; Myneni et al., 1997), ecosystem respiration (Jung et al.,**  
 3732 **2010; Lasslop et al., 2010), soil carbon (Hugelius et al., 2013; Todd-Brown et al., 2013), evapotranspiration (De Kauwe et al.,**  
 3733 **2011), and runoff (Dai and Trenberth, 2002). For each model-observation comparison a series of error metrics are**  
 3734 **calculated, scores are then calculated as an exponential function of each error metric, finally for each variable the multiple**  
 3735 **scores from different metrics and observational data sets are combined to give the overall variable scores shown in the left**  
 3736 **panel. Overall variable scores increase from 0 to 1 with improvements in model performance. The set of error metrics vary**  
 3737 **with data set and can include metrics based on the period mean, bias, root mean squared error, spatial distribution,**  
 3738 **interannual variability and seasonal cycle. The relative skill score shown in the right panel is a Z-score, which indicates in**  
 3739 **units of standard deviation the model scores relative to the multi-model mean score for a given variable. Grey boxes**  
 3740 **represent missing model data.**

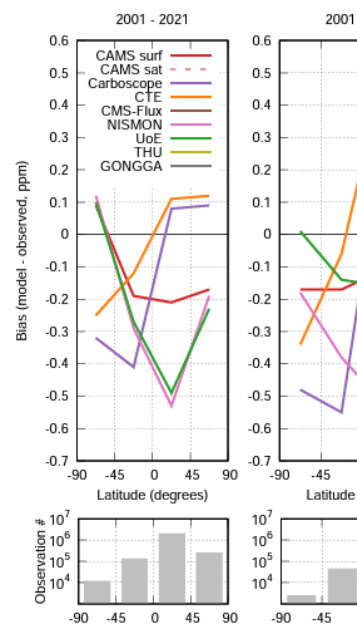
3741





3743  
3744  
3745  
3746  
3747  
3748  
3749  
3750  
3751

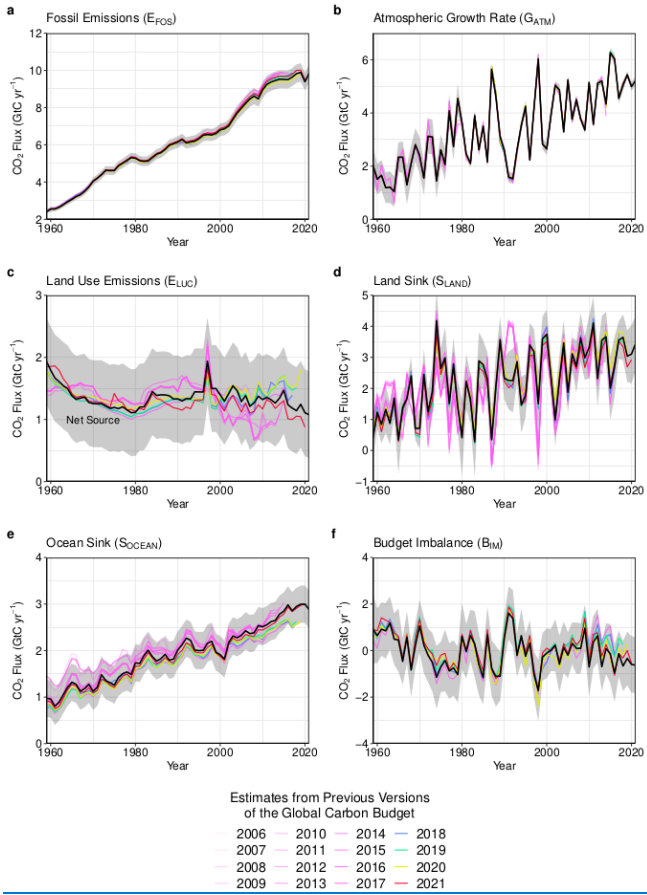
Figure B4. Evaluation of the atmospheric inversion products. The mean of the model minus observations is shown for four latitude bands in four periods: (first panel) 2001-2021, (second panel) 2001-2010, (third panel) 2011-2021, (fourth panel) 2015-2021. The 9 systems are compared to independent CO<sub>2</sub> measurements made onboard aircraft over many places of the world between 2 and 7 km above sea level. Aircraft measurements archived in the Cooperative Global Atmospheric Data Integration Project (Schuldt et al. 2021, Schuldt et al. 2022) from sites, campaigns or programs that have not been assimilated and cover at least 9 months (except for SH programs) between 2001 and 2021, have been used to compute the biases of the differences in four 45° latitude bins. Land and ocean data are used without distinction, and observation density varies strongly with latitude and time as seen on the lower panels.



Deleted:

Formatted: Subscript

Formatted: Font: (Default) Calibri, 12 pt, Not Bold



3753

3754

3755

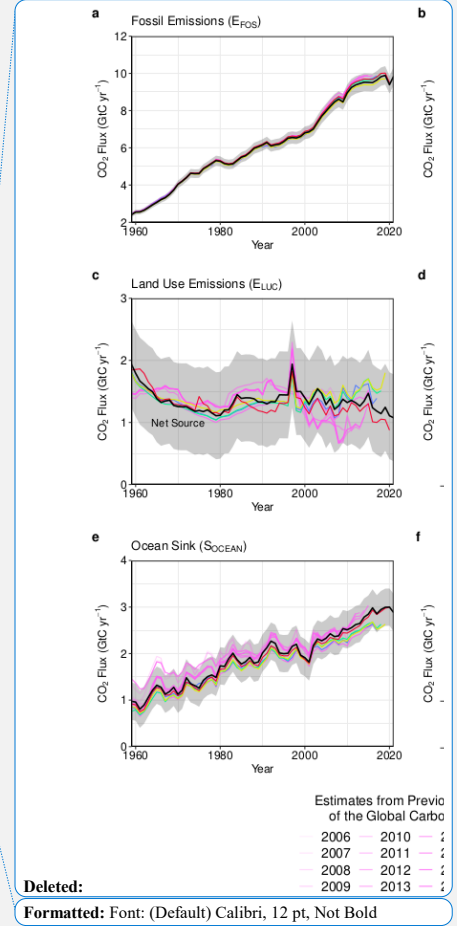
3756

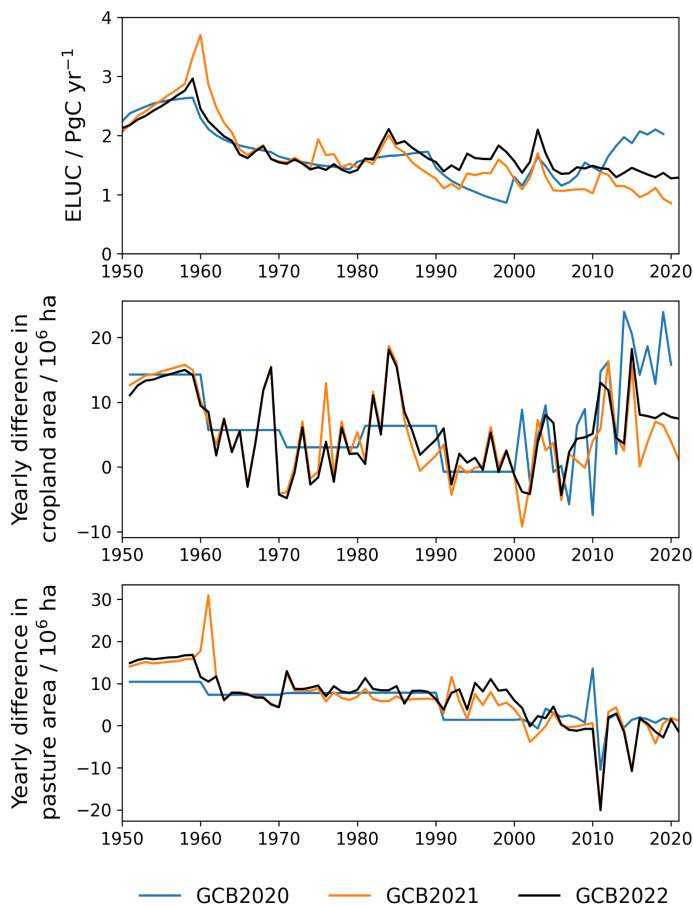
3757

3758

3759

**Figure B5.** Comparison of the estimates of each component of the global carbon budget in this study (black line) with the estimates released annually by the GCP since 2006. Grey shading shows the uncertainty bounds representing  $\pm 1$  standard deviation of the current global carbon budget, based on the uncertainty assessments described in Appendix C. CO<sub>2</sub> emissions from (a) fossil CO<sub>2</sub> emissions ( $E_{FOS}$ ), and (b) land-use change ( $E_{LUC}$ ), as well as their partitioning among (c) the atmosphere ( $G_{ATM}$ ), (d) the land ( $S_{LAND}$ ), and (e) the ocean ( $S_{OCEAN}$ ). See legend for the corresponding years, and Tables 3 and A7 for references. The budget year corresponds to the year when the budget was first released. All values are in GtC yr<sup>-1</sup>.





3761

3762 **Figure B6.** Differences in the HYDE/LUH2 land-use forcing used for the global carbon budgets GCB2020 (Friedlingstein et  
 3763 al., 2021), GCB2021 (Friedlingstein et al., 2022a), and GCB2022 (Friedlingstein et al., 2022b). Shown are year-to-year  
 3764 changes in cropland area (middle panel) and pasture area (bottom panel). To illustrate the relevance of the update in the  
 3765 land-use forcing to the recent trends in ELUC, the top panel shows the land-use emission estimate from the bookkeeping model  
 3766 BLUE (original model output, i.e. excluding peat fire and drainage emissions).

This block contains three smaller line graphs, each mirroring one of the panels from the main figure on the left. They are arranged vertically and share a common x-axis from 1950 to 2020.

- Top Graph:** ELUC / PgC. Y-axis from 1.0 to 3.5. Shows the same trends as the main top panel.
- Middle Graph:** Yearly difference in cropland area / Mha. Y-axis from -10 to 20. Shows the same trends as the main middle panel.
- Bottom Graph:** Yearly difference in pasture area / Mha. Y-axis from -20 to 30. Shows the same trends as the main bottom panel.

Below the graphs is a list of text boxes:

- Deleted:
- Deleted: and for
- Deleted: /
- Deleted: 2022a, Friedlingstein et al.,
- Formatted: Font: 10 pt, Not Bold

3771 **Appendix C. Extended Methodology**

3772 **C.1 Methodology Fossil Fuel CO<sub>2</sub> emissions (E<sub>Fos</sub>)**

3773 **C.1.1 Cement carbonation**

3774 From the moment it is created, cement begins to absorb CO<sub>2</sub> from the atmosphere, a process known as ‘cement  
3775 carbonation’. We estimate this CO<sub>2</sub> sink, from 1931 onwards, as the average of two studies in the literature (Cao et al.,  
3776 2020; Guo et al., 2021). The Global Cement and Concrete Association reports a much lower carbonation rate, but this is  
3777 based on the highly conservative assumption of 0% mortar (GCCA, 2021). Modelling cement carbonation requires  
3778 estimation of a large number of parameters, including the different types of cement material in different countries, the  
3779 lifetime of the structures before demolition, of cement waste after demolition, and the volumetric properties of  
3780 structures, among others (Xi et al., 2016). Lifetime is an important parameter because demolition results in the exposure  
3781 of new surfaces to the carbonation process. The main reasons for differences between the two studies appear to be the  
3782 assumed lifetimes of cement structures and the geographic resolution, but the uncertainty bounds of the two studies  
3783 overlap.

3784 **C.1.2 Emissions embodied in goods and services**

3785 CDIAC, UNFCCC, and BP national emission statistics ‘include greenhouse gas emissions and removals taking place  
3786 within national territory and offshore areas over which the country has jurisdiction’ (Rypdal et al., 2006), and are called  
3787 territorial emission inventories. Consumption-based emission inventories allocate emissions to products that are  
3788 consumed within a country, and are conceptually calculated as the territorial emissions minus the ‘embodied’ territorial  
3789 emissions to produce exported products plus the emissions in other countries to produce imported products  
3790 (Consumption = Territorial – Exports + Imports). Consumption-based emission attribution results (e.g. Davis and  
3791 Caldeira, 2010) provide additional information to territorial-based emissions that can be used to understand emission  
3792 drivers (Hertwich and Peters, 2009) and quantify emission transfers by the trade of products between countries (Peters  
3793 et al., 2011b). The consumption-based emissions have the same global total, but reflect the trade-driven movement of  
3794 emissions across the Earth’s surface in response to human activities. We estimate consumption-based emissions from  
3795 1990-2020 by enumerating the global supply chain using a global model of the economic relationships between  
3796 economic sectors within and between every country (Andrew and Peters, 2013; Peters et al., 2011a). Our analysis is  
3797 based on the economic and trade data from the Global Trade and Analysis Project (GTAP; Narayanan et al., 2015), and  
3798 we make detailed estimates for the years 1997 (GTAP version 5), 2001 (GTAP6), and 2004, 2007, 2011, and 2014  
3799 (GTAP10.0a), covering 57 sectors and 141 countries and regions. The detailed results are then extended into an annual  
3800 time series from 1990 to the latest year of the Gross Domestic Product (GDP) data (2020 in this budget), using GDP  
3801 data by expenditure in current exchange rate of US dollars (USD; from the UN National Accounts main Aggregates  
3802 database; UN, 2021) and time series of trade data from GTAP (based on the methodology in Peters et al., 2011a). We  
3803 estimate the sector-level CO<sub>2</sub> emissions using the GTAP data and methodology, add the flaring and cement emissions  
3804 from our fossil CO<sub>2</sub> dataset, and then scale the national totals (excluding bunker fuels) to match the emission estimates  
3805 from the carbon budget. We do not provide a separate uncertainty estimate for the consumption-based emissions, but  
3806 based on model comparisons and sensitivity analysis, they are unlikely to be significantly different than for the  
3807 territorial emission estimates (Peters et al., 2012a).

Deleted: <#>.....Page Break.....  
<#>

Formatted: Heading 3, Indent: First line: 1.27 cm

Moved (insertion) [1]

Deleted: Both studies use the same model, developed by Xi et al. (2016), with different parameterisations and input data, with the estimate of Guo and colleagues being a revision of Xi et al (2016). The trends of the two studies are very similar.

Deleted: In the present budget, we include the cement carbonation carbon sink in the fossil CO<sub>2</sub> emission component (E<sub>Fos</sub>).

Formatted: Indent: First line: 1.27 cm

### 3817 C.1.3 Uncertainty assessment for $E_{FOS}$

3818 We estimate the uncertainty of the global fossil CO<sub>2</sub> emissions at ±5% (scaled down from the published ±10% at ±2σ  
3819 to the use of ±1σ bounds reported here; Andres et al., 2012). This is consistent with a more detailed analysis of  
3820 uncertainty of ±8.4% at ±2σ (Andres et al., 2014) and at the high-end of the range of ±5-10% at ±2σ reported by  
3821 (Ballantyne et al., 2015). This includes an assessment of uncertainties in the amounts of fuel consumed, the carbon and  
3822 heat contents of fuels, and the combustion efficiency. While we consider a fixed uncertainty of ±5% for all years, the  
3823 uncertainty as a percentage of emissions is growing with time because of the larger share of global emissions from  
3824 emerging economies and developing countries (Marland et al., 2009). Generally, emissions from mature economies  
3825 with good statistical processes have an uncertainty of only a few per cent (Marland, 2008), while emissions from  
3826 strongly developing economies such as China have uncertainties of around ±10% (for ±1σ; Gregg et al., 2008; Andres  
3827 et al., 2014). Uncertainties of emissions are likely to be mainly systematic errors related to underlying biases of energy  
3828 statistics and to the accounting method used by each country.

### 3829 C.1.4 Growth rate in emissions

3830 We report the annual growth rate in emissions for adjacent years (in percent per year) by calculating the difference  
3831 between the two years and then normalising to the emissions in the first year:  $(E_{FOS}(t+1)-$   
3832  $E_{FOS}(t))/E_{FOS}(t) \times 100\%$ . We apply a leap-year adjustment where relevant to ensure valid interpretations of annual  
3833 growth rates. This affects the growth rate by about 0.3% yr<sup>-1</sup> (1/366) and causes calculated growth rates to go up  
3834 approximately 0.3% if the first year is a leap year and down 0.3% if the second year is a leap year.

3835 The relative growth rate of  $E_{FOS}$  over time periods of greater than one year can be rewritten using its logarithm  
3836 equivalent as follows:

$$3837 \frac{1}{E_{FOS}} \frac{dE_{FOS}}{dt} = \frac{d(\ln E_{FOS})}{dt} \quad (2)$$

3838 Here we calculate relative growth rates in emissions for multi-year periods (e.g. a decade) by fitting a linear trend to  
3839  $\ln(E_{FOS})$  in Eq. (2), reported in percent per year.

### 3840 C.1.5 Emissions projection for 2022

3841 To gain insight on emission trends for 2022, we provide an assessment of global fossil CO<sub>2</sub> emissions,  $E_{FOS}$ , by  
3842 combining individual assessments of emissions for China, USA, the EU, and India (the four countries/regions with the  
3843 largest emissions), and the rest of the world.

3844 The methods are specific to each country or region, as described in detail below.

3845 **China:** We use a regression between monthly data for each fossil fuel and cement, and annual data for consumption of  
3846 fossil fuels / production of cement to project full-year growth in fossil fuel consumption and cement production. The  
3847 monthly data for each product consists of the following:

- 3848 • Coal: Proprietary estimate for monthly consumption of main coal types, from SX Coal
- 3849 • Oil: Production data from the National Bureau of Statistics (NBS), plus net imports from the China Customs  
3850 Administration (i.e., gross supply of oil, not including inventory changes)
- 3851 • Natural gas: Same as for oil

Formatted: Indent: First line: 1.27 cm

Formatted: Indent: First line: 1.27 cm

Formatted: Indent: First line: 1.27 cm

Formatted: Outline numbered + Level: 1 + Numbering  
Style: Bullet + Aligned at: 0.63 cm + Indent at: 1.27 cm

3852 • Cement: Production data from NBS

3853 For oil, we use data for production and net imports of refined oil products rather than crude oil. This choice is made  
3854 because refined products are one step closer to actual consumption, and because crude oil can be subject to large  
3855 market-driven and strategic inventory changes that are not captured by available monthly data.

3856 For each fuel and cement, we make a Bayesian linear regression between year-on-year cumulative growth in supply  
3857 (production for cement) and full-year growth in consumption (production for cement) from annual consumption data. In  
3858 the regression model, the growth rate in annual consumption (production for cement) is modelled as a regression  
3859 parameter multiplied by the cumulative year-on-year growth rate from the monthly data through July of each year for  
3860 past years (through 2021). We use broad Gaussian distributions centered around 1 as priors for the ratios between  
3861 annual and through-July growth rates. We then use the posteriors for the growth rates together with cumulative monthly  
3862 supply/production data through July of 2022 to produce a posterior predictive distribution for the full-year growth rate  
3863 for fossil fuel consumption / cement production in 2022.

3864 If the growth in supply/production through July were an unbiased estimate of the full-year growth in  
3865 consumption/production, the posterior distribution for the ratio between the monthly and annual growth rates would be  
3866 centered around 1. However, in practice the ratios are different from 1 (in most cases below 1). This is a result of  
3867 various biasing factors such as uneven evolution in the first and second half of each year, inventory changes that are  
3868 somewhat anti-correlated with production and net imports, differences in statistical coverage, and other factors that are  
3869 not captured in the monthly data.

3870 For fossil fuels, the mean of the posterior distribution is used as the central estimate for the growth rate in 2022, while  
3871 the edges of a 68% credible interval (analogous to a 1-sigma confidence interval) are used for the upper and lower  
3872 bounds.

3873 For cement, the evolution from January to July has been highly atypical owing to the ongoing turmoil in the  
3874 construction sector, and the results of the regression analysis are heavily biased by equally atypical but different  
3875 dynamics in 2021. For this reason, we use an average of the results of the regression analysis and the plain growth in  
3876 cement production through July 2022, since this results in a growth rate that seems more plausible and in line with  
3877 where the cumulative cement production appears to be headed at the time of writing.

3878 USA: We use emissions estimated by the U.S. Energy Information Administration (EIA) in their Short-Term Energy  
3879 Outlook (STEO) for emissions from fossil fuels to get both YTD and a full year projection (EIA, 2022). The STEO also  
3880 includes a near-term forecast based on an energy forecasting model which is updated monthly (last update with  
3881 preliminary data through August 2022), and takes into account expected temperatures, household expenditures by fuel  
3882 type, energy markets, policies, and other effects. We combine this with our estimate of emissions from cement  
3883 production using the monthly U.S. cement clinker production data from USGS for January-June 2022, assuming  
3884 changes in cement production over the first part of the year apply throughout the year.

3885 **India:** We use monthly emissions estimates for India updated from Andrew (2020b) through July 2022. These  
3886 estimates are derived from many official monthly energy and other activity data sources to produce direct estimates of  
3887 national CO<sub>2</sub> emissions, without the use of proxies. Emissions from coal are then extended to August using a regression  
3888 relationship based on power generated from coal, coal dispatches by Coal India Ltd., the composite PMI, time, and days  
3889 per month. For the last 3-5 months of the year, each series is extrapolated assuming typical trends.

Deleted: ¶

3891 **EU:** We use a refinement to the methods presented by Andrew (2021), deriving emissions from monthly energy data  
 3892 reported by Eurostat. Some data gaps are filled using data from the Joint Organisations Data Initiative (JODI, 2022).  
 3893 Sub-annual cement production data are limited, but data for Germany and Poland, the two largest producers, suggest a  
 3894 small decline. For fossil fuels this provides estimates through July. We extend coal emissions through August using a  
 3895 regression model built from generation of power from hard coal, power from brown coal, total power generation, and  
 3896 the number of working days in Germany and Poland, the two biggest coal consumers in the EU. These are then  
 3897 extended through the end of the year assuming typical trends. We extend oil emissions by building a regression model  
 3898 between our monthly CO<sub>2</sub> estimates and oil consumption reported by the EIA for Europe in its Short-Term Energy  
 3899 Outlook (September edition), and then using this model with EIA's monthly forecasts. For natural gas, the strong  
 3900 seasonal signal allows the use of the bias-adjusted Holt-Winters exponential smoothing method (Chatfield, 1978).

3901 **Rest of the world:** We use the close relationship between the growth in GDP and the growth in emissions (Raupach et  
 3902 al., 2007) to project emissions for the current year. This is based on a simplified Kaya Identity, whereby E<sub>FOS</sub> (GtC yr<sup>-1</sup>)  
 3903 is decomposed by the product of GDP (USD yr<sup>-1</sup>) and the fossil fuel carbon intensity of the economy (I<sub>FOS</sub>; GtC USD<sup>-1</sup>)  
 3904 as follows:

$$3905 E_{FOS} = GDP \times I_{FOS} \quad (3)$$

3906 Taking a time derivative of Equation (3) and rearranging gives:

$$3907 \frac{1}{E_{FOS}} \frac{dE_{FOS}}{dt} = \frac{1}{GDP} \frac{dGDP}{dt} + \frac{1}{I_{FOS}} \frac{dI_{FOS}}{dt} \quad (4)$$

3908 where the left-hand term is the relative growth rate of E<sub>FOS</sub>, and the right-hand terms are the relative growth rates of  
 3909 GDP and I<sub>FOS</sub>, respectively, which can simply be added linearly to give the overall growth rate.

3910 The I<sub>FOS</sub> is based on GDP in constant PPP (Purchasing Power Parity) from the International Energy Agency (IEA) up to  
 3911 2017 (IEA/OECD, 2019) and extended using the International Monetary Fund (IMF) growth rates through 2021 (IMF,  
 3912 2022). Interannual variability in I<sub>FOS</sub> is the largest source of uncertainty in the GDP-based emissions projections. We  
 3913 thus use the standard deviation of the annual I<sub>FOS</sub> for the period 2012-2021 as a measure of uncertainty, reflecting a  
 3914 ±1σ as in the rest of the carbon budget. For rest-of-world oil emissions growth, we use the global oil demand forecast  
 3915 published by the EIA less our projections for the other four regions, and estimate uncertainty as the maximum absolute  
 3916 difference over the period available for such forecasts using the specific monthly edition (e.g. August) compared to the  
 3917 first estimate based on more solid data in the following year (April).

3918 **World:** The global total is the sum of each of the countries and regions.

3919

## 3920 C.2 Methodology CO<sub>2</sub> emissions from land-use, land-use change and forestry (E<sub>LUC</sub>)

3921 The net CO<sub>2</sub> flux from land-use, land-use change and forestry (E<sub>LUC</sub>, called land-use change emissions in the rest of the  
 3922 text) includes CO<sub>2</sub> fluxes from deforestation, afforestation, logging and forest degradation (including harvest activity),  
 3923 shifting cultivation (cycle of cutting forest for agriculture, then abandoning), and regrowth of forests following wood  
 3924 harvest or abandonment of agriculture. Emissions from peat burning and drainage are added from external datasets (see  
 3925 [Appendix C.2.1](#) below). Only some land-management activities are included in our land-use change emissions  
 3926 estimates (Table A1). Some of these activities lead to emissions of CO<sub>2</sub> to the atmosphere, while others lead to CO<sub>2</sub>

Deleted: section

sinks.  $E_{LUC}$  is the net sum of emissions and removals due to all anthropogenic activities considered. Our annual estimate for 1960-2021 is provided as the average of results from three bookkeeping approaches (Appendix C.2.1 below): an estimate using the Bookkeeping of Land Use Emissions model (Hansis et al., 2015; hereafter BLUE) and one using the compact Earth system model OSCAR (Gasser et al., 2020), both BLUE and OSCAR being updated here to new land-use forcing covering the time period until 2021, and an updated version of the estimate published by Houghton and Nassikas (2017) (hereafter updated H&N2017). All three data sets are then extrapolated to provide a projection for 2022 (Appendix C.2.5 below). In addition, we use results from Dynamic Global Vegetation Models (DGVMs; see Appendix 2.5 and Table 4) to help quantify the uncertainty in  $E_{LUC}$  (Appendix C.2.4), and thus better characterise our understanding. Note that in this budget, we use the scientific  $E_{LUC}$  definition, which counts fluxes due to environmental changes on managed land towards  $S_{LAND}$ , as opposed to the national greenhouse gas inventories under the UNFCCC, which include them in  $E_{LUC}$  and thus often report smaller land-use emissions (Grassi et al., 2018; Petrescu et al., 2020). However, we provide a methodology of mapping of the two approaches to each other further below (Appendix C.2.3).

Deleted: Section

Deleted: Section

Deleted: Section

Deleted: Section

Deleted: Section

### C.2.1 Bookkeeping models

Formatted: Indent: First line: 1.27 cm

Land-use change  $CO_2$  emissions and uptake fluxes are calculated by three bookkeeping models. These are based on the original bookkeeping approach of Houghton (2003) that keeps track of the carbon stored in vegetation and soils before and after a land-use change (transitions between various natural vegetation types, croplands, and pastures). Literature-based response curves describe decay of vegetation and soil carbon, including transfer to product pools of different lifetimes, as well as carbon uptake due to regrowth. In addition, the bookkeeping models represent long-term degradation of primary forest as lowered standing vegetation and soil carbon stocks in secondary forests, and include forest management practices such as wood harvests.

BLUE and the updated H&N2017 exclude land ecosystems' transient response to changes in climate, atmospheric  $CO_2$  and other environmental factors, and base the carbon densities on contemporary data from literature and inventory data. Since carbon densities thus remain fixed over time, the additional sink capacity that ecosystems provide in response to  $CO_2$ -fertilisation and some other environmental changes is not captured by these models (Pongratz et al., 2014). On the contrary, OSCAR includes this transient response, and it follows a theoretical framework (Gasser and Ciais, 2013) that allows separating bookkeeping land-use emissions and the loss of additional sink capacity. Only the former is included here, while the latter is discussed in Appendix D4. The bookkeeping models differ in (1) computational units (spatially explicit treatment of land-use change for BLUE, country-level for the updated H&N2017 and OSCAR), (2) processes represented (see Table A1), and (3) carbon densities assigned to vegetation and soil of each vegetation type (literature-based for BLUE and the updated H&N2017, calibrated to DGVMs for OSCAR). A notable difference between models exists with respect to the treatment of shifting cultivation. The update of H&N2017, introduced for the GCB2021 (Friedlingstein et al., 2022) changed the approach over the earlier H&N2017 version: H&N2017 had assumed the "excess loss" of tropical forests (i.e., when the Global Forest Resources Assessment (FRA; FAO 2020) indicated a forest loss larger than the increase in agricultural areas from FAO (FAOSTAT 2021) resulted from converting forests to croplands at the same time older croplands were abandoned. Those abandoned croplands began to recover to forests after 15 years. The updated H&N2017 now assumes that forest loss in excess of increases in cropland and pastures represented an increase in shifting cultivation. When the excess loss of forests was negative, it was assumed that shifting cultivation was returned to forest. Historical areas in shifting cultivation were extrapolated taking into account country-based estimates of areas in fallow in 1980 (FAO/UNEP, 1981) and expert opinion (from Heinemann et al.,

Deleted: and BLUE

2017). In contrast, the BLUE and OSCAR models include sub-grid-scale transitions between all vegetation types. Furthermore, the updated H&N2017 [assumes](#) conversion of natural grasslands to pasture, while BLUE and OSCAR allocate pasture [transitions](#) proportionally on all natural vegetation that exists in a grid-cell. This is one reason for generally higher emissions in BLUE and OSCAR. Bookkeeping models do not directly capture carbon emissions from peat fires, which can create large emissions and interannual variability due to synergies of land-use and climate variability in Southeast Asia, particularly during El-Niño events, nor emissions from the organic layers of drained peat soils. To correct for this, we add peat fire emissions based on the Global Fire Emission Database (GFED4s; van der Werf et al., 2017) to the bookkeeping models' output. [Emissions are calculated by multiplying the mass of dry matter emitted by peat fires with the C emission factor for peat fires indicated in the GFED4s database. Emissions from deforestation fires used to derive ELUC projections for 2022 are calculated analogously. As these satellite-derived estimates of peat fire emissions](#) start in 1997 only, we follow the approach by Houghton and Nassikas (2017) for earlier years, which ramps up from zero emissions in 1980 to  $0.04 \text{ Pg C yr}^{-1}$  in 1996, reflecting the onset of major clearing of peatlands in equatorial Southeast Asia in the 1980s. Similarly, we add estimates of peat drainage emissions. In recent years, more peat drainage estimates that provide spatially explicit data have become available, and we thus extended the number of peat drainage datasets considered: We employ FAO peat drainage emissions 1990–2019 from croplands and grasslands (Conchedda and Tubiello, 2020), peat drainage emissions 1700–2010 from simulations with the DGVM ORCHIDEE-PEAT (Qiu et al., 2021), and peat drainage emissions 1701–2021 from simulations with the DGVM LPX-Bern (Lienert and Joos, 2018; Müller and Joos, 2021) applying the updated LUH2 forcing as also used by BLUE, OSCAR and the DGVMs. We extrapolate the FAO data to 1850–2021 by keeping the post-2019 emissions constant at 2019 levels, by linearly increasing tropical drainage emissions between 1980 and 1990 starting from  $0 \text{ GtC yr}^{-1}$  in 1980, consistent with H&N2017's assumption (Houghton and Nassikas, 2017), and by keeping pre-1990 emissions from the often old drained areas of the extra-tropics constant at 1990 emission levels. ORCHIDEE-PEAT data are extrapolated to 2011–2021 by replicating the average emissions in 2000–2010 (pers. comm. C. Qiu). Further, ORCHIDEE-PEAT only provides peat drainage emissions north of  $30^\circ\text{N}$ , and thus we fill the regions south of  $30^\circ\text{N}$  by the average peat drainage emissions from FAO and LPX-Bern. The average of the carbon emission estimates by the three different peat drainage dataset is added to the bookkeeping models to obtain net ELUC and gross sources.

The three bookkeeping estimates used in this study differ with respect to the land-use change data used to drive the models. The updated H&N2017 base their estimates directly on the Forest Resource Assessment of the FAO which provides statistics on forest-area change and management at intervals of five years currently updated until 2020 (FAO, 2020). The data is based on country reporting to FAO and may include remote-sensing information in more recent assessments. Changes in land-use other than forests are based on annual, national changes in cropland and pasture areas reported by FAO (FAOSTAT, 2021). On the other hand, BLUE uses the harmonised land-use change data LUH2-GCB2022 covering the entire 850–2021 period (an update to the previously released LUH2 v2h dataset; Hurtt et al., 2017; Hurtt et al., 2020), which was also used as input to the DGVMs ([Appendix C.2.2](#)). It describes land-use change, also based on the FAO data as described in [Appendix C.2.2](#) as well as the HYDE3.3 dataset (Klein Goldewijk et al., 2017a, 2017b), but provided at a quarter-degree spatial resolution, considering sub-grid-scale transitions between primary forest, secondary forest, primary non-forest, secondary non-forest, cropland, pasture, rangeland, and urban land (Hurtt et al., 2020; Chini et al., 2021). LUH2-GCB2022 provides a distinction between rangelands and pasture, based on inputs from HYDE. To constrain the models' interpretation on whether rangeland implies the original natural vegetation to be transformed to grassland or not (e.g., browsing on shrubland), a forest mask was provided with LUH2-

Deleted: assume

Deleted: As these satellite-derived estimates

Deleted:

Formatted: Superscript

Formatted: Font colour: Black

Deleted: Section

Deleted: Section

4018 GCB2021; forest is assumed to be transformed to grasslands, while other natural vegetation remains (in case of  
4019 secondary vegetation) or is degraded from primary to secondary vegetation (Ma et al., 2020). This is implemented in  
4020 BLUE. OSCAR was run with both LUH2-GCB2022 and FAO/FRA (as used with the updated H&N2017), where the  
4021 drivers of the latter were linearly extrapolated to 2021 using their 2015–2020 trends. The best-guess OSCAR estimate  
4022 used in our study is a combination of results for LUH2-GCB2022 and FAO/FRA land-use data and a large number of  
4023 perturbed parameter simulations weighted against a constraint (the cumulative  $S_{LAND}$  over 1960-2020 of last year's  
4024 GCB) . As the record of the updated H&N2017 ends in 2020, we extend it to 2021 by adding the difference of the  
4025 emissions from tropical deforestation and degradation, peat drainage, and peat fire between 2020 and 2021 to the  
4026 model's estimate for 2020 (i.e. considering the yearly anomalies of the emissions from tropical deforestation and  
4027 degradation, peat drainage, and peat fire). The same method is applied to all three bookkeeping estimates to provide a  
4028 projection for 2022.

4029 For  $E_{LUC}$  from 1850 onwards we average the estimates from BLUE, the updated H&N2017 and OSCAR. For the  
4030 cumulative numbers starting 1750 an average of four earlier publications is added ( $30 \pm 20$  PgC 1750-1850, rounded to  
4031 nearest 5; Le Quéré et al., 2016).

4032 We provide estimates of the gross land use change fluxes from which the reported net land-use change flux,  $E_{LUC}$ , is  
4033 derived as a sum. Gross fluxes are derived internally by the three bookkeeping models: Gross emissions stem from  
4034 decaying material left dead on site and from products after clearing of natural vegetation for agricultural purposes or  
4035 wood harvesting, emissions from peat drainage and peat burning, and, for BLUE, additionally from degradation from  
4036 primary to secondary land through usage of natural vegetation as rangeland. Gross removals stem from regrowth after  
4037 agricultural abandonment and wood harvesting. Gross fluxes for the updated H&N2017 for 2020 and for the 2022  
4038 projection of all three models were calculated by the change in emissions from tropical deforestation and degradation  
4039 and peat burning and drainage as described for the net  $E_{LUC}$  above: As tropical deforestation and degradation and peat  
4040 burning and drainage all only lead to gross emissions to the atmosphere, only gross (and net) emissions are adjusted this  
4041 way, while gross sinks are assumed to remain constant over the previous year. .

4042 This year, we provide an additional split of the net  $E_{LUC}$  into component fluxes to better identify reasons for divergence  
4043 between bookkeeping estimates and to give more insight into the drivers of sources and sinks. This split distinguishes  
4044 between fluxes from deforestation (including due to shifting cultivation), fluxes from organic soils (i.e., peat drainage  
4045 and fires), ~~re/afforestation and wood harvest (i.e., fluxes in forests from slash and product decay following wood~~  
4046 ~~harvesting; regrowth associated with wood harvesting or after abandonment, including reforestation and in shifting~~  
4047 ~~cultivation cycles; afforestation) and fluxes associated with all other transitions.~~

#### 4048 **C.2.2 Dynamic Global Vegetation Models (DGVMs)**

4049 Land-use change  $CO_2$  emissions have also been estimated using an ensemble of 16 DGVMs simulations. The DGVMs  
4050 account for deforestation and regrowth, the most important components of  $E_{LUC}$ , but they do not represent all processes  
4051 resulting directly from human activities on land (Table A1). All DGVMs represent processes of vegetation growth and  
4052 mortality, as well as decomposition of dead organic matter associated with natural cycles, and include the vegetation  
4053 and soil carbon response to increasing atmospheric  $CO_2$  concentration and to climate variability and change. Most  
4054 models explicitly simulate the coupling of carbon and nitrogen cycles and account for atmospheric N deposition and N

Deleted: on

Deleted: (

Formatted: English (UK)

Formatted: Indent: First line: 1.27 cm

4057 fertilisers (Table A1). The DGVMs are independent from the other budget terms except for their use of atmospheric  
4058 CO<sub>2</sub> concentration to calculate the fertilisation effect of CO<sub>2</sub> on plant photosynthesis.

4059 All DGVMs use the LUH2-GCB2022 dataset as input, which includes the HYDE cropland/grazing land dataset (Klein  
4060 Goldewijk et al., 2017a, 2017b), and additional information on land-cover transitions and wood harvest. DGVMs use  
4061 annual, half-degree (regridded from 5 minute resolution), fractional data on cropland and pasture from HYDE3.3.

4062 DGVMs that do not simulate subgrid scale transitions (i.e., net land-use emissions; see Table A1) used the HYDE  
4063 information on agricultural area change. For all countries, with the exception of Brazil and the Democratic Republic of  
4064 the Congo, these data are based on the available annual FAO statistics of change in agricultural land area available from  
4065 1961 up to and including 2017. The FAO retrospectively revised their reporting for [the Democratic Republic of the](#)  
4066 [Congo](#), which was newly available until 2020. In addition to FAO country-level statistics the HYDE3.3  
4067 cropland/grazing land dataset is constrained spatially based on multi-year satellite land cover maps from ESA CCI LC  
4068 (see below). After the year 2017, LUH2 extrapolates, on a gridcell-basis, the cropland, pasture, and urban data linearly  
4069 based on the trend over the previous 5 years, to generate data until the year 2021. This extrapolation methodology is not  
4070 appropriate for countries which have experienced recent rapid changes in the rate of land-use change, e.g. Brazil which  
4071 has experienced a recent upturn in deforestation. Hence, for Brazil we replace FAO state-level data for cropland and  
4072 grazing land in HYDE by those from in-country land cover dataset MapBiomias (collection 6) for 1985-2020 (Souza et  
4073 al. 2020). ESA-CCI is used to spatially disaggregate as described below. Similarly, an estimate for the year 2021 is  
4074 based on the MapBiomias trend 2015-2020. The pre-1985 period is scaled with the per capita numbers from 1985 from  
4075 MapBiomias, so this transition is smooth.

4076 HYDE uses satellite imagery from ESA-CCI from 1992 – 2018 for more detailed yearly allocation of cropland and  
4077 grazing land, with the ESA area data scaled to match the FAO annual totals at country-level. The original 300 metre  
4078 spatial resolution data from ESA was aggregated to a 5 arc minute resolution according to the classification scheme as  
4079 described in Klein Goldewijk et al (2017a).

4080 DGVMs that simulate subgrid scale transitions (i.e., gross land-use emissions; see Table A1) use more detailed land use  
4081 transition and wood harvest information from the LUH2-GCB2022 data set. LUH2-GCB2022 is an update of the more  
4082 comprehensive harmonised land-use data set (Hurt et al., 2020), that further includes fractional data on primary and  
4083 secondary forest vegetation, as well as all underlying transitions between land-use states (850-2020; Hurt et al., 2011,  
4084 2017, 2020; Chini et al., 2021; Table A1). This data set is of quarter degree fractional areas of land-use states and all  
4085 transitions between those states, including a new wood harvest reconstruction, new representation of shifting  
4086 cultivation, crop rotations, management information including irrigation and fertiliser application. The land-use states  
4087 include five different crop types in addition to splitting grazing land into managed pasture and rangeland. Wood harvest  
4088 patterns are constrained with Landsat-based tree cover loss data (Hansen et al. 2013). Updates of LUH2-GCB2022 over  
4089 last year's version (LUH2-GCB2021) are using the most recent HYDE release (covering the time period up to 2017,  
4090 revision to Brazil and [the Democratic Republic of the Congo](#), as described above). We use the same FAO wood harvest  
4091 data as last year for all dataset years from 1961 to 2019, and extrapolate to the year 2022. The HYDE3.3 population  
4092 data is also used to extend the wood harvest time series back in time. Other wood harvest inputs (for years prior to  
4093 1961) remain the same in LUH2. These updates in the land-use forcing are shown in comparison to the more  
4094 pronounced version change from the GCB2020 (Friedlingstein et al., 2020) to GCB2021, which was discussed in  
4095 Friedlingstein et al. (2022a) in Figure B6 and their relevance for land-use emissions discussed in Section 3.2.2. DGVMs

Deleted: (DRC),

Deleted: DRC

Deleted: DRC

4099 implement land-use change differently (e.g., an increased cropland fraction in a grid cell can either be at the expense of  
4100 grassland or shrubs, or forest, the latter resulting in deforestation; land cover fractions of the non-agricultural land differ  
4101 between models). Similarly, model-specific assumptions are applied to convert deforested biomass or deforested area,  
4102 and other forest product pools into carbon, and different choices are made regarding the allocation of rangelands as  
4103 natural vegetation or pastures.

4104 The difference between two DGVMs simulations (see Appendix C4.1 below), one forced with historical changes in  
4105 land-use and a second with time-invariant pre-industrial land cover and pre-industrial wood harvest rates, allows  
4106 quantification of the dynamic evolution of vegetation biomass and soil carbon pools in response to land-use change in  
4107 each model ( $E_{LUC}$ ). Using the difference between these two DGVMs simulations to diagnose  $E_{LUC}$  means the DGVMs  
4108 account for the loss of additional sink capacity (around  $0.4 \pm 0.3$  GtC yr<sup>-1</sup>; see Section 2.7 and Appendix D4), while the  
4109 bookkeeping models do not.

4110 As a criterion for inclusion in this carbon budget, we only retain models that simulate a positive  $E_{LUC}$  during the 1990s,  
4111 as assessed in the IPCC AR4 (Denman et al., 2007) and AR5 (Ciais et al., 2013). All DGVMs met this criterion,  
4112 although one model was not included in the  $E_{LUC}$  estimate from DGVMs as it exhibited a spurious response to the  
4113 transient land cover change forcing after its initial spin-up.

### 4114 C.2.3 Mapping of national GHG inventory data to $E_{LUC}$

4115 An approach was implemented to reconcile the large gap between land-use emissions estimates from bookkeeping  
4116 models and from national GHG Inventories (NGHGI) (see Tab. A8). This gap is due to different approaches to  
4117 calculating “anthropogenic” CO<sub>2</sub> fluxes related to land-use change and land management (Grassi et al. 2018). In  
4118 particular, the land sinks due to environmental change on managed lands are treated as non-anthropogenic in the global  
4119 carbon budget, while they are generally considered as anthropogenic in NGHGIs (“indirect anthropogenic fluxes”;  
4120 Eggleston et al., 2006). Building on previous studies (Grassi et al. 2021), the approach implemented here adds the  
4121 DGVMs estimates of CO<sub>2</sub> fluxes due to environmental change from countries’ managed forest area (part of  $S_{LAND}$ ) to  
4122 the  $E_{LUC}$  flux. This sum is expected to be conceptually more comparable to LULUCF than  $E_{LUC}$ .

4123  $E_{LUC}$  data are taken from bookkeeping models, in line with the global carbon budget approach. To determine  $S_{LAND}$  on  
4124 managed forest, the following steps were taken: Spatially gridded data of “natural” forest NBP ( $S_{LAND}$  i.e., due to  
4125 environmental change and excluding land use change fluxes) were obtained with S2 runs from DGVMs up to 2021  
4126 from the TRENDY v11 dataset. Results were first masked with a forest map that is based on Hansen (Hansen et  
4127 al.2013) tree cover data. To do this conversion (“tree” cover to “forest” cover), we exclude gridcells with less than 20%  
4128 tree cover and isolated pixels with maximum connectivity less than 0.5 ha following the FAO definition of forest.  
4129 Forest NBP are then further masked with the “intact” forest map for the year 2013, i.e. forest areas characterised by no  
4130 remotely detected signs of human activity (Potapov et al. 2017). This way, we obtained the  $S_{LAND}$  in “intact” and  
4131 “non-intact” forest area, which previous studies (Grassi et al. 2021) indicated to be a good proxy, respectively, for  
4132 “unmanaged” and “managed” forest area in the NGHGI. Note that only 4 models (CABLE-POP, CLASSIC, JSBACH  
4133 and YIBs) had forest NBP at grid cell level. For the other DGVMs, when a grid cell had forest, all the NBP was  
4134 allocated to forest. However, since S2 simulations use pre-industrial forest cover masks that are at least 20% larger than  
4135 today’s forest (Hurt et al. 2020), we corrected this NBP by a ratio between observed (based on Hansen) and prescribed  
4136 (from DGVMs) forest cover. This ratio is calculated for each individual DGVM that provides information on prescribed

Deleted: See Section

Deleted: 4,

Formatted: Indent: First line: 1.27 cm

Deleted:  $E_{LUC}$

Deleted: land use, land-use change and forestry (LULUCF)

Deleted: the

Deleted: original

Deleted: simply

4144 forest cover (LPX-Bern, OCN, JULES, VISIT, VISIT-NIES, SDGVM). For the others (IBIS, CLM5.0, ORCHIDEE,  
4145 ISAM, DLEM, LPJ-GUESS) a common ratio (median ratio of all the 10 models that provide information on prescribed  
4146 forest cover) is used. The details of the method used are explained here:

4147 [https://github.com/RamAlkama/LandCarbonBudget\\_IntactAndNonIntactForest](https://github.com/RamAlkama/LandCarbonBudget_IntactAndNonIntactForest)

4148 LULUCF data from NGHGs are from Grassi et al. (2022a). While Annex I countries report a complete time series  
4149 1990-2020, for Non-Annex I countries gap-filling was applied through linear interpolation between two points and/or  
4150 through extrapolation backward (till 1990) and forward (till 2020) using the single closest available data. For all  
4151 countries, the estimates of the year 2021 are assumed to be equal to those of 2020. This data includes all CO<sub>2</sub> fluxes  
4152 from land considered managed, which in principle encompasses all land uses (forest land, cropland, grassland,  
4153 wetlands, settlements, and other land), changes among them, emissions from organic soils and from fires. In practice,  
4154 although almost all Annex I countries report all land uses, many non-Annex I countries report only on deforestation and  
4155 forest land, and only few countries report on other land uses. In most cases, NGHGs include most of the natural  
4156 response to recent environmental change, because they use direct observations (e.g., national forest inventories) that do  
4157 not allow separating direct and indirect anthropogenic effects (Eggleston et al., 2006).

4158 To provide additional, largely independent assessments of fluxes on unmanaged vs managed lands, we include a  
4159 DGVM that allows diagnosing fluxes from unmanaged vs managed lands by tracking vegetation cohorts of different  
4160 ages separately. This model, ORCHIDEE-MICT (Yue et al., 2018), was run using the same LUH2 forcing as the  
4161 DGVMs used in this budget (Section 2.5) and the bookkeeping models BLUE and OSCAR (Section 2.2). Old-aged  
4162 forest was classified as primary forest after a certain threshold of carbon density was reached again, and the model-  
4163 internal distinction between primary and secondary forest used as proxies for unmanaged vs managed forests;  
4164 agricultural lands are added to the latter to arrive at total managed land.

4165 Tab. A8 shows the resulting mapping of global carbon cycle models' land flux definitions to that of the NGHGI  
4166 (discussed in Section 3.2.2). ORCHIDEE-MICT estimates for SLAND on intact forests are expected to be higher than  
4167 based on DGVMs in combination with the NGHGI managed/unmanaged forest data because the unmanaged forest  
4168 area, with about 27 mio km<sup>2</sup>, is estimated to be substantially larger by ORCHIDEE-MICT than, with less than 10 mio  
4169 km<sup>2</sup>, by the NGHGI, while managed forest area is estimated to be smaller (22 compared to 32 mio km<sup>2</sup>). Related to  
4170 this, E<sub>LUC</sub> plus S<sub>LAND</sub> on non-intact lands is a larger source estimated by ORCHIDEE-MICT compared to NGHGI. We  
4171 also show as comparison FAOSTAT emissions totals (FAO, 2021), which include emissions from net forest conversion  
4172 and fluxes on forest land (Tubiello et al., 2021) as well as CO<sub>2</sub> emissions from peat drainage and peat fires. The 2021  
4173 data was estimated by including actual 2021 estimates for peatlands drainage and fire and a carry forward from 2020 to  
4174 2021 for the forest land stock change. The FAO data shows a global source of 0.24 GtC yr<sup>-1</sup> averaged over 2012-2021,  
4175 in contrast to the sink of -0.54 GtC yr<sup>-1</sup> of the gap-filled NGHGI data. Most of this difference is attributable to different  
4176 scopes: a focus on carbon fluxes for the NGHGI and a focus on area and biomass for FAO. In particular, the NGHGI  
4177 data includes a larger forest sink for non-Annex 1 countries resulting from a more complete coverage of non-biomass  
4178 carbon pools and non-forest land uses. NGHGI and FAO data also differ in terms of underlying data on forest land  
4179 (Grassi et al., 2022a).

Deleted:

Deleted:

Deleted: is

Deleted: ..

Deleted: NGHGI

4185 **C.2.4 Uncertainty assessment for  $E_{LUC}$**

4186 Differences between the bookkeeping models and DGVMs models originate from three main sources: the different  
4187 methodologies, which among others lead to inclusion of the loss of additional sink capacity in DGVMs (see Appendix  
4188 D1.4), the underlying land-use/land cover data set, and the different processes represented (Table A1). We examine the  
4189 results from the DGVMs models and of the bookkeeping method and use the resulting variations as a way to  
4190 characterise the uncertainty in  $E_{LUC}$ .

4191 Despite these differences, the  $E_{LUC}$  estimate from the DGVMs multi-model mean is consistent with the average of the  
4192 emissions from the bookkeeping models (Table 5). However there are large differences among individual DGVMs  
4193 (standard deviation at around 0.5 GtC yr<sup>-1</sup>; Table 5), between the bookkeeping estimates (average difference 1850-2020  
4194 BLUE-updated H&N2017 of 0.8 GtC yr<sup>-1</sup>, BLUE-OSCAR of 0.4 GtC yr<sup>-1</sup>, OSCAR-updated H&N2017 of 0.3 GtC yr<sup>-1</sup>),  
4195 and between the updated estimate of H&N2017 and its previous model version (Houghton et al., 2012). A factorial  
4196 analysis of differences between BLUE and H&N2017 attributed them particularly to differences in carbon densities  
4197 between natural and managed vegetation or primary and secondary vegetation (Bastos et al., 2021). Earlier studies  
4198 additionally showed the relevance of the different land-use forcing as applied (in updated versions) also in the current  
4199 study (Gasser et al., 2020). Ganzenmüller et al. (2022) recently showed that  $E_{LUC}$  estimates with BLUE are  
4200 substantially smaller when the model is driven by a new high-resolution land-use dataset (HILDA+). They identified  
4201 shifting cultivation and the way it is implemented in LUH2 as a main reason for this divergence. They further showed  
4202 that a higher spatial resolution reduces the estimates of both sources and sinks because successive transitions are not  
4203 adequately represented at coarser resolution, which has the effect that—despite capturing the same extent of transition  
4204 areas—overall less area remains pristine at the coarser compared to the higher resolution.

4205 The uncertainty in  $E_{LUC}$  of  $\pm 0.7$  GtC yr<sup>-1</sup> reflects our best value judgement that there is at least 68% chance ( $\pm 1\sigma$ ) that  
4206 the true land-use change emission lies within the given range, for the range of processes considered here. Prior to the  
4207 year 1959, the uncertainty in  $E_{LUC}$  was taken from the standard deviation of the DGVMs. We assign low confidence to  
4208 the annual estimates of  $E_{LUC}$  because of the inconsistencies among estimates and of the difficulties to quantify some of  
4209 the processes in DGVMs.

4210 **C.2.5 Emissions projections for  $E_{LUC}$**

4211 We project the 2022 land-use emissions for BLUE, the updated H&N2017 and OSCAR, starting from their estimates  
4212 for 2021 assuming unaltered peat drainage, which has low interannual variability, and the highly variable emissions  
4213 from peat fires, tropical deforestation and degradation as estimated using active fire data (MCD14ML; Giglio et al.,  
4214 2016). Those latter scale almost linearly with GFED over large areas (van der Werf et al., 2017), and thus allows for  
4215 tracking fire emissions in deforestation and tropical peat zones in near-real time.

4216

4217 **C.3 Methodology Ocean CO<sub>2</sub> sink**

4218 **C.3.1 Observation-based estimates**

4219 We primarily use the observational constraints assessed by IPCC of a mean ocean CO<sub>2</sub> sink of  $2.2 \pm 0.7$  GtC yr<sup>-1</sup> for the  
4220 1990s (90% confidence interval; Ciais et al., 2013) to verify that the GOBMs provide a realistic assessment of  $S_{OCEAN}$ .

Formatted: Indent: First line: 1.27 cm

Formatted: Indent: First line: 1.27 cm

Formatted: Indent: First line: 1.27 cm

4221 This is based on indirect observations with seven different methodologies and their uncertainties, and further using  
4222 three of these methods that are deemed most reliable for the assessment of this quantity (Denman et al., 2007; Ciais et  
4223 al., 2013). The observation-based estimates use the ocean/land CO<sub>2</sub> sink partitioning from observed atmospheric CO<sub>2</sub>  
4224 and O<sub>2</sub>/N<sub>2</sub> concentration trends (Manning and Keeling, 2006; Keeling and Manning, 2014), an oceanic inversion  
4225 method constrained by ocean biogeochemistry data (Mikaloff Fletcher et al., 2006), and a method based on penetration  
4226 time scale for chlorofluorocarbons (McNeil et al., 2003). The IPCC estimate of 2.2 GtC yr<sup>-1</sup> for the 1990s is consistent  
4227 with a range of methods (Wanninkhof et al., 2013). We refrain from using the IPCC estimates for the 2000s (2.3 ± 0.7  
4228 GtC yr<sup>-1</sup>), and the period 2002-2011 (2.4 ± 0.7 GtC yr<sup>-1</sup>, Ciais et al., 2013) as these are based on trends derived mainly  
4229 from models and one data-product (Ciais et al., 2013). Additional constraints summarised in AR6 (Canadell et al.,  
4230 2021) are the interior ocean anthropogenic carbon change (Gruber et al., 2019) and ocean sink estimate from  
4231 atmospheric CO<sub>2</sub> and O<sub>2</sub>/N<sub>2</sub> (Tohjima et al., 2019) which are used for model evaluation and discussion, respectively.

4232 We also use eight estimates of the ocean CO<sub>2</sub> sink and its variability based on surface ocean fCO<sub>2</sub> maps obtained by the  
4233 interpolation of surface ocean fCO<sub>2</sub> measurements from 1990 onwards due to severe restriction in data availability prior  
4234 to 1990 (Figure 10). These estimates differ in many respects: they use different maps of surface fCO<sub>2</sub>, different  
4235 atmospheric CO<sub>2</sub> concentrations, wind products and different gas-exchange formulations as specified in Table A3. We  
4236 refer to them as fCO<sub>2</sub>-based flux estimates. The measurements underlying the surface fCO<sub>2</sub> maps are from the Surface  
4237 Ocean CO<sub>2</sub> Atlas version 2022 (SOCATv2022; Bakker et al., 2022), which is an update of version 3 (Bakker et al.,  
4238 2016) and contains quality-controlled data through 2021 (see data attribution Table A5). Each of the estimates uses a  
4239 different method to then map the SOCAT v2022 data to the global ocean. The methods include a data-driven diagnostic  
4240 method combined with a multi linear regression approach to extend back to 1957 (Rödenbeck et al., 2022; referred to  
4241 here as Jena-MLS), three neural network models (Landschützer et al., 2014; referred to as MPI-SOMFFN; Chau et al.,  
4242 2022; Copernicus Marine Environment Monitoring Service, referred to here as CMEMS-LSCE-FFNN; and Zeng et al.,  
4243 2014; referred to as NIES-NN), one cluster regression approaches (Gregor and Gruber, 2021, referred to as OS-ETHZ-  
4244 GRaCER), and a multi-linear regression method (Hida et al., 2021; referred to as JMA-MLR), and one method that  
4245 relates the fCO<sub>2</sub> misfit between GOBMs and SOCAT to environmental predictors using the extreme gradient boosting  
4246 method (Gloege et al., 2022). The ensemble mean of the fCO<sub>2</sub>-based flux estimates is calculated from these seven  
4247 mapping methods. Further, we show the flux estimate of Watson et al. (2020) who also use the MPI-SOMFFN method  
4248 to map the adjusted fCO<sub>2</sub> data to the globe, but resulting in a substantially larger ocean sink estimate, owing to a  
4249 number of adjustments they applied to the surface ocean fCO<sub>2</sub> data. Concretely, these authors adjusted the SOCAT  
4250 fCO<sub>2</sub> downward to account for differences in temperature between the depth of the ship intake and the relevant depth  
4251 right near the surface, and included a further adjustment to account for the cool surface skin temperature effect. The  
4252 Watson et al. flux estimate hence differs from the others by their choice of adjusting the flux to a cool, salty ocean  
4253 surface skin. Watson et al. (2020) showed that this temperature adjustment leads to an upward correction of the ocean  
4254 carbon sink, up to 0.9 GtC yr<sup>-1</sup>, that, if correct, should be applied to all fCO<sub>2</sub>-based flux estimates. A reduction of this  
4255 adjustment to 0.6 GtC yr<sup>-1</sup> was proposed by Dong et al. (2022). The impact of the cool skin effect on air-sea CO<sub>2</sub> flux is  
4256 based on established understanding of temperature gradients (as discussed by Goddijn-Murphy et al 2015), and  
4257 laboratory observations (Jähne and Haussecker, 1998; Jähne, 2019), but in situ field observational evidence is lacking  
4258 (Dong et al., 2022). The Watson et al flux estimate presented here is therefore not included in the ensemble mean of the  
4259 fCO<sub>2</sub>-based flux estimates. This choice will be re-evaluated in upcoming budgets based on further lines of evidence.

Deleted:

4261 Typically, data products do not cover the entire ocean due to missing coastal oceans and sea ice cover. The CO<sub>2</sub> flux  
4262 from each fCO<sub>2</sub>-based product is already at or above 99% coverage of the ice-free ocean surface area in two products  
4263 (Jena-MLS, OS-ETHZ-GRaCER), and filled by the data-provider in three products (using Fay et al., 2021a, method for  
4264 JMA-MLR and LDEO-HPD; and Landschützer et al., 2020, methodology for MPI-SOMFFN). The products that  
4265 remained below 99% coverage of the ice-free ocean (CMEMS-LSCE-FFNN, MPI-SOMFFN, NIES-NN, UOx-Watson)  
4266 were scaled by the following procedure.

4267 In previous versions of the GCB, the missing areas were accounted for by scaling the globally integrated fluxes by the  
4268 fraction of the global ocean coverage (361.9e6 km<sup>2</sup> based on ETOPO1, Amante and Eakins, 2009; Eakins and Sharman,  
4269 2010) with the area covered by the CO<sub>2</sub> flux predictions. This approach may lead to unnecessary scaling when the  
4270 majority of the missing data are in the ice-covered region (as is often the case), where flux is already assumed to be  
4271 zero. To avoid this unnecessary scaling, we now scale fluxes regionally (North, Tropics, South) to match the ice-free  
4272 area (using NOAA's OISSTv2, Reynolds et al., 2002):

$$4273 \text{FCO}_2^{\text{reg-scaled}} = \frac{A_{(1-\text{ice})}^{\text{region}}}{A_{\text{FCO}_2}^{\text{region}}} \cdot \text{FCO}_2^{\text{region}}$$

4274 In the equation,  $A$  represents area,  $(1 - \text{ice})$  represents the ice free ocean,  $A_{\{\text{FCO}_2\}^{\text{region}}}$  represents the coverage  
4275 of the data product for a region, and  $\text{FCO}_2^{\text{region}}$  is the integrated flux for a region.

4276 We further use results from two diagnostic ocean models, Khatiwala et al. (2013) and DeVries (2014), to estimate the  
4277 anthropogenic carbon accumulated in the ocean prior to 1959. The two approaches assume constant ocean circulation  
4278 and biological fluxes, with  $S_{\text{OCEAN}}$  estimated as a response in the change in atmospheric CO<sub>2</sub> concentration calibrated to  
4279 observations. The uncertainty in cumulative uptake of  $\pm 20$  GtC (converted to  $\pm 1\sigma$ ) is taken directly from the IPCC's  
4280 review of the literature (Rhein et al., 2013), or about  $\pm 30\%$  for the annual values (Khatiwala et al., 2009).

### 4281 C.3.2 Global Ocean Biogeochemistry Models (GOBMs)

4282 The ocean CO<sub>2</sub> sink for 1959-20121 is estimated using ten GOBMs (Table A2). The GOBMs represent the physical,  
4283 chemical, and biological processes that influence the surface ocean concentration of CO<sub>2</sub> and thus the air-sea CO<sub>2</sub> flux.  
4284 The GOBMs are forced by meteorological reanalysis and atmospheric CO<sub>2</sub> concentration data available for the entire  
4285 time period. They mostly differ in the source of the atmospheric forcing data (meteorological reanalysis), spin up  
4286 strategies, and in their horizontal and vertical resolutions (Table A2). All GOBMs except two (CESM-ETHZ, CESM2)  
4287 do not include the effects of anthropogenic changes in nutrient supply (Duce et al., 2008). They also do not include the  
4288 perturbation associated with changes in riverine organic carbon (see Section 2.7 and Appendix D.3).

4289 Four sets of simulations were performed with each of the GOBMs. Simulation A applied historical changes in climate  
4290 and atmospheric CO<sub>2</sub> concentration. Simulation B is a control simulation with constant atmospheric forcing (normal  
4291 year or repeated year forcing) and constant pre-industrial atmospheric CO<sub>2</sub> concentration. Simulation C is forced with  
4292 historical changes in atmospheric CO<sub>2</sub> concentration, but repeated year or normal year atmospheric climate forcing.  
4293 Simulation D is forced by historical changes in climate and constant pre-industrial atmospheric CO<sub>2</sub> concentration. To  
4294 derive  $S_{\text{OCEAN}}$  from the model simulations, we subtracted the slope of a linear fit to the annual time series of the control  
4295 simulation B from the annual time series of simulation A. Assuming that drift and bias are the same in simulations A  
4296 and B, we thereby correct for any model drift. Further, this difference also removes the natural steady state flux  
4297 (assumed to be 0 GtC yr<sup>-1</sup> globally without rivers) which is often a major source of biases. This approach works for all  
4298 model set-ups, including IPSL, where simulation B was forced with constant atmospheric CO<sub>2</sub> but observed historical

Formatted: Indent: First line: 1.27 cm

4303 changes in climate (equivalent to simulation D). This approach assures that the interannual variability is not removed  
4304 from IPSL simulation A.

4305 The absolute correction for bias and drift per model in the 1990s varied between  $<0.01 \text{ GtC yr}^{-1}$  and  $0.41 \text{ GtC yr}^{-1}$ , with  
4306 seven models having positive biases, two having negative biases and one model having essentially no bias (NorESM).  
4307 The MPI model uses riverine input and therefore simulates outgassing in simulation B. By subtracting simulation B,  
4308 also the ocean carbon sink of the MPI model follows the definition of  $\text{So}_{\text{OCEAN}}$ . This correction reduces the model mean  
4309 ocean carbon sink by  $0.04 \text{ GtC yr}^{-1}$  in the 1990s. The ocean models cover 99% to 101% of the total ocean area, so that  
4310 area-scaling is not necessary.

### 4311 C.3.3 GOBM evaluation and uncertainty assessment for $\text{So}_{\text{OCEAN}}$

Formatted: Indent: First line: 1.27 cm

4312 The ocean  $\text{CO}_2$  sink for all GOBMs and the ensemble mean falls within 90% confidence of the observed range, or 1.5  
4313 to  $2.9 \text{ GtC yr}^{-1}$  for the 1990s (Ciais et al., 2013) before and after applying adjustments. An exception is the MPI model,  
4314 which simulates a low ocean carbon sink of  $1.38 \text{ GtC yr}^{-1}$  for the 1990s in simulation A owing to the inclusion of  
4315 riverine carbon flux. After adjusting to the GCB's definition of  $\text{So}_{\text{OCEAN}}$  by subtracting simulation B, the MPI model falls  
4316 into the observed range with an estimated sink of  $1.69 \text{ GtC yr}^{-1}$ .

4317 The GOBMs and data products have been further evaluated using the fugacity of sea surface  $\text{CO}_2$  ( $\text{fCO}_2$ ) from the  
4318 SOCAT v2022 database (Bakker et al., 2016, 2022). We focused this evaluation on the root mean squared error  
4319 (RMSE) between observed and modelled  $\text{fCO}_2$  and on a measure of the amplitude of the interannual variability of the  
4320 flux (modified after Rödenbeck et al., 2015). The RMSE is calculated from detrended, annually and regionally  
4321 averaged time series calculated from GOBMs and data-product  $\text{fCO}_2$  subsampled to SOCAT sampling points to  
4322 measure the misfit between large-scale signals (Hauck et al., 2020). To this end, we apply the following steps: (i)  
4323 subsample data points for where there are observations (GOBMs/data-products as well as SOCAT), (ii) average  
4324 spatially, (iii) calculate annual mean, (iv) detrend both time-series (GOBMs/data-products as well as SOCAT), (v)  
4325 calculate RMSE. This year, we do not apply an open ocean mask of 400 m, but instead a mask based on the minimum  
4326 area coverage of the data-products. This ensures a fair comparison over equal areas. The amplitude of the  $\text{So}_{\text{OCEAN}}$   
4327 interannual variability (A-IAV) is calculated as the temporal standard deviation of the detrended annual  $\text{CO}_2$  flux time  
4328 series after area-scaling (Rödenbeck et al., 2015, Hauck et al., 2020). These metrics are chosen because RMSE is the  
4329 most direct measure of data-model mismatch and the A-IAV is a direct measure of the variability of  $\text{So}_{\text{OCEAN}}$  on  
4330 interannual timescales. We apply these metrics globally and by latitude bands. Results are shown in Figure B2 and  
4331 discussed in Section 3.5.5.

4332 We quantify the  $1\text{-}\sigma$  uncertainty around the mean ocean sink of anthropogenic  $\text{CO}_2$  by assessing random and systematic  
4333 uncertainties for the GOBMs and data-products. The random uncertainties are taken from the ensemble standard  
4334 deviation ( $0.3 \text{ GtC yr}^{-1}$  for GOBMs,  $0.3 \text{ GtC yr}^{-1}$  for data-products). We derive the GOBMs systematic uncertainty by  
4335 the deviation of the DIC inventory change 1994-2007 from the Gruber et al (2019) estimate ( $0.4 \text{ GtC yr}^{-1}$ ) and suggest  
4336 these are related to physical transport (mixing, advection) into the ocean interior. For the data-products, we consider  
4337 systematic uncertainties stemming from uncertainty in  $\text{fCO}_2$  observations ( $0.2 \text{ GtC yr}^{-1}$ , Takahashi et al., 2009;  
4338 Wanninkhof et al., 2013), gas-transfer velocity ( $0.2 \text{ GtC yr}^{-1}$ , Ho et al., 2011; Wanninkhof et al., 2013; Roobaert et al.,  
4339 2018), wind product ( $0.1 \text{ GtC yr}^{-1}$ , Fay et al., 2021a), river flux adjustment ( $0.3 \text{ GtC yr}^{-1}$ , Regnier et al., 2022, formally  
4340  $2\text{-}\sigma$  uncertainty), and  $\text{fCO}_2$  mapping ( $0.2 \text{ GtC yr}^{-1}$ , Landschützer et al., 2014). Combining these uncertainties as their

4341 squared sums, we assign an uncertainty of  $\pm 0.5 \text{ GtC yr}^{-1}$  to the GOBMs ensemble mean and an uncertainty of  $\pm 0.6$   
4342  $\text{GtC yr}^{-1}$  to the data-product ensemble mean. These uncertainties are propagated as  $\sigma(\text{Socean}) = (1/2^2 * 0.5^2 + 1/2^2 * 0.6^2)^{1/2}$   
4343  $\text{GtC yr}^{-1}$  and result in an  $\pm 0.4 \text{ GtC yr}^{-1}$  uncertainty around the best estimate of  $\text{Socean}$ .  
4344 We examine the consistency between the variability of the model-based and the  $\text{fCO}_2$ -based data products to assess  
4345 confidence in  $\text{Socean}$ . The interannual variability of the ocean fluxes (quantified as A-IAV, the standard deviation after  
4346 detrending, Figure B2) of the seven  $\text{fCO}_2$ -based data products plus the Watson et al. (2020) product for 1990-2021,  
4347 ranges from 0.12 to 0.32  $\text{GtC yr}^{-1}$  with the lower estimates by the two ensemble methods (CMEMS-LSCE-FFNN, OS-  
4348 ETHZ-GRaCER). The inter-annual variability in the GOBMs ranges between 0.09 and 0.20  $\text{GtC yr}^{-1}$ , hence there is  
4349 overlap with the lower A-IAV estimates of two data-products.  
4350 Individual estimates (both GOBMs and data products) generally produce a higher ocean  $\text{CO}_2$  sink during strong El  
4351 Niño events. There is emerging agreement between GOBMs and data-products on the patterns of decadal variability of  
4352  $\text{Socean}$  with a global stagnation in the 1990s and an extra-tropical strengthening in the 2000s (McKinley et al., 2020,  
4353 Hauck et al., 2020). The central estimates of the annual flux from the GOBMs and the  $\text{fCO}_2$ -based data products have a  
4354 correlation  $r$  of 0.94 (1990-2021). The agreement between the models and the data products reflects some consistency  
4355 in their representation of underlying variability since there is little overlap in their methodology or use of observations.  
4356

#### 4357 C.4 Methodology Land $\text{CO}_2$ sink

##### 4358 C.4.1 DGVM simulations

4359 The DGVMs model runs were forced by either the merged monthly Climate Research Unit (CRU) and 6 hourly  
4360 Japanese 55-year Reanalysis (JRA-55) data set or by the monthly CRU data set, both providing observation-based  
4361 temperature, precipitation, and incoming surface radiation on a  $0.5^\circ \times 0.5^\circ$  grid and updated to 2021 (Harris et al., 2014,  
4362 2020). The combination of CRU monthly data with 6 hourly forcing from JRA-55 (Kobayashi et al., 2015) is performed  
4363 with methodology used in previous years (Viovy, 2016) adapted to the specifics of the JRA-55 data.

4364 Introduced in GCB2021 (Friedlingstein et al., 2022a), incoming short-wave radiation fields to take into account aerosol  
4365 impacts and the division of total radiation into direct and diffuse components as summarised below.

4366 The diffuse fraction dataset offers 6-hourly distributions of the diffuse fraction of surface shortwave fluxes over the  
4367 period 1901-2021. Radiative transfer calculations are based on monthly-averaged distributions of tropospheric and  
4368 stratospheric aerosol optical depth, and 6-hourly distributions of cloud fraction. Methods follow those described in the  
4369 Methods section of Mercado et al. (2009), but with updated input datasets.

4370 The time series of speciated tropospheric aerosol optical depth is taken from the historical and RCP8.5 simulations by  
4371 the HadGEM2-ES climate model (Bellouin et al., 2011). To correct for biases in HadGEM2-ES, tropospheric aerosol  
4372 optical depths are scaled over the whole period to match the global and monthly averages obtained over the period  
4373 2003-2020 by the CAMS Reanalysis of atmospheric composition (Inness et al., 2019), which assimilates satellite  
4374 retrievals of aerosol optical depth.

4375 The time series of stratospheric aerosol optical depth is taken from the by Sato et al. (1993) climatology, which has  
4376 been updated to 2012. Years 2013-2020 are assumed to be background years so replicate the background year 2010.  
4377 That assumption is supported by the Global Space-based Stratospheric Aerosol Climatology time series (1979-2016;

Formatted: Indent: First line: 1.27 cm

4378 Thomason et al., 2018). The time series of cloud fraction is obtained by scaling the 6-hourly distributions simulated in  
4379 the Japanese Reanalysis (Kobayashi et al., 2015) to match the monthly-averaged cloud cover in the CRU TS v4.06  
4380 dataset (Harris et al., 2020). Surface radiative fluxes account for aerosol-radiation interactions from both tropospheric  
4381 and stratospheric aerosols, and for aerosol-cloud interactions from tropospheric aerosols, except mineral dust.  
4382 Tropospheric aerosols are also assumed to exert interactions with clouds.

4383 The radiative effects of those aerosol-cloud interactions are assumed to scale with the radiative effects of aerosol-  
4384 radiation interactions of tropospheric aerosols, using regional scaling factors derived from HadGEM2-ES. Diffuse  
4385 fraction is assumed to be 1 in cloudy sky. Atmospheric constituents other than aerosols and clouds are set to a constant  
4386 standard mid-latitude summer atmosphere, but their variations do not affect the diffuse fraction of surface shortwave  
4387 fluxes.

4388 In summary, the DGVMs forcing data include time dependent gridded climate forcing, global atmospheric CO<sub>2</sub>  
4389 (Dlugokencky and Tans, 2022), gridded land cover changes (see Appendix C.2.2), and gridded nitrogen deposition and  
4390 fertilisers (see Table A1 for specific models details).

4391 Four simulations were performed with each of the DGVMs. Simulation 0 (S0) is a control simulation which uses fixed  
4392 pre-industrial (year 1700) atmospheric CO<sub>2</sub> concentrations, cycles early 20th century (1901-1920) climate and applies a  
4393 time-invariant pre-industrial land cover distribution and pre-industrial wood harvest rates. Simulation 1 (S1) differs  
4394 from S0 by applying historical changes in atmospheric CO<sub>2</sub> concentration and N inputs. Simulation 2 (S2) applies  
4395 historical changes in atmospheric CO<sub>2</sub> concentration, N inputs, and climate, while applying time-invariant pre-  
4396 industrial land cover distribution and pre-industrial wood harvest rates. Simulation 3 (S3) applies historical changes in  
4397 atmospheric CO<sub>2</sub> concentration, N inputs, climate, and land cover distribution and wood harvest rates.

4398 S2 is used to estimate the land sink component of the global carbon budget (S<sub>LAND</sub>). S3 is used to estimate the total land  
4399 flux but is not used in the global carbon budget. We further separate S<sub>LAND</sub> into contributions from CO<sub>2</sub> (=S1-S0) and  
4400 climate (=S2-S1+S0).

#### 4401 C.4.2 DGVM evaluation and uncertainty assessment for S<sub>LAND</sub>

4402 We apply three criteria for minimum DGVMs realism by including only those DGVMs with (1) steady state after  
4403 spin up, (2) global net land flux (S<sub>LAND</sub> – E<sub>LUC</sub>) that is an atmosphere-to-land carbon flux over the 1990s ranging  
4404 between -0.3 and 2.3 GtC yr<sup>-1</sup>, within 90% confidence of constraints by global atmospheric and oceanic observations  
4405 (Keeling and Manning, 2014; Wanninkhof et al., 2013), and (3) global E<sub>LUC</sub> that is a carbon source to the atmosphere  
4406 over the 1990s, as already mentioned in [Appendix C.2.2](#). All DGVMs meet these three criteria.

4407 In addition, the DGVMs results are also evaluated using the International Land Model Benchmarking system (ILAMB;  
4408 Collier et al., 2018). This evaluation is provided here to document, encourage and support model improvements through  
4409 time. ILAMB variables cover key processes that are relevant for the quantification of S<sub>LAND</sub> and resulting aggregated  
4410 outcomes. The selected variables are vegetation biomass, gross primary productivity, leaf area index, net ecosystem  
4411 exchange, ecosystem respiration, evapotranspiration, soil carbon, and runoff (see Figure B3 for the results and for the  
4412 list of observed databases). Results are shown in Figure B3 and discussed in Section 3.6.5.

4413 For the uncertainty for S<sub>LAND</sub>, we use the standard deviation of the annual CO<sub>2</sub> sink across the DGVMs, averaging to  
4414 about ± 0.6 GtC yr<sup>-1</sup> for the period 1959 to 2021. We attach a medium confidence level to the annual land CO<sub>2</sub> sink and

Formatted: Indent: First line: 1.27 cm

Deleted: section

4416 its uncertainty because the estimates from the residual budget and averaged DGVMs match well within their respective  
4417 uncertainties (Table 5).

4418

## 4419 C.5 Methodology Atmospheric Inversions

### 4420 C.5.1 Inversion System Simulations

4421 Nine atmospheric inversions (details of each in Table A4) were used to infer the spatio-temporal distribution of the CO<sub>2</sub>  
4422 flux exchanged between the atmosphere and the land or oceans. These inversions are based on Bayesian inversion  
4423 principles with prior information on fluxes and their uncertainties. They use very similar sets of surface measurements  
4424 of CO<sub>2</sub> time series (or subsets thereof) from various flask and in situ networks. One inversion system also used satellite  
4425 xCO<sub>2</sub> retrievals from GOSAT and OCO-2.

4426 Each inversion system uses different methodologies and input data but is rooted in Bayesian inversion principles. These  
4427 differences mainly concern the selection of atmospheric CO<sub>2</sub> data and prior fluxes, as well as the spatial resolution,  
4428 assumed correlation structures, and mathematical approach of the models. Each system uses a different transport model,  
4429 which was demonstrated to be a driving factor behind differences in atmospheric inversion-based flux estimates, and  
4430 specifically their distribution across latitudinal bands (Gaubert et al., 2019; Schuh et al., 2019).

4431 The inversion systems all prescribe similar global fossil fuel emissions for E<sub>FOS</sub>; specifically, the GCP's Gridded Fossil  
4432 Emissions Dataset version 2022 (GCP-GridFEDv2022.2; Jones et al., 2022), which is an update through 2021 of the  
4433 first version of GCP-GridFED presented by Jones et al. (2021), or another recent version of GCP-GridFED (Table A4).  
4434 All GCP-GridFED versions scale gridded estimates of CO<sub>2</sub> emissions from EDGARv4.3.2 (Janssens-Maenhout et al.,  
4435 2019) within national territories to match national emissions estimates provided by the GCP for the years 1959-2021,  
4436 which are compiled following the methodology described in Appendix C.1. GCP-GridFEDv2022.2 adopts the  
4437 seasonality of emissions (the monthly distribution of annual emissions) from the Carbon Monitor (Liu et al., 2020a,b;  
4438 Dou et al., 2022) for Brazil, China, all EU27 countries, the United Kingdom, the USA and shipping and aviation bunker  
4439 emissions. The seasonality present in Carbon Monitor is used directly for years 2019-2021, while for years 1959-2018  
4440 the average seasonality of 2019 and 2021 are applied (avoiding the year 2020 during which emissions were most  
4441 impacted by the COVID-19 pandemic). For all other countries, seasonality of emissions is taken from EDGAR  
4442 (Janssens-Maenhout et al., 2019; Jones et al., 2022), with small annual correction to the seasonality present in year  
4443 2010 based on heating or cooling degree days to account for the effects of inter-annual climate variability on the  
4444 seasonality of emissions (Jones et al., 2021). Earlier versions of GridFED used Carbon Monitor-based seasonality only  
4445 during the years 2019 onwards. In addition, we note that GCP-GridFEDv2022.1 and v2022.2 include emissions from  
4446 cement production and the cement carbonation CO<sub>2</sub> sink (Appendix C.1.1), whereas earlier versions of GCP-GridFED  
4447 did not include the cement carbonation CO<sub>2</sub> sink.

4448 The consistent use of recent versions of GCP-GridFED for E<sub>FOS</sub> ensures a close alignment with the estimate of E<sub>FOS</sub>  
4449 used in this budget assessment, enhancing the comparability of the inversion-based estimate with the flux estimates  
4450 deriving from DGVMs, GOBMs and fCO<sub>2</sub>-based methods. To ensure that the estimated uptake of atmospheric CO<sub>2</sub> by  
4451 the land and oceans was fully consistent with the sum of the fossil emissions flux from GCP-GridFEDv2022.2 and the  
4452 atmospheric growth rate of CO<sub>2</sub>, small corrections to the fossil fuel emissions flux were applied to inversions systems  
4453 using other versions of GCP-GridFED.

Formatted: Indent: First line: 1.27 cm

4454 The land and ocean CO<sub>2</sub> fluxes from atmospheric inversions contain anthropogenic perturbation and natural pre-  
4455 industrial CO<sub>2</sub> fluxes. On annual time scales, natural pre-industrial fluxes are primarily land CO<sub>2</sub> sinks and ocean CO<sub>2</sub>  
4456 sources corresponding to carbon taken up on land, transported by rivers from land to ocean, and outgassed by the  
4457 ocean. These pre-industrial land CO<sub>2</sub> sinks are thus compensated over the globe by ocean CO<sub>2</sub> sources corresponding to  
4458 the outgassing of riverine carbon inputs to the ocean, using the exact same numbers and distribution as described for the  
4459 oceans in Section 2.4. To facilitate the comparison, we adjusted the inverse estimates of the land and ocean fluxes per  
4460 latitude band with these numbers to produce historical perturbation CO<sub>2</sub> fluxes from inversions.

### 4461 C.5.2 Inversion System Evaluation

4462 All participating atmospheric inversions are checked for consistency with the annual global growth rate, as both are  
4463 derived from the global surface network of atmospheric CO<sub>2</sub> observations. In this exercise, we use the conversion  
4464 factor of 2.086 GtC/ppm to convert the inverted carbon fluxes to mole fractions, as suggested by Prather (2012). This  
4465 number is specifically suited for the comparison to surface observations that do not respond uniformly, nor  
4466 immediately, to each year's summed sources and sinks. This factor is therefore slightly smaller than the GCB  
4467 conversion factor in Table 1 (2.142 GtC/ppm, Ballantyne et al., 2012). Overall, the inversions agree with the growth  
4468 rate with biases between 0.03-0.08 ppm (0.06-0.17 GtCyr<sup>-1</sup>) on the decadal average.

4469 The atmospheric inversions are also evaluated using vertical profiles of atmospheric CO<sub>2</sub> concentrations (Figure B4).  
4470 More than 30 aircraft programs over the globe, either regular programs or repeated surveys over at least 9 months, have  
4471 been used in order to draw a robust picture of the system performance (with space-time data coverage irregular and  
4472 denser in the 0-45°N latitude band; Table A6). The nine systems are compared to the independent aircraft CO<sub>2</sub>  
4473 measurements between 2 and 7 km above sea level between 2001 and 2021. Results are shown in Figure B4, where the  
4474 inversions generally match the atmospheric mole fractions to within 0.7 ppm at all latitudes, except for CT Europe in  
4475 2011-2021 over the more sparsely sampled southern hemisphere.

4476

## 4477 Appendix D: Processes not included in the global carbon budget

### 4478 D.1 Contribution of anthropogenic CO and CH<sub>4</sub> to the global carbon budget

4479 Equation (1) includes only partly the net input of CO<sub>2</sub> to the atmosphere from the chemical oxidation of reactive  
4480 carbon-containing gases from sources other than the combustion of fossil fuels, such as: (1) cement process emissions,  
4481 since these do not come from combustion of fossil fuels, (2) the oxidation of fossil fuels, (3) the assumption of  
4482 immediate oxidation of vented methane in oil production. However, it omits any other anthropogenic carbon-containing  
4483 gases that are eventually oxidised in the atmosphere, [forming a diffuse source of CO<sub>2</sub>](#), such as anthropogenic emissions  
4484 of CO and CH<sub>4</sub>. An attempt is made in this section to estimate their magnitude and identify the sources of uncertainty.  
4485 Anthropogenic CO emissions are from incomplete fossil fuel and biofuel burning and deforestation fires. The main  
4486 anthropogenic emissions of fossil CH<sub>4</sub> that matter for the global (anthropogenic) carbon budget are the fugitive  
4487 emissions of coal, oil and gas sectors (see below). These emissions of CO and CH<sub>4</sub> contribute a net addition of fossil  
4488 carbon to the atmosphere.

Formatted: Indent: First line: 1.27 cm

Formatted: Indent: First line: 1.27 cm

4489 In our estimate of  $E_{FOS}$  we assumed (Section 2.1.1) that all the fuel burned is emitted as  $CO_2$ , thus  $CO$  anthropogenic  
4490 emissions associated with incomplete fossil fuel combustion and its atmospheric oxidation into  $CO_2$  within a few  
4491 months are already counted implicitly in  $E_{FOS}$  and should not be counted twice (same for  $E_{LUC}$  and anthropogenic  $CO$   
4492 emissions by deforestation fires). ~~The diffuse atmospheric source of  $CO_2$  deriving from anthropogenic~~ emissions of  
4493 fossil  $CH_4$  ~~is~~ not included in  $E_{FOS}$ . ~~In reality,~~ the ~~diffuse source of  $CO_2$  from  $CH_4$  oxidation contributes~~ to the annual  
4494  $CO_2$  growth~~r~~. Emissions of fossil  $CH_4$  represent 30% of total anthropogenic  $CH_4$  emissions (Saunois et al. 2020; their  
4495 top-down estimate is used because it is consistent with the observed  $CH_4$  growth rate), that is  $0.083 \text{ GtC yr}^{-1}$  for the  
4496 decade 2008-2017. Assuming steady state, an amount equal to this fossil  $CH_4$  emission is all converted to  $CO_2$  by  $OH$   
4497 oxidation, and thus explain  $0.083 \text{ GtC yr}^{-1}$  of the global  $CO_2$  growth rate with an uncertainty range of 0.061 to  $0.098$   
4498  $\text{GtC yr}^{-1}$  taken from the min-max of top-down estimates in Saunois et al. (2020). If this min-max range is assumed to  
4499 be  $2 \sigma$  because Saunois et al. (2020) did not account for the internal uncertainty of their min and max top-down  
4500 estimates, it translates into a  $1-\sigma$  uncertainty of  $0.019 \text{ GtC yr}^{-1}$ .

4501 Other anthropogenic changes in the sources of  $CO$  and  $CH_4$  from wildfires, vegetation biomass, wetlands, ruminants, or  
4502 permafrost changes are similarly assumed to have a small effect on the  $CO_2$  growth rate. The  $CH_4$  and  $CO$  emissions  
4503 and sinks are published and analysed separately in the Global Methane Budget and Global Carbon Monoxide Budget  
4504 publications, which follow a similar approach to that presented here (Saunois et al., 2020; Zheng et al., 2019).

#### 4505 **D.2 Contribution of other carbonates to $CO_2$ emissions**

4506 Although we do account for cement carbonation (a carbon sink), the contribution of emissions of fossil carbonates  
4507 (carbon sources) other than cement production is not systematically included in estimates of  $E_{FOS}$ , except for Annex I  
4508 countries and lime production in China (Andrew and Peters, 2021). The missing processes include  $CO_2$  emissions  
4509 associated with the calcination of lime and limestone outside of cement production. Carbonates are also used in various  
4510 industries, including in iron and steel manufacture and in agriculture. They are found naturally in some coals.  $CO_2$   
4511 emissions from fossil carbonates other than cement not included in our dataset are estimated to amount to about 0.3%  
4512 of  $E_{FOS}$  (estimated based on Crippa et al., 2019).

#### 4513 **D.3 Anthropogenic carbon fluxes in the land-to-ocean aquatic continuum**

4514 The approach used to determine the global carbon budget refers to the mean, variations, and trends in the perturbation  
4515 of  $CO_2$  in the atmosphere, referenced to the pre-industrial era. Carbon is continuously displaced from the land to the  
4516 ocean through the land-ocean aquatic continuum (LOAC) comprising freshwaters, estuaries, and coastal areas (Bauer et  
4517 al., 2013; Regnier et al., 2013). A substantial fraction of this lateral carbon flux is entirely 'natural' and is thus a steady  
4518 state component of the pre-industrial carbon cycle. We account for this pre-industrial flux where appropriate in our  
4519 study (see Appendix C.3). However, changes in environmental conditions and land-use change have caused an increase  
4520 in the lateral transport of carbon into the LOAC – a perturbation that is relevant for the global carbon budget presented  
4521 here.

4522 The results of the analysis of Regnier et al. (2013) can be summarised in two points of relevance for the anthropogenic  
4523  $CO_2$  budget. First, the anthropogenic perturbation of the LOAC has increased the organic carbon export from terrestrial  
4524 ecosystems to the hydrosphere by as much as  $1.0 \pm 0.5 \text{ GtC yr}^{-1}$  since pre-industrial times, mainly owing to enhanced  
4525 carbon export from soils. Second, this exported anthropogenic carbon is partly respired through the LOAC, partly

Deleted: Anthropogenic

Deleted: are however

Deleted: , because these fugitive emissions are not included in

Deleted: fuel inventories. Yet they contribute

Deleted: rate after  $CH_4$  gets oxidized into  $CO_2$

Formatted: Indent: First line: 1.27 cm

Formatted: Indent: First line: 1.27 cm

4532 sequestered in sediments along the LOAC and to a lesser extent, transferred to the open ocean where it may accumulate  
4533 or be outgassed. The increase in storage of land-derived organic carbon in the LOAC carbon reservoirs (burial) and in  
4534 the open ocean combined is estimated by Regnier et al. (2013) at  $0.65 \pm 0.35 \text{ GtC yr}^{-1}$ . The inclusion of LOAC related  
4535 anthropogenic  $\text{CO}_2$  fluxes should affect estimates of  $S_{\text{LAND}}$  and  $S_{\text{OCEAN}}$  in Eq. (1) but does not affect the other terms.  
4536 Representation of the anthropogenic perturbation of LOAC  $\text{CO}_2$  fluxes is however not included in the GOBMs and  
4537 DGVMs used in our global carbon budget analysis presented here.

#### 4538 **D.4 Loss of additional land sink capacity**

4539 Historical land-cover change was dominated by transitions from vegetation types that can provide a large carbon sink  
4540 per area unit (typically, forests) to others less efficient in removing  $\text{CO}_2$  from the atmosphere (typically, croplands).  
4541 The resultant decrease in land sink, called the 'loss of additional sink capacity', can be calculated as the difference  
4542 between the actual land sink under changing land-cover and the counterfactual land sink under pre-industrial land-  
4543 cover. This term is not accounted for in our global carbon budget estimate. Here, we provide a quantitative estimate of  
4544 this term to be used in the discussion. Seven of the DGVMs used in Friedlingstein et al. (2019) performed additional  
4545 simulations with and without land-use change under cycled pre-industrial environmental conditions. The resulting loss  
4546 of additional sink capacity amounts to  $0.9 \pm 0.3 \text{ GtC yr}^{-1}$  on average over 2009-2018 and  $42 \pm 16 \text{ GtC}$  accumulated  
4547 between 1850 and 2018 (Obermeier et al., 2021). OSCAR, emulating the behaviour of 11 DGVMs finds values of the  
4548 loss of additional sink capacity of  $0.7 \pm 0.6 \text{ GtC yr}^{-1}$  and  $31 \pm 23 \text{ GtC}$  for the same time period (Gasser et al., 2020).  
4549 Since the DGVM-based ELUC estimates are only used to quantify the uncertainty around the bookkeeping models'  
4550 ELUC, we do not add the loss of additional sink capacity to the bookkeeping estimate.

Formatted: Indent: First line: 1.27 cm

